JOINT THREE-FLAVOUR OSCILLATION ANALYSIS OF ν_μ DISAPPEARANCE AND ν_e APPEARANCE IN THE T2K NEUTRINO BEAM

by

Patrick de Perio

A thesis submitted in conformity with the requirements
for the degree of Doctor of Philosophy
Graduate Department of Physics
University of Toronto

Abstract

Joint Three-Flavour Oscillation Analysis of ν_μ Disappearance and ν_e Appearance in the
T2K Neutrino Beam

Patrick de Perio
Doctor of Philosophy
Graduate Department of Physics
University of Toronto
2014

The Tokai to Kamioka (T2K) experiment is a long-baseline neutrino oscillation experiment based in Japan. An off-axis, high purity muon neutrino (ν_μ) beam is produced at the Japan Proton Accelerator Research Complex by colliding a proton beam with a graphite target. The neutrinos are detected at a near detector complex (ND280), situated 280 m from the neutrino production target, and the Super-Kamiokande (SK) far detector at 295 km. This thesis first outlines current knowledge and challenges in the physics of neutrinos, then describes the T2K beam and detectors, including a novel optical transition radiation monitor for precisely measuring the proton beam in order to determine the neutrino beam direction. A framework for evaluating the uncertainties in neutrino interactions and pion hadronic interactions in ND280 and SK is presented. A new SK event reconstruction algorithm is described and the SK detector systematic errors are evaluated based on atmospheric neutrino and cosmic ray muon data. These developments are used in a Markov Chain Monte Carlo neutrino oscillation analysis of the T2K Run $1-4$ data corresponding to 0.657×10^{21} protons on target. The analysis simultaneously considers the 2013 ND280 ν_μ samples, and SK single muon and single electron samples, producing a measurement of ν_μ disappearance and $\nu_\mu \rightarrow \nu_e$ appearance. The estimated oscillation parameters and 68% Bayesian credible intervals (CI) at $\delta_{CP} = 0$ are as follows: $\sin^2\theta_{23} = 0.520^{+0.045}_{-0.050}$, $\sin^2\theta_{13} = 0.0454^{+0.011}_{-0.014}$ and $|\Delta m^2_{32}| = 2.57 \pm 0.11$, with the point of highest posterior probability in the inverted neutrino mass hierarchy. Recent measurements of θ_{13} from reactor neutrino experiments are combined with the T2K data resulting in the following estimates: $\sin^2\theta_{23} = 0.528^{+0.055}_{-0.038}$, $\sin^2\theta_{13} = 0.0250 \pm 0.0026$ and $|\Delta m^2_{32}| = 2.51 \pm 0.11$, with the point of highest posterior probability in the normal hierarchy. Furthermore, the data hint toward $\delta_{CP} \approx -\pi/2$ with a 90% CI excluding values between 0.14π–0.87π.

Contributions

This thesis is based on the work of around 500 people over a period of 15 years. This section will clarify my personal contributions to the T2K experiment.

My first contribution was on the prototyping and development of the calibration system for the OTR proton beam monitor. This involved several experiments in the lab at Toronto, fabrication of components, software development (analysis and end-user GUIs), and the installation and commissioning at J-PARC. The on-site work involved mechanical assembly, cabling and electronics wiring, surveying and alignment. I also analyzed beam and survey data for beamline monitor alignment. This is described in Chapter 4, though most of the later analysis must be credited to Slavic Galymov and Mark Hartz.

I inherited the T2KReWeight software package from Jim Dobson, which I implemented for the treatment of most of the systematics in the neutrino oscillation and cross section analyses. I coded many of the cross section systematics as well as the interface for the flux systematics. I used this software to develop a framework for fitting cross section data from other experiments. However, I soon dropped this effort, which was then completed by Peter Sinclair and Philip Rodrigues. The results of this work are presented in Chapter 5.

I helped develop the pion interaction model within our neutrino interaction software, NEUT, by modifying some of the fundamental physics models with code written by Roman Tacik and myself. I also performed an extensive literature search for pion scattering and photoproduction data, which I used to tune the model and evaluate systematic uncertainties. I developed the cascade reweighting algorithm, which I interfaced to T2KReWeight and used to propagate the systematics to the oscillation analyses. I was invited to the NuInt11 conference to present this work. Furthermore, I coded the model into the SK detector simulation and wrote the corresponding reweighting algorithm. These developments are described in Chapter 6 and Appendix A. I led the validation of the modified detector simulation and reweighting, but most of that work was done by Hirohisa Tanaka and Sophie Berkman.

The bulk of the new SK reconstruction, introduced in Chapter 8, was coded by Shimpei Tobayama and Mike Wilking. I developed the sub-event algorithm and performed the validation studies with cosmic ray muon and atmospheric neutrino data described in the rest of the chapter and Appendix B.

My work with the NEUT, T2KReWeight and SK software led me to a software support role, assisting end-users of all the packages with installation, running and debugging. I took a leading role in porting the SK software from *g77* to *gFortran* so it may be used on our newer machines. I also helped develop the NEUT-ND280 software interface for ND280 simulations. All this experience led me to take charge of an official MC simulation production for both ND280 and SK, which was carried out at large computer clusters around the world. This also involved the distribution of files to the entire collaboration. I continued to provide support for later productions.

The final oscillation analysis presented in Chapter 9 was performed by Richard Calland and Asher Kaboth. I used the software they developed, MaCh3, to evaluate the SK detector systematic uncertainties, which was a necessary input to the analysis. Chapter 8 and Appendix C describes my implementation of the SK atmospheric data into the MaCh3 framework. The final combination of SK systematic errors was done by James Imber. Being part of the MaCh3 group, I was able to follow the oscillation analysis closely and offer suggestions where possible. I was chosen by the collaboration to give the first public presentation of these results, at the Moriond conference in March 2014.

The rest of the content in this thesis was produced by others and, along with everyone mentioned above, they are properly referenced throughout the text. The table below is a summary of internal technical notes resulting from my work, with references to the chapters they apply to. Those without a chapter reference were auxiliary studies for previous oscillation analyses and are not explicitly discussed in this thesis.

Technical Note Title	Chapter
Technical Design Report for the T2K Optical Transition Radiation Monitor	4
Prototyping and Simulation of the T2K OTR Monitor	4
2010a neutrino interaction systematic uncertainty choices for the NEUT generator	5
NEUT Systematic Studies for 2010a Analysis	5
NEUT Nuclear Effects	6
Pion Hadronic Secondary Interactions in Super-Kamiokande	6
Constraining the Flux and Cross Section Models with Data from the ND280 Detector for the 2012a Oscillation Analysis	
Cross section parameters for the 2012a oscillation analysis	5
Implementation of the NIWG Cross Section Parameterization	5
Multi-ring Events in T2K Runs 1 and 2	
fiTQun: A New Reconstruction Algorithm for Super-K	8
Data/MC Simulation Comparisons with fiTQun v3r1	8
Super-K Systematic Uncertainties for RUN1-4 Joint $\nu_e + \nu_\mu$ Analyses	8

Acknowledgements

My journey through graduate school and the T2K experiment has been the most enlightening and enjoyable experience. I owe it all to the people who have supported me, shared their kindness and ideas, and taught me everything I needed to know. My path was somewhat of a meandering one, which led me to meet many individuals, many more than I can mention here. You have all influenced me and contributed to who I am as a scientist and a human being. For this I am truly grateful and I thank you all.

It began with a phone call to John Martin, my supervisor, who then took me on as a lowly undergraduate. His calm and deliberate approach to everything convinced me to transition into graduate school with him. He has always provided a strong, parentlike foundation from which I could freely explore and take the path that I did. His wisdom permeates, but focused whenever I had a critical problem, whether scientific, political, social or moral. John is also an entertaining singer and dancer.

The OTR group has been with me since the beginning. Sampa Bhadra was quite the motivating figure with high levels of energy and enthusiasm. She made sure I was happy and that I ate well. Alysia Marino introduced me to the world of particle physics analysis. She consistently strived for perfection, which became a beacon to follow. Mircea Cadabeschi and Dave Morris bestowed upon me their expertise in mechanical and systems design engineering. My gratitude to my seniors Slavic Galymov and Brian Kirby who paved the way. Thanks to Elder Pinzon and Mitchell Yu who continued on the detector during my final years. When Mark Hartz joined the team, he picked up the entire system with astonishing speed. He demonstrated analytical prowess by developing high profile analyses while simultaneously assisting with my own projects and endless questioning (in the jazz bars of Mito). Akira Konaka closely followed my work on the OTR, as well as all my subsequent work. He would always pinpoint the most important question or implication and offer very helpful ideas. Akira's excitement about physics shone and was quite contagious.

My first experience of international collaboration was with the T2K beam group in Japan. I especially thank Kodai Matsuoka, Hajime Kubo, Kento Suzuki, Ken Sakashita, Atsuko Ichikawa, Takanobu Ishii, Hidekazu Kakuno, Takeshi Nakadaira, Yoshikazu Yamada, Tetsuro Sekiguchi, Masaru Tada and Takuya Hasegawa. Their discussions with me personally, in meetings, radiation areas and even during the stressful times of beam operation in the CCR were instrumental to my understanding of all the aspects of a neutrino beam. It was a great honour to be a member of this exceptional group, which was awarded the Suwa prize in 2013.

Yoichiro Suzuki granted me the opportunity to work for several months at Super-Kamiokande, based in the secluded and beautiful mountain village, Mozumi. This was my first long-term period away from home in Canada, and really tested my ability to adjust and thrive in such a different environment. I could not have accomplished what I did without the mentorship of Yoshinari Hayato. He held my hand as I delved into the labyrinth of Fortran, neutrino interaction software and all things Super-K. My emotional sanity in such a potentially isolating environment was kept in check by Motoyasu Ikeda. Moto never failed to collect me for meshi, acted as my Japanese mentor and interpreter, and in general integrated me into the Mozumi lifestyle and social setting.

My work at Super-K led me into the T2K neutrino interactions group. The combined knowledge of Morgan Wascko, Kevin McFarland and Hayato-san guided my analyses to fruition and they readily defended me whenever I faltered. I thank Roman Tacik and Jan Sobcyk for valuable discussions about pions. Together with Peter Sinclair, Philip Rodrigues and Ryan Terri, we built a seemingly impossible analysis up from scratch. They took it beyond what I would have imagined into a most sophisticated analysis of neutrino cross section data. I greatly appreciated the work by Jordan Myslik, Kevin Connolly, Flor de Maria Blaszczyk, Kei Ieki, Ikeda-san and the whole DUET team for continuing the exploration of pions.

The T2K-SK group is a bottomless pit of knowledge and experience. Joshua Hignight, Shunichi Mine, Hide Tanaka, Yasuhiro Nishimura, James Imber, Jun Kameda, Kimihiro Okumura, Makoto Miura, Roger Wendell, Shoei Nakayama, Hiroshi Kaji, Josh Albert, Taritree Wongjirad, Tarek Akiri, Alex Himmel, Yusuke Koshio, Chris Walter and Masato Shiozawa, have all sat down with me several times to guide me, help me understand their work or bring me up to speed in all the projects I undertook.

Computing was a significant part of my work and I must mention several groups who taught me the skills and dealt with my problems. I thank Compute Canada and SciNet for awarding us computing time on one of the most powerful clusters in the world. I usually felt like I was taking the system down, but the SciNet team was always helpful and ready to answer my questions regardless of what time zone I was in. I especially thank Leslie Groer and Neil Knecht who worked with me personally on getting the entire framework setup for what would be a significant amount of computing for the whole T2K collaboration. Thanks to Renee Poutissou, Thomas Lindner and Ben Still for helping me figure out the ND280 production and GRID system. Hayato-san also managed the computing cluster at Kamioka and taught me how to use the system there. And to the PCS team, especially Gregory Wu who helped setup all my local computers and even hard reset my machines on request.

I will miss being a part of the SKanada group: Mike Wilking, Sophie Berkman, Shimpei Tobayama, Hirohisa Tanaka, Akira and Roman. First, I must offer my gratitude to all the Super-K members for accepting us into their collaboration, giving us the opportunity to grow and explore our ideas; in particular, a new reconstruction program brought on by Mike. He led the team with zeal and made every discussion fun(ny). I thank Shimpei Tobayama who worked out the guts of the reconstruction and Sophie for helping me with the pions. Thanks to Andy Missert, Eric Zimmerman and Blair Jamieson who helped implement and validate the reconstruction. It was a pleasure to make such a huge impact with this ingenious team. But what I will fondly remember are the road trips, fountain drinking, freezing cold swimming and midnight vocal practice (I'm amazed I graduated).

It was a privilege to work with the oscillation analysis group, which tied together the work of an entire collaboration and produced the analyses that would ultimately become my thesis results. I was fortunate to witness the evolution of the analysis from the beginning, led by Tsuyoshi Nakaya. I worked closely with Josh Albert and Claudio Giganti who gave my first insight on how everything could fit together. I thank Jim Dobson for leaving with me the reweighting package that allowed the easy interface of all my work into the oscillation analyses. The successive leaders, Kendall Mahn and Ichikawa-san, continuously motivated and made sure we were always on track and organized. Kendall's consistent self-sacrifice and willingness to help me and everyone is to be commended. I thank Lorena Escudero for responding to my countless requests for plots and numbers. And a great thank you to the MuSiC/MaCh3 team, Richard Calland, Asher Kaboth, David Payne and Casey Bojechko, and our statistics gurus Dean Karlen and Scott Oser, who laid the groundwork for my SK analysis. Dean and Scott readily addressed all the issues brought up by the group and me and I was always impressed by the power and clarity of their speech. I am especially indebted to Richard and Asher who got me up to speed with Markov chains and tenaciously generated the results that conclude this thesis.

I salute Takashi Kobayashi and Chang Kee Jung, the fearless leaders of T2K. Their encouragement of the young people, especially to me personally, was very much taken to heart. Furthermore, they have raised my expectations for a fun, social and physically active collaboration, whether in a karaoke box or on the volleyball court.

My time with the T2K-Canada group will not be forgotten. The wide variety of expertise, enthusiasm and vibrant discourse was invigorating. They are like a second family to me, even so far as hosting me in their homes in Vancouver and living together in Minouchi. The work parties, late night talks, BBQs and countless meals together were something I looked forward to on every visit.

I sincerely thank Hiro, a great mentor and friend. Somehow, he was always within a Skype-chat away. However, he seemed to respond to every question with another question, teaching me to find the answer myself. This applied to most situations in physics, as well as in discussions about life and purpose in general. In other cases he demonstrated graduate student-like capabilities whenever we tackled problems together. Hiro is a quiet driving force, not only in most of my analyses, but within the whole collaboration. With him, I had the courage to walk through pitch dark tunnels and explore ghostly, abandoned mining towns.

My heartfelt thanks goes out to all my friends across Japan. I wish I could list them all; in addition to T2K, the XMASS, SK LowE and ATMPD, KamLAND-Zen and KGB48 groups. They brought me into their lives and made me feel most welcome in a foreign country, all the way from Sendai through Kyoto. I cherish the moments we discussed our work, philosophy and personal lives. And of course the office parties, conference volunteering, karaoke, izakayas and wagyu. They have truly coloured my life and made this a once-in-a-lifetime experience (actually I hope to come back and see you all again).

I appreciate the J-PARC User's Office and Kamioka administrative staff for their efficiency and friendliness. They were always up for a conversation, whether in English or Japanese. The Kamioka security guards routinely made sure I was safe and not locked out of my room. And I thoroughly enjoyed our scenic drives into the mountain, punctuated by our struggles to communicate. I thank Winnie Kam and Krystyna Biel for promptly dealing with all my administrative issues back at home in Toronto.

Thanks to Dan Iaboni and the Parkour community. They have provided me an invaluable experience in leadership, teaching and communication. Dan was instrumental in tearing down my ego, but then also helped me secure the prestigious Vanier award. His genuine curiosity in physics motivates me to improve my communication to the layman.

To my friends and family at home. I realize a graduate student's life requires a significant commitment. The fact that my experiment is in another country does not make things any easier. I admit I sometimes become too absorbed in my work and disappear for long periods of time. I wholeheartedly appreciate the fact that when I do reappear, they are all as accepting and supportive as ever. I thank my mom and dad, Terry and Rey, for their continuous support and raising me into who I am today. Up to this day, they encourage me to ask questions about the world and keep up with my studies.

Finally, I thank my wonderful partner, Jia Liu. She has supported me even through the most difficult separations and stressful periods. She catalyzed a new effort of self-growth by motivating not only my questioning of the universe, but of myself as a person, for which I am deeply grateful.

Dedication

To my parents.

Contents

List of Tables

List of Figures

Chapter 1

Introduction

The field of physics aims to develop models or mathematical theories that govern our physical world. The best models describe existing data and predict new, yet unobserved phenomena. An outstanding example is the Standard Model (SM) of particle physics, which has been remarkably successful in explaining a wide variety of experimental results and making accurate predictions. The SM consists of a set of fundamental particles: six quarks, six leptons and four gauge bosons, as shown in Figure 1.1. The quarks and leptons are grouped into 3 families or generations, which are identical except for the particle masses. The gauge bosons are responsible for the three types of interactions or forces between particles: the strong, electromagnetic and weak forces. The model also predicts the existence of a Higgs boson, arising from a mechanism that generates the mass of each particle. The recent discovery of a SM Higgs-like boson in proton-proton collisions at the Large Hadron Collider (LHC) at CERN is a monumental achievement in the field, completing the set of SM particles.

Intrinsic properties of each particle, the mass, electric charge and spin, are shown in the top left corner of each block in Figure 1.1. Particles with fractional spin, quarks and leptons, are called fermions while particles with integer spin are called bosons. For each charged fermion there exists an anti-fermion, also referred to as an anti-particle, with the

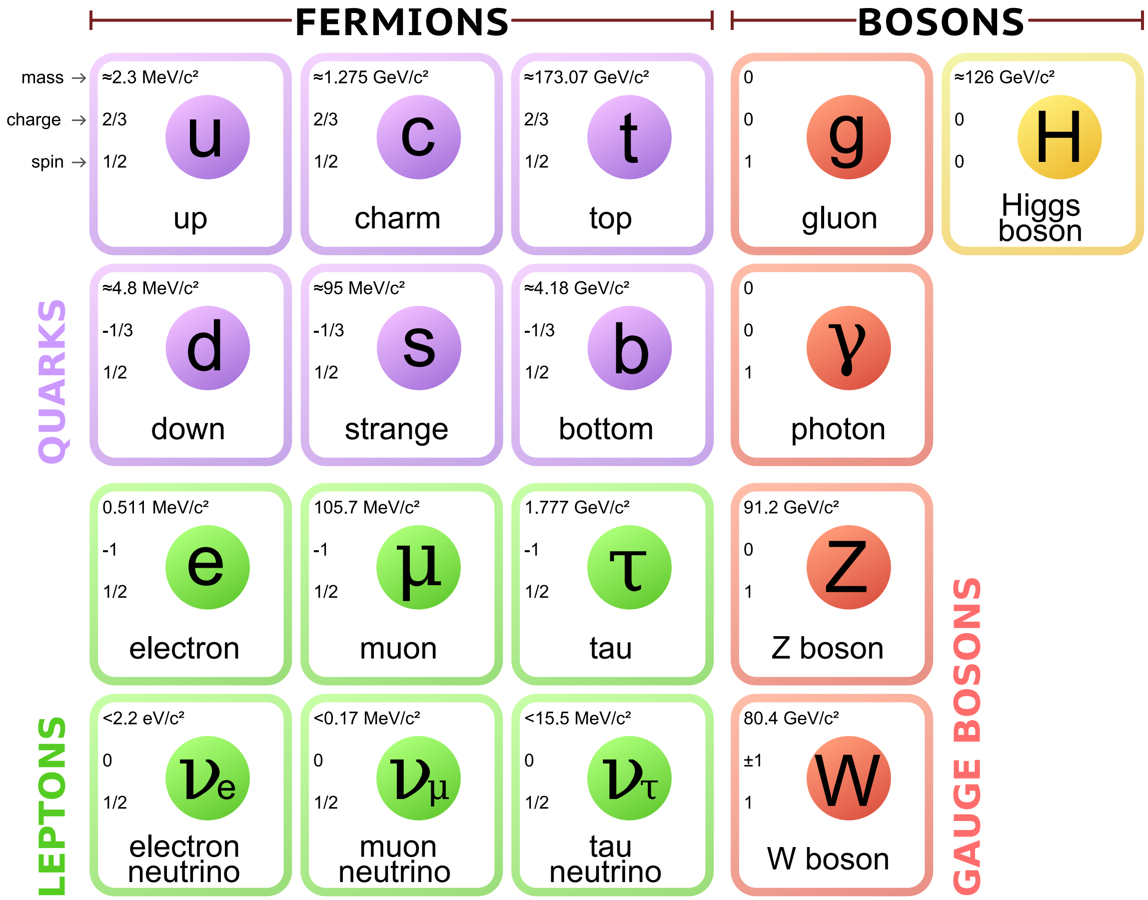

Figure 1.1: The Standard Model of particle physics. The three generations of fermions make up the first three columns. The fermions in each row are identical except for increasing mass.

same mass but opposite charge. An anti-particle is denoted by a bar over the particle symbol or by explicitly showing the charge, for example $\bar{u}$ or e^+. For a chargeless fermion (neutrino), a lepton number is defined to determine its particle or anti-particle nature[1]. Matter (anti-matter) is then a collection of particles (anti-particles).

An interaction between particles is modelled by the exchange of a gauge boson. The strong force is mediated by gluons, which couple only to the quarks. Thus, for example, it is responsible for binding the quarks inside a proton or neutron, which are members of a set of composite particles called hadrons. The strong force also describes the collisions between hadrons such as those in the LHC. The electromagnetic (EM) force is mediated by the photon, which couples to any particle with non-zero charge. Finally, the weak force is mediated by the W and Z bosons, which couple to all the fermions. It is responsible for processes such as radioactive decay and any interaction involving a neutrino or anti-neutrino.

The neutrino was first proposed in 1930 [1] in an attempt to explain the continuous electron energy spectrum observed in the $\beta(e)$-decay of a heavy nucleus into a lighter nucleus [2]:

$$n \rightarrow p + e^- + \bar{\nu}_e. \tag{1.1}$$

One way to infer the existence of the neutrino is by observing the electron in the inverse β decay process:

$$\bar{\nu}_e + p \rightarrow n + e^+. \tag{1.2}$$

However, the predicted cross section or probability of occurrence of this weak force process is extremely small [3]. It required an intense source of neutrinos from a nuclear reactor, a large detector and ~100 days of data collection for the first detection of the neutrino (actually $\bar{\nu}_e$), over 20 years after its proposal [4]. A second flavour or type of neutrino, ν_μ,

---

[1] The charge conjugation (C) transformation is defined as flipping the sign of the charge and lepton number of a particle. C-symmetry implies that the laws of physics should be the same with the interchange of a particle with its anti-particle, for example in electromagnetic interactions.

was discovered in 1962 from the decay of charged pions (the pion is a hadron) [5]. The third and last flavour neutrino of the SM, ν_τ, was discovered in 2001 [6]. Measurements of the Z boson decay determine that there are only these three light, active neutrinos that couple via the weak interaction [7].

The helicity or handedness of a particle is defined as the projection of the spin (intrinsic angular momentum) onto the direction of motion. A particle is right-handed (RH) or left-handed (LH) if the spin is aligned or anti-aligned to its direction, respectively. In 1958, the light neutrino was measured to be LH assuming conservation of angular momentum [8]. The non-observation of a RH neutrino led to the belief that the neutrino was massless, since if they did have mass then it should be possible to move into a reference frame that overtakes the neutrino, which flips the observed helicity. Furthermore, this was consistent with the detection of the neutrino through the weak interaction of the SM, which couples only to LH particles (and RH anti-particles)[2]. Thus, the SM assumes massless neutrinos.

In 1998 the phenomenon of neutrino oscillation was discovered [9]. Neutrino oscillation, the quantum-mechanical transformation of a neutrino from one flavour to another during its travel, can only occur if the neutrino has finite mass. This discovery opens the door to a rich theoretical and experimental program beyond the SM. For example, it is believed that matter and anti-matter were created in equal amounts at the Big Bang; however, the present day Universe is matter dominated suggesting some asymmetry in the evolution of the early Universe. Some of the leading theories that explain this require a source of CP violation or an asymmetry in the laws of physics upon charge conjugation and parity transformation. CP violation has been observed in the quark sector [10, 11], though at an insufficient level to explain the matter asymmetry. Neutrino oscillation provides another possible source of CP violation in the lepton sector. Furthermore, the

---

[2] The weak interaction theory maximally violates parity, where a parity transformation (P) inverts the sign of one spatial coordinate corresponding to inverting the helicity.

chargeless neutrino can be a Majorana particle, or its own anti-particle, which supports the theories above and gives rise to new physics beyond the SM. The possible Majorana nature of neutrinos, their tiny absolute mass and neutrino oscillation are intimately related, as discussed in Chapter 2, and represent a field ripe for further discovery.

1.1 Thesis Overview

This thesis focuses on the elucidation of CP violation in neutrinos, through a measurement of neutrino oscillations with the T2K (Tokai to Kamioka) experiment in Japan. A neutrino oscillation *appearance* experiment searches for the transformation from one type of neutrino ν_α, to a different type ν_β, after some distance of travel to a *far* detector. In a complementary manner, a *disappearance* experiment measures the survival rate of one type of neutrino, where $\nu_\beta = \nu_\alpha$. Experimentally, the number of interactions N_{ν_β} in the far detector can be measured and compared to the prediction:

$$N_{\nu_\beta} \sim P_{\nu_\alpha \to \nu_\beta} \cdot \varphi_{\nu_\alpha} \cdot \sigma_{\nu_\beta} \cdot \varepsilon_{\nu_\beta}, \tag{1.3}$$

where φ_{ν_α} is the initial flux of ν_α, σ_{ν_β} is the cross section (or probability) for a ν_β interaction in the detector, ε_{ν_β} is the efficiency for detecting that interaction and $P_{\nu_\alpha \to \nu_\beta}$ is the probability of oscillation.

The interesting physics (for example, CP violation) is contained in the P factor. In order to extract information about P based on some measurement N, one must have a good understanding and control of the other three factors. All four factors come from some theoretical model whose parameters are measured with (or tuned to) experimental data (or constrained by theory).

This thesis describes specific contributions to each factor in Equation 1.3 in the context of T2K:

- Chapter 2 describes the neutrino oscillation model and current experimental measurements.

- Chapter 3 gives an overview of the T2K experimental apparatus.
- Chapter 4 describes an optical transition radiation proton beam monitor used to constrain φ.
- Chapter 5 describes the simulations for each factor and the experimental constraints.
- Chapter 6 describes the development and constraints for the pion interaction model in the neutrino interaction and detector simulations.
- Chapter 7 describes a statistical framework used for the analysis in the following chapters.
- Chapter 8 describes the analysis of the Super-Kamiokande detector, the far detector for T2K, and the constraints on ε.
- Chapter 9 describes oscillation analysis, combining all the inputs for each factor, to extract measurements of the oscillation parameters.

Chapter 2

Neutrino Physics

This chapter discusses the aspects of the physics of neutrinos relevant to this thesis, beginning by outlining the formalism of neutrino oscillations in vacuum and matter in Section 2.1. Experimental measurements have validated this oscillation model and placed constraints on the parameters, as summarized in Section 2.2. The topic of the absolute neutrino mass is discussed in Section 2.3. Finally, Section 2.4 introduces a leading candidate theory for the explanation of the matter anti-matter asymmetry, which outlines the importance of the experimental study of neutrino oscillation and neutrino mass.

2.1 Neutrino Oscillation Theory

According to the electroweak theory of the SM [12], neutrinos (anti-neutrinos) are created in a flavour or weak state, ν_α ($\bar{\nu}_\alpha$) where $\alpha \in \{e, \mu, \tau\}$, from some charged current (CC) interaction such as π decay or μ decay as shown in Figure 2.1. These flavour states are produced as a quantum mechanical superposition of mass states ν_k ($\bar{\nu}_k$) with masses m_k that we are currently unable to resolve experimentally. This is written mathematically as:

$$|\nu_\alpha\rangle = \sum_k U^*_{\alpha k}|\nu_k\rangle \tag{2.1}$$

$$|\bar{\nu}_\alpha\rangle = \sum_k U_{\alpha k}|\bar{\nu}_k\rangle \tag{2.2}$$

where $U_{\alpha k}$ are elements of a unitary mixing matrix.

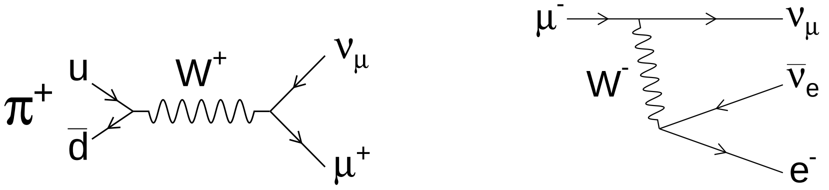

Figure 2.1: Feynman diagrams for pion decay (left) and muon decay (right) showing the charged current (W^+) weak interaction process.

Equations 2.1 and 2.2 for neutrino and anti-neutrino differ only by a complex conjugate of the matrix elements. Thus, this derivation will assume neutrino and the result for anti-neutrino follows similarly.

The mass states $|\nu_k\rangle$ are eigenstates of the Hamiltonian with energy

$$E_k = \sqrt{\mathbf{p}^2 + m_k^2}, \tag{2.3}$$

where $\mathbf{p}$ is the momentum of the neutrino. The time evolution of ν_α is derived by using Schrödinger's equation so that Equation 2.1 becomes

$$|\nu_\alpha(t)\rangle = \sum_k U^*_{\alpha k} e^{-iE_k t}|\nu_k\rangle. \tag{2.4}$$

The amplitude for finding some ν_β after the original neutrino propagates for some time t is given by the inner product of Equation 2.1 with Equation 2.4 and then using orthonormality of the mass eigenstates:

$$\langle\nu_\beta|\nu_\alpha(t)\rangle = \sum_{k,j}\langle\nu_j|U_{\beta j}U^*_{\alpha k}e^{-iE_k t}|\nu_k\rangle = \sum_k U^*_{\alpha k}U_{\beta k}e^{-iE_k t}. \tag{2.5}$$

The probability for observing ν_β, P as in Equation 1.3, is then

$$P_{\nu_\alpha\to\nu_\beta}(t) = |\langle\nu_\beta|\nu_\alpha(t)\rangle|^2 = \sum_{k,j} U^*_{\alpha k}U_{\beta k}U_{\alpha j}U^*_{\beta j}e^{-i(E_k - E_j)t}. \tag{2.6}$$

Assuming that the neutrino is ultra-relativistic, the time of propagation t is approximately equal to the distance of travel L and Equation 2.3 can be Taylor expanded such that Equation 2.6 becomes

$$P_{\nu_\alpha \to \nu_\beta}(L, E) = \sum_{k,j} U^*_{\alpha k} U_{\beta k} U_{\alpha j} U^*_{\beta j} \exp\left(-i \frac{\Delta m^2_{kj} L}{2E}\right), \tag{2.7}$$

where $E = |\mathbf{p}|$ is the neutrino energy neglecting m_k, and $\Delta m^2_{kj} \equiv m^2_k - m^2_j$ are the *mass-squared differences* which are physical constants to be measured. This oscillatory function (complex exponential), where $\frac{\Delta m^2_{jk} L}{2E}$ defines the phase and U defines the amplitude, gives rise to the term *neutrino oscillation.* If ν_k are massive and differ in mass, it is in principle possible to observe the transition from one neutrino state to another. Conversely, the observation of neutrino oscillation implies that neutrinos are massive.

It is instructive to rewrite Equation 2.7 in the form

$$\begin{aligned} P_{\nu_\alpha \to \nu_\beta}(L, E) = \delta_{\alpha\beta} &- 4 \sum_{k>j} \mathfrak{Re}[U^*_{\alpha k} U_{\beta k} U_{\alpha j} U^*_{\beta j}] \sin^2\left(\frac{\Delta m^2_{kj} L}{4E}\right) \\ &+ 2 \sum_{k>j} \mathfrak{Im}[U^*_{\alpha k} U_{\beta k} U_{\alpha j} U^*_{\beta j}] \sin\left(\frac{\Delta m^2_{kj} L}{2E}\right). \end{aligned} \tag{2.8}$$

Then in the anti-neutrino case if a similar derivation is followed from Equation 2.2 by replacing U with U^*, the transition probability becomes (by simply negating the imaginary part)

$$\begin{aligned} P_{\bar\nu_\alpha \to \bar\nu_\beta}(L, E) = \delta_{\alpha\beta} &- 4 \sum_{k>j} \mathfrak{Re}[U^*_{\alpha k} U_{\beta k} U_{\alpha j} U^*_{\beta j}] \sin^2\left(\frac{\Delta m^2_{kj} L}{4E}\right) \\ &- 2 \sum_{k>j} \mathfrak{Im}[U^*_{\alpha k} U_{\beta k} U_{\alpha j} U^*_{\beta j}] \sin\left(\frac{\Delta m^2_{kj} L}{2E}\right). \end{aligned} \tag{2.9}$$

The remaining factor to define is the mixing matrix U or the amplitude of the oscillation. In general, U will be a $(3+n) \times (3+n)$ unitary matrix, corresponding to the three active neutrino states (that interact weakly) plus $n = (0, 1, \cdots)$ additional *sterile* states ν_s (that do not interact weakly). The possibility that sterile neutrinos exist is beyond the scope of this thesis. So for 3-neutrino mixing, U is given by the Pontecorvo-Maki-

Nakagawa-Sakata (PMNS) matrix

$$U = \begin{array}{cc} & \begin{array}{ccc} \nu_1 \qquad\qquad\qquad & \nu_2 \qquad\qquad\qquad & \nu_3 \end{array} \\ \begin{array}{c} \nu_e \\ \nu_\mu \\ \nu_\tau \end{array} & \begin{pmatrix} c_{12}c_{13} & s_{12}c_{13} & s_{13}e^{-i\delta} \\ -s_{12}c_{23} - c_{12}s_{23}s_{13}e^{i\delta} & c_{12}c_{23} - s_{12}s_{23}s_{13}e^{i\delta} & s_{23}c_{13} \\ s_{12}s_{23} - c_{12}c_{23}s_{13}e^{i\delta} & -c_{12}s_{23} - s_{12}c_{23}s_{13}e^{i\delta} & c_{23}c_{13} \end{pmatrix} \end{array} \begin{pmatrix} 1 & 0 & 0 \\ 0 & e^{i\lambda_2} & 0 \\ 0 & 0 & e^{i\lambda_3} \end{pmatrix} \tag{2.10}$$

where $s_{ij} \equiv \sin\theta_{ij}$ and $c_{ij} \equiv \cos\theta_{ij}$, θ_{ij} are three mixing angles and δ (also called δ_{CP}) and λ_i are CP-violating phases. The *Majorana* phases λ_i are physically relevant only if neutrinos are identical to their anti-particles, discussed more in Section 2.3.1. However upon substitution of Equation 2.10 into Equation 2.7 it can be shown that the Majorana phases do not affect the neutrino oscillation probabilities. Equation 2.10 can be factorized and written in the form (ignoring the Majorana part)

$$U = \begin{pmatrix} 1 & 0 & 0 \\ 0 & c_{23} & s_{23} \\ 0 & -s_{23} & c_{23} \end{pmatrix} \begin{pmatrix} c_{13} & 0 & s_{13}e^{-i\delta} \\ 0 & 1 & 0 \\ -s_{13}e^{i\delta} & 0 & c_{13} \end{pmatrix} \begin{pmatrix} c_{12} & s_{12} & 0 \\ -s_{12} & c_{12} & 0 \\ 0 & 0 & 0 \end{pmatrix}. \tag{2.11}$$

Thus we are left with six parameters describing the three-flavour case: the mixing angles θ_{12}, θ_{23}, θ_{13}, the mass-squared differences Δm^2_{21}, Δm^2_{32} (with $\Delta m^2_{31} = \Delta m^2_{32} - \Delta m^2_{12}$)[1], and a CP-violating phase δ. There is also some ambiguity in the sign of Δm^2_{32} (and Δm^2_{31}) since neutrino oscillations are only concerned with differences in neutrino mass squared. By convention, we call $\Delta m^2_{31,32} > 0$ *normal hierarchy* (NH) and $\Delta m^2_{31,32} < 0$ *inverted hierarchy* (IH) depicted in Figure 2.5, and the sign affects the exact calculation of oscillation probabilities as discussed in Section 2.2.4.

The full derivation of oscillation probabilities in the 3-neutrino framework is cumbersome and not very enlightening. In the literature, depending on the specific parameters of interest or oscillation channel, authors make approximations to derive probability formulas that can be easily interpreted in the context of experimental results or design.

---

[1] It turns out experimentally that $\Delta m^2_{21} \ll |\Delta m^2_{32}|$ as shown in Table 2.1, and thus $|\Delta m^2_{32}| \approx |\Delta m^2_{31}|$.

One such approximation is the 2-neutrino approximation, where one of the mass-squared differences is much smaller than the other[1] and θ_{13} is also very small[2]. For most experiments it is useful to consider this simple effective 2-neutrino case where one neutrino is assumed to not mix with the others. Then the mixing matrix U becomes

$$U_{2\times 2} = \begin{pmatrix} \cos\theta & \sin\theta \\ -\sin\theta & \cos\theta \end{pmatrix} \tag{2.12}$$

and the probability of oscillation, Equation 2.7, becomes

$$P_{\nu_\alpha \to \nu_\beta} = \sin^2(2\theta)\sin^2\left(\frac{\Delta m^2 L}{4E}\right). \tag{2.13}$$

Correspondingly, the *survival probability* is given as

$$P_{\nu_\alpha \to \nu_\alpha} = 1 - \sin^2(2\theta)\sin^2\left(\frac{\Delta m^2 L}{4E}\right) \tag{2.14}$$

by unitarity.

The parameters θ and Δm^2 are fixed by nature, so experiments must choose L and E to be sensitive to oscillations occurring through a given Δm^2. In particular the argument of the sine function in Equation 2.13 should be approximately some odd-integer multiple of $\frac{\pi}{2}$. In practice, it is useful to write Equation 2.13 in SI units:

$$P_{\nu_\alpha \to \nu_\beta} = \sin^2(2\theta)\sin^2\left(\frac{1.267\Delta m^2(\mathrm{eV}^2)L(\mathrm{km})}{E(\mathrm{GeV})}\right). \tag{2.15}$$

Then the *sensitivity* of an experiment to *some* Δm^2 is given by

$$\frac{1.267\Delta m^2(\mathrm{eV}^2)L(\mathrm{km})}{E(\mathrm{GeV})} \approx \frac{\pi}{2} \Longrightarrow \frac{\Delta m^2(\mathrm{eV}^2)L(\mathrm{km})}{E(\mathrm{GeV})} \approx 1. \tag{2.16}$$

The 2-neutrino formalism is commonly used when interpreting solar and reactor neutrino experiments (Sections 2.2.1 and 2.2.3), atmospheric and accelerator neutrino experiments (Section 2.2.2) and understanding matter effects (Section 2.1.2).

---

[2] See again Table 2.1.

Furthermore, experiments typically denote $\Delta m^2_{21} \approx \Delta m^2_{\odot}$, $\theta_{21} \approx \theta_{\odot}$ (solar) and $|\Delta m^2_{31}| \approx \Delta m^2_{Atm}$, $\theta_{23} \approx \theta_{Atm}$ (atmospheric), named after the type of experiments that discovered the respective oscillations[3]. For example, these solar and atmospheric parameters can be substituted into Equation 2.14 to approximate the behaviour of the respective experiments. These experiments and many others determine all the neutrino oscillation parameters, as described in later sections of this chapter.

2.1.1 CP Violation

The CP transformation interchanges negative helicity neutrinos with positive helicity anti-neutrinos. CP violation in the lepton sector can be observed by measuring the CP asymmetry in neutrino oscillations, defined by taking the difference of Equations 2.8 and 2.9:

$$\begin{aligned} A^{CP}_{\alpha\beta}(L,E) &= P_{\nu_\alpha\to\nu_\beta}(L,E) - P_{\bar{\nu}_\alpha\to\bar{\nu}_\beta}(L,E) \\ &= 4\sum_{k>j} \mathfrak{Im}[U^*_{\alpha k}U_{\beta k}U_{\alpha j}U^*_{\beta j}] \sin\left(\frac{\Delta m^2_{kj}L}{2E}\right). \end{aligned} \tag{2.17}$$

This is the difference between neutrino and anti-neutrino beam oscillation.

In the PMNS parameterization

$$A^{CP}_{\alpha\beta}(L,E) = 4J\sum_{k>j} \epsilon_{\alpha\beta;kj} \sin\left(\frac{\Delta m^2_{kj}L}{2E}\right) \tag{2.18}$$

where $\epsilon_{\alpha\beta;kj}$ is an anti-symmetric tensor coefficient such that $\epsilon_{\alpha\beta;kj} = -\epsilon_{\beta\alpha;kj}$, $\epsilon_{\alpha\beta;21} = \epsilon_{\alpha\beta;32} = -\epsilon_{\alpha\beta;31} = 1$ and $\epsilon_{\alpha\alpha;kj} = 0$, and J is given by [12]

$$\begin{aligned} J &= c_{12}s_{12}c_{23}s_{23}c^2_{13}s_{13}\sin\delta \\ &= \frac{1}{8}\sin 2\theta_{12}\sin 2\theta_{23}\cos\theta_{13}\sin 2\theta_{13}\sin\delta. \end{aligned} \tag{2.19}$$

Thus all three mixing angles must be non-zero and precisely measured in order to measure the CP violating phase δ.

---

[3] For the mixing angles, this assignment is exact only if the U_{e3} element of the mixing matrix in Equation 2.10, which was unknown until recently (Section 2.2.3), is 0.

2.1.2 Matter Effect

The formalism in the previous sections is valid in vacuum only. As a neutrino propagates through matter it experiences an additional potential due to coherent interactions with particles in the medium. All neutrino flavours can interact with matter (electrons, protons and neutrons) via neutral current (NC) as in Figure 2.2 (right). This just produces a common phase in the mixing matrix and is irrelevant in the calculation of oscillation probabilities, as is the case for the Majorana phases. However, ν_e can also interact via charged current (CC) interactions with the electrons in the medium as in Figure 2.2 (left), contributing the potential

$$V_{CC} = \sqrt{2} G_F N_e \tag{2.20}$$

to the neutrino Hamiltonian, where G_F is the Fermi coupling constant and N_e is the electron number density. Thus the derivation of the oscillation probabilities from Equation 2.4 is modified leading to an effective mixing matrix.

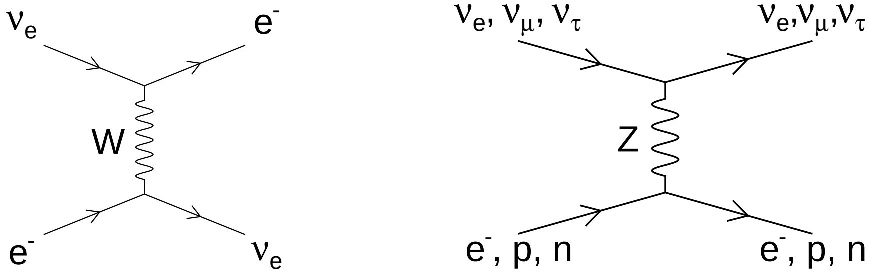

Figure 2.2: Feynman diagrams for CC (left) and NC (right) elastic scattering weak interaction processes.

In the 2-neutrino case, for example considering ν_e and ν_x where ν_x can be some linear combination of ν_μ and ν_τ since they feel the same matter potential, the effective matrix is given similarly to Equation 2.12 as

$$U_M = \begin{pmatrix} \cos\theta_M & \sin\theta_M \\ -\sin\theta_M & \cos\theta_M \end{pmatrix}, \tag{2.21}$$

where

$$\tan 2\theta_M = \frac{\tan 2\theta}{1-\frac{A^M}{\Delta m^2 \cos 2\theta}}, \tag{2.22}$$

$$\Delta m_M^2 = \Delta m^2 \sqrt{(A^M/\Delta m^2 - \cos 2\theta)^2 + \sin^2 2\theta} \tag{2.23}$$

and

$$A^M = 2EV_{CC}. \tag{2.24}$$

The 2-neutrino oscillation probability from Equation 2.13 then becomes

$$P_{\nu_e \to \nu_x} = \sin^2(2\theta_M) \sin^2\left(\frac{\Delta m_M^2 L}{4E}\right). \tag{2.25}$$

From Equation 2.22 it can be seen that a resonance occurs when $A^M = \Delta m^2 \cos 2\theta$ and the mixing becomes maximal (total transition or 100% oscillation probability). This is known as the Mikheyev-Smirnov-Wolfenstein (MSW) effect [13, 14].

Matter effects are important for solar neutrinos (Section 2.2.1) since they are created in the dense matter environment of the sun. Atmospheric and accelerator neutrinos (Section 2.2.2) are also susceptible as they travel through the Earth, with the matter effect depending on the baseline L.

Also, since matter itself is CP asymmetric (electrons, but no positrons) neutrinos and anti-neutrinos experience opposite signs of the potential from Equation 2.20 (flipping the sign of A^M). The matter effect introduces an additional source of CP violation into the oscillation probabilities causing a degeneracy with the *intrinsic* CP violation discussed in Section 2.1.1. In other words, a CP asymmetry can be observed in experiments with neutrinos passing through a significant amount of matter even if $\sin\delta = 0$ [15]. This degeneracy must be lifted by combining several experiments as described in Section 2.2.4.

2.2 Neutrino Oscillation Experiments

This section summarizes various experiments measuring neutrinos and their fluxes, which ultimately determine the oscillation parameters introduced in Section 2.1.

2.2.1 Solar and Reactor Neutrino Experiments

The sun is a powerful source of electron neutrinos. They are emitted from nuclear fusion reactions that ultimately convert protons and electrons into helium and neutrinos as follows

$$4p + 2e^- \rightarrow {}^4\mathrm{He} + 2\nu_e + 26.731\ \mathrm{MeV}. \tag{2.26}$$

A Standard Solar Model (SSM) was developed [16] to model all the processes in the sun and precisely predict the neutrino flux. Since neutrinos rarely interact, they can travel uninhibited through the interior of the sun and act as probes of the stellar core when we measure them on Earth.

However, when the first radiochemical experiment, based in the Homestake mine [17, 18], attempted to measure solar neutrinos through the reaction

$$\nu_e + {}^{37}\mathrm{Cl} \rightarrow e^- + {}^{37}\mathrm{Ar}, \tag{2.27}$$

the resulting ν_e flux was only about 1/3 of the SSM prediction. This was known as the *Solar Neutrino Problem* (SNP). The deficit was later confirmed by the gallium experiments GALLEX [19, 20] and SAGE [21, 22] measuring the reaction

$$\nu_e + {}^{71}\mathrm{Ga} \rightarrow e^- + {}^{71}\mathrm{Ge} \tag{2.28}$$

and the water Čerenkov experiments Kamiokande [23–25], SNO (Sudbury Neutrino Observatory) [26] and Super-Kamiokande (SK) [27] through elastic scattering

$$\mathrm{ES}: \nu_\alpha + e^- \rightarrow \nu_\alpha + e^-. \tag{2.29}$$

The SNO experiment used heavy water (D_2O) instead of water allowing the additional two reactions

$$\mathrm{CC}: \quad \nu_e + d \rightarrow p + p + e^- \tag{2.30}$$

$$\textit{and} \quad \mathrm{NC}: \quad \nu_\alpha + d \rightarrow p + n + \nu_\alpha. \tag{2.31}$$

The CC reaction is sensitive only to ν_e while the NC reaction provides a measure of the total neutrino flux of all flavours. Their measurement [28, 29] provided definitive evidence of neutrino flavour transitions because the measured neutrino flux via NC agreed with the SSM prediction while the ν_e flux was about 1/3, consistent with the SNP seen in the earlier experiments.

The non-observation of seasonal variations in the aforementioned solar neutrino data of e.g. [30] refutes the hypothesis of vacuum oscillations, which predicts a dependence on the distance between Earth and the sun [31]. Thus, the MSW effect (Section 2.1.2) is the most likely explanation for solar neutrino oscillation [32, 33]. A global fit to solar neutrino data gives the following results for the mixing parameters [34]:

$$\Delta m^2_\odot = 6.5^{+4.4}_{-2.3} \times 10^{-5}\ \mathrm{eV}^2, \quad \tan^2\theta_\odot = 0.45^{+0.09}_{-0.08}. \tag{2.32}$$

From Equation 2.16, it follows that oscillations should be observable at an $\frac{L}{E} \sim 10^4$. On Earth, nuclear fission reactors are a powerful source of $\overline{\nu}_e$ with energies around a few MeV. Thus, the expected oscillation length is 10-100 km, which is a reasonable distance relative to a reactor to place a detector and observe $\overline{\nu}_e$ disappearance. The reactor $\overline{\nu}_e$ are detected through the inverse β decay process (Equation 1.1), by observing prompt light from the positron and delayed light from the neutron capture.

The KamLAND reactor neutrino experiment [35] was surrounded by $\sim$ 50 reactors in Japan varying in distance from 80-800 km. This range of distances combined with the reconstructed neutrino energy information from the measured positron energy, allowed the experiment to measure $\overline{\nu}_e$ flux suppression as a function of $\frac{L_{eff}}{E}$, where L_{eff} is the effective baseline averaged over all reactors. This is shown in Figure 2.4 (top left), producing a precise measurement of $\Delta m^2_\odot$.

A combined analysis of the most recent solar neutrino data [36] and complementary KamLAND data gives [37][4]

$$\Delta m^2_\odot = 7.53^{+0.19}_{-0.18} \times 10^{-5}\ \mathrm{eV}^2, \quad \tan^2\theta_\odot = 0.437^{+0.029}_{-0.026}. \tag{2.33}$$

2.2.2 Atmospheric and Accelerator Neutrino Experiments

The collision of high energy cosmic ray protons with nuclei in Earth's atmosphere produce showers of hadrons, mostly pions and some kaons, that subsequently decay into neutrinos. The pions decay as follows:

$$\pi^+ \rightarrow \mu^+ + \nu_\mu \qquad\qquad \pi^- \rightarrow \mu^- + \nu_\mu \tag{2.34}$$

$$\hookrightarrow e^+ + \nu_e + \bar{\nu}_\mu \qquad\qquad \hookrightarrow e^- + \bar{\nu}_e + \nu_\mu, \tag{2.35}$$

corresponding to the diagrams in Figure 2.1. These neutrinos are referred to as *atmospheric neutrinos* and are in the energy range of about 0.1-100 GeV, peaking around 1 GeV. They can be observed by detectors deep underground, which are shielded from cosmic ray muons. Since the cosmic ray flux is isotropic, the resulting neutrino flight length can vary from $\sim 10 - 10^4$ km, the limits corresponding to production directly above the detector and directly below the detector through the diameter of the Earth. Thus, from Equation 2.16, atmospheric neutrino experiments can be sensitive to a wide range of Δm^2, about 10^{-4} to 1 eV^2.

Super-Kamiokande (SK), described more in Section 3.3, is a high resolution detector capable of separating electrons from muons and measuring the zenith angle of each particle. The experiment measured a large deficit in the upward-going muons, produced by neutrinos with a longer flight length through the earth, relative to the downward-going

---

[4] This also includes the constraint on θ_{13} provided by more recent reactor neutrino experiments described in Section 2.2.3.

muons, providing strong evidence for ν_μ disappearance [9, 38]. In particular, the $\nu_\mu \to \nu_\tau$ maximal mixing ($\sin^2 2\theta_{Atm} = 1$) hypothesis is favoured since there is no evidence of oscillation in the electron channel ($\nu_\mu \leftrightarrows \nu_e$) nor NC channels ($\nu_\mu \to \nu_s$). Furthermore, SK can map out the flux suppression as a function of $\frac{L}{E}$, similar to KamLAND, producing a precise measurement on Δm^2_{Atm} [39], as shown in Figure 2.4 (top right) and further confirming the neutrino oscillation hypothesis. The results from the SK zenith angle analysis using the full data set is typically used to quote measurements on the oscillation parameters [40]:

$$\begin{gathered} |\Delta m^2_{Atm}| = 2.1^{+0.9}_{-0.4} \times 10^{-3}\ \mathrm{eV}^2 \\ \sin^2 2\theta_{Atm} > 0.93 \text{at the 90\% confidence level (C.L.).} \end{gathered} \tag{2.36}$$

Analogous to the case of reactor neutrino experiments confirming the solar neutrino oscillation, accelerator-based neutrino experiments have confirmed the atmospheric oscillation. These experiments accelerate protons that collide with a target to produce hadronic showers similar to those produced by cosmic rays. However, in this case the incident energy of the protons and the direction and charge of the secondary hadrons can be controlled, producing a neutrino beam with a narrower range of energies and higher "purity" (ratio of neutrino to anti-neutrino) compared to atmospheric neutrinos. This process is described in more detail in the context of the T2K experiment in Section 3.1. The average beam energies are typically ∼ 1 GeV, so detectors can be situated at long-baseline distances of a few 100 km to probe Δm^2_{Atm}.

The first of such experiments were K2K [41] and MINOS [42]. Both used relatively pure ν_μ beam and had "near" detectors close to the neutrino production target to measure the neutrino beam prior to oscillations. The latter provides a constraint on the neutrino flux normalization and some cancellation of systematic errors with the "far" detector that measures the oscillated neutrino spectrum. These experiments observed ν_μ disappearance through a lower than expected event rate and distorted energy spectrum at the far detectors consistent with the atmospheric measurements. The strongest constraints on the atmospheric parameters, prior to the T2K results presented in this thesis, were produced by MINOS [43]:

$$|\Delta m^2_{Atm}| = 2.41^{+0.09}_{-0.10} \times 10^{-3}\ \mathrm{eV}^2, \quad \sin^2 2\theta_{Atm} = 0.950^{+0.035}_{-0.036}. \tag{2.37}$$

They were able to tune their $\frac{L}{E}$ to map the first oscillation maximum precisely, as shown in Figure 2.4 (bottom left). The result of this thesis will include the most precise measurement of θ_{23} to date (and a very competitive Δm^2_{Atm} measurement), made by the T2K experiment using a similar technique.

2.2.3 Measurement of θ_{13}

The past experiments measuring the solar and atmospheric parameters ($\theta_{\odot}$, θ_{Atm}) have thus far been insensitive to the value of $|U_{e3}|$ or θ_{13}, for example [44, 45], suggesting that the angle is very small. Thus, it has been adequate to interpret their results in a 2-neutrino framework. However, in order to measure CP violation in neutrino oscillations, θ_{13} must be non-zero (Equation 2.19) and the full 3-neutrino framework must be considered. Therefore, the determination of θ_{13} has been a subject of intense research in the past few years.

The "θ_{13} race" began with the CHOOZ [46] and Palo Verde [47] reactor neutrino experiments attempting to measure $\overline{\nu}_e$ disappearance, similar in principle to the KamLAND experiment described in Section 2.2.1, except at shorter baselines $\sim$ 1 km, to probe the oscillation through Δm^2_{Atm}. However, they were not sensitive enough to the apparently small value of θ_{13}, reporting an upper limit of [46]

$$\sin^2 2\theta_{13} < 0.15 \text{ at } 90\% \text{ C.L.}. \tag{2.38}$$

The measurements of the experiments mentioned thus far (except solar neutrinos) could be approximated by the survival probability in the 2-neutrino case of Equation 2.14. However, θ_{13} can also be probed through the $\nu_\mu \rightarrow \nu_e$ appearance channel, now considering the 3-neutrino framework to leading order:

$$P_{\nu_\mu \to \nu_e} \approx \sin^2(2\theta_{13}) \sin^2(2\theta_{23}) \sin^2\left(\frac{\Delta m^2_{31} L}{4E}\right). \tag{2.39}$$

To this end, accelerator neutrino experiments, introduced in Section 2.2.2, can search for ν_e appearance in their far detector from the relatively pure ν_μ beam. The first of such experiments was T2K, which reported non-zero θ_{13} at 2.5σ significance (p-value of 0.013) [48] in 2011, followed by MINOS with p-value of 0.11 [49].

Another suite of reactor neutrino experiments, upgraded with increased detector size as well as near detectors, also entered the race. Double CHOOZ was the first to report, albeit still with just an indication of non-zero θ_{13} (p-value of 0.055) [50]. A definitive measurement was produced by Daya Bay with a significance of 5.2σ [51] in 2012, followed by RENO at 4.9σ [52].

The latest results from Double CHOOZ and RENO can be found in [53] and [54] respectively, while Daya Bay currently has the most precise measurement of θ_{13} from the measurement shown in Figure 2.4 (bottom right) resulting in [55]

$$|\Delta m^2_{ee}| = 2.59^{+0.19}_{-0.20} \times 10^{-3}\ \mathrm{eV}^2, \quad \sin^2 2\theta_{13} = 0.090^{+0.008}_{-0.009}. \tag{2.40}$$

The result of this thesis includes the first definitive discovery of ν_e appearance through non-zero θ_{13} by T2K in 2013 [56], further confirming the 3-flavour oscillation model.

2.2.4 Mass Hierarchy, θ_{23} Octant and δ_{CP}

With all three mixing angles determined to be non-zero, the full nature of 3-neutrino oscillations, including CP violation as shown in Equation 2.19, can be explored. However, the derivation of oscillation probabilities must now go beyond the 2-neutrino approximation of Equation 2.13 in order to make predictions and interpret experimental results. The existence of matter effects as discussed in Section 2.1.2 also complicates the picture. The sub-leading effects introduced in this section will be discussed in the context of accelerator neutrino experiments, since CP violation is easily accessible through appearance channels[5]. However, it should be noted that there are other ongoing efforts with, for example, atmospheric neutrinos [45, 57, 58] and reactor neutrinos [59–61].

Since current accelerator neutrino experiments are tuned to the larger Δm^2_{Atm}, oscillations due to $\Delta m^2_{\odot}$ can be approximated by expanding Equations 2.8 and 2.9 in terms of

$$\alpha = \frac{\Delta m^2_{21}}{\Delta m^2_{31}} \sim 3.1\%. \tag{2.41}$$

The $\overset{(-)}{\nu}_\mu \to \overset{(-)}{\nu}_e$ oscillation probability is expanded as [15]

$$P_{\overset{(-)}{\nu}_\mu \to \overset{(-)}{\nu}_e} \approx \sin^2 2\theta_{13} T_1 \mp \alpha \sin 2\theta_{13} T_2 + \alpha \sin 2\theta_{13} T_3 + \alpha^2 T_4, \tag{2.42}$$

where the negative (positive) solution corresponds to neutrinos (anti-neutrinos), and

$$T_1 = \sin^2\theta_{23} \tfrac{\sin^2[(1-x)\Delta]}{(1-x)^2} \tag{2.43}$$

$$T_2 = \sin\delta \sin 2\theta_{12} \sin 2\theta_{23} \sin\Delta \tfrac{\sin(x\Delta)}{x} \tfrac{\sin[(1-x)\Delta]}{(1-x)} \tag{2.44}$$

$$T_3 = \cos\delta \sin 2\theta_{12} \sin 2\theta_{23} \cos\Delta \tfrac{\sin(x\Delta)}{x} \tfrac{\sin[(1-x)\Delta]}{(1-x)} \tag{2.45}$$

$$T_4 = \cos^2\theta_{23} \sin^2 2\theta_{12} \tfrac{\sin^2(x\Delta)}{x^2}, \tag{2.46}$$

with

$$\Delta = \frac{\Delta m^2_{31} L}{4E}. \tag{2.47}$$

The correction due to the matter effect with constant density is included in the term

$$x = \frac{A^M}{\Delta m^2_{31}} = \frac{2\sqrt{2} G_F N_e E}{\Delta m^2_{31}} \tag{2.48}$$

from Equations 2.20 and 2.24, where $+A^M \to -A^M$ in the case of anti-neutrinos. The vacuum case can be recovered by letting $x \to 0$. Also, when switching to inverted hierarchy, $+\Delta m^2_{31} \to -\Delta m^2_{31}$ anywhere it appears (in α, Δ and x) and thus care must be taken when determining the overall sign changes in different parameter configurations.

Some characteristics of the oscillation probability can be deduced immediately:

---

[5] Disappearance measurements are not sensitive to CP violation since the survival probabilities $P_{\nu_\alpha \to \nu_\alpha}$ and $P_{\bar{\nu}_\alpha \to \bar{\nu}_\alpha}$ are equal assuming CPT symmetry.

- There is a dependence on the mass hierarchy through T_3 which becomes negative in the inverted hierarchy case (even in vacuum), decreasing the appearance probability.

- With matter effects ($x > 0$), which is the case for all current long-baseline accelerator neutrino experiments, the dependence on the mass hierarchy is stronger. To leading order (T_1), the probability decreases with inverted hierarchy.

- ν_e appearance is enhanced relative to $\overline{\nu}_e$ appearance due to the matter effect (T_1). Furthermore, the CP asymmetry $A^{CP}_{\alpha\beta}$ can no longer be written as simply as Equation 2.18, since there is an additional matter induced CP asymmetry in addition to the $\sin\delta_{CP}$ (T_2) term.

- The parameter θ_{23} has been determined by disappearance experiments to be near maximal ($\theta_{23} \approx \frac{\pi}{4}$). However, to leading order they measure $\sin^2 2\theta_{23}$ (Equation 2.14), which is degenerate in the θ_{23} *octant*[6]. Thus, any deviation from maximal mixing will affect the appearance probability through the leading term T_1 which contains $\sin^2\theta_{23}$. For example, θ_{23} in the first octant ($0 \leqslant \theta_{23} < \frac{\pi}{4}$) would produce a smaller probability compared to θ_{23} in the second octant ($\frac{\pi}{4} \leqslant \theta_{23} < \frac{\pi}{2}$).[7]

Thus, for measurements of $\overset{(-)}{\nu}_\mu \to \overset{(-)}{\nu}_e$ appearance there is a degeneracy in 3 parameters: the mass hierarchy, the θ_{23} octant and δ_{CP}. In order to measure the intrinsic CP violation (δ_{CP}), experiments at different baselines (with differing values of x) measuring both ν_e

---

[6] In other words, $\sin^2 2\theta_{23} = \sin^2 2(\frac{\pi}{2} - \theta_{23})$.

[7] On the other hand, ν_μ disappearance is not as sensitive to the θ_{23} octant. At next-to-leading order, the 3-neutrino survival probability is given as

$$P_{\nu_\mu\to\nu_\mu} \approx 1 - (\cos^4\theta_{13}\sin^2 2\theta_{23} + \sin^2 2\theta_{13}\sin^2\theta_{23})\sin^2\Delta, \tag{2.49}$$

which can be rearranged to

$$P_{\nu_\mu\to\nu_\mu} \approx 1 - [1 - (2\sin^2\theta_{23}\cos^2\theta_{13} - 1)^2]\sin^2\Delta. \tag{2.50}$$

Thus, $P_{\nu_\mu\to\nu_\mu}$ is approximately symmetric about the minimum and so current disappearance measurements (which favour near-maximal mixing) are not sensitive to the θ_{23} octant.

and $\overline{\nu}_e$ appearance should be combined to fully constrain the parameter space.

The MINOS experiment [62], with a baseline of 735 km, has begun this effort using the new reactor constraints on θ_{13} as shown in Figure 2.3. They are able to place some constraint on the 3-parameter space. The NOνA [63] experiment has a similar baseline (810 km), but with a more intense neutrino beam, narrower energy spectrum (similar to T2K described in Section 3.1.3) and larger detectors. They are expected to start data taking in the near future and produce similar but more precise measurements in the 3-parameter space. These results can be combined with T2K, which has a shorter baseline of 295 km, to lift the degeneracy. A constraint on the 3-parameter space from the combined analysis of T2K ν_e appearance and ν_μ disappearance data with reactor data input is one of the main results of this thesis.

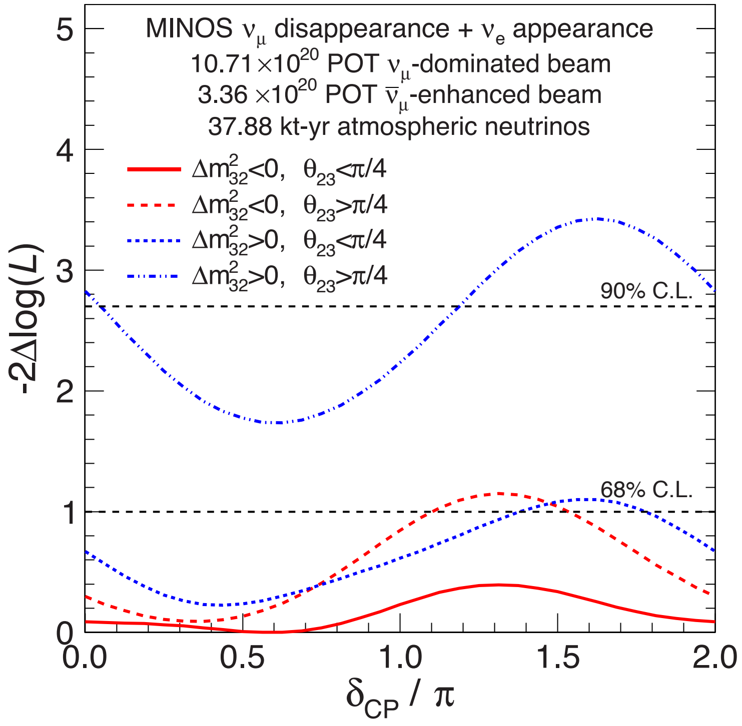

Figure 2.3: Fitted likelihood as a function of δ combining MINOS accelerator and atmospheric data with the reactor constraint on θ_{13} [52, 64, 65] for each combination of the mass hierarchy and θ_{23} octant. Figure taken from [66].

2.2.5 Summary of Oscillation Parameter Measurements

As reviewed above, there has been considerable progress on the measurement of neutrino oscillation parameters within the past two decades. The 3-neutrino model has been verified to high confidence by many independent experiments. The oscillatory signature from four of the experiments is shown in Figure 2.4. Now the field is moving towards high precision measurements.

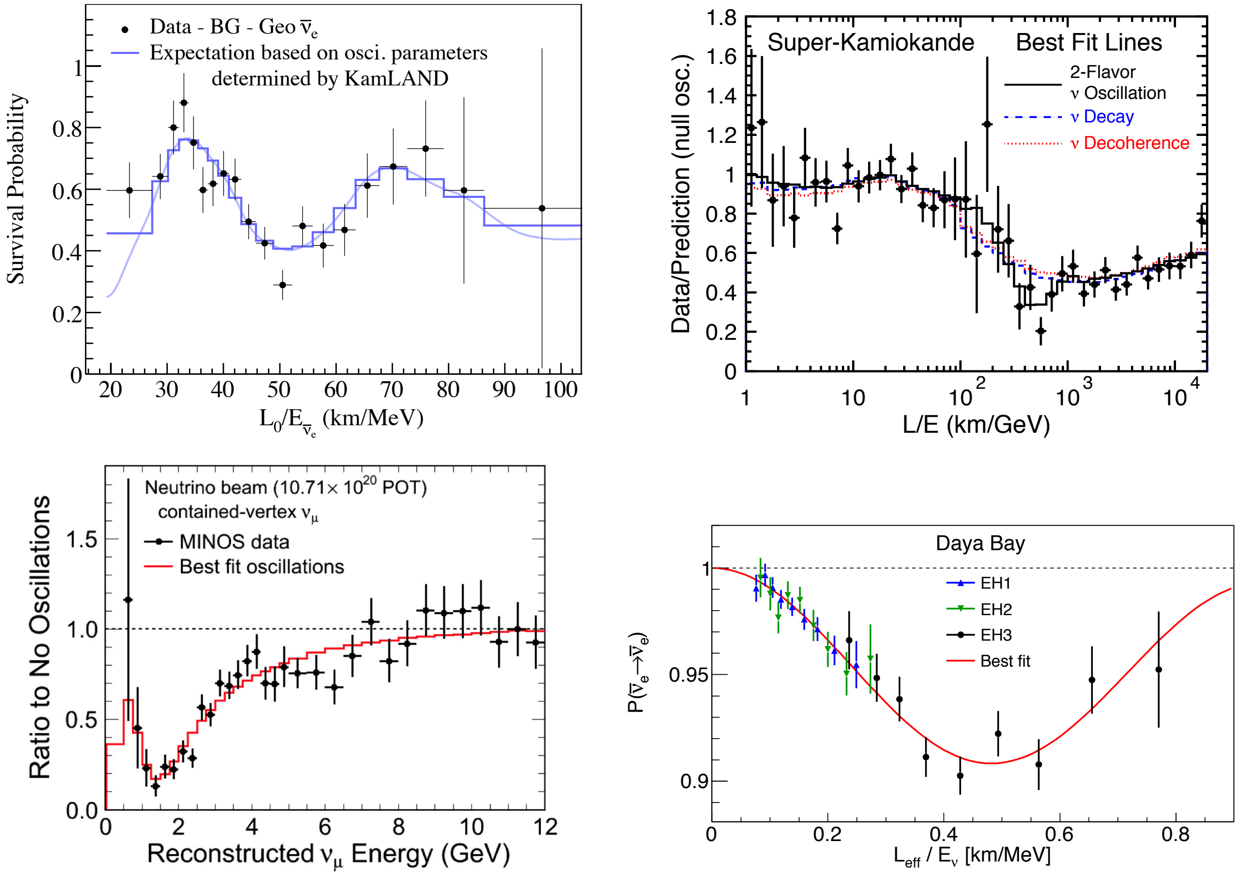

Figure 2.4: Survival probabilities for four disappearance experiments. For the Δm^2_{21} oscillation, KamLAND versus L_{eff}/E [35] (top left). For the $\Delta m^2_{32} \approx \Delta m^2_{31}$ oscillation, SK versus L/E [39] (top right), MINOS versus E ($L = 735$ km) [43, 67] (bottom left, baseline $L = 735$ km) and Daya Bay versus L/E [55] (bottom right).

As alluded to in the previous section (2.2.4), the combination of experimental data will be necessary to elucidate the full 3-neutrino framework including sub-leading effects. This is technically difficult due to the complications and peculiarities of each experiment, including unique detection methods and analysis techniques used to report results. Thus, effort must be made to produce a set of observables and systematic parameterizations from each experiment that can then be used in a global fit which takes into account correlated inputs such as the neutrino flux, cross sections and of course the oscillation model.

Phenomenologists have been attempting such fits (e.g. [68, 69]), to determine the allowed regions and correlations for all the oscillation parameters. Their latest oscillation parameter results [70, 71], shown in Table 2.1, are typically used to summarize all the most significant data in the field. These include input from most of the experiments mentioned in previous sections except some of the latest results, but is still useful for understanding the magnitude of the parameters and the mixing matrix U from Equation 2.10. The 3σ regions for each matrix element are as follows [71]:

$$|U| = \begin{array}{c} \\ \nu_e \\ \nu_\mu \\ \nu_\tau \end{array} \begin{array}{c} \begin{array}{ccc} \nu_1 & \nu_2 & \nu_3 \end{array} \\ \begin{pmatrix} 0.795 - -0.846 & 0.513 - -0.585 & 0.126 - -0.178 \\ 0.205 - -0.543 & 0.416 - -0.730 & 0.579 - -0.808 \\ 0.215 - -0.548 & 0.409 - -0.725 & 0.567 - -0.800 \end{pmatrix} \end{array} \tag{2.51}$$

This is represented graphically in Figure 2.5, which shows the relative flavour contribution to each mass state.

2.3 Massive Neutrinos

The evidence for neutrino oscillations described in the previous sections requires that neutrinos be massive, which is the first *beyond the Standard Model* phenomenon. Thus, the neutrino part of the SM must be reformulated, as outlined below in Section 2.3.1. As derived in Section 2.1, neutrino oscillation experiments are only sensitive to the differences in neutrino masses. Dedicated experiments to measure the absolute mass scale and true nature of the neutrino must be performed as summarized in Sections 2.3.2 and 2.3.3.

Parameter	Normal Hierarchy	Inverted Hierarchy
Δm^2_{21} $[10^{-5}\ \mathrm{eV}^2]$	$7.54^{+0.26}_{-0.22}$	
Δm^2 $[10^{-3}\ \mathrm{eV}^2]$	$2.43^{+0.06}_{-0.10}$	$-2.42^{+0.11}_{-0.07}$
$\sin^2\theta_{12}$	$0.307^{+0.018}_{-0.016}$	
$\sin^2\theta_{23}$	$0.386^{+0.024}_{-0.021}$	$0.392^{+0.039}_{-0.022}$
$\sin^2\theta_{13}$	0.0241 ± 0.0025	$0.0244^{+0.0023}_{-0.0025}$
δ $[\pi]$	$1.08^{+0.28}_{-0.31}$	$1.09^{+0.38}_{-0.26}$

Table 2.1: Summary of best-fit values and $\pm 1\sigma$ allowed ranges for the neutrino oscillation parameters as reported by a global fit of world neutrino data [70, 72]. The mass-squared difference $\Delta m^2 = m_3^2 - (m_1^2 + m_2^2)/2$ is defined to simplify comparisons between NH and IH.

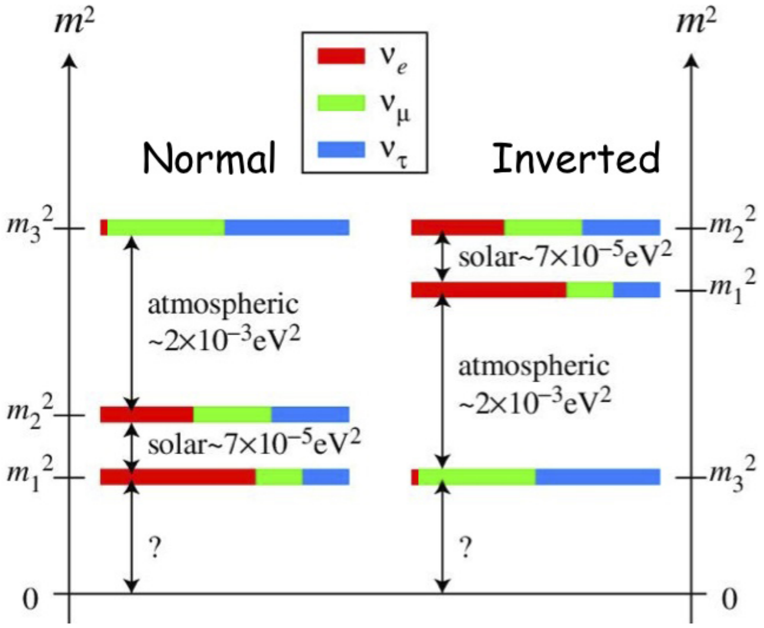

Figure 2.5: Diagram summarizing the current neutrino oscillation mixing parameter measurements. The coloured bars show the flavour contribution to each neutrino mass state determined by the mixing angles. The vertical separation between bars (not to scale) shows the relative size of the mass-squared differences with the approximate values listed. The two possible neutrino mass hierarchies are shown: ν_3 is the heaviest neutrino in the NH (left) or the lightest in the IH (right). The absolute scale of neutrino mass is unknown. Figure taken from e.g. [73].

2.3.1 Dirac and Majorana Mass

The form of the Lagrangian for a fermionic “Dirac mass” (m_D) term is given by

$$\mathcal{L}_D = -m_D\bar{\psi}\psi = -m_D\bar{\psi}_R\psi_L + h.c., \tag{2.52}$$

where $\psi_{L,R}$ are the LH and RH components of the fermion field ψ ($\psi = \psi_L + \psi_R$). However, the SM assumes that neutrinos are massless. Since the weak interaction only couples to left-handed particles, the SM massless neutrino does not have a right-handed component, which is necessary for generating the mass term in Equation 2.52.

To give the neutrino mass, the *minimally extended SM* simply adds three sterile right-handed neutrino states required to define the Dirac mass for each neutrino. Furthermore, since the neutrino has no electric charge, it could be a *Majorana* particle (e.g. [74]), identical to its anti-particle, where the charge conjugated field $\psi^C = \psi$. Then a *Majorana mass* part of the Lagrangian can be written as

$$\mathcal{L}_M = \frac{1}{2}m_R\overline{\psi_R^C}\psi_R + h.c., \tag{2.53}$$

such that the full neutrino mass Lagrangian becomes

$$\mathcal{L}_{mass} = \mathcal{L}_D + \mathcal{L}_M. \tag{2.54}$$

Equation 2.54 can be rewritten as

$$\mathcal{L}_{mass} = \frac{1}{2}\overline{\Psi_L^C}M\Psi_L + h.c., \tag{2.55}$$

where

$$\Psi_L = \begin{pmatrix} \psi_L \\ \psi_R^C \end{pmatrix} \tag{2.56}$$

and

$$M = \begin{pmatrix} 0 & m_D \\ m_D & m_R \end{pmatrix}. \tag{2.57}$$

Thus, the neutrino states $\psi_{L,R}$ do not have definite mass since M is in general non-diagonal. However, the Majorana massive neutrino fields, (ψ_1, ψ_2), could be defined such that M is diagonalized, with corresponding masses given by the eigenvalues

$$m_{2,1} = \frac{1}{2}\left[m_R \pm \sqrt{m_R^2 + 4m_D^2}\right]. \tag{2.58}$$

If (ψ_1, ψ_2) is a very small rotation relative to Ψ_L, that is if ψ_1 is composed mostly of the active neutrino state ψ_L while ψ_2 is mostly sterile ψ_R, then $m_D \ll m_R$ giving

$$m_1 \approx \frac{m_D^2}{m_R},\ m_2 \approx m_R. \tag{2.59}$$

This is referred to as the *see-saw mechanism* since a large m_R gives rise to a small m_1, which can potentially explain the fact, discussed in the next section (2.3.2), that neutrinos have much smaller mass than the charged fermions.

This formalism can be extended to any number of sterile neutrino states [12] and can lead to a breadth of interesting new physics. For example, the heavy sterile neutrino state ψ_2 here could be the heavy neutrino required by leptogenesis, described in Section 2.4, or ψ_1 could be a mass state in Equation 2.1 giving rise to neutrino oscillations.

2.3.2 Absolute Mass Scale

The most promising process to determine the absolute neutrino mass scale currently is the β decay of tritium:

$$^3H \rightarrow\ ^3He + e^- + \bar{\nu_e}, \tag{2.60}$$

as depicted in Figure 2.6 (left). Here, a small neutrino mass would distort the decay electron energy spectrum near the end-point, which is what current experiments attempt to observe.

Since the amplitude calculated from normal β decay depends on the ν_e mass and mixing matrix U (recalling that a ν_e is produced as a linear combination of mass states as in Equation 2.1), then

$$\begin{aligned} m_\beta^2 &= \sum_{k=1}^{3} |U_{ek}|^2 m_k^2 \\ &= |U_{e1}|^2 m_1^2 + |U_{e2}|^2 m_2^2 + |U_{e3}|^2 m_3^2, \end{aligned} \tag{2.61}$$

where U is given by Equation 2.10. When considering the current knowledge on the mass-squared differences, as given in Equations 2.33 and 2.37 and summarized in Table 2.1, Equation 2.61 can be approximated as

$$m_\beta^2 \approx \begin{cases} |U_{e1}|^2 m_1^2 + |U_{e2}|^2 (m_1^2 + \Delta m_\odot^2) + |U_{e3}|^2 (m_1^2 + \Delta m_{Atm}^2) & \text{[for NH]} \\ (|U_{e1}|^2 + |U_{e2}|^2)(m_3^2 + \Delta m_{Atm}^2) + |U_{e3}|^2 m_3^2 & \text{[for IH].} \end{cases} \tag{2.62}$$

with the values of the mixing matrix elements given in Equation 2.51. Thus, not only can β decay experiments determine the absolute scale of neutrino mass, it is also possible to determine the MH, resulting in a complementarity with neutrino oscillation experiments which constrain the mixing matrix elements of U.

The Mainz [75] and Troitsk [76] β decay experiments place 95% C.L. upper bounds on the neutrino mass of

$$m_\beta < 2.3 \text{ eV and } m_\beta < 2.1 \text{ eV}, \tag{2.63}$$

respectively. The next generation experiments like KATRIN [77, 78] expect to push this limit down to 0.2 eV, although still too high to be sensitive to the MH.

Neutrinos also play an important role in cosmology and the evolution of the Universe. In particular the sum of neutrino masses can affect the observed fluctuations of the *Cosmic Microwave Background* (CMB) radiation. Data from the Plank experiment combined with other astronomical data [79] give a 95% C.L. upper bound of

$$\sum m_\nu < 0.23 \text{ eV}, \tag{2.64}$$

which is a complementary result approaching the expected sensitivity of KATRIN and future neutrinoless double beta decay experiments described in the next section.

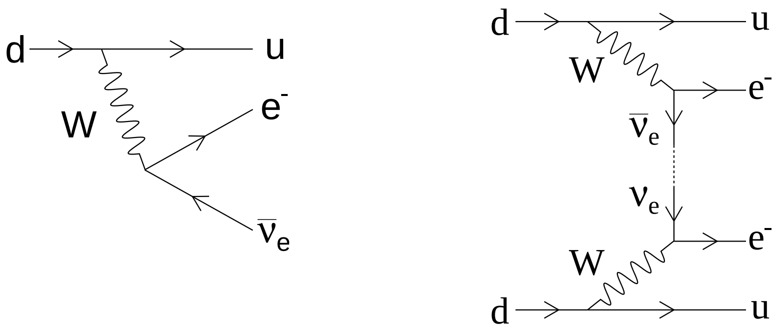

Figure 2.6: Feynman diagrams for the single β decay process (left) and $0\nu\beta\beta$ process (right), where the dotted line connects the two neutrino lines if the neutrino is its own anti-particle and they have the same helicity.

2.3.3 Neutrinoless Double Beta Decay

The Majorana nature of neutrinos can be probed by searching for *neutrinoless double beta decay* ($0\nu\beta\beta$) [80]. One diagram of interest for the $0\nu\beta\beta$ process is depicted in Figure 2.6 (right), where a Majorana neutrino ($\bar{\nu} = \nu$), emitted from the upper vertex is reabsorbed at the lower vertex resulting in no neutrinos in the final state. The helicity of the neutrinos at both vertices must also match giving the additional requirement that they are massive (which we now know from neutrino oscillations).

In 2-neutrino double β decay ($2\nu\beta\beta$) [81], the neutrinos are emitted in the final state, resulting in a continuous spectrum for the total energy of the observable decay electrons. Since the recoil energy of the heavy nucleus can be neglected, $0\nu\beta\beta$ experiments can search for a sharp peak at the end of the $2\nu\beta\beta$ energy spectrum.

Furthermore, a measurement of the $0\nu\beta\beta$ half-life or decay rate [82] can provide a measure of the effective Majorana neutrino mass $m_{2\beta}$ (or the mass of the ν_e in Figure 2.6 right), similar to the single β case described in Section 2.3.2. In this case, however, the amplitude depends on U^2 and m_k so that [83]

$$\begin{aligned} m_{2\beta} &= \sum_{k=1}^{3} U_{ek}^2 m_k \\ &= |U_{e1}|^2 m_1 + e^{i2\lambda_2}|U_{e2}|^2 m_2 + e^{i2(\lambda_3-\delta)}|U_{e3}|^2 m_3 \end{aligned} \tag{2.65}$$

where U is given by Equation 2.10. As for Equation 2.62, Equation 2.65 can be approximated as

$$m_{2\beta} \approx \begin{cases} |U_{e1}|^2 m_1 + e^{i2\lambda_2}|U_{e2}|^2\sqrt{m_1^2 + \Delta m_\odot^2} + e^{i2(\lambda_3-\delta)}|U_{e3}|^2\sqrt{m_1^2 + \Delta m_{Atm}^2} & \text{[for NH]} \\ (|U_{e1}|^2 + e^{i2\lambda_2}|U_{e2}|^2)\sqrt{m_3^2 + \Delta m_{Atm}^2} + e^{i2(\lambda_3-\delta)}|U_{e3}|^2 m_3^2 & \text{[for IH].} \end{cases} \tag{2.66}$$

Thus, an intimate relationship arises between neutrino oscillation and $0\nu\beta\beta$ experiments, where the mixing parameters are determined by oscillation and $0\nu\beta\beta$ can potentially determine the MH in addition to the absolute mass scale and Majorana nature of the neutrino.

Some current and prospective experiments are, for example, EXO [84], SNO+ [85], KamLAND-Zen [86] and MAJORANA [87, 88]. EXO has produced a limit of

$$m_{2\beta} \lesssim 0.38 \text{ eV} \tag{2.67}$$

and is continuing to accumulate more data. A discovery of $0\nu\beta\beta$, together with CP violation through neutrino oscillation, would be important clues to solving the matter anti-matter asymmetry puzzle.

2.4 Leptogenesis

One of the major questions in physics is how the matter anti-matter asymmetry of the universe arose. From current measurements of the CMB and light element abundances, this asymmetry can be quantified as [89]

$$\eta = \frac{n_B - n_{\bar{B}}}{n_\gamma} = 6.079 \pm 0.090 \times 10^{-10}, \tag{2.68}$$

where n is a number density and B and $\bar{B}$ refer to baryon and anti-baryon, respectively. It is very plausible that matter and anti-matter were created in equal parts ($n_B = n_{\bar{B}}$) in the Big Bang, in which case the asymmetry must have been generated dynamically early in the history of the universe, in a process generally referred to as *baryogenesis*.

The basic requirements for any theory of baryogenesis are given by the *Sakharov conditions* [90]:

- Baryon number (B) violation,
- C and CP violation and
- departure from thermal equilibrium.

One such candidate theory is *leptogenesis* [91] which presumes the existence of heavy Majorana neutrinos via the see-saw mechanism as described in Section 2.3.1. These neutrinos could provide the necessary source of CP violation, similar to the light neutrinos as mentioned in Section 2.1.1. Thus the rate of decay of the heavy neutrino to a light lepton would differ from the rate to an anti-lepton, potentially producing an excess of leptons. This lepton number asymmetry can be translated into baryon number asymmetry through SM *sphaleron* processes [92]. Thus, leptogenesis qualitatively satisfies the Sakharov conditions, and it is now a question if all the factors quantitatively add up to the observed baryon asymmetry, η [93].

It is not clear if light neutrino CP violation is connected to heavy neutrino CP violation [94], however given our current technological capabilities, it seems natural to continue to explore and precisely understand the properties light neutrinos, namely their absolute mass and oscillations, as first evidence towards theories beyond the Standard Model.

Chapter 3

The T2K Experiment

T2K (Tokai to Kamioka) is a long-baseline, accelerator neutrino oscillation experiment based in Japan [95]. The experimental setup is shown in Figure 3.1. A high intensity and high purity ν_μ beam is produced at the Japan Proton Accelerator Research Complex (J-PARC), described in Section 3.1. A near detector called ND280 (Section 3.2), 280 m from the neutrino production point, characterizes the neutrino beam prior to oscillation. The oscillated beam is then measured at the far detector, Super-Kamiokande (SK), described in Section 3.3, 295 km from the production point.

The primary physics goal of T2K is the precision measurement of neutrino oscillations as follows:

1. Atmospheric parameters $\sin^2 2\theta_{23}$ and Δm^2_{32} to 1% and 4% respectively through the ν_μ disappearance channel, towards answering the question of maximal mixing or not.
2. θ_{13} through the discovery of $\nu_\mu \rightarrow \nu_e$ appearance.
3. New constraints on the θ_{23} octant, mass hierarchy and δ_{CP} degenerate parameter space.
4. Indirect confirmation of $\nu_\mu \rightarrow \nu_\tau$ oscillation through NC measurements.

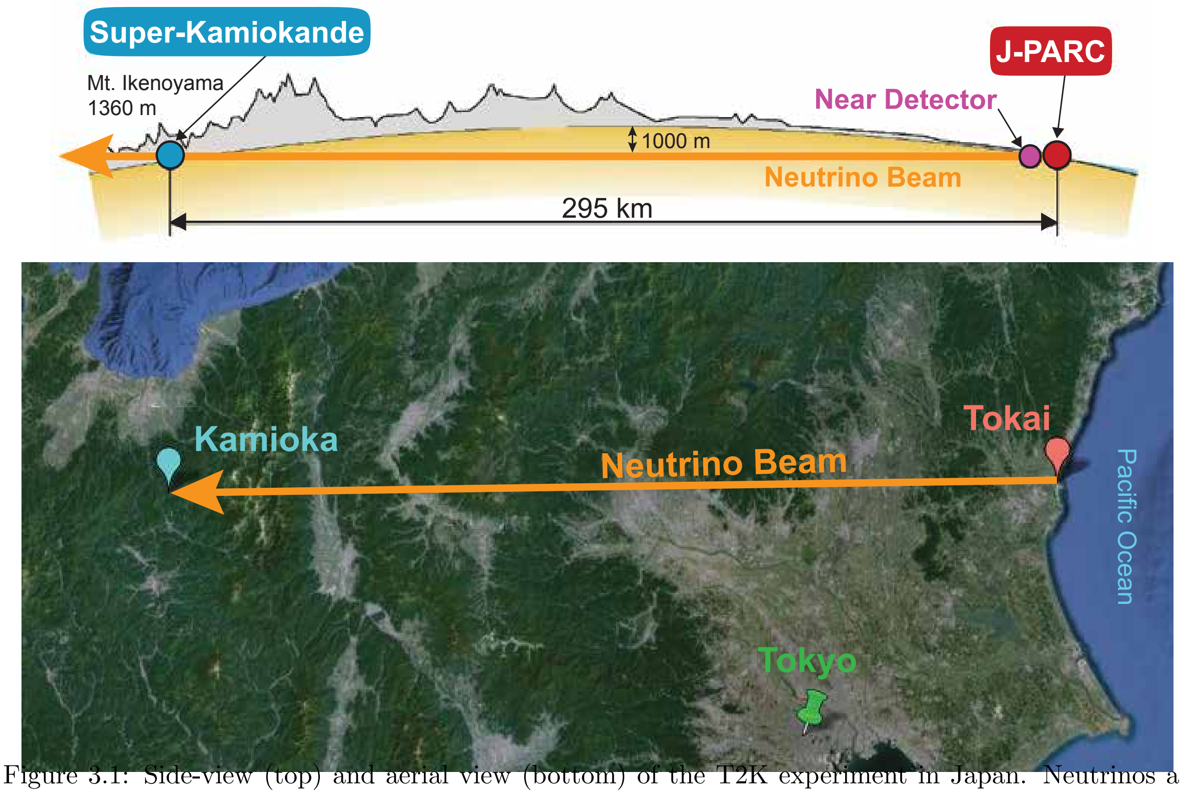

Figure 3.1: Side-view (top) and aerial view (bottom) of the T2K experiment in Japan. Neutrinos are produced at J-PARC in Tokai, Ibaraki Prefecture, detected at a near detector (ND280) prior to traversing 295 km to the far detector, Super-Kamiokande, in Kamioka, Gifu Prefecture.

Currently with only a fraction of the full expected data set, T2K reports the most precise measurement of $\sin^2 2\theta_{23}$ [96]. Also, as mentioned in Section 2.2.3, T2K has achieved a definitive observation of ν_e appearance from a ν_μ beam at 7.3σ significance [56], confirming the reactor measurements of θ_{13} and providing further evidence of the 3-neutrino oscillation model. This thesis details contributions towards these results as well as towards goal 3 with a joint ν_μ disappearance and ν_e appearance analysis.

3.1 T2K Neutrino Beam

The T2K neutrino beam is produced at J-PARC from the collision of 30 GeV protons with a graphite target. The charged particles in the resulting hadronic showers are focused by a set of magnetic horns and then decay in flight to neutrinos as in Equations 2.34 and 2.35.

An overview of J-PARC is shown in Figure 3.2. The proton beam accelerator complex is described in Section 3.1.1. The *primary neutrino beamline* after proton extraction and the *secondary neutrino beamline*, including the *target station* are described in Section 3.1.2. Section 3.1.3 explains a novel technique for placing the detectors (ND280 and SK) off-axis to achieve a narrow neutrino energy spectrum. This technique requires several components of the beamline designed to determine the beam direction with high precision.

3.1.1 J-PARC

There are three main components to J-PARC as shown in Figure 3.2: a linear accelerator (LINAC), a rapid-cycling synchrotron (RCS) and a main ring (MR) synchrotron. The LINAC accelerates H^- ions up to 181 MeV kinetic energy. The ions subsequently pass through a foil which strips the electrons from the protons. The protons are injected into the RCS, accelerated to 3 GeV kinetic energy, then fed into the MR and accelerated finally to 30 GeV. The MR can deliver a *spill* of up to 8 *bunches* of protons, which are

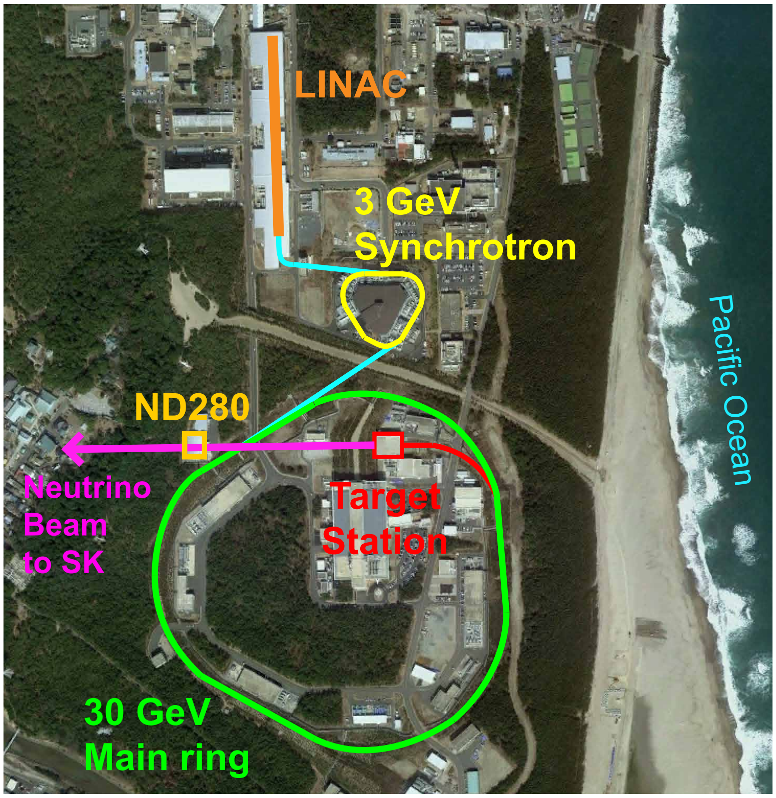

Figure 3.2: Overview of J-PARC, including the system of proton accelerators, the ν beamline and ND280.

extracted into the neutrino beam line by a set of five *kicker* magnets. The MR machine parameters are given in Table 3.1. The spill timing and bunch structure provide a distinct signature for downstream detectors to reduce non-beam backgrounds.

3.1.2 Neutrino Beamline

After the protons are extracted from the MR, they are directed towards ND280 and SK in the primary beamline consisting of preparation, arc and final focusing sections, as shown in Figure 3.3. The protons collide with the neutrino production target in the secondary beamline where the resulting hadrons are focused and decay into neutrinos.

Primary Neutrino Beamline

The preparation and final focusing (FF) sections, shown in more detail in Figure 3.4, use normal conducting magnets, while the arc section contains superconducting magnets, to

Circumference	1567 m
Beam power	~750 kW
Beam kinetic energy	30 GeV
Beam intensity	$\sim 3 \times 10^{14}$ p/spill
Spill cycle	~0.5 Hz
Number of bunches	6 or 8/spill
RF Frequency	1.67 - 1.72 MHz
Spill width	~ 5 μsec

Table 3.1: Design parameters of the J-PARC main ring synchrotron [95].

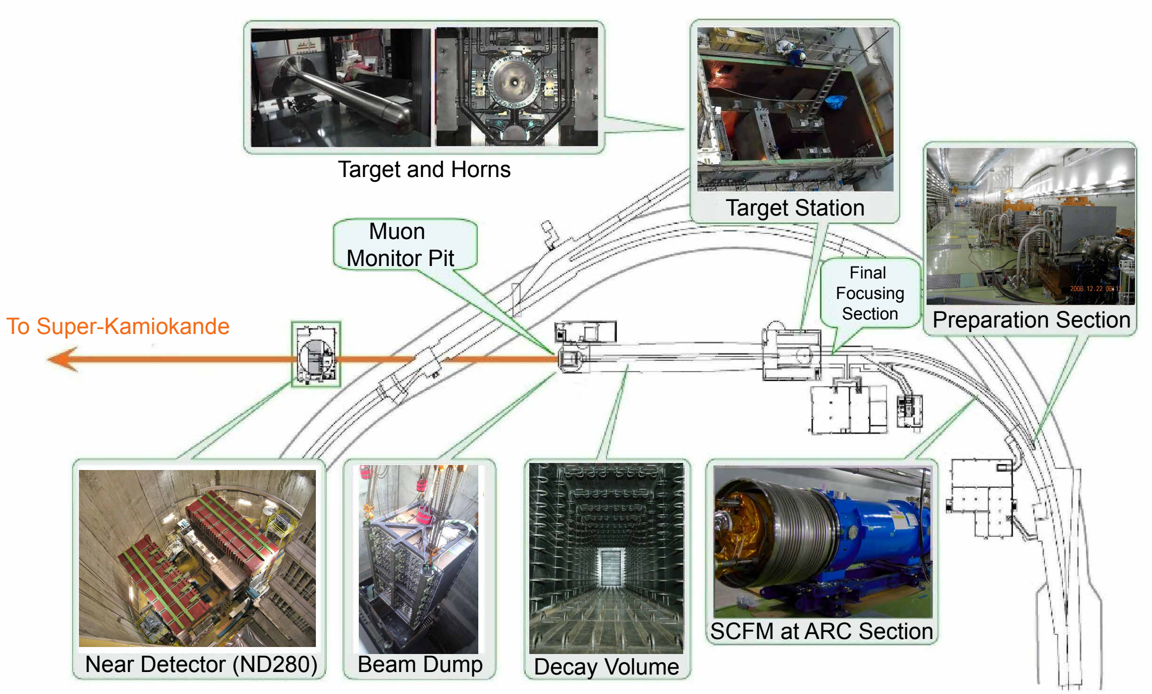

Figure 3.3: Overview of the neutrino beamline including photographs of various components and the near detector pit.

guide and focus the proton beam. Several monitors throughout the primary beamline provide information about the beam to optimize the magnet tuning, which is necessary to minimize beam loss and precisely control the final beam direction.

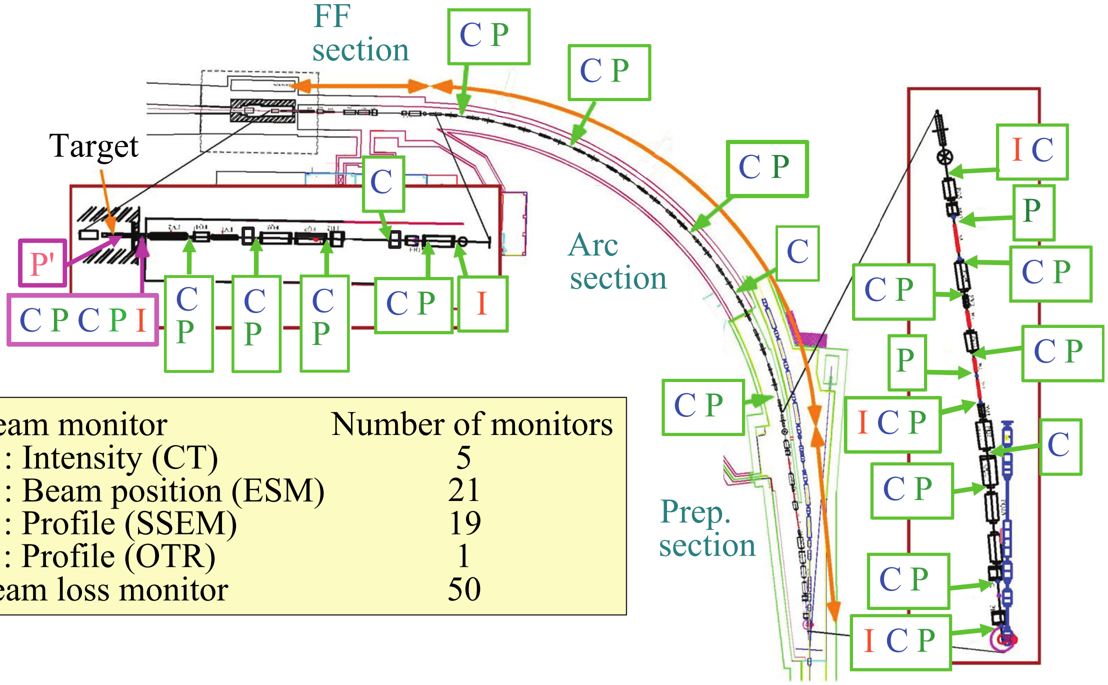

Beam monitor	Number of monitors
I : Intensity (CT)	5
C : Beam position (ESM)	21
P : Profile (SSEM)	19
P' : Profile (OTR)	1
Beam loss monitor	50

Figure 3.4: Overview of the primary neutrino beamline including positioning of all the beam monitors described in the text. The beam loss monitors are scattered throughout the beamline. The FF and preparation sections include zoomed-in panels.

Several gaseous proportional counters are placed around the primary beamline and serve as beam loss monitors (BLM). Electrostatic monitors (ESMs) measure the beam position while segmented secondary emission monitors (SSEMs) measure the whole beam profile at points along the beamline. Current transformers (CTs) provide a measure of the number of protons in each bunch, giving an uncertainty of 2.6% on the proton beam intensity [97][1].

---

[1] Beam power is typically reported as

$$P[\mathrm{W}] = n_p f_{rep}[\mathrm{Hz}] E[\mathrm{J}] \tag{3.1}$$

where n_p is the number of protons per spill, f_{rep} is the repetition rate or spill cycle as in Table 3.1 and E is the proton beam energy.

Information from all the beam monitors is used for optimizing the magnet currents to maximize the delivered protons-on-target (POT) and to precisely steer and control the beam profile at the target. The latter is important for target protection and the resulting neutrino beam direction described in the following sections.

Secondary Neutrino Beamline

The secondary beamline consists of the target station (TS), decay volume, beam dump and a muon monitor, as shown in Figure 3.5. The target station contains a helium vessel which houses the neutrino production target and magnetic focusing horns. The horns are protected from stray protons by an upstream collimator. Immediately upstream of the target, an optical transition radiation (OTR) monitor, described in more detail in Chapter 4, provides the final measurement of the proton beam profile.

Protons from the primary beamline enter the TS through a titanium-alloy beam window separating the vacuum in the primary beamline from the helium vessel. The OTR monitor in conjunction with the monitors in the FF section are critical for guiding the beam, with the proper width and direction, precisely onto the target. Figure 3.6 shows schematically the relative positions of the magnets used to tune the beam and the monitors providing feedback.

The protons strike a 1.8 g/cm^3 solid graphite target, 91.4 cm long (1.9 interaction lengths) and 2.6 cm in diameter. The target is encased by titanium and cooled by flowing helium gas. The beam width must be controlled, since if it is too narrow the concentrated heat load can damage the target, and if it is too wide a significant amount of the beam will miss the target.

The positively charged secondaries, from proton interactions in the target, are collected and focused by three magnetic *horns* in order to maximize the resulting neutrino flux [98]. Each horn is made from aluminum inner and outer conductors, which are pulsed with 250 kA to provide a toroidal magnetic field in time with the proton beam arrival.

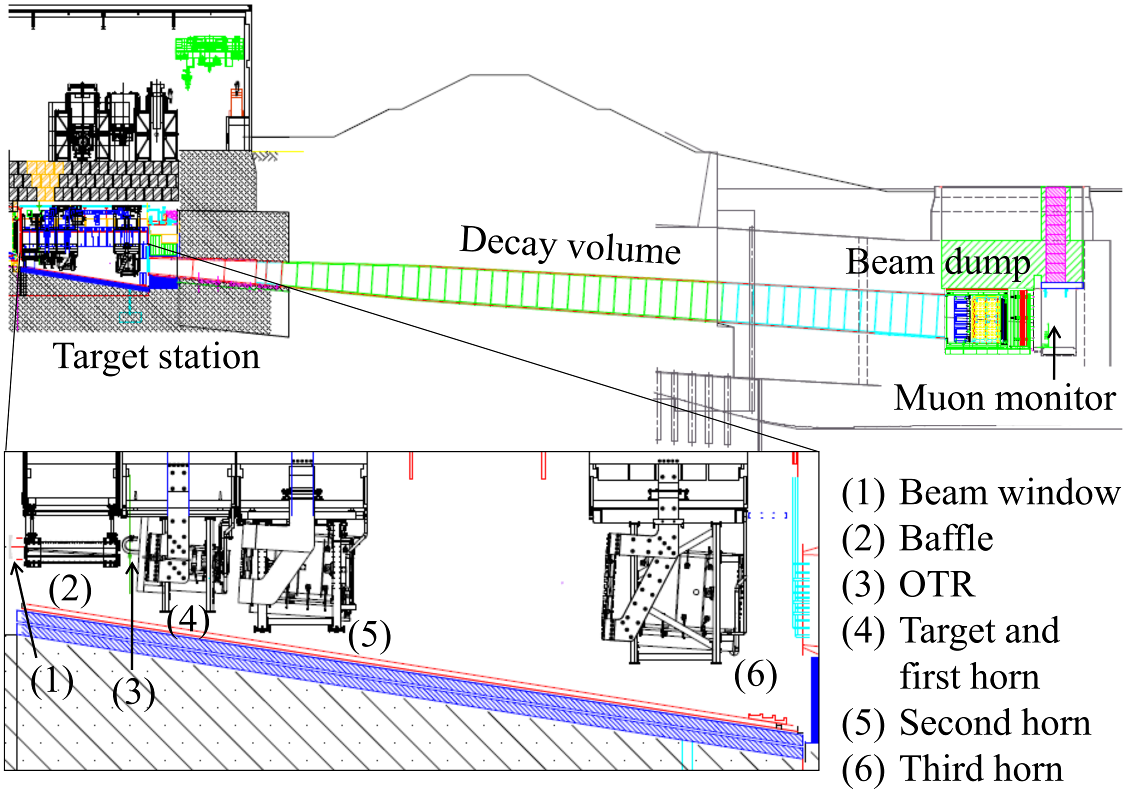

Figure 3.5: Side view of the secondary neutrino beamline. The proton beam travels to the right and passes through the OTR monitor downstream of the collimator (baffle) before colliding with the target. The horns focus the resulting charged particles (mostly π and K), which decay in the decay volume to produce neutrinos. Any remaining hadrons and some muons are absorbed by the beam dump. Higher energy penetrating muons are measured by the muon monitor.

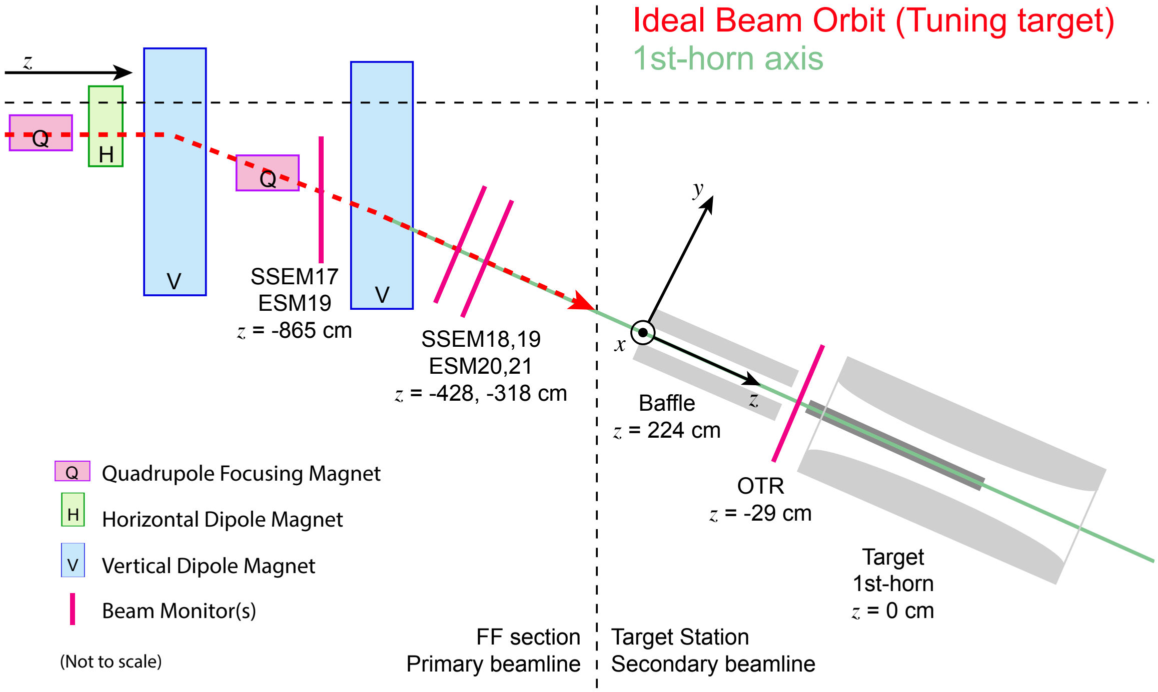

Figure 3.6: Schematic side view of the beamline components and the beam orbit in the FF section and TS. The beam is directed 3.637° below the horizontal by the last vertical bending magnet to achieve the desired off-axis angle (Section 3.1.3). The 1st-horn axis is surveyed relative to the last vertical bending magnet and defines the ideal beam orbit.

The field can be reversed by reversing the applied current, resulting in the focusing of negative particles and a primarily anti-neutrino beam instead.

The secondaries decay in a $\sim$ 100 m long *decay volume*, attached to the helium vessel downstream of the third horn. The cross section increases from 1.4 m wide by 1.7 m high at the upstream end to 3.0 m wide by 5.0 m high at the downstream end. A 75 ton (1.7 g/cm^3) graphite *beam dump*, 1.94 m wide, 3.174 m long, and 4.69 m high, is placed at the end of the decay volume. Iron plates amounting to a thickness of 2.40 m are placed at the downstream side. Together the graphite and iron stop all hadrons and most muons below 5 GeV/c momentum. The rest of the muons are measured bunch-by-bunch by a muon monitor (MUMON) consisting of ionization chambers and silicon photodetectors, which can further constrain the neutrino beam direction.

3.1.3 Off-Axis Configuration

Neutrino beams before T2K had broad energy spectra, not ideal for studying energy dependent phenomenon such as neutrino oscillation. The neutrino energy spectrum and magnitude of the flux depend on the angle of emission of the neutrino relative to the decaying pion "beam". It is possible to place a detector *off-axis* such that it observes a pseudo-mono-energetic beam [99]. This can be derived from the kinematics of the 2-body decay of pions. The outgoing neutrino 4-momentum is given by

$$\begin{aligned} p_\nu &= (E_\nu, E_\nu \sin\theta, 0, E_\nu \cos\theta) && (3.2) \\ &= (\gamma E_\nu^{CM}(1+\beta\cos\theta^{CM}), E_\nu^{CM}\sin\theta^{CM}, 0, \gamma E_\nu^{CM}(\beta+\cos\theta^{CM})), && (3.3) \end{aligned}$$

where E_ν is the neutrino energy, θ is the angle relative to the pion direction and the superscript CM denotes the same quantities except in the centre-of-mass frame. Equation 3.3 relates the CM frame to the lab frame in Equation 3.2 by a Lorentz boost with $\gamma = E_\pi/m_\pi$ and $\beta = v_\pi/c$, where E_π, m_π and v_π are the energy, mass and velocity of the pion, respectively. Taking the ratio of the second to fourth component of the 4-momenta gives

$$\tan\theta = \frac{E_\nu^{CM}\sin\theta^{CM}}{\gamma E_\nu^{CM}(\beta+\cos\theta^{CM})} \approx \frac{E_\nu^{CM}\sin\theta^{CM}}{E_\nu}, \tag{3.4}$$

where the approximate equality assumes $\beta \approx 1$ for $E_\pi \gg m_\pi$. Therefore, since $|\sin\theta^{CM}| < 1$, the maximum allowed angle for a given neutrino energy E_ν is

$$\tan\theta^{max} = \frac{E_\nu^{CM}}{E_\nu} = \frac{29.8\text{ MeV}}{E_\nu}, \tag{3.5}$$

where $E_\nu^{CM} = (m_\pi^2 - m_\mu^2)/2m_\pi) = 29.8$ MeV. Similarly, the maximum neutrino energy for a given off-axis angle θ is

$$E_\nu^{max} = \frac{29.8\text{ MeV}}{\tan\theta}, \tag{3.6}$$

as depicted in Figure 3.7 (left), which shows the neutrino energy dependence on pion energy for on-axis and two off-axis angles.

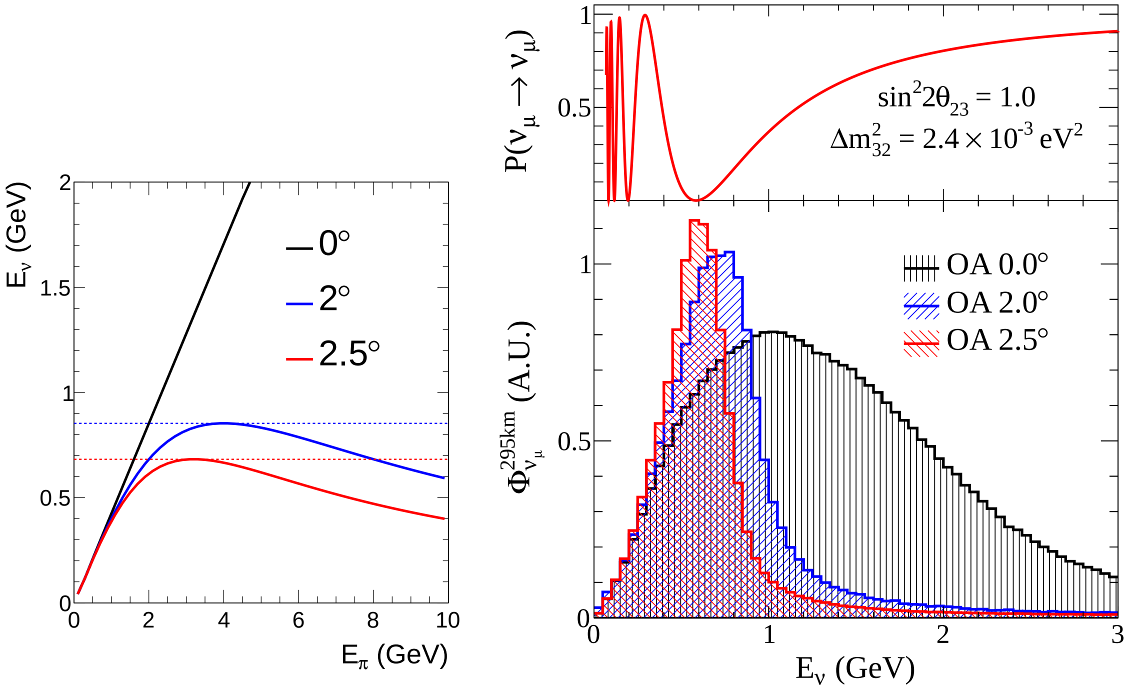

Figure 3.7: Left: Neutrino energy dependence on decaying pion energy from 4-momentum conservation for three off-axis angles. The dotted lines show the maximum achievable neutrino energy as given by Equation 3.6. Top right: ν_μ survival probability as a function of neutrino energy (Equation 2.15) with L = 295 km, the T2K baseline. Bottom right: The T2K neutrino flux spectrum prediction at three off-axis angles as calculated by simulation described in Section 3.6 [100].

Therefore, by shifting the detector off-axis from the proton beam, the peak of the neutrino energy spectrum can be selected as shown in Figure 3.7 (bottom right). For T2K, an off-axis angle of 2.5° was adopted such that the peak coincides with the ν_μ disappearance (and ν_e appearance) maximum in Figure 3.7 (top right), motivated by the previous measurements of Δm^2_{32} by SK [39] and K2K [41] (Section 2.2.2). Furthermore, the high energy tail is substantially decreased relative to the on-axis case, which helps reduce *feed-down* from high energy NC interactions that can be misidentified at lower energy causing backgrounds for the ν_e appearance search.

3.2 Near Detector: ND280

A precise measurement of neutrino oscillation requires a detailed understanding of the neutrino beam prior to oscillation. A near detector complex, called ND280, is situated 280 m downstream of the neutrino production target as shown in Figures 3.2 and 3.1. It consists of two components as shown in Figure 3.8: the ND280-on-axis detector (INGRID) and the ND280-off-axis detector (hereafter shortened to ND280). The main purpose of INGRID is to measure the neutrino beam profile and determine the beam direction, which is necessary for determining the off-axis angle (Section 3.1.3). The off-axis detector was designed to perform detailed measurements of neutrino interactions and characterize the neutrino beam prior to oscillation in order to constrain the event rate prediction at SK, which is at the same off-axis angle.

3.2.1 INGRID On-axis Detector

The Interactive Neutrino GRID (INGRID) [101] is centred on the proton beam axis to directly monitor the neutrino beam profile and intensity. It consists of 16 modules arranged as shown in Figure 3.8 (bottom right) to measure the axial symmetry. Each 7.1 ton module contains alternating planes of iron plates and scintillator bars read out

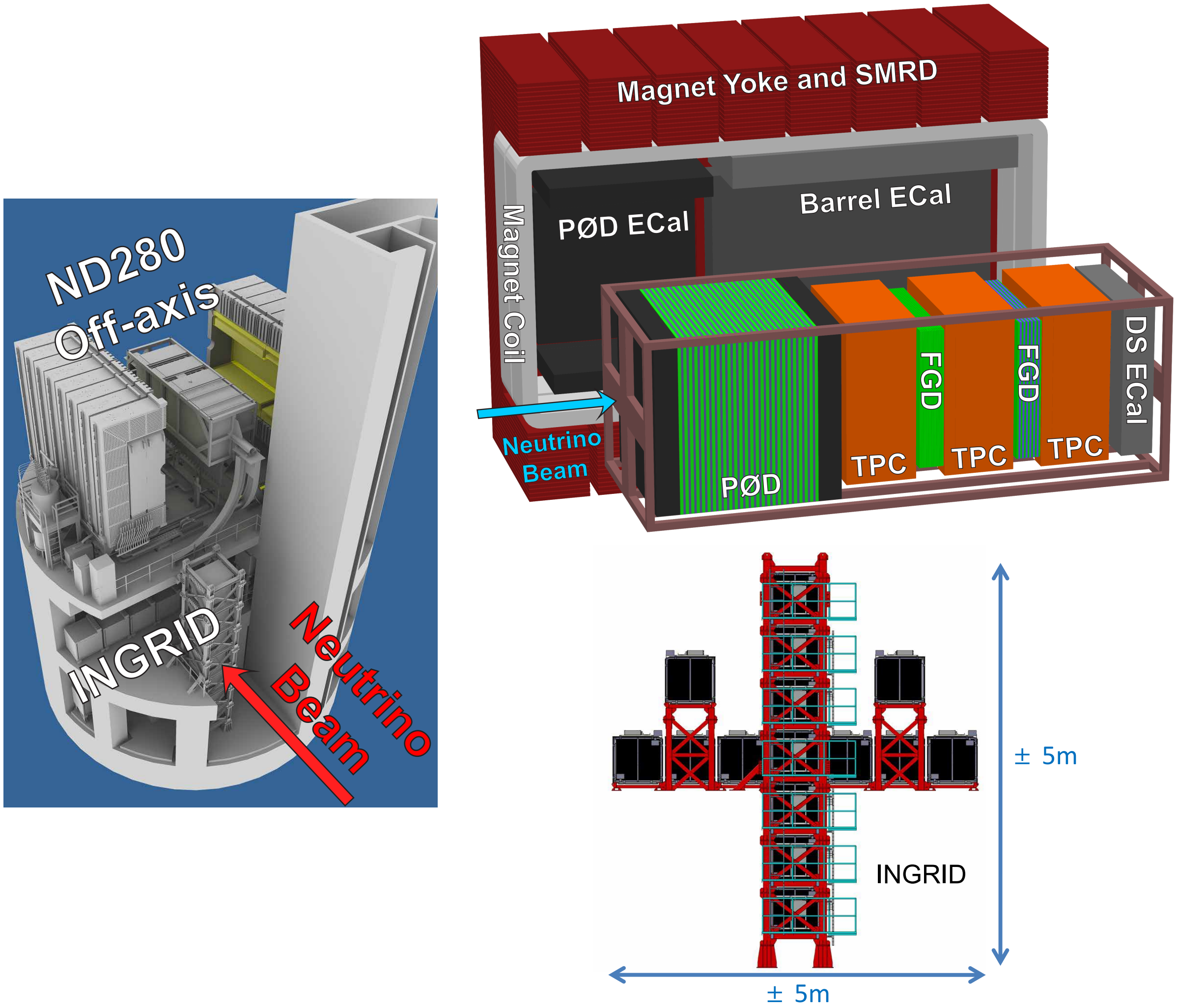

Figure 3.8: Left: The ND280 detector complex showing the relative positions of the INGRID detector and the ND280 off-axis detector. The pit is 37 m deep and 19 m in diameter. Top right: Components of the ND280 off-axis detector. Bottom right: 16 modules of the INGRID on-axis detector covering a $10 \times 10\ \mathrm{m}^2$ region centred on the proton beam axis.

by wavelength shifting (WLS) fibres.

INGRID detects about 1.5 neutrino interactions per 10^{14} POT corresponding to 10-20k events per day with a beam power around 100 kW. This is sufficient statistics to monitor the neutrino beam profile and determine the beam centre with a precision better than 10 cm or 0.4 mrad. This measurement combined with measurements from the neutrino beamline precisely determine the off-axis angle for ND280 and SK, reducing the systematic uncertainty on the neutrino energy spectra and absolute flux.

3.2.2 Off-axis Detector

There are several requirements for the near detector ND280 in order to achieve the oscillation physics goals mentioned previously, including:

- Determination of the ν_μ flux spectrum prior to oscillation.
- Measurement of the ν_e component of the neutrino beam, coming from the decays of muons and kaons, which produces an irreducible background for the ν_e appearance search at SK.
- Separation of exclusive CC and NC interaction channels, in particular NC π^0 and $\pi^\pm$, which are backgrounds for the ν_e and ν_μ analyses at SK, respectively.

For this purpose, ND280 consists of many sub-detectors as shown in Figure 3.8 (top right). The *basket* contains a π^0 detector (PØD) and a *tracker* made up of three time projection chambers (TPCs) and two fine grained detectors (FGDs). Surrounding the basket are several electromagnetic calorimeters (ECals). The ECals and the basket are enclosed within a 0.2 T magnet.

The UA1 Magnet

To measure the momentum of charged particles, the basket is housed within the aluminum coils of the UA1 [102] magnet, donated by CERN. The magnetic field of 0.2 T perpendicular to the neutrino beam direction, produced by a current of ∼3 kA in the coils, is returned by an 850 ton iron yoke. The 3 spatial components of the magnetic field within the basket were mapped using Hall probes in order to minimize the contribution field distortions to the systematic error in momentum determination.

π^0 Detector (P∅D)

The P∅D [103] was designed to detect π^0 s, in particular for the measurement of NC π^0 production. It is located at the most upstream end of the basket. The upstream and downstream sides of the detector consist of alternating layers of scintillator bars readout by WLS fibres and lead. The central region of the detector consist of alternating layers of scintillator, brass and water bags. The electromagnetic showers of the photons from π^0 decay are contained in the P∅D due to the small radiation length of lead and brass.

Much of ND280 contains carbon scintillator as the active target material. However, the far detector target is water, so it is necessary to understand the differences in interactions between the two materials so by having some water target in ND280. For the P∅D, the water bags can be drained to measure the differences in interactions rates, which is important for extrapolation to SK. The dimensions of the P∅D are approximately $2.10 \times 2.24 \times 2.40$ m providing a total target mass with and without water of 16.1 tons and 13.3 tons, respectively.

Tracker: FGDs and TPCs

The tracker, immediately downstream of the P∅D, consists of three time projection chambers (TPCs) with two fine-grained detectors (FGDs) interspersed. It was designed to provide particle identification (PID) and precisely measure the momentum spectrum and charge of those particles. In particular, the momentum of the muons or electrons from CC neutrino interactions is used to reconstruct the neutrino energy.

The TPCs [104], labelled 1–3 from upstream, measure particles mostly produced in other components of ND280. Each TPC is a 2.3 × 2.4 × 1.0 m box filled with an argon gas mixture that is ionized by passing charged particles. The box is divided by a central cathode which produces an electric field for drifting the electrons from the ionized gas toward one of the readout planes on either end of the TPC. The arrival time of the drift electrons and their pattern allows for the 3D reconstruction of the charged particle trajectories. The momentum of each particle is determined from its curvature in the magnetic field with a resolution of $< 2\%$ below 1 GeV/c. Furthermore, the amount of ionization combined with the momentum information provides PID capability.

The FGDs [105], labelled 1 and 2 from upstream, provide the main target mass for neutrino interactions in the tracker. Each FGD consists of finely segmented scintillator bars read out by WLS fibres, which provide high resolution tracking in the vicinity of the interaction vertex. Energy loss within the scintillator can be used for PID. FGD2 has water layers interspersed between the scintillator layers, similar to the P∅D. Each FGD weights 1.1 ton and has dimensions of approximately $2.3 \times 2.4 \times 0.4$ m^3.

Electromagnetic Calorimeters (ECals)

The detectors contained in the basket are surrounded on all sides by the ECals [106] for the purpose of detecting exiting particles and vetoing particles originating from outside the basket. There are 13 modules in total. The four sides of the basket parallel to the beam are enclosed by 6 modules around the P∅D (P∅D ECal) and 6 modules around the tracker (Barrel ECal), all attached to the inside of the UA1 magnet. The most downstream end of the tracker is instrumented with the DS ECal within the basket.

Similar to the P∅D, these ECals consist of alternating planes of scintillator bars and lead for converting photons and containing electromagnetic showers. The ECals around the tracker are important for detecting photons that originate from π^0 decays within the tracker and provide complementary PID and energy information from shower reconstruction.

Side Muon Range Detector (SMRD)

The SMRD [107] consists of scintillator slabs instrumented with WLS fibres interspersed in the air gaps of the UA magnet yoke. It provides energy and direction information for muons produced in the tracker that exit at large angles relative to the beam. The muons range out in the iron providing a measurement of the momentum if the muon clips or misses the TPCs completely. The SMRD acts as a veto for beam neutrino interaction events that originate outside the tracker, especially in the large mass of the magnet and the near detector pit walls. It also acts as a trigger for cosmic ray muons, which are used for calibration studies of the inner detectors.

3.3 Far Detector: Super-Kamiokande

The Super Kamiokande (SK) detector [108] acts as the far detector of T2K to measure the neutrino beam and search for neutrino oscillation. It is a large water Čerenkov detector situated about 1 km underground and 295 km west of the neutrino production target at J-PARC (Figure 3.1). The detector has been in operation since 1996 with a broad physics program including solar, atmospheric and accelerator neutrinos (Section 2.2), as well as searches for proton decay [109–112], dark matter [113], supernova relic neutrinos [114] and magnetic monopoles [115].

The detector consists of a cylindrical tank, 41.4 m tall and 39.3 m in diameter, filled with 50 kton of ultra-pure water and imaged by ∼13000 photo-multiplier tubes (PMTs). The volume is optically separated into two concentric compartments: the inner detector (ID) and outer detector (OD) as shown in Figure 3.9. The ID is 36.2 m tall and 33.8 m in diameter and contains 32 kton of water, while the OD surrounds the ID with a ∼2 m thick layer of water around the circumference and at the top and bottom.

Charged particles, such as those produced in neutrino interactions, can emit optical radiation called Čerenkov light as they traverse the water, as described below in

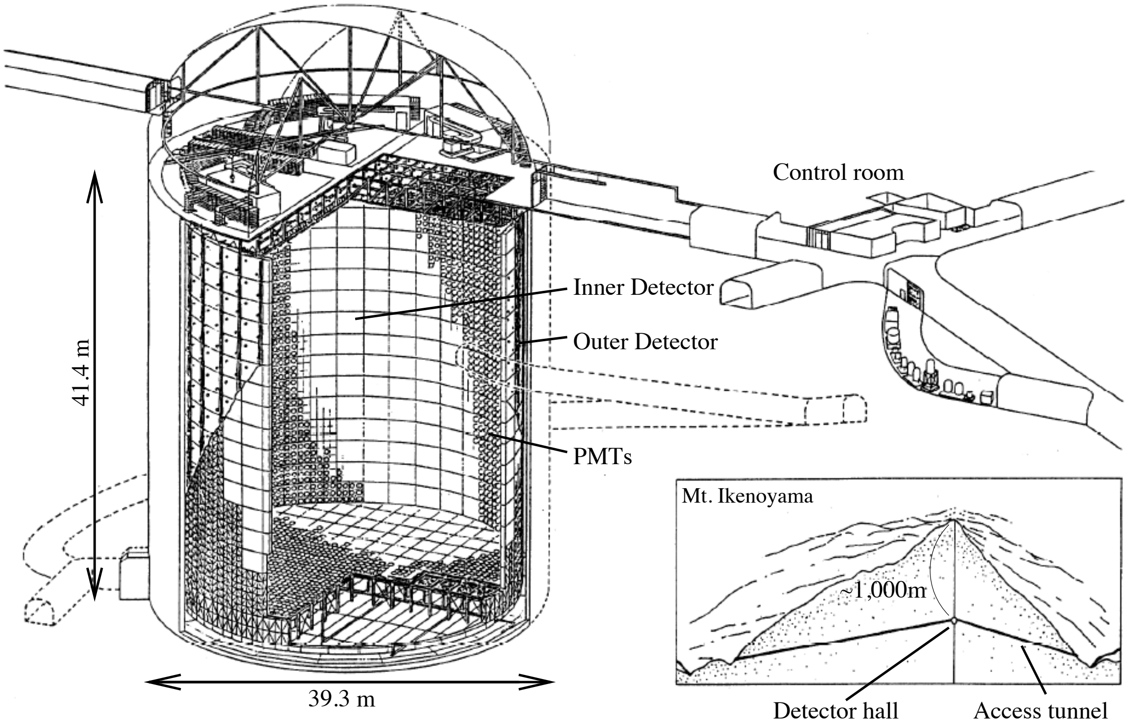

Figure 3.9: Schematic diagram of the SK Detector and its location inside Mount Ikenoyama (bottom right inset).

Section 3.3.1. This light is detected by 11129 20-inch PMTs lining the ID wall facing inward, corresponding to a spatial coverage of 40%. The information given by the light patterns on the wall is used to determine particle momenta and PID, as described in more detail in Chapter 8. The OD mainly acts as a veto for incoming backgrounds such as cosmic rays which do not require precise event reconstruction. Therefore, the walls are lined with a highly reflective material and the 1885 8-inch PMTs are each fitted with a 60 × 60 cm wavelength shifting plate to increase light collection efficiency.

3.3.1 Čerenkov Radiation

The SK detector relies on the phenomenon of Čerenkov radiation [116], which occurs when the speed v of a charged particle exceeds the phase velocity of light in some medium with refractive index n:

$$v > \frac{c}{n}. \tag{3.7}$$

In this case, the particle creates an electromagnetic *shock wave* similar to a *sonic boom* from objects travelling faster than the speed of sound. The Čerenkov threshold in momentum as a function of particle mass can be determined from Equation 3.7, and is shown for various particles in Table 3.2 assuming $n = 1.33$ for water.

Particle	Mass (MeV/c^2)	Čerenkov Threshold (MeV/c)
Electron	0.511	0.583
Muon	105.7	120.5
Pion	139.6	159.2
Kaon	493.7	563.0
Proton	938.3	1070.

Table 3.2: The mass and Čerenkov threshold in momentum for various charged particles.

The wavefront of the shock wave, or the Čerenkov light, is emitted at a polar angle

θ_C relative to the particle direction given by

$$\cos\theta_C = \frac{1}{\beta n}, \tag{3.8}$$

where $\beta = \frac{v}{c}$. Thus, the light forms a cone around the particle trajectory, projecting a ring on the detector walls. For an ultra-relativistic particle ($\beta \approx 1$), the Čerenkov angle is maximum, 41.2° in water, and the cone collapses ($\theta_C \rightarrow 0$) as the particle slows and approaches the Čerenkov threshold. The energy loss is determined by counting the number of Čerenkov photons produced, proportional to $\sin^2\theta_C$ [117], while the particle is above threshold. This provides PID information, since both the Čerenkov threshold and energy loss in the medium depend on the mass of the particle. Furthermore, the development of an electromagnetic shower from an electron causes a *fuzzy* ring from the overlap of multiple rings, providing additional PID separation power from muons that travel relatively straight, as demonstrated in Figure 3.10.

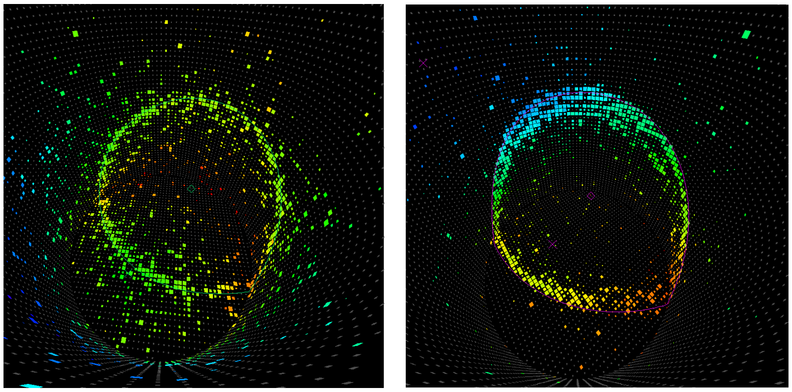

Figure 3.10: Example SK event displays of an e-like (left) and μ-like (right) Čerenkov ring.

Chapter 4

Optical Transition Radiation (OTR) Monitor

The T2K experiment uses an off-axis neutrino beam to achieve a narrow-band energy spectrum (Section 3.1.3). The off-axis angle is tuned to match the oscillation maximum (Figure 3.7) whose position in energy depends on Δm^2_{32}, one of the primary physics measurements of T2K. Thus, in order to achieve the stated goal of $< 4\%$ precision on Δm^2_{32}, the beam direction must be measured to within 1 mrad[1]. This is achieved by the combination of proton beam monitor measurements (Section 3.1.2) and measurements from the on-axis neutrino detector INGRID (Section 3.2.1). In particular, the proton beam position[2] and direction at the target must be measured with an accuracy of 1 mm and 0.5 mrad, respectively. A measurement of the beam size (to about 10%) near the target also facilitates target protection and minimization of beam loss.This chapter will describe the T2K optical transition radiation (OTR) proton beam monitor, which has been instrumental to achieving these goals.

The OTR monitor measures the profile of the proton beam by imaging transition

---

[1] A 1 mrad shift of the off-axis angle corresponds to about a 3% uncertainty in the energy spectrum peak using Equation 3.6 with $\theta = 2.5^\circ$.

[2] Due to the focusing nature of the horns, a translation of the proton beam from the center of the target-horn axis results in a shift of the resulting neutrino beam direction.

radiation as the protons pass through a thin foil (Section 4.1). It is positioned 29 cm upstream from the target (Figure 3.5), which is a high radiation environment where conventional detectors (SSEMs, ESMs) would fail. The radiation would also quickly destroy any electronics placed nearby, requiring an optical system that transports the light through the shielding to a camera above the helium vessel (Section 4.2). The mechanical design, calibration, analysis and performance are described in Sections 4.4 to 4.8.

4.1 Transition Radiation

Transition radiation occurs when a charged particle travels between two media with different electromagnetic characteristics. This phenomenon was first predicted in [118] and experimentally verified in [119]. Transition radiation detectors have been implemented in many accelerators [120–122] to characterize the beam by placing a thin foil in the beamline, producing OTR light which is imaged by a camera.

As a charged particle crosses the boundary between two materials of different permittivities, the electric fields of the particle induce a polarization in the medium. This polarization emits radiation which combines coherently to produce transition radiation. The formation depth, or approximate distance required for sufficient radiation intensity, is given by [117]

$$D = \frac{\gamma c}{\omega_p}, \tag{4.1}$$

where $\gamma = \frac{1}{1-\beta^2}$ and ω_p is the *plasma frequency* for a specific medium. The plasma frequency depends on the electron number density n_e as follows:

$$\omega_p^2 = \frac{n_e e^2}{\varepsilon_0 m_e}. \tag{4.2}$$

For example, in pure titanium $\omega_p \approx 1.34 \times 10^{16}\ \mathrm{s}^{-1}$ and for a 30 GeV proton ($\gamma \approx 32$) $D \sim 1$ micron. Therefore, only a thin layer of material is needed to produce transition radiation, which is necessary to prevent significant beam loss.

The number of photons N emitted via transition radiation in a frequency range $d\omega$ and solid angle $d\Omega$ is given by [123]

$$\begin{aligned}\frac{d^2N}{d\omega d\Omega} =& \frac{2e^2\beta^2}{\pi hc\omega} \times \frac{\sqrt{\epsilon_2}\sin^2\theta\cos^2\theta}{|1-\beta^2\epsilon_2\cos^2\theta|^2} \\ & \times \left| \frac{(\epsilon_1-\epsilon_2)\left(1-\beta^2\epsilon_2-\beta\sqrt{\epsilon_1-\epsilon_2\sin^2\theta}\right)}{\left(1-\beta\sqrt{\epsilon_1-\epsilon_2\sin^2\theta}\right)\left(\epsilon_1\cos\theta+\sqrt{\epsilon_1\epsilon_2-\epsilon_2^2\sin^2\theta}\right)} \right|^2 ,\end{aligned} \tag{4.3}$$

where ϵ_1 and ϵ_2 are the relative permittivities of the first and second media, respectively, and θ is the angle between the particle direction and the photon direction.

For a relativistic particle ($\beta \sim 1$) travelling from a medium with $|\epsilon_1| > 1$ into vacuum ($\epsilon_2 = 1$), Equation 4.3 is approximated by [124]

$$\frac{d^2N}{d\omega d\Omega} = \frac{2e^2}{\pi hc\omega}\frac{\sin^2\theta}{(1-\beta\cos\theta)^2}. \tag{4.4}$$

The polar angular distribution is shown in Figure 4.1 (left, black curve). Photons are emitted in a narrow forward cone, with a maximum at $\theta \approx 1/\gamma$.

For a particle entering a medium from vacuum, $\epsilon_1 = 1$ and $\epsilon_2 = \epsilon > 1$ are reversed from the previous case. In this case Equation 4.3 is approximated by

$$\frac{d^2N}{d\omega d\Omega} = \frac{2e^2}{\pi hc\omega}\left|\frac{\sqrt{\epsilon}-1}{\sqrt{\epsilon}+1}\right|^2\frac{\sin^2\theta}{(1-\beta\cos\theta)^2}. \tag{4.5}$$

where θ is now relative to the backward direction (opposite the particle direction). As suggested by the form of the factor depending on ϵ (amplitude of a reflected electromagnetic wave), the radiation is actually reflected along the reflection axis defined by twice the angle between the particle and the normal to the boundary, as shown in Figure 4.1 (right). With a foil placed at an angle of 45° relative to the proton beamline, the optical component of the backward radiation (or OTR) can be collected and imaged.

4.2 Optical System

Due to the extremely high radiation environment around the neutrino production target, a novel and more complicated system for collecting OTR, compared to those in [120–122],

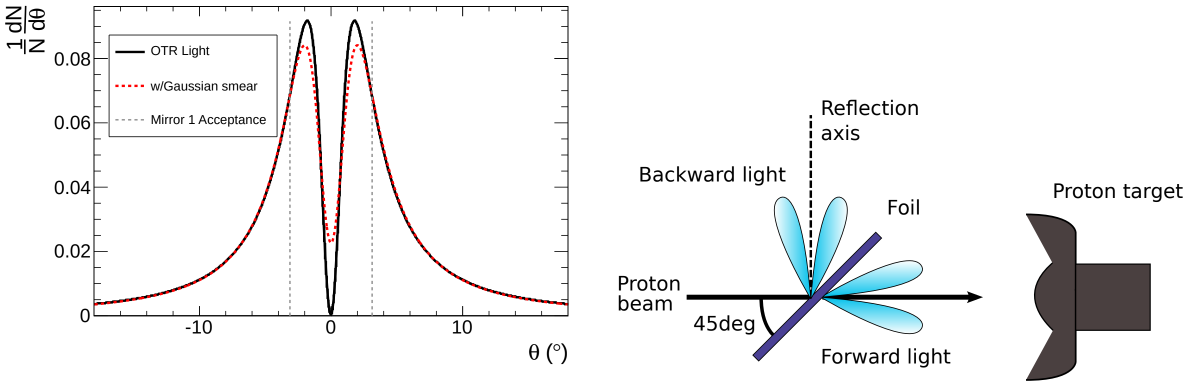

Figure 4.1: Left: Angular distribution of OTR (black), smeared by a Gaussian with $\sigma = 0.55^\circ$ to simulate diffuse reflection by the titanium foil (red, dotted). The vertical grey lines show the angular acceptance of the optical system (mirror 1). Right: Illustration of the forward and backward OTR lobes from a foil oriented at 45° relative to the beam.

must be designed. The proton beam passes through a foil positioned at 45° relative to the beam axis such that OTR is reflected in the transverse horizontal direction as shown in Figure 4.2. A series of four 90° off-axis parabolic mirrors (Section 4.2.1) transport the light through two bends in the radiation shielding. Intermediate and final images are formed between mirrors 2 and 3, and at the camera, respectively. The light exits the helium vessel through a quartz window. In the previous systems with no collision target nearby [120–122], a camera could be simply located at the mirror 1 or 2 positions and at closer distances.

Mirror 1 is placed 110 cm away from the foil, as far as possible from the target to minimize radiation damage, but keeping the mirrors a reasonable size to collect the light and minimize the bore size in the shielding. This defines a focal length of 55 cm for mirror 1 and mirror diameter of 12 cm. The approximate angular acceptance for OTR light from the foil in this geometry is illustrated in Figure 4.1 (left). Mirrors 2 and 3 are the same size and focal length as mirror 1. The camera (Section 4.2.2) sensor is only 7.5 mm wide, therefore the image of the foil (50 mm in diameter) must be reduced in size. This is accomplished with mirror 4 having a shorter focal length of 30 cm (∼55%

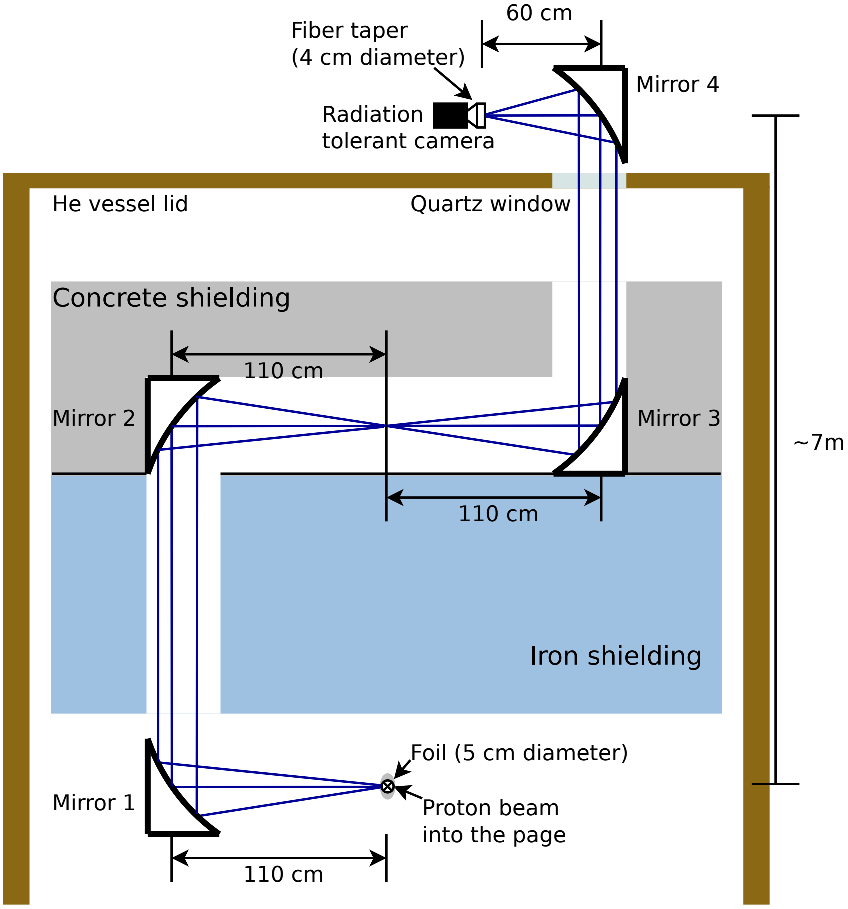

Figure 4.2: A cross section of the optical path of OTR produced by the proton beam travelling into the page through the foil. The focusing effect of the mirrors is illustrated by three example light rays. The mirror dimensions are given in Section 4.2.1. (Not to scale.)

reduction) and a fiber-optic taper attached to the front of the camera (∼28% reduction).

4.2.1 Mirrors

The 90° off-axis parabolic mirrors were manufactured out of solid aluminum and coated with a uniform 400 nm thick layer of Al_2O_3 [125]. This coating provides reflectivity near 100% in order to reduce light loss at each mirror and resistance to darkening due to radiation damage. The reflectivity of a smaller mirror with this coating was shown to be unaffected after irradiation by a proton beam at TRIUMF equivalent to the dose expected after 130 years of beam operation at the location of mirror 1 [126].

4.2.2 Camera

A charge injection device (CID) monochrome camera, radiation tolerant up to 10 kGy [127], is used to withstand the expected dose rate above the helium vessel (∼1 kGy/year at 750 kW beam power). The 11 mm diagonal sensor consists of 755×484 pixels with dimensions $12.0\ \mu\text{m} \times 13.7\ \mu\text{m}$.

A fiber-optic taper is used in front of the camera to reduce the image size instead of a lens in order to minimize aberrations. The angular acceptance and transmittance of the taper were characterized using laser light, which are used as input to absolute light yield predictions [126]. For example, the intensity of a laser spot incident on the taper face was measured at various angles, with results as shown in Figure 4.3 (left). Thus, assuming the maximum angle from mirror 4 to the center of the taper ($\sim 6^\circ$), the light collection efficiency due to the taper angular acceptance is approximately 90%. For reconstruction of the beam profile, however, this factor is automatically taken into account by the efficiency correction described in Section 4.7.1.

A non-linearity at low light levels was observed in the camera response [126]. To bring the camera out of the non-linear region, an ambient light source constructed from multiple LEDs was placed behind mirror 4 facing the camera. This prevents the need for

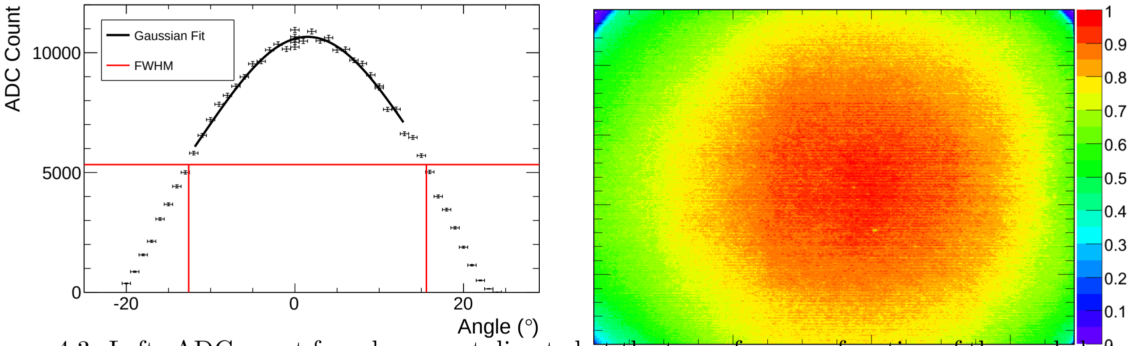

Figure 4.3: Left: ADC count for a laser spot directed at the taper face as a function of the angle between the laser and normal to the face of the taper. A Gaussian is fitted around the maximum (black curve), which is used to estimate the half width at half maximum ∼ 14.1° (red lines). Right: Image through the taper of an LCD screen displaying white (a uniform Lambertian light source). The z-axis is normalized to the peak value showing the relative transmission efficiency across the taper face, which is ∼ 30 mm (x) by ∼ 24 mm (y).

a complicated correction in the analysis at a small expense of dynamic range.

4.3 Prototype System

A prototype system, scaled to 13.8% of the full size, was assembled to demonstrate the measurement concept, practice mirror alignment procedures (Section 4.5.2), test various lighting systems (Section 4.5.1) and develop image analysis software (Section 4.7). A picture of the prototype setup is shown in Figure 4.4.

The prototype was successfully tested at the National Research Council in Ottawa [126] in an electron beam of γ factor similar to the J-PARC proton beam, giving confidence to construct of the full scale system.

The prototype system was also used to develop and practice alignment procedures by using a laser and adjusting mirror positions and angles. Various laser, LED and filament light sources were tested in two configurations: *back-lighting* where the direction of light passes through the foil position towards mirror 1, and *front-lighting* where the light source is placed near mirror 1 and directed towards the foil. It was determined that

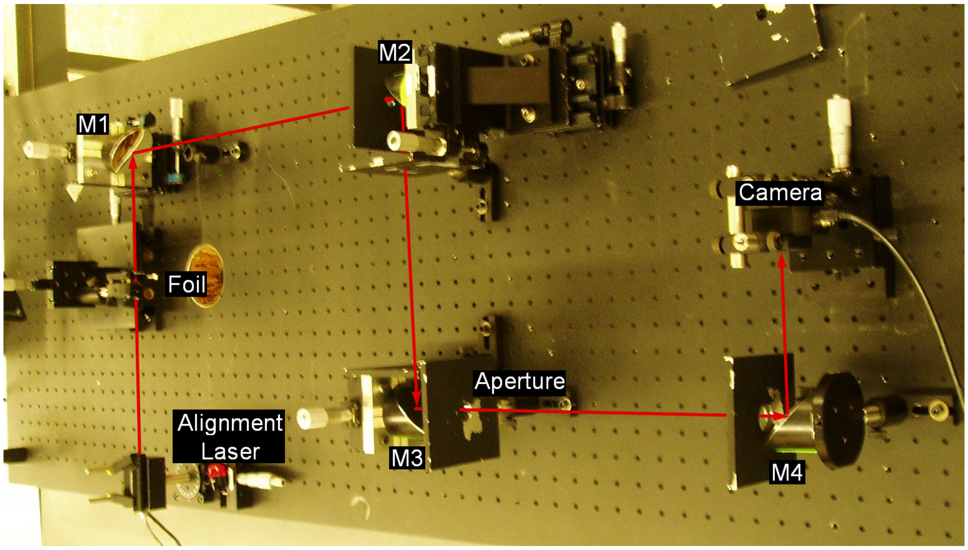

Figure 4.4: Photograph of the prototype system with an illustrated path of the light from an alignment laser.

a back-lighting filament-style source provided the most uniform light and best contrast when imaging a foil with machined holes for calibration [128] (Section 4.4.1).

4.4 Mechanical design

The full-scale system is located in a high-radiation environment which prevents direct access to the camera location during beam operation and never to components near the beam. Thus, the mechanical systems were designed to satisfy the following criteria:

- Ability to continually and remotely calibrate the optics.
- Stability with temperature.
- Long-term (∼ several years) robustness.
- Ease of remote maintenance for component replacement.

An overview of the design is shown in Figure 4.5(a). The system, including 2 tubes holding the first 3 mirrors, is mounted onto the first horn and its support module. Various OTR monitor components near the beam, including the target foil disk system

(Section 4.4.1), are attached to the horn-target assembly as shown in the rotated zoom in Figure 4.5(c). An optical table is placed on top of the helium vessel lid (not shown) and supports mirror 4 and the camera system. The mirror tubes and target position are shown more clearly in the rear view in Figure 4.5(b). A vertical bore runs through the right side of the front plate to an extension tube below to guide various cables to the components near the beam. Figure 4.6 shows the details of the monitor components near the beam, which are described in the following sections.

4.4.1 Foil Disk System

The foils that are inserted into the beam line are mounted on an 8-slot disk carousel as shown in Figures 4.6 and 4.7. Each slot has a diameter of 5 cm which, when mounted at 45° to the beam axis, covers the maximum beam acceptance defined by the 3 cm diameter collimator (Figure 3.5).

Seven slots are occupied by various foils summarized in Table 4.1 while one slot is left empty for calibrating the optical system (Section 4.7.1). A Demarquest AF995R 100 μm thick ceramic wafer [129] and a 50 μm thick aluminum foil are used during low proton beam intensity operation for increased light yield. A titanium alloy was chosen for higher intensities for its superior strength, and four 50 μm thick foils are installed for redundancy. A set of holes is precisely laser-machined into the fifth titanium *calibration foil*, described in Section 4.4.2.

Each foil is clamped onto the disk (Figure 4.7 (right)) providing sufficient tension to keep the foil flat during the thermal shock of the beam pulse. The disk is mounted on an *arm* attached by two *legs* to an aluminum plate of the target-horn assembly (Figure 4.5(c)). The disk, arm and legs are made of titanium, with a low coefficient of thermal expansion, to minimize shifts relative to the target and horn.

The disk is rotated to position the desired slot in the beamline by a remote controlled stepper motor at the top of the horn module below the helium vessel lid. The motor

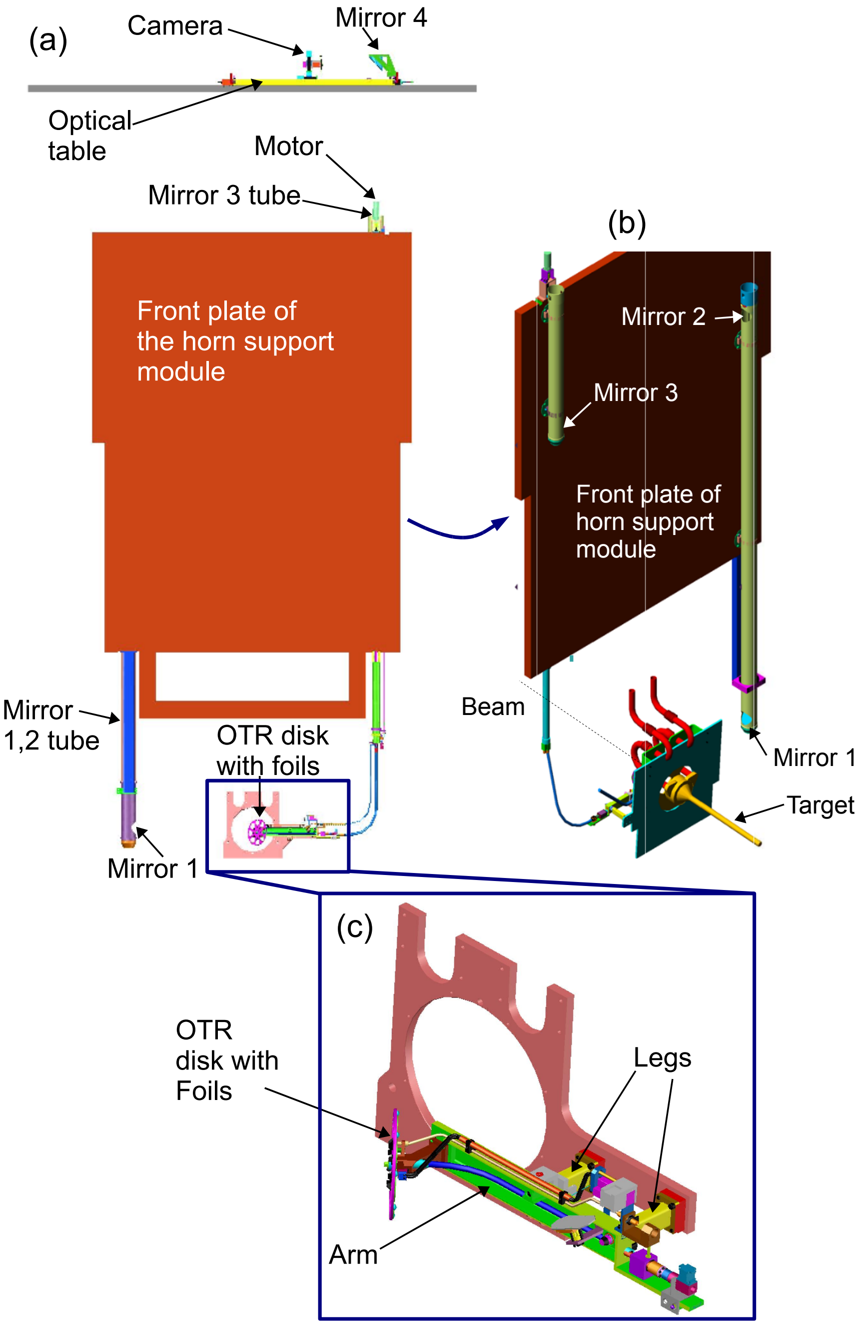

Figure 4.5: CAD drawings of the OTR system in various perspectives. (a) A view of the horn support module and surrounding area with the beam going into the page. The target-horn assembly below the module, which the monitor components at the bottom of the figure are attached to, is not shown for clarity. (b) The rear view of the horn module showing the mirror tubes and part of the target-horn assembly. (c) A zoomed-in view of the monitor components near the beam.

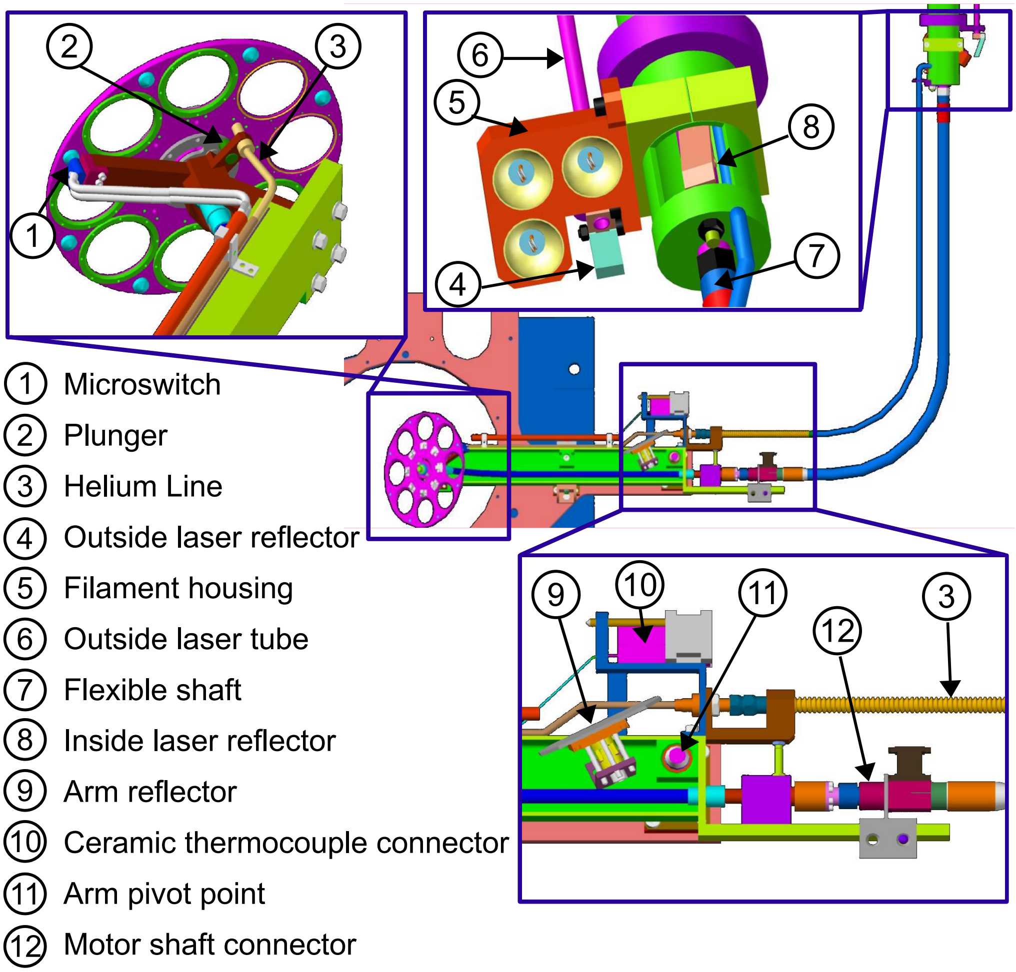

Figure 4.6: Several zoomed-in views of the OTR monitor components near the beam.

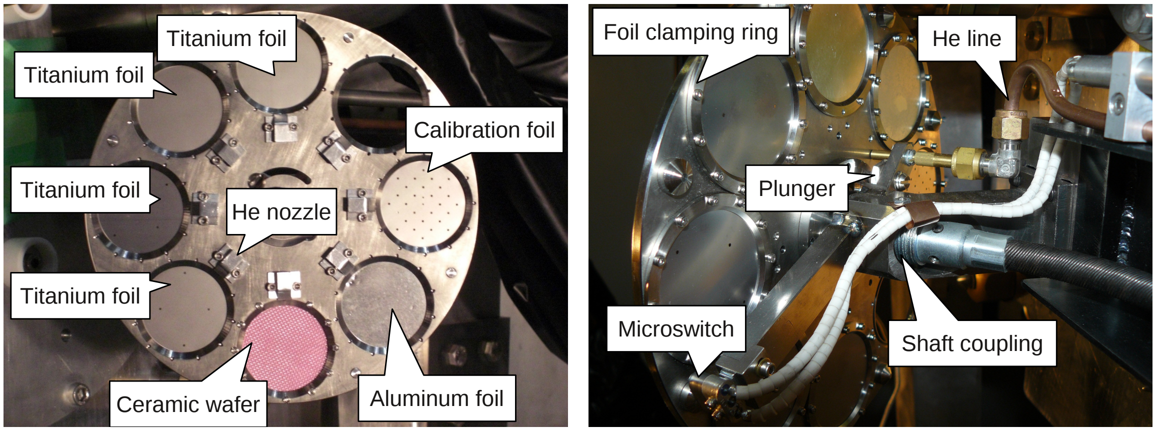

Figure 4.7: The upstream (left) and downstream (right) sides of the foil disk.

Material	# of slots	Thickness	Beam Power (kW)	Intensity (pps)
Ceramic (AF995R)	1	100 μm	< 1	$< 10^{12}$
Aluminum (1100)	1	50 μm	$1 - 40$	$10^{12} - 10^{13}$
Titanium (15-3-3-3)	4		> 8	$> 5 \times 10^{12}$
Titanium (15-3-3-3)	1		Calibration with no beam	

Table 4.1: The target foils used in the OTR system. The approximate operational range of beam power in kW and corresponding intensity in protons per spill (pps) is given for each foil.

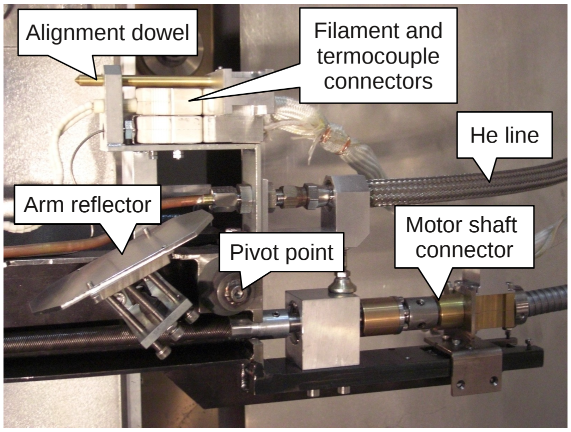

Figure 4.8: Outer end of the arm holding the disk.

drives a long rigid steel shaft passing vertically through the front plate (Figure 4.5(a)), coupling to a flexible steel shaft that bends 90° to the arm and then to another flexible shaft along the arm which connects to the disk (Figures 4.6 to 4.8).

This motor system with several drive shafts suffers from significant backlash during operation. Therefore, in order to precisely reproduce foil positions, which is especially important for the calibration foil, a depression was machined into the disk near each slot position. A spring-loaded steel ball plunger presses into the disk and locks firmly into the depression, pulling the disk into the correct position as it rotates (Figures 4.6 and 4.7 (right)). A microswitch engaged by a titanium button on the disk prompts the motor to stop immediately prior to the activation of the plunger mechanism.

In case of failure of the microswitch and plunger system, a pressure switch was also implemented as a backup system. A nozzle at the end of a pressurized helium gas line is positioned about 0.1 mm from the surface of the disk (Figures 4.6 and 4.7 (right)). Holes are machined through the disk at each slot position which pass the nozzle as the disk rotates, reducing the pressure in the line and triggering a pressure switch that disengages the motor. This method is sufficiently accurate without the plunger for positioning a disk slot to ensure that thicker parts of the disk remain out of the beamline.

4.4.2 Calibration Foil

The calibration foil is used to provide a position reference relative to the target and horn described in Section 4.4.3, and for image analysis described in Section 4.7.2. It contains a 7 mm spacing grid of precisely laser-machined holes as shown in Figure 4.9. The two central holes[3] are 0.8 mm in diameter while the rest are 1.2 mm.

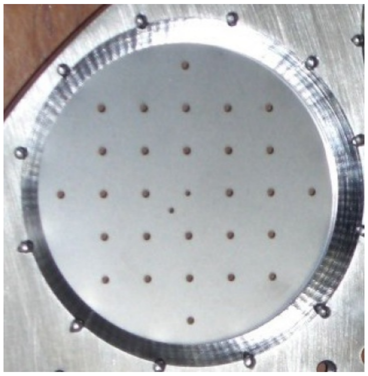

Figure 4.9: The calibration foil with a grid of laser-machined holes, clamped to the disk.

4.4.3 Alignment

The calibration foil provides a reference for translating beam images obtained by the camera into the real coordinate system relative to proton beam line. Thus, the position

---

[3] The off-center hole facilitates the the interpretation of images.

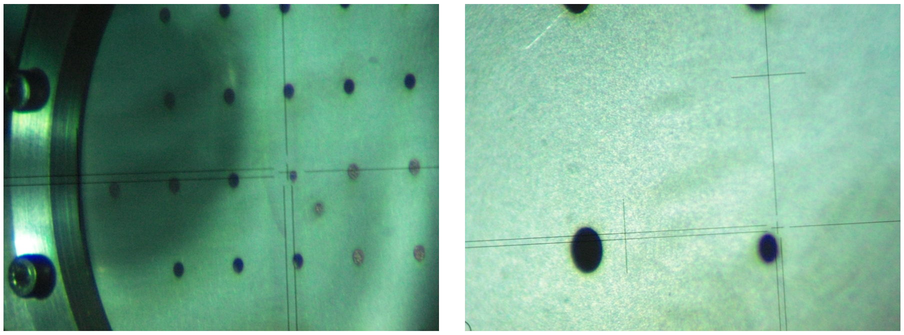

Figure 4.10: Survey of the calibration foil from downstream (left) and upstream (right). The black cross-hairs of the viewfinder were aligned to the horn axis by viewing through the empty slot.

and rotation of grid must be measured precisely after the disk has been locked into position. A theodolite was aligned to the beamline defined by two sets of cross-hairs centered on the horn at both ends. The center hole of the foil was then surveyed as shown in Figure 4.10 providing a measurement of the position with 0.3 mm precision, but still one of the dominant systematic uncertainties. (Table 4.2).

4.5 Mechanical Design of the Optical System

Mirrors 1 and 2 are mounted in a long steel tube while mirror 3 is mounted in a shorter steel tube (Figure 4.5(b)) such that they can be easily installed and replaced through ports in the helium vessel lid. The tubes hang precisely on ball support mounts protruding from the back of the horn module front plate and can be adjusted vertically. Mirrors 1 to 3 can be rotationally adjusted about the horizontal axis normal to the front plate. Mirror 4 and the camera are mounted on an optical table which can be translated horizontally. Furthermore, the camera is mounted on three remote controlled motorized stages for fine-tuning the focus and centering on the optical axis.

Quartz Window

A 25 cm diameter fused silica or quartz window (BK7-G18) is used to seal the helium vessel while allowing light to pass from mirror 3 to mirror 4 above the vessel lid. The technical specifications state radiation tolerance up to 10 kGy [130] with a transmittance loss of less than 5% after such irradiation. The absolute transmittance around the central region was measured to be $\gtrsim 93\%$, which is taken into account in the efficiency correction described in Section 4.7.1.

4.5.1 Calibration Lighting Systems

Based on studies with the prototype system (Section 4.3), the back-lighting method was chosen to illuminate the calibration foil and monitor the efficiency of the optical system. Two laser light systems and a filament light system were installed for this purpose and their light path is illustrated in Figure 4.11 (left).

The laser light systems use small red LED lasers [131], one mounted on the optical table (outside laser) and the other near the disk rotation motor (inside laser). Two steel pipes ~ 1 cm in diameter guide the light from each laser from above the horn module to the extension tube (Figures 4.6 and 4.11). The feasibility of these *light pipes* was confirmed by measuring the light output at the end of the pipe [128]. A small steel reflector is attached to the bottom of each tube to direct the light to a reflector on the arm (Figure 4.8). The outside laser can be replaced relatively easily when the beam is off, while an inside laser replacement requires a long shutdown and removal of the helium vessel lid.

The filament lamps are constructed from Alchrome wire coiled inside a parabolic reflector and installed near the extension tube (Figures 4.6 and 4.11). Three lamps are deployed for redundancy, since they cannot be accessed after beam running. Destruction tests in air showed that these filaments break at ~ 15 A. Thus, they are operated at 12 A

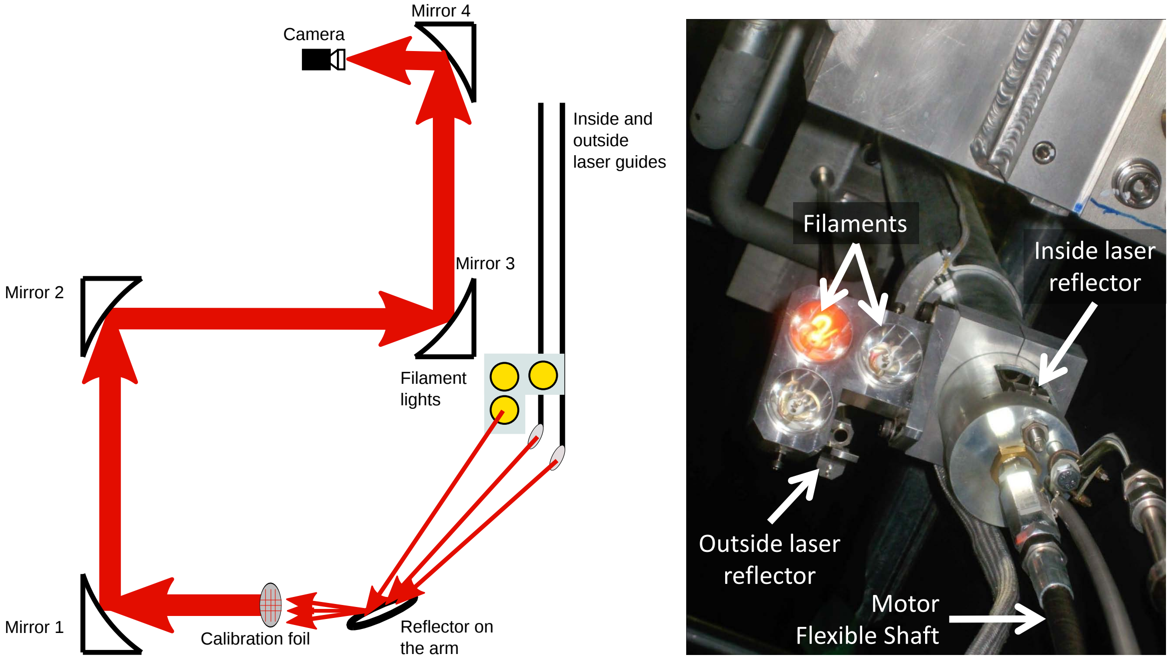

Figure 4.11: Left: Schematic of the calibration lighting systems and light path. Right: Upward view of the extension tube region below the front plate of the horn support module. One of the filament lights is turned on.

to be conservative while still producing sufficient light output. The threshold is expected to be higher in helium due to the larger thermal conductivity compared to air[4].

4.5.2 Alignment

The optical system was aligned using a laser. The laser was mounted at the center of the empty slot position on the disk and aligned to the beamline by using crosshairs at the front and rear of the horn. A plane mirror was then inserted flush into the empty slot to reflect the laser towards the mirror system as shown in Figure 4.12 (left). Each mirror was adjusted so that the laser hit the center of each mirror. To align the arm reflector, a laser was placed at the camera position shining backwards through the optical system. The arm reflector was then adjusted so that the peak of the reflected light distribution appeared on the filaments as shown in Figure 4.12 (right). The reflector angle was optimized for the filaments since they provide the most uniform light source [128].

When imaging the calibration foil, the angle of the incident light affects the apparent hole positions. The deviations caused by the various calibration light sources were characterized by comparing to a temporary light source deployed between the arm reflector and the disk, aligned to the axis defined by the calibration foil and mirror 1 centers. The variation in the imaged hole positions was ~ 0.25 mm, a major contribution to the systematic uncertainty (Table 4.2).

Variations in the optical system alignment are expected from effects such as temperature change and earthquakes. Thus, the calibration foil is imaged regularly with the calibration light sources to provide a time dependent correction (Section 4.7.2).

---

[4] The intensity of a filament was measured to be smaller in helium than air for a given current (power) by a factor of ~ 1.75, corresponding to the ratio of the specific heat capacities at constant volume.

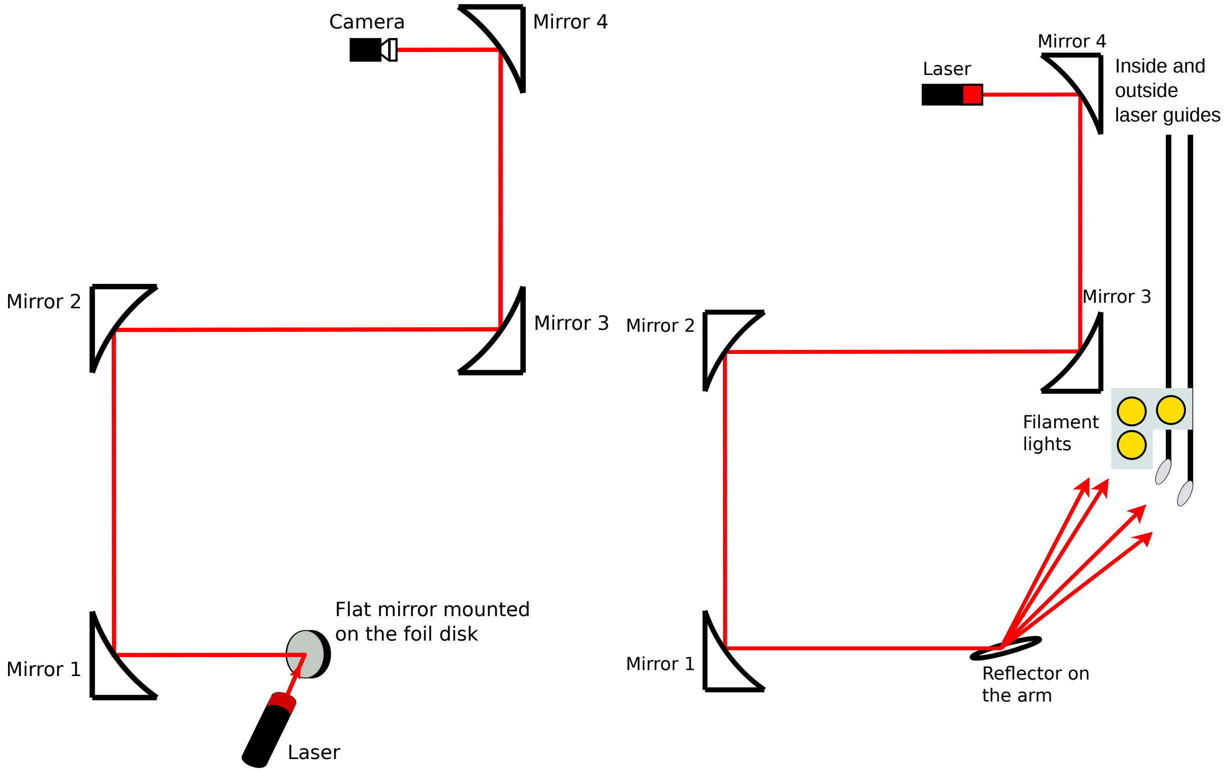

Figure 4.12: Left: Laser and flat mirror setup for initial alignment of the parabolic mirrors. Right: Subsequent alignment of the arm reflector using a laser at the camera position.

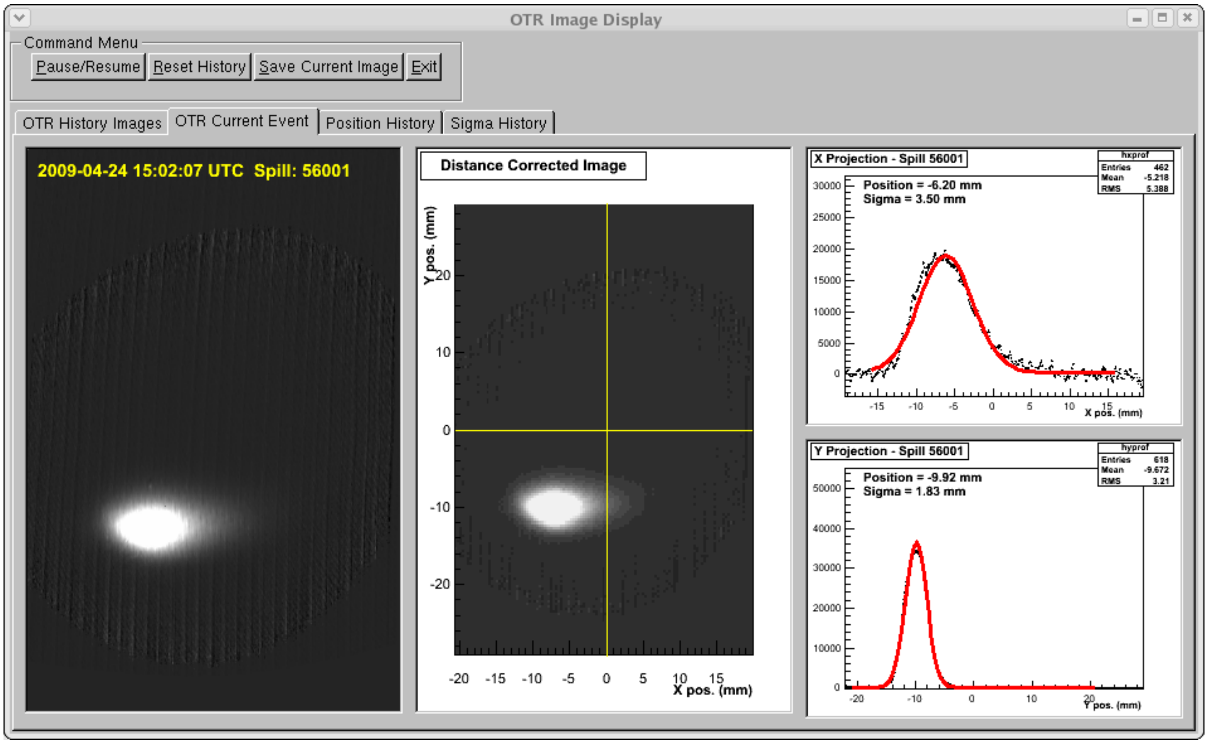

2009-04-24 15:02:07 UTC Spill: 56001

Position = -6.20 mm
Sigma = 3.50 mm

Entries 462
Mean -5.218
RMS 5.388

Position = -9.92 mm
Sigma = 1.83 mm

Entries 618
Mean -9.672
RMS 3.21

Figure 4.13: OTR event display of the first proton beam successfully guided to the target. The crosshair is centered on the horn (target) axis. The top-right and bottom-right panels show the horizontal and vertical projections, respectively, with the results of a 2D Gaussian fit overlaid in red.

4.6 Data Acquisition and Slow Control

The data acquisition (DAQ) system, described in detail in [126, 132], collects and processes the image data. A trigger signal is received from the beamline which prompts a reset of the camera readout before the beam spill arrives. Three full image frames, the first of which is synchronized to the actual spill arrival time, are archived and sent to an online monitoring program. The event display, which includes a 2D fit of the beam profile, is shown in Figure 4.13. If the measured position or width is not within tolerance, a signal is delivered to abort further beam extraction into the neutrino beamline. The *slow control* system provides the remote lighting and motor control, as well as delivering a beam interlock signal while the disk is rotating.

4.7 Image Correction and Analysis

The optical system introduces a light collection efficiency loss as well as image distortion due to the parabolic mirrors. This section describes the corrections for these effects in order to reconstruct the real beam position and profile.

4.7.1 Efficiency Correction

The geometry of the optical system as well as the fiber taper attached to the camera introduce a light collection efficiency loss that is dependent on the transverse position of the light source. Figure 4.14 (left) shows the image at the camera position (without the taper) of a uniform light source placed at the disk position, based on a ray tracing simulation of the optical system. The falloff in the radial direction biases the reconstructed beam position and width.

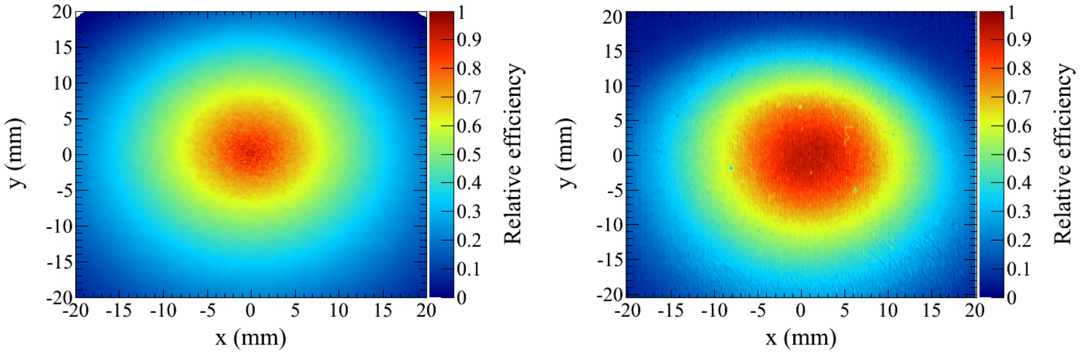

Figure 4.14: Simulated (left, no fiber taper) and measured (right, with fiber taper) light collection efficiencies. The z-axis is normalized to the peak value.

An integrating sphere [133] was used to characterize the efficiency in the real system. It was constructed from a 30.5 cm diameter hollow cardboard globe shown in Figure 4.15. Eight laser diodes point inward, the light from which reflects multiple times off the painted white surface prior to escaping through a 12 cm opening. The diffuse reflections produce a light intensity output measured to be uniform within 5% across the opening. Prior to the horn module installation, the sphere was deployed at the disk position. The

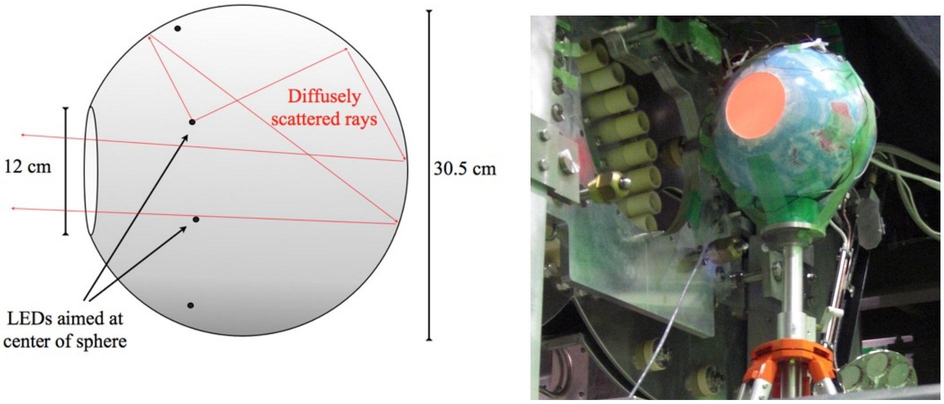

Figure 4.15: Left: A schematic diagram of the integrating sphere. Right: The actual sphere (globe) positioned at the disk position facing mirror 1, to characterize the full optical system light collection efficiency.

image taken through the optical system and fiber taper with the camera is shown in Figure 4.14 (right). The impact of the fiber taper on the efficiency map can be seen from the comparison with the simulation in Figure 4.14 (left). The measured efficiency map is used to correct all subsequent images.

Images are also taken periodically with each of the light sources illuminating the empty slot in the disk. However, these light sources are less uniform than the integrating sphere and the images are mainly used to monitor efficiency changes over time.

4.7.2 Distortion Correction

Distortion in the image is introduced by the parabolic mirrors as shown in Figure 4.16 (left) where the calibration foil was illuminated by a laser and imaged through the optical system. The hole centroids are marked by triangular points, determined from a *hole-finding* algorithm. These points are compared to the true hole positions (Section 4.4.2), which include the results of the calibration foil survey (Section 4.4.3), to build a transformation map [132]. This map then translates images from camera space into the real beam coordinate system. Figure 4.16 (right) demonstrates how the distortion correction recovers the true hole positions marked by the circular points.

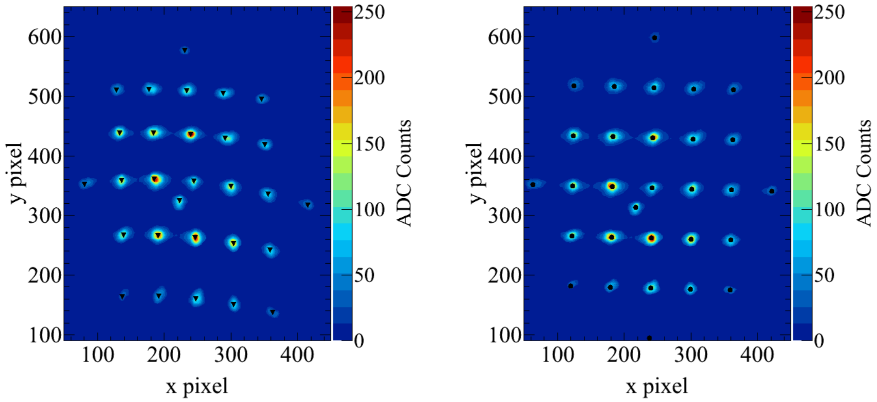

Figure 4.16: Distorted (left) and corrected (right) images of the calibration foil illuminated by a laser. The centroids of the distorted holes (left, triangles) and the true hole positions (right, circles) are superimposed.

4.7.3 Overview of the Image Analysis

The proton beam position and width as well as the total light yield is measured for each spill. The analysis involves several steps as follows:

1. Pedestal subtraction using the two images obtained after the beam spill image.
2. Light collection efficiency correction using the map measured with the integrating sphere (Section 4.7.1).
3. Correction for leakage currents in the camera sensor [126].
4. Distortion correction using the transformation map obtained from an image of the calibration foil (Section 4.7.2).
5. Two-dimensional fit to the image to extract the proton beam position and width, and the total light yield.

4.8 Performance of the OTR Monitor

The OTR monitor has operated with proton beam intensities ranging from 1×10^{11} to 1×10^{14} protons per spill (pps), switching between foils depending on the intensity as shown in Table 4.1. Images of an example beam spill using the titanium and aluminum alloy foils are shown in Figure 4.17.

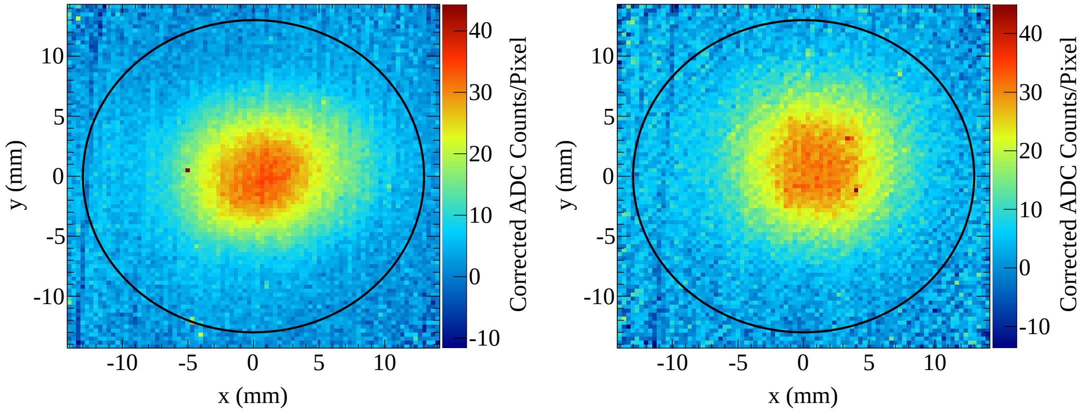

Figure 4.17: Example OTR images of the proton beam with typical beam conditions, 9.0×10^{13} pps for titanium (left), and 2.3×10^{13} pps for aluminum (right) alloy foils. The black circle shows the edge of the target.

4.8.1 Systematic Errors

The systematic errors on the reconstructed beam position and width are summarized in Table 4.2. The uncertainty on the position measurement is dominated by the uncertainties from the calibration foil survey (Section 4.4.3) and lighting system alignment (Section 4.5.2). The uncertainty in the beam width measurement is dominated by the choice of the signal fitting function, which has some freedom due to insufficient understanding of an apparent background [126]. Overall, the total systematic error is < 0.5 mm, within the required goals of the beam measurement at the target.

4.8.2 Beam position and direction measurements

The OTR monitor is used in conjunction with the upstream SSEM and ESM monitors (Section 3.1.2) to determine the beam position and angle. A linear fit is performed with the last three (two) SSEM/ESM pairs and the OTR measurement to extrapolate the

Source	$\delta x(\mu\text{m})$	$\delta y(\mu\text{m})$	$\delta\sigma_x(\mu\text{m})$	$\delta\sigma_y(\mu\text{m})$
Calib. foil alignment	302	300	87	102
Signal model	5	3	436	376
Background model	90	115	10	31
Fitter bias	4	15	105	140
Calib. light alignment	210	251	46	38
Pixel charge decay	101	84	19	30
Distortion correction	29	39	83	111
Others sources	95	57	79	85
Total	404	432	473	441

Table 4.2: Systematic uncertainties for a single spill OTR proton beam position and width measurement [126].

beam x (y) position and angle at the target (Figure 3.6). An example fit to a single spill is shown in Figure 4.18. The uncertainty in the extrapolation is dominated by alignment uncertainties. The measured beam position and direction is stable within design requirements throughout each running period, so the average beam position and direction over each period is used as input to the neutrino flux prediction in Section 5.1.

4.8.3 Consistency with upstream proton beam monitors

The OTR position measurement can be removed from the linear fit and instead compared to the extrapolation to the OTR position using only the upstream monitors. Figure 4.19 shows the difference between the OTR position measurements and the extrapolation over a period of time including variations in the beam conditions. The mean of the differences is within the alignment uncertainty (1 mm) and stable with an RMS < 0.3 mm.

The beam width and divergence are also extrapolated from the proton beam measure-

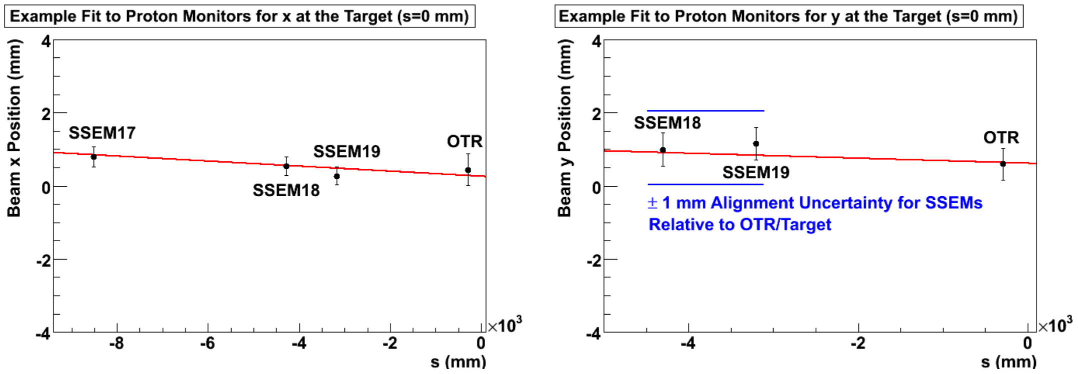

Figure 4.18: Example extrapolation of the beam position and direction using the SSEM and OTR measurements.

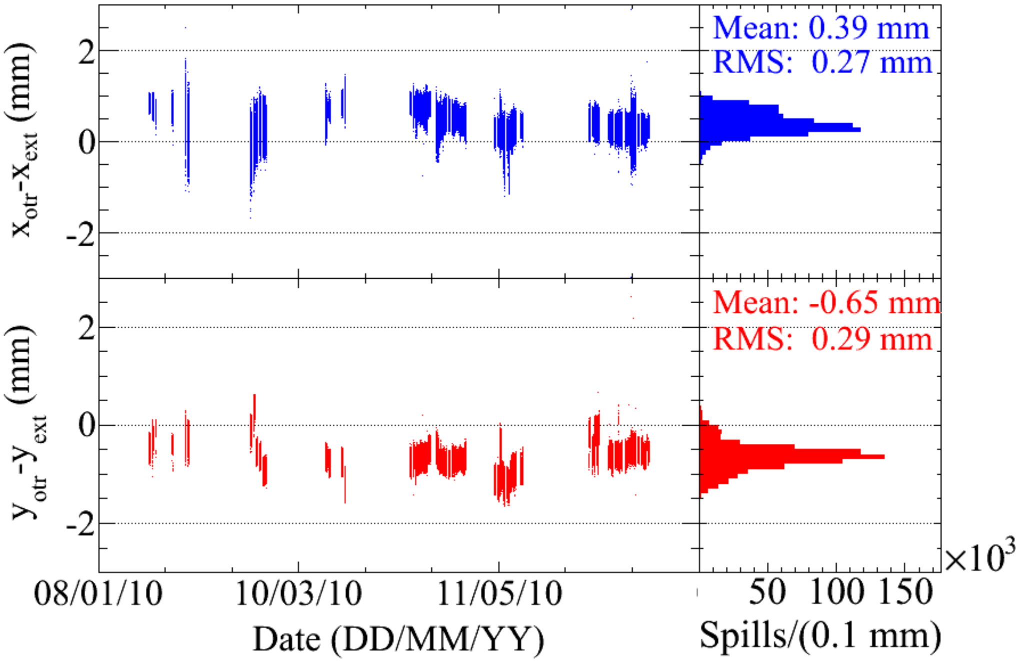

Figure 4.19: The difference between the OTR x (top) or y (bottom) measurements of the beam position and the extrapolation from upstream proton beam monitor measurements. The data points were collected from January through June of 2010.

ments and used as input to the neutrino flux prediction. There is a ∼25% discrepancy in the OTR measured width which is currently unexplained, but this has a negligible effect on the flux prediction [132].

Chapter 5

Physics Simulation

The oscillation parameters are extracted by comparing the observed number of events N in the near and far detector with the predicted number of events $\hat{N}$ as introduced in Section 1.1:

$$\hat{N}_{\nu_\beta}(E_{rec}) \sim P_{\nu_\alpha \to \nu_\beta}(E; \mathbf{o}) \cdot \varphi_{\nu_\alpha}(E; \mathbf{b}) \cdot \sigma_{\nu_\beta}(E; \mathbf{x}) \cdot \varepsilon_{\nu_\beta}(E_{rec}, E; \mathbf{d}). \tag{5.1}$$

This equation is the same as Equation 1.3, except explicitly showing the functional dependence on the true and reconstructed neutrino energies E and E_{rec}. Each factor in Equation 5.1 is calculated with separate software packages that depend on the following sets of parameters:

- $\mathbf{o}$: the oscillation parameters as described in Chapter 2.
- $\mathbf{b}$: the neutrino beam parameters.
- $\mathbf{x}$: the neutrino interaction cross section parameters.
- $\mathbf{d}$: the detector parameters for ND280 and SK.

The latter three factors are calculated from separate simulations using a Monte Carlo (MC) method. The output of the neutrino beam simulation described in Section 5.1 is propagated to the neutrino interaction simulation described in Section 5.2. The output from that is then propagated to the ND280 and SK detector simulations described in Sections 5.3 and 5.4, respectively. The oscillation probability P is calculated at the oscillation analysis stage (Chapter 9) with the *Prob3++* program [134] based on an analytic derivation including matter effects [135].

The precision of the prediction $\hat{N}$, which in turn affects the precision of the oscillation parameter measurement, depends on the uncertainties of all the inputs to each simulation. Each simulation consists of several models that depend on various parameters which are tuned and constrained to some experimental data or theory. Uncertainties in these parameters are propagated to $\hat{N}$ using the simulations. These models and their parameters and constraints are described in this chapter.

5.1 Neutrino Flux Prediction

The neutrino flux prediction is calculated from a simulation of the 30 GeV proton beam starting upstream of the baffle (immediately downstream of the beam window in Figure 3.5), producing hadrons after collisions with the target and surrounding material, and ending with the decay of hadrons or muons that produce neutrinos. External hadron production data as well as in-situ measurements of the proton beam and horns are used to tune the simulation and constrain systematic uncertainties. The flux prediction and systematics are described in more detail in [100, 132].

Hadronic interactions in the baffle and target are simulated with FLUKA2008 [136]. The particles emerging from the baffle and target are then used as input to a GEANT3-based [137] simulation called JNUBEAM, which includes the realistic geometry and survey-based positioning of all the beamline components shown in Figure 3.5. GEANT3 propagates all the particles through the geometry accounting for the magnetic fields produced by the horns, as well as subsequent hadronic interactions which are modelled by GCALOR [138]. The particles decay according to the current best knowledge of branching ratios [72] as shown for the neutrino production modes in Table 5.1. The decay products (except neutrinos) are tracked further until they subsequently decay or fall below 10 MeV kinetic energy. All the neutrinos that are produced are recorded and used to calculate the neutrino flux at the ND280 and SK positions[1] as shown in Figures 5.1 and 5.2 (left). This corresponds to the φ factor in Equation 5.1.

	π^+	K^+		K^0_L	μ^+
ν_μ	$\mu^+\ \nu_\mu$ 99.9877	$\mu^+\ \nu_\mu$, 63.55	$\pi^0\ \mu^+\ \nu_\mu$ 3.353	$\pi^-\ \mu^+\ \nu_\mu$ 27.04	
ν_e	$e^+\ \nu_e$ 1.23×10^{-4}	$\pi^0\ e^+\ \nu_e$ 5.07		$\pi^-\ e^+\ \nu_e$ 40.55	$e^+\ \overline{\nu}_\mu\ \nu_e$ 100

Table 5.1: Branching fractions in % for decay modes that produce neutrinos for various particles. The π^-, K^- and μ^- modes are charge conjugates of their respective positive modes.

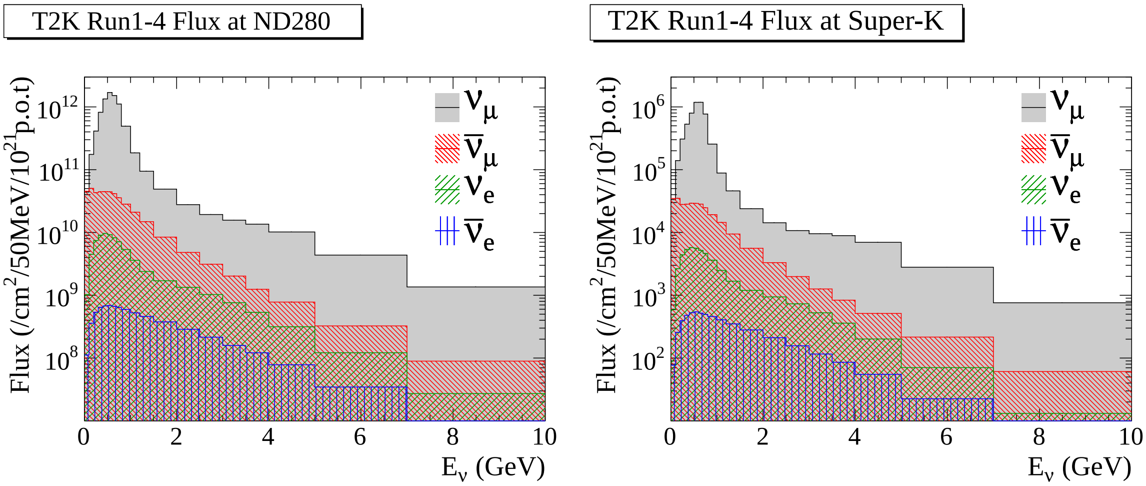

Figure 5.1: The tuned flux prediction at ND280 (left) and SK (right) for each neutrino species in the T2K beam.

Several sources of systematic error are considered for the flux prediction [100, 132]. Hadron production differential cross section measurements are used to constrain the

---

[1] The neutrino detector positions were determined by GPS survey and are also input to the simulation.

hadron interaction models. The horn current and magnetic field are measured in-situ. The proton beam measurements, including those from the OTR monitor, are used to define the simulated beam parameters. The INGRID detector provides an additional constraint on the off-axis angle. Each of these components of the flux prediction are modelled by a set of parameters, for example momentum and angle *bins* (or ranges) for hadron production, or proton beam position and direction, which correspond to **b** in Equation 5.1. The measurements are used to tune (define the central value for) **b**, which modifies the predicted flux in Figures 5.1 and 5.2 (left). The uncertainties in **b** are defined by the measurement uncertainties and are propagated to the flux prediction by varying the parameters in the simulation. The tuning and variation are performed by a combination of MC regeneration and *reweighting*[2] methods.

A covariance matrix describing the total systematic uncertainty can be calculated from several simultaneous variations of **b** within their measurement uncertainty. This procedure is referred to as *toy MC*. The matrix also encodes the correlations between neutrino energy bins resulting from the underlying parameterization **b**. The total systematic error and contributions from the various sources for the ν_μ flux is shown in Figure 5.2 (right). The corresponding correlation matrix, which also relates the neutrino energy bins between different detectors and neutrino species, is shown in Figure 5.3. The tuned flux prediction and covariance matrix are propagated to the oscillation analysis in Chapter 9.

---

[2] Reweighting depends on the probabilistic nature of MC. For example, when building a distribution from some set of MC events, if the cross section (probability) for producing some sub-set of those events is doubled, then this can be reflected in the distribution by applying a weight of 2 to those events when building the distribution. This prevents the need for running multiple compute-intensive MC with parameter variations.

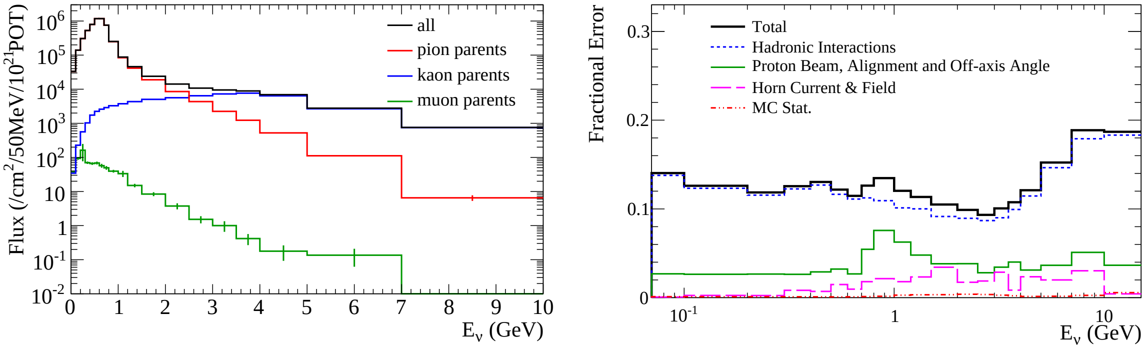

Figure 5.2: Left: The tuned ν_μ flux prediction showing the contribution from various parent particles. Right: The total diagonal error in the ν_μ flux prediction and contribution from various systematic error sources. The corresponding correlation matrix is shown in Figure 5.3.

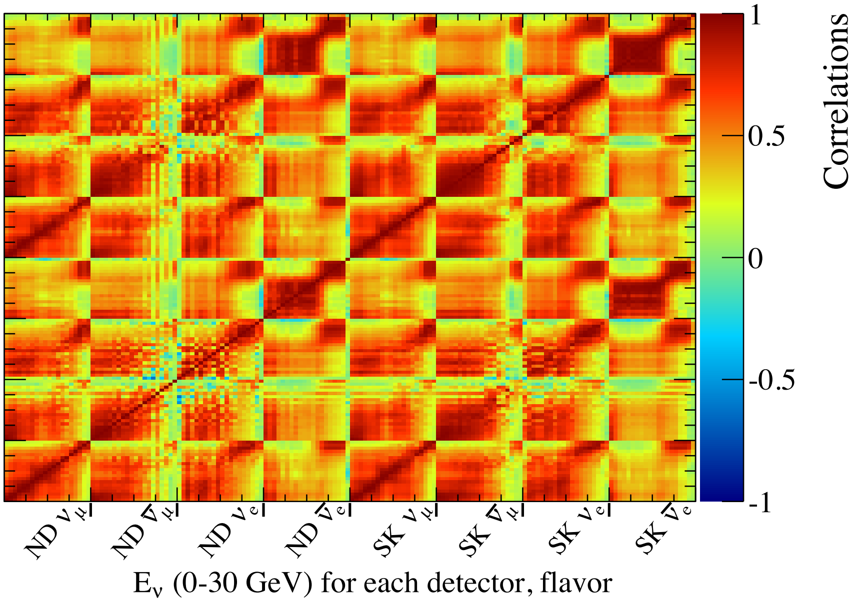

Figure 5.3: The correlations between the ND280 and SK flux bins and all neutrino species in the T2K beam. The bin boundaries in energy are [0, 0.1, 0.2, 0.3, 0.4, 0.5, 0.6, 0.7, 0.8, 1.0, 1.2, 1.5, 2.0, 2.5, 3.0, 3.5, 4.0, 5.0, 7.0, 10, 30] GeV. The full covariance matrix can be calculated from this and the diagonal errors in, e.g., Figure 5.2 (right).

5.2 Neutrino Interaction Generator: NEUT

Neutrinos interact via the weak force with the nucleons and electrons in and surrounding the detectors. The energy distribution of neutrino interaction events is determined from the input flux multiplied by the total cross section as calculated by the simulation package NEUT [139, 140]. Since the detectors can only observe the resulting final state, NEUT must also determine the interaction mode and kinematics of the outgoing particles based on a calculation of the differential cross section for each mode. The following CC and NC interaction modes are considered:

- (quasi-)elastic (QE) scattering: $\nu + N \rightarrow l + N'$,
- single meson or photon production via baryon resonance (RES): $\nu + N \rightarrow l + N' + m$,
- deep inelastic scattering (DIS): $\nu + N \rightarrow l + \textit{hadrons}$ and
- coherent pion production: $\nu + A \rightarrow l + A + \pi$,

where N and N' are nucleons, l is a charged lepton (neutrino) for a CC (NC) interaction, $m = \pi,\ K,\ \eta$ or γ and A is the target nucleus. The relative contribution of each mode is shown in Figure 5.5 (left)[3] including the data summarized in [142]. A subset of this data is used to tune and estimate systematic uncertainties in the NEUT simulation, described in this section. In particular, MiniBooNE data are well-suited for constraining the interactions at T2K since the neutrino energy spectrum [143] is wider, as shown in Figure 5.4. The T2K flux, overlaid in Figure 5.5 (left), shows that QE scattering is the dominant interaction mode, which is useful for reconstructing the neutrino energy based on 2-body kinematics.

For interactions that occur within a nucleus, the resulting hadrons are transported through the nuclear medium to account for re-interactions or *final state interactions*

---

[3] The curves in Figure 5.5 (left) are based on NUANCE [141], another neutrino interaction event generator similar to NEUT.

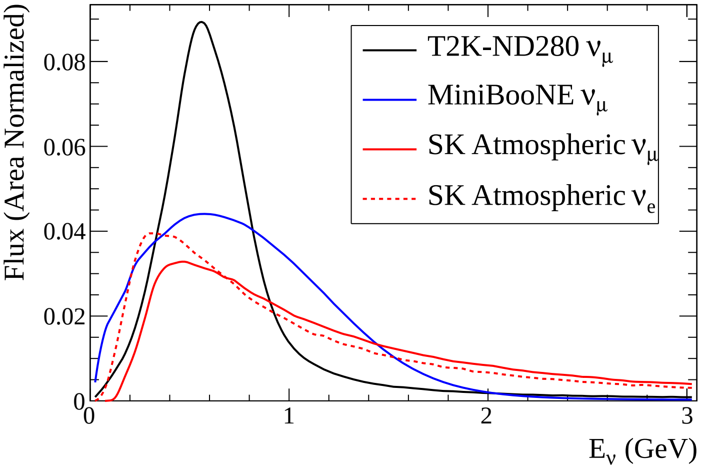

Figure 5.4: Comparison of the ν_μ flux at ND280, MiniBooNE [143] and for SK atmospheric neutrinos [144] (used in Chapter 8).

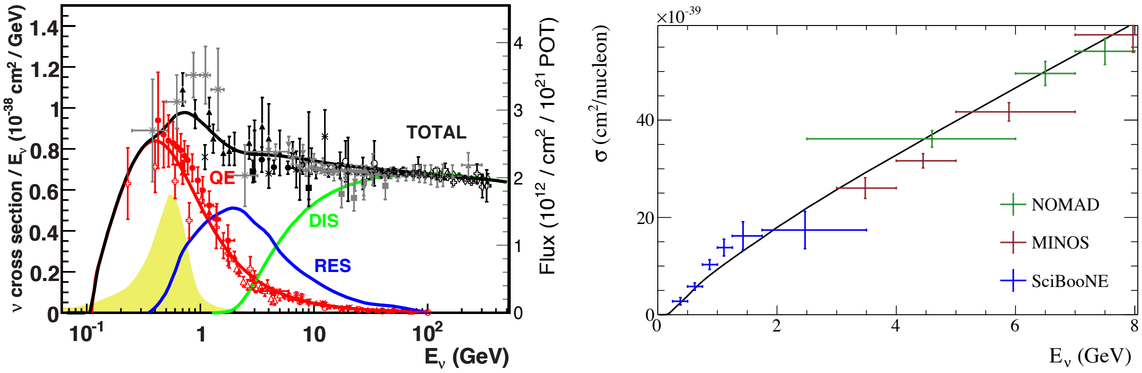

Figure 5.5: Left: CC $\nu_\mu + N$ cross section data summarized by [142] with the T2K ND280 flux (filled area) and NUANCE [141] predictions (lines) overlaid. Right: NEUT ν_μ CC total cross section compared to the SciBooNE [145], MINOS [146] and NOMAD [147] data.

that can modify the observable particles emitted from the nucleus. The NEUT package includes a custom simulation for this process and is discussed in Chapter 6.

5.2.1 Quasi-Elastic Scattering

NEUT uses the Llewellyn-Smith model [148] to simulate QE scattering of a neutrino by a free nucleon. The model contains a (form) factor F_A that can only be determined from neutrino scattering and is typically parameterized in dipole form as

$$F_A(q) = \frac{-1.232}{1 - q^2/M_A^2}, \tag{5.2}$$

where $q = p_\nu - p_l$ is the 4-momentum transfer and M_A is called the *axial-vector mass*. It is denoted M_A^{QE} hereafter to distinguish it from the axial-vector mass associated with resonance production (Section 5.2.2). For interactions on bound nucleons, the relativistic Fermi gas model developed by Smith and Moniz [149, 150] is used to take into account nuclear effects.

Neutrino interaction data from K2K [151] and MiniBooNE [152] motivate the central value of $M_A^{QE} = 1.21$ GeV/c^2, with an uncertainty of 0.45 GeV/c^2 coming from a fit to the MiniBooNE data [153]. An uncertainty of 11% is also applied to the overall normalization of the total CCQE cross section below 1.5 GeV neutrino energy, coming from the MiniBooNE flux uncertainty.

5.2.2 Single Meson or Photon Production

Single meson production is simulated with the Rein and Sehgal model [154, 155], which considers the amplitude and decay probabilities of baryon resonances with invariant mass $W < 2$ GeV/c^2. Baryon resonance absorption within the nucleus, referred to as *pionless Delta decay* (PDD), is modelled such that 20% of resonance events do not produce decay products [156].

Similar to QE scattering, an axial-vector mass parameter is set to a nominal value of $M_A^{RES} = 1.21$ GeV/c^2 according to external data [139]. MiniBooNE pion production data [157–159] are fit simultaneously as shown in Figures 5.6 to 5.8 to extract new central values and uncertainties including correlations for M_A^{RES} and CC1π and NC1π^0 cross section normalization parameters.

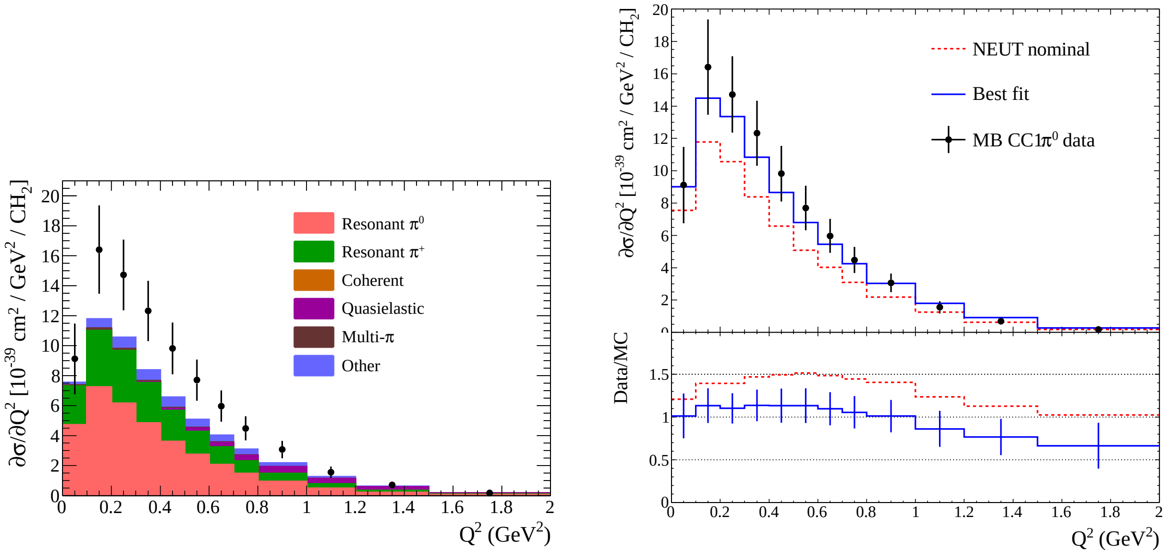

Figure 5.6: MiniBooNE flux-integrated CC1π^0 Q^2 distribution with the nominal NEUT CC prediction and true interaction components (left) and best-fit (right). Data points from [157].

5.2.3 Deep Inelastic Scattering

The DIS cross section for $W > 1.3$ GeV/c^2 is calculated using nucleon structure functions [160, 161]. The outgoing particle multiplicities for $W < 2$ GeV/c^2 are estimated from bubble chamber data [162, 163]. For $W > 2$ GeV/c^2, the kinematics of the hadronic system are determined by the PYTHIA/JETSET simulation package [164].

An uncertainty on the total normalization is assigned based on the CC inclusive measurement by MINOS [146] as shown in Figure 5.9. The difference at 4 GeV from the high energy average is taken as reference and the systematic error is modelled as $\delta(\sigma_{CCother}) = 0.4/E_\nu$[GeV] to account for the increasing (decreasing) precision towards

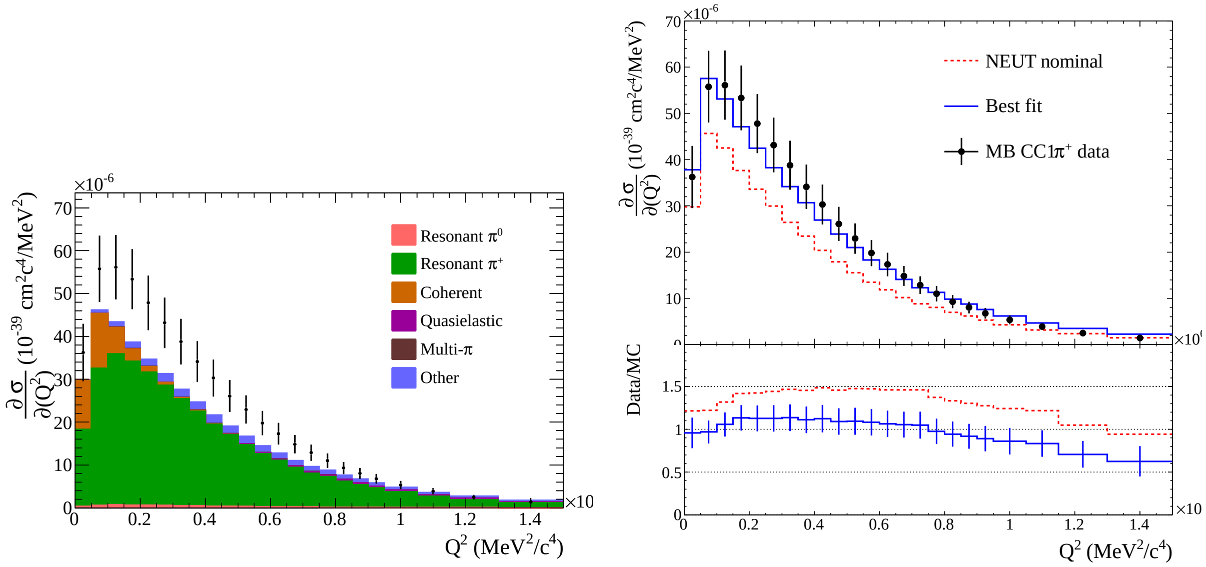

Figure 5.7: MiniBooNE flux-integrated CC1π^+ Q^2 distribution with the nominal NEUT CC prediction and true interaction components (left) and best-fit (right). Data points from [158].

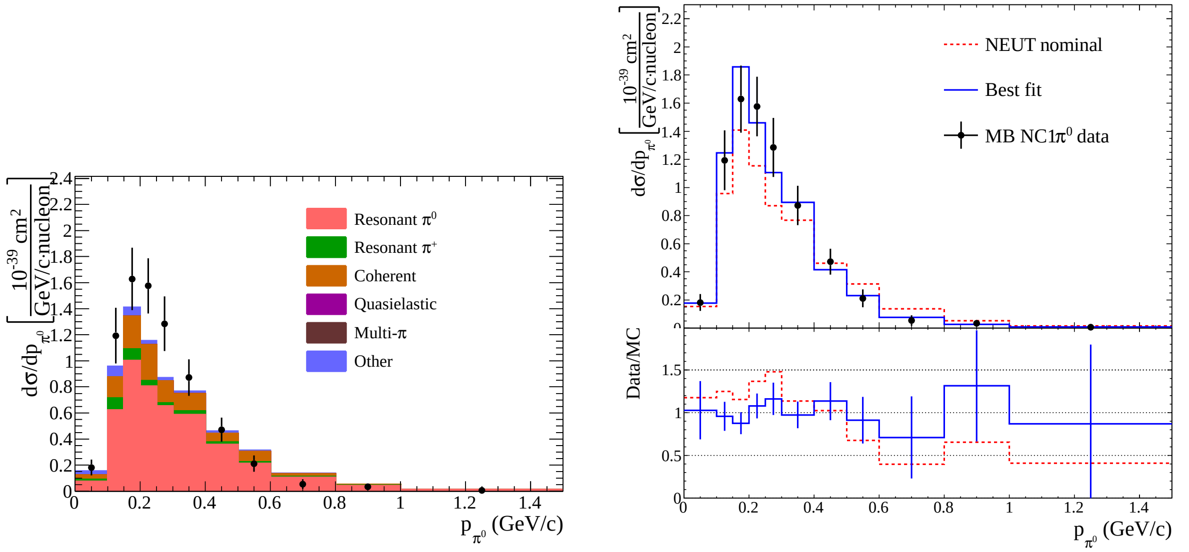

Figure 5.8: MiniBooNE flux-integrated NC1π^0 p_π distribution with the nominal NEUT NC prediction and true interaction components (left) and best-fit (right). Data points from [159].

higher (lower) energies.

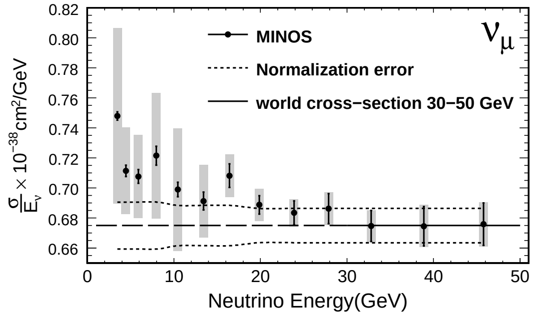

Figure 5.9: Total ν_μ inclusive CC cross section reported by MINOS [146]. The difference from the high energy average is $\sim$ 10% at 4 GeV.

5.2.4 Coherent pion production

Coherent pion production is characterized by a small momentum transfer to the nucleus leaving it in the ground state and producing a pion which is of the same charge as the incoming weak current. The angular distribution of the outgoing lepton and pion are strongly peaked in the forward direction. This process is simulated using the Rein and Sehgal model [165, 166].

Current measurements are consistent with no CC coherent π^+ production around neutrino energies of $\mathcal{O}(1\text{ GeV})$ [167, 168] at the 90% confidence level, as shown in Figure 5.10 compared to the NEUT prediction. Thus, a conservative 100% systematic uncertainty on the total cross section is assigned. A 30% systematic uncertainty is assigned to the total cross section for NC coherent π^0 production based on the discrepancy between NEUT and the SciBooNE measurement [169] shown in Figure 5.10.

5.2.5 Summary of Systematic Errors

The tuned cross section parameters and systematic errors, including additional systematic error sources described in [153], are summarized in Table 5.2. These are propagated to the oscillation analysis in Chapter 9.

Parameter	E_ν Range	Nominal	Error
M_A^{QE}	all	1.21 GeV/c^2	0.45
M_A^{RES}	all	1.41 GeV/c^2	$0.11^\dagger$
p_F ^{12}C (^{16}O)	all	217 (225) MeV/c	30
E_B ^{12}C (^{16}O)	all	25 (27) MeV	9
Spectral Function ^{12}C (^{16}O)	all	0	+1
NC RES W-Shape (SK only)	all	0.0	0.20
Pionless Delta Decay	all	0.0	0.2
CCQE E1	$0 < E_\nu < 1.5$	1.0	0.11
CCQE E2	$1.5 < E_\nu < 3.5$	1.0	0.30
CCQE E3	$E_\nu > 3.5$	1.0	0.30
CC1π E1	$0 < E_\nu < 2.5$	1.15	$0.43^\dagger$
CC1π E2	$E_\nu > 2.5$	1.0	0.40
CC Other scaling ND280 (SK)	all	0.0 GeV	0.40
CC Coherent $\pi^\pm$	all	1.0	1.0
NC1π^0	all	0.96	$0.43^\dagger$
NC1$\pi^\pm$	all	1.0	0.3
NC Coherent π^0	all	1.0	0.3
NC Other	all	1.0	0.3
ν_μ / ν_e [170]	all	1.0	0.03
$\nu/\bar{\nu}$	all	1.0	0.40

Table 5.2: Cross section parameters for the oscillation analysis in Chapter 9, showing the applicable range of neutrino energy, nominal value and prior error. Nominal refers to the new central values after all the tuning described in this section. All the errors are assumed to be independent except for those marked by † which are correlated from the MiniBooNE fit described in Section 5.2.2. Text enclosed in () brackets indicates an additional independent parameter for the far detector.

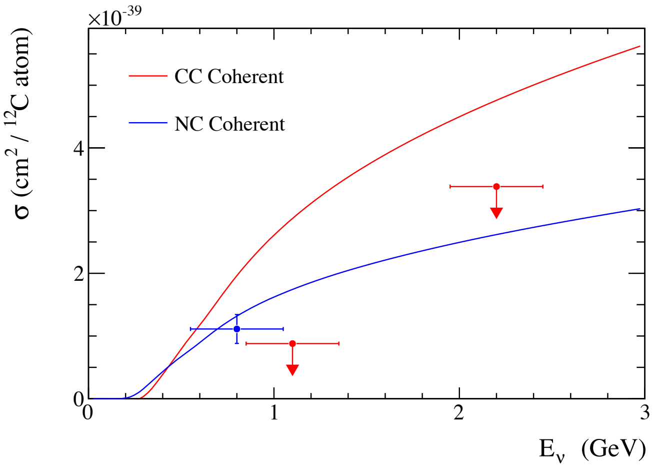

Figure 5.10: The NEUT ν_μ CC (red) and NC (blue) coherent π cross sections compared to the SciBooNE data from [168] and [169] respectively. The data is reported as a ratio to the total CC cross section and is normalized here by the NEUT CC cross section shown in Figure 5.5 (right) times 12 (for carbon). The CC points are 90% CL upper limits.

5.3 ND280 Detector Simulation

The complexity of the ND280 geometry requires a custom interface to NEUT to distribute the interaction vertices in space. The full detector geometry including all the various materials is represented as a GEANT4 [171] geometry object. The simulated flux vectors are then propagated through this geometry to account for the different materials when calculating interaction probabilities and determining the spatial distribution of interaction vertices. NEUT determines the outgoing particles at each vertex, which are used by the detector MC at the given position. The detector MC is based on GEANT4, which simulates the subsequent propagation of the particles through the geometry including energy loss, hadronic interactions and the magnetic field. The response of the active detectors such as the scintillator bars and electronics is simulated with custom software [95].

Detector systematic uncertainties are evaluated in the context of the specific event reconstruction and selection algorithms [172] that are used to build the interaction samples of interest. They are constrained by, for example, measurements of the magnetic field or control samples built from beam data and cosmic ray muons [173].

5.4 Super-Kamiokande Detector Simulation

The Super-Kamiokande detector simulation (SKDETSIM) is based on GEANT3 [137] and tracks the particles generated by NEUT from neutrino interaction vertices distributed uniformly throughout the detector geometry. Hadronic interactions are simulated with GCALOR [138], except for pions with momentum below 500 MeV/c which are simulated by the custom model in NEUT discussed in Chapter 6. The propagation of Čerenkov photons in water is simulated including the effects of scattering and absorption. The charge and timing response of the PMTs are based on calibration data [174].

The overall detector response such as energy scale is tuned to control samples built from cosmic ray muons and atmospheric neutrinos. The systematic uncertainties in the detector simulation and event reconstruction and selection are constrained using these control samples as described in Chapter 8.

Chapter 6

NEUT Pion Interaction Model

Hadrons that are produced by neutrino interactions within a nucleus propagate through the nuclear medium prior to observation. There is a significant probability of interactions within the nucleus prior to escape. These re-interactions, referred to as a *final state interactions* (FSI), affect the observable particles via absorption, scattering and particle production. Furthermore, after the hadrons exit the nucleus, they may experience subsequent or *secondary interactions* (SI) in the detector medium. Thus, there is no direct relation between the observable event topology and the true interaction mode. This affects the neutrino energy reconstruction assuming 2-body kinematics as well as attempts to measure fundamental cross section parameters. Therefore, an accurate model of hadron interactions is required for oscillation parameter measurements.

The FSI simulation for nucleons and heavy mesons (K and η) in the NEUT neutrino interaction generator (Section 5.2) is based on cascade models and external data [175–179]. This chapter focuses on the NEUT [180] and SKDETSIM pion interaction models since pion production is more significant at T2K neutrino energies, while nucleons are typically below Čerenkov threshold at SK.

The NEUT model, including new modifications and tuning, is described in Section 6.1. In principle, the fundamental physics governing hadronic interactions should be common

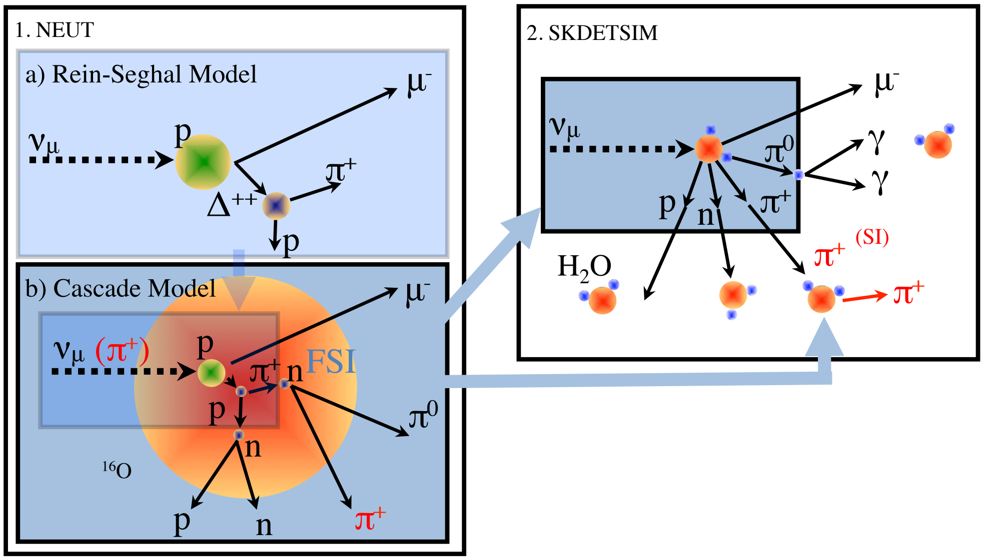

Figure 6.1: Cartoon of the pion interaction simulation in NEUT and SKDETSIM. The pion kinematics and position within the nucleus are determined by the neutrino interaction model described in Section 5.2 (1a). The resulting pions are passed to the FSI cascade simulation (1b). The pions exiting the nucleus are then propagated through the detector, which models SI using the same cascade (2).

to interactions of pions produced within or outside the target nucleus. For example, the model should be able to describe pion beam scattering experiments where the pion is incident from outside the target nucleus, as well as photon (*photoproduction*) and neutrino beam experiments where the pion is produced inside the target nucleus. Thus, comparisons and validation against external data are shown in Section 6.2. The evaluation of systematic error using the external data and propagation to the oscillation analysis is described in Section 6.3. A novel implementation of the model into a detector simulation, in particular SKDETSIM, is described in Section 6.4, unifying the treatment of pion interactions in the neutrino interaction and detector simulations. An overview of the simulation chain is shown in Figure 6.1.

6.1 The Cascade Model

The NEUT pion FSI model is a microscopic cascade where the pion is propagated classically through the nuclear medium in finite steps. The starting position and momentum (including direction) of a pion within the nucleus depends on how it is produced. For a neutrino interaction or photoproduction, the vertex is chosen based on a Woods-Saxon [181] nuclear density profile shown in Figure 6.2, while the the momentum is based on the interaction kinematics. For pion scattering, a pion of a given momentum is incident at some defined boundary of the nucleus.

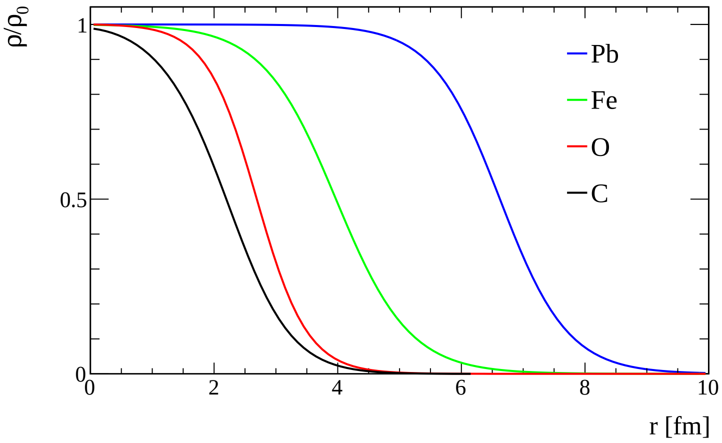

Figure 6.2: Normalized nuclear density distributions for various nuclei modelled by Woods-Saxon distributions with parameters extracted from electron scattering data [182].

The probabilities for various interactions are calculated at each step using [183] for low momentum pions (p_π <500 MeV/c) as described in Section 6.1.1, and from free πp scattering cross sections for high momentum pions (p_π >500 MeV/c) as described in Section 6.1.2. The interaction probabilities scale as the nuclear density. A pion can undergo multiple interactions prior to escape.

6.1.1 Low Momentum

The model in [183] calculates interaction probabilities for quasi-elastic (QE) scattering, including single charge exchange (SCX) and absorption. These probabilities were calculated for oxygen and provided in tables as a function of $p_\pi \in [180, 450]$ MeV/c, as shown in Figure 6.3 (left, dotted line), and radial distance r, as shown in Figure 6.3 (right). The probabilities are extrapolated to 0 and 500 MeV/c. The model predicts a larger scattering probability near the surface compared to absorption. For other nuclei, the same table is used by determining the effective position in oxygen based on the nuclear density profiles.

The QE scattering and absorption probabilities as a function of momentum were tuned using a pion-nucleus scattering simulation, described in Section 6.2.1, to obtain good agreement with $\pi^{+}{}^{12}$C scattering data (Figure 6.6). The tuned model is shown in Figure 6.3 (left, solid line).

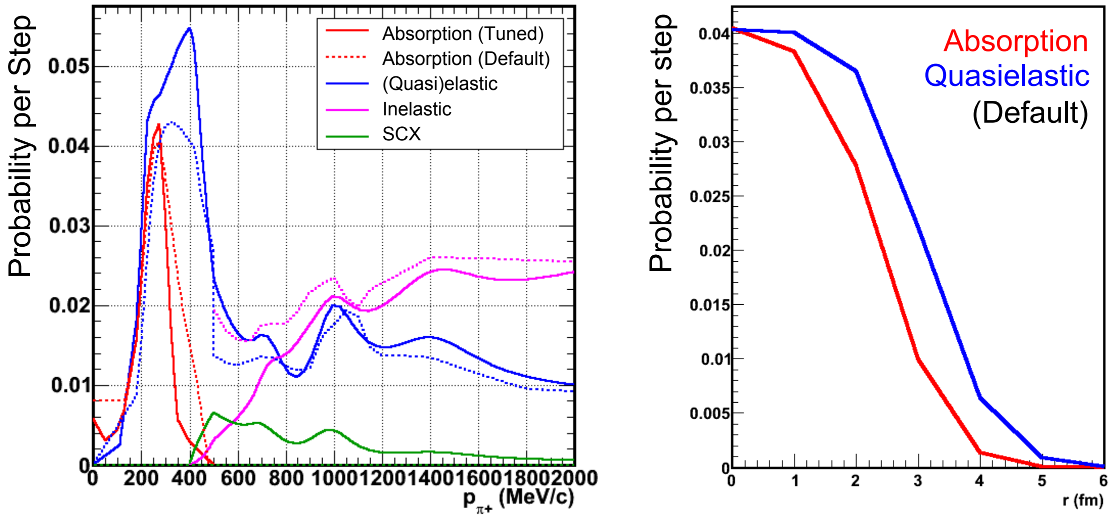

Figure 6.3: Left: The probabilities per step at the center of ^{16}O, p/n averaged, for QE scattering and absorption at low momentum ($p_\pi \leqslant 500$ MeV/c); and elastic scattering, hadron production (inelastic) and SCX at high momentum ($p_\pi > 500$ MeV/c). The default calculation and extrapolation (dotted line) and new tuned model (solid line) is shown. Note that low energy SCX is included in the QE probability. Right: The default absorption and quasi-elastic probabilities as a function of radial position in the nucleus.

Interaction Kinematics

For each QE scatter within the nucleus, the kinematics of the outgoing pion and nucleon are determined from fits to free $\pi^{\pm}$p data [184] with in-medium corrections. The probabilities for single charge exchange, $\pi^+ \leftrightarrow \pi^0$ and $\pi^- \leftrightarrow \pi^0$, are calculated in [183] and weighted according to the proton/neutron (p/n) ratio of the target nucleus.

For pion absorption, the outgoing nucleon multiplicity and charge states are determined from data [185]. The kinematics of 2-nucleon emission is based on π^+-deuteron absorption data [186], and phase space for $>$ 2-nucleon emission. Photon emission from nuclear de-excitation is also considered [187].

6.1.2 High Momentum

For $p_\pi > 500$ MeV/c, the interaction probabilities P_i are given by

$$P_i = \rho_0 \sigma_i \left(\frac{\rho}{\rho_0}\right) \mathrm{d}x, \tag{6.1}$$

where i denotes elastic scattering, SCX or hadron production (inelastic scattering), dx is the step size, ρ_0 is the nucleon number density at the center of the nucleus and $\left(\frac{\rho}{\rho_0}\right)$ is the normalized density distribution shown in Figure 6.2. The σ_i are given by $\pi^{\pm}$ scattering by free proton ($\sigma^{\pi^{\pm}p}$) and deuteron ($\sigma^{\pi^{+}d}$) cross section data compiled by the PDG [72] and shown in Figures 6.4 to 6.5. A fit by the SAID group[1] [188–190] is overlaid.

For the default NEUT FSI model, an iso-scalar nucleus is assumed regardless of the actual target nucleus. Thus, the cross sections are defined relative to the deuteron cross section for π^+ elastic scattering as

$$\sigma_{elastic} = \frac{1}{2}\sigma_{\pi^+ d}\left(\frac{\sigma^{\pi^{\pm}p}_{elastic}}{\sigma^{\pi^{\pm}p}_{tot}}\right) \tag{6.2}$$

---

[1] The SAID group provides an online database and partial wave analysis (PWA) program developed by the Center for Nuclear Studies at The George Washington University.

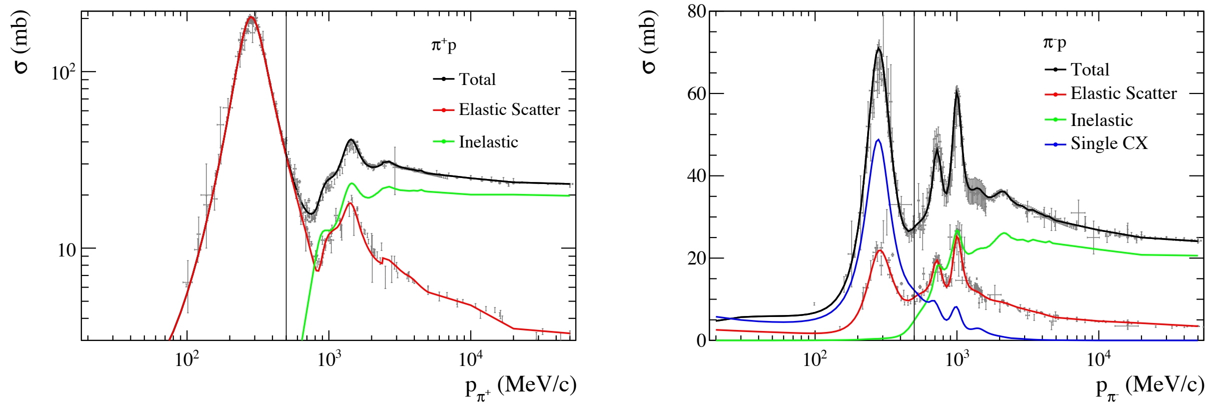

Figure 6.4: World data of π^+ (left) and π^- (right) on free proton scattering cross sections [72] with the SAID fit [188–190] overlaid.

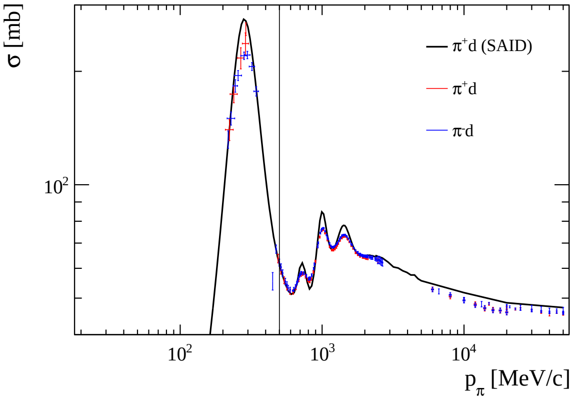

Figure 6.5: World data of $\pi^\pm d$ scattering cross sections [72] with the SAID fit [188–190] overlaid.

and for hadron production as

$$\sigma_{inelastic} = \frac{1}{2}\sigma_{\pi^+ d}\left(1 - \frac{\sigma^{\pi^\pm p}_{elastic}}{\sigma^{\pi^\pm p}_{tot}}\right), \tag{6.3}$$

where the ± (∓ for input π^-) is chosen based on the random selection of a proton (neutron) target. However, this results in a discontinuity in the interaction probabilities at 500 MeV/c as shown in Figure 6.3.

The tuned model mostly removes the discontinuity by using the free proton cross sections directly, or $\sigma_{elastic} = \sigma^{\pi^\pm p}_{elastic}$, $\sigma_{had} = \sigma^{\pi^\pm p}_{inel}$ and $\sigma_{SCX} = \sigma^{\pi^\pm p}_{SCX}$, as given by the SAID fit. A proton or neutron target is chosen based on the actual p/n ratio of the nucleus. Finally, $P_{elastic}$ and P_{SCX} are scaled by a factor of 1.8, motivated by the π^{+12}C high momentum scattering data (Figure 6.6). The tuned model is shown in Figure 6.3 (left, solid line).

Interaction Kinematics

The default NEUT model uses a forward ($< 22^\circ$) scattering model for the elastic scattering of high momentum pions. The tuned model uses the actual differential cross sections of $\pi^\pm p$ scattering calculated from the SAID fits [189], allowing for a larger amount of backward scattering.

For inelastic scattering (hadron production), the outgoing pion multiplicity is determined from bubble chamber data [191]. The kinematics of the outgoing particles are determined by phase space.

6.2 Data Comparisons

The microscopic cascade model provides a common framework with which to simulate macroscopic measurements of interactions of pions. This fundamental nature of the model connects measurements where the pion is created either outside the target nucleus as in pion scattering experiments or within the nucleus as in pion photoproduction or neutrino scattering. Pion-nucleus scattering data, shown in Section 6.2.1, is used to tune the NEUT FSI cascade model since it is not complicated by the additional interaction physics in photoproduction or neutrino scattering. Photoproduction data, used to validate the tuning, is shown in Sections 6.2.2. Comparisons with neutrino data [157–159], though with relatively large systematic and statistical errors, show slight improvements with the tuning. However, there is still some remaining discrepancy in the neutrino data, which is being investigated actively in the field [192] including future measurements by ND280.

6.2.1 Pion Scattering

The pion-nucleus scattering simulation is based on the method in [183]. Some number N_T of pions are generated at a certain momentum with a uniform circular spatial distribution of radius R_N encompassing most of the nuclear density distribution. The pions are incident at the boundary of the nucleus and are propagated through the cascade until they escape (when the radial position $r > R_N$).

A set of selection criteria (interaction channels) is defined in order to compare to experimental (macroscopic) measurements:

- *Absorption*: No pion in the final state (FS).
- *Quasi-elastic (QE) Scattering*: Only 1 scattered pion in the FS of the same charge as the incident beam.
- *Single Charge Exchange (SCX)*: Only 1 π^0 in the final state.
- *Double Charge Exchange (DCX)*: Only 1 pion in the FS of opposite charge to the incident beam.
- *Hadron Production (HP)*: 2 or more pions in the final state.
- *Reactive*: The sum of all of the above.

Note there is some ambiguity in the terms used here, which were previously defined in Section 6.1 but referring to the microscopic interaction mechanisms. The cross section is calculated as

$$\sigma_i = \pi R_N^2 \frac{N_i}{N_T} \tag{6.4}$$

where N_i is the number of events selected in a given interaction channel i.

Experimental Data

ND280 includes a wide variety of materials including lead. Thus, pion-nucleus scattering data with various nuclear targets up to lead are used for comparison. About 97% (70%) of pions produced at SK with the T2K neutrino beam have momentum less than 2000 MeV/c (500 MeV/c), so data with pion beam momenta within this range was studied. The cross sections for various interaction channels are reported by each experiment. A summary of the data is given in Table A.1 of Appendix A.1 and shown for both beam polarities and increasing target size in Figures 6.6 to 6.9. The results of the default simulation and the tuned simulation are overlaid.

The low momentum model tuning (Section 6.1.1) is based on the π^{+12}C data below 500 MeV/c in Figure 6.6 (left). Only the microscopic interaction probabilities, P_{abs} and P_{QE}, are tuned to produce good agreement in the observable absorption and QE channels. The resulting agreement in the SCX channel gives confidence in the default calculation for the microscopic SCX probability.

The modification of the scattering kinematics at high momentum (Section 6.1.2) improves the agreement in the shape of the absorption channel for $p_\pi > 500$ MeV/c. This is due to more backward scattering, which reduces the incoming pion momenta to the region where there is a larger absorption probability (Figure 6.3). The high energy probabilities, P_{QE} and P_{SCX}, are scaled by 1.8 motivated by the $\pi^{\pm 12}$C reactive data and a small amount of SCX and QE scattering data above $p_\pi = 500$ MeV/c[2].

The tuning focused on reproducing the light nuclei (carbon and oxygen) data since these are the most abundant targets used in the current T2K analysis. However, there

---

[2] A similar scaling factor was determined from proton-nucleus data ($\sigma^A_{QE} = 1.6\sigma^{\pi^\pm p}_{elastic} A^{1/3}$) [193].

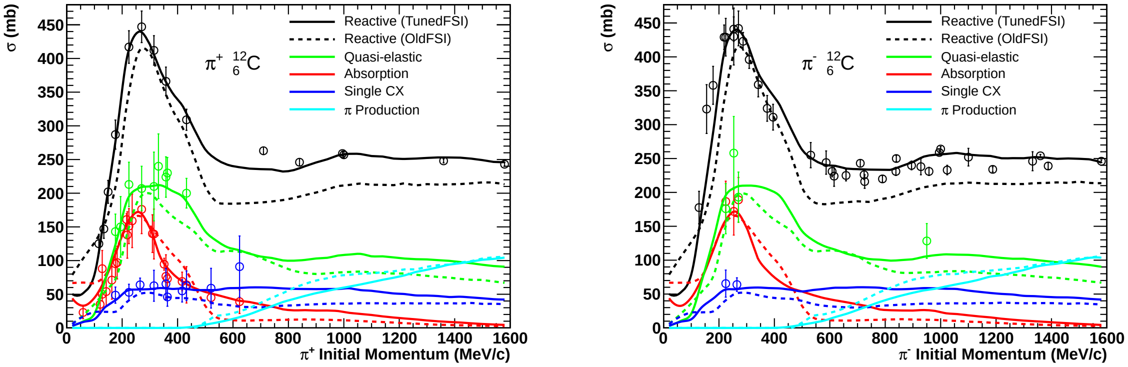

Figure 6.6: π^+ (left) and π^- (right) interaction cross sections on ^{12}C.

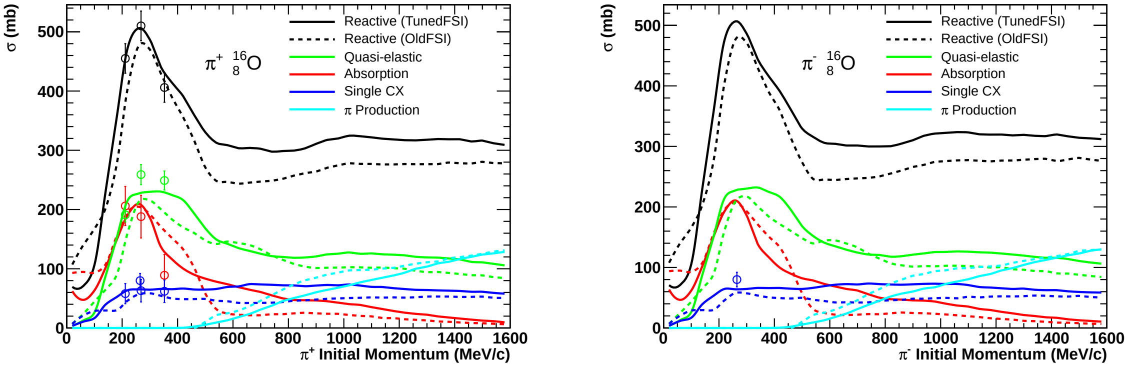

Figure 6.7: π^+ (left) and π^- (right) interaction cross sections on ^{16}O.

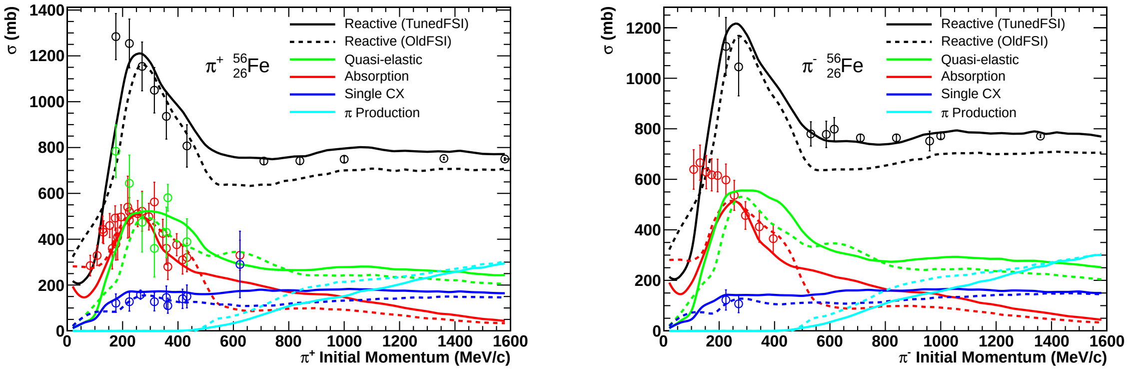

Figure 6.8: π^+ (left) and π^- (right) interaction cross sections on ^{56}Fe.

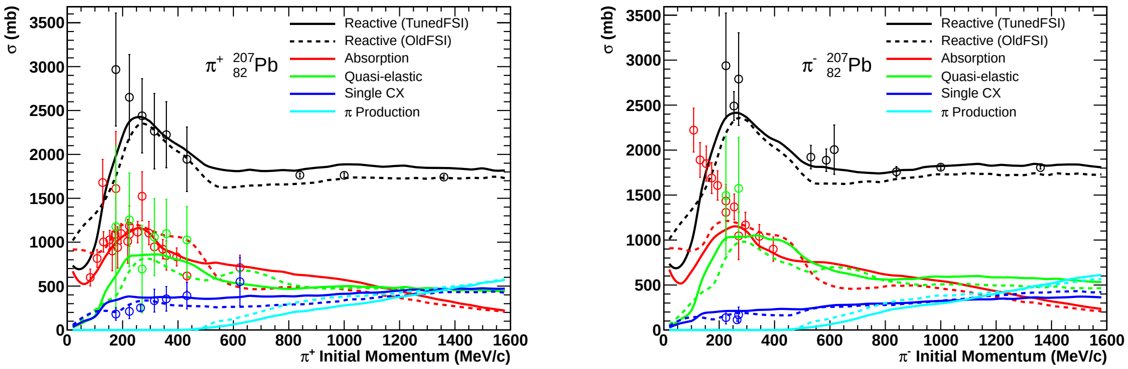

Figure 6.9: π^+ (left) and π^- (right) interaction cross sections on ^{207}Pb.

may still be interactions on detector support materials and entering backgrounds that need to be modelled accurately, for example from the magnet in ND280 or the surrounding rock at SK. Future analyses also aim to use the entering events at SK and interactions in the PØD, which contains a large amount of heavy metals. Hence, the validity of the tuned FSI model is checked against pion scattering data using iron and lead targets in Figures 6.8 and 6.9. The simulation, which simply modifies the nuclear density distribution as in Figure 6.2, agrees well in most interaction channels. However, there is a significant discrepancy in the π^- absorption channel at low energy as the target mass increases, which is likely due to an increased capture rate from stronger Coulomb attraction. This is negligible in current analyses but should be reconsidered in the future.

6.2.2 Pion Photoproduction

Pion photoproduction in nuclei is similar to neutrino scattering in that the pion is produced within the nucleus. A simple simulation, similar to [194], was developed to compare the FSI model to data, described in Appendix A.2.

Experimental Data

The simulation is compared to differential cross section data from [195] in Figure 6.10. The tuning modifications improve the agreement in the cross section at high energy ($E_\gamma > 500$ MeV) and forward angles due to the increase in pion backward scattering and absorption, similarly to the pion scattering comparison described in Section 6.2.1.

The simplicity of the photoproduction simulation prevents further quantitative comparisons with data. Thus, more detailed double differential cross section data is relegated to Appendix A.2.1, presenting a qualitative comparison to validate the FSI model and tuning.

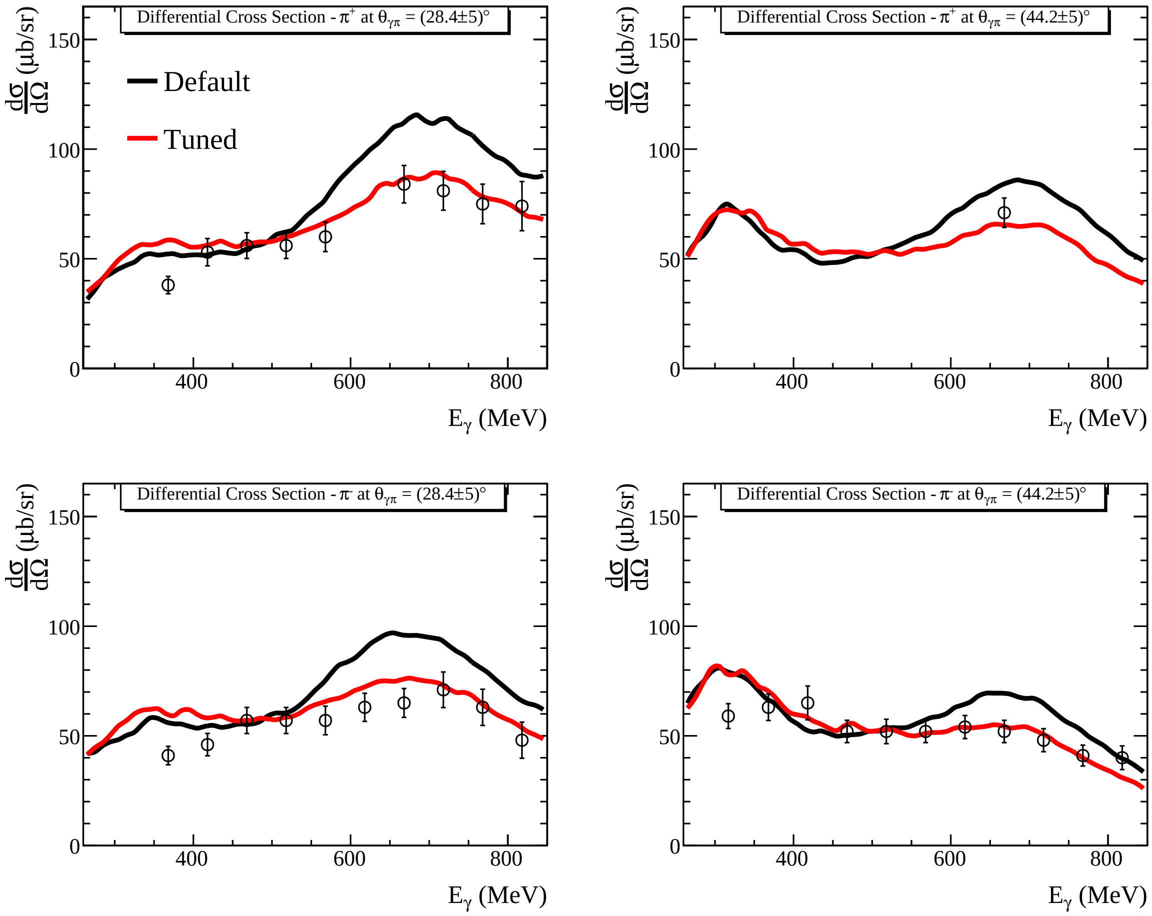

Figure 6.10: Default (black) and tuned (red) NEUT predictions for $\frac{d\sigma}{d\Omega}$ of π^+ (top) and π^- (bottom) photoproduction from carbon, as a function of incoming photon energy. Two outgoing angles are considered: $\theta_{\gamma\pi} = 28.4°$ (left) and $\theta_{\gamma\pi} = 44.2°$ (right). Data points are from [195].

6.3 Systematic Error

Proper treatment of FSI systematics in neutrino experiments is complicated by the nature of pions produced within a nuclear medium. It is further convoluted by the current imprecise understanding of neutrino-nucleus interactions due to lack of data. In this case, the more abundant pion scattering data are used to tune and constrain the microscopic FSI model. This constraint is then propagated to the neutrino interaction simulation.

The model is parameterized by six scale factors f_i summarized in Table 6.1. Each parameter scales the corresponding microscopic probability of interaction P_i (Section 6.1.1 and Equation 6.1) except for f_{CXL}, which scales the charge exchange fraction of low momentum QE scattering. The generation of ND280 and SK detector MC and event reconstruction is a compute-intensive task, so a reweighting scheme was developed to propagate variations in these parameters. It is described in Appendix A.3.

Parameter	Description	Momentum Region (MeV/c)
f_{ABS}	Absorption probability	< 500 MeV/c
f_{QEL}	Quasi-elastic scattering probability	< 500 MeV/c
f_{CXL}	Charge exchange fraction of QE scattering	< 500 MeV/c
f_{ELH}	Elastic scattering probability	> 500 MeV/c
f_{CXH}	Charge exchange probability	> 500 MeV/c
f_{HAD}	Inelastic scattering probability	> 500 MeV/c

Table 6.1: Microscopic scaling parameters in the NEUT FSI model that are constrained by pion scattering data and propagated to the neutrino interaction simulation. The applicable momentum region is given and the "Description" shows what quantity is modified by each parameter.

A constraint on the low momentum parameters (f_{QEL}, f_{ABS}, f_{CXL}) is obtained by comparing variations with $\pi^{\pm 12}$C data below 600 MeV/c. The three low momentum parameters are varied simultaneously to build a χ^2 surface given by

$$\chi^2(f_{ABS}, f_{QEL}, f_{CXL}) = \frac{1}{n}\sum_i \sum_{\pi^+,\pi^-} \frac{\sigma_i^{MC}(f_{ABS}, f_{QEL}, f_{CXL}) - \sigma_i^{data}}{\delta(\sigma_i^{data})}, \tag{6.5}$$

where i runs across all interaction channels, δ is the reported systematic and statistical uncertainty and n is the total number of data points. The factor $\frac{1}{n}$ conservatively scales the error to account for lack of knowledge about correlations between the data. Eight parameter sets are chosen on the *1-sigma surface*, in the corner of each octant of the 3-parameter space to represent the constraint and correlations from the data. These are summarized in Table 6.1 (sets 1–8 except with tuned high momentum parameters) and the prediction for each set is shown in Figure 6.11.

Additionally, two sets of high momentum parameters (f_{ELH}, f_{HAD}, f_{CXH}) are chosen to span the errors in the high momentum data as shown in Figure 6.12 in such a way that more or less inelastic (hadron production and charge exchange) interactions are produced. These two variations are combined with the low momentum variations resulting in the 16 parameter sets shown in Table 6.2.

This somewhat unwieldy method of constraining the parameter space is used because the FSI reweighting is compute-intensive and any fit that attempts to vary these parameters directly would require a prohibitively long time. To propagate the constraint to the neutrino interaction MC samples, each sample is reweighted for each parameter set k in Table 6.2. Then for each sample, a covariance matrix V relating the observables p (for example, lepton (p_μ, θ_μ) bin or reconstructed E_ν bin) is calculated as

$$V_{i,j} = \frac{1}{16}\sum_{k=1}^{16}(p_i^k - p_i^{\text{tuned}})(p_j^k - p_j^{\text{tuned}}). \tag{6.6}$$

This covariance V, which encodes the constraint from the pion scattering data, is propagated to the oscillation analysis in Chapter 9[3].

---

[3] The systematic error from pion secondary interactions in SKDETSIM is also included, described in Section 6.4.2.

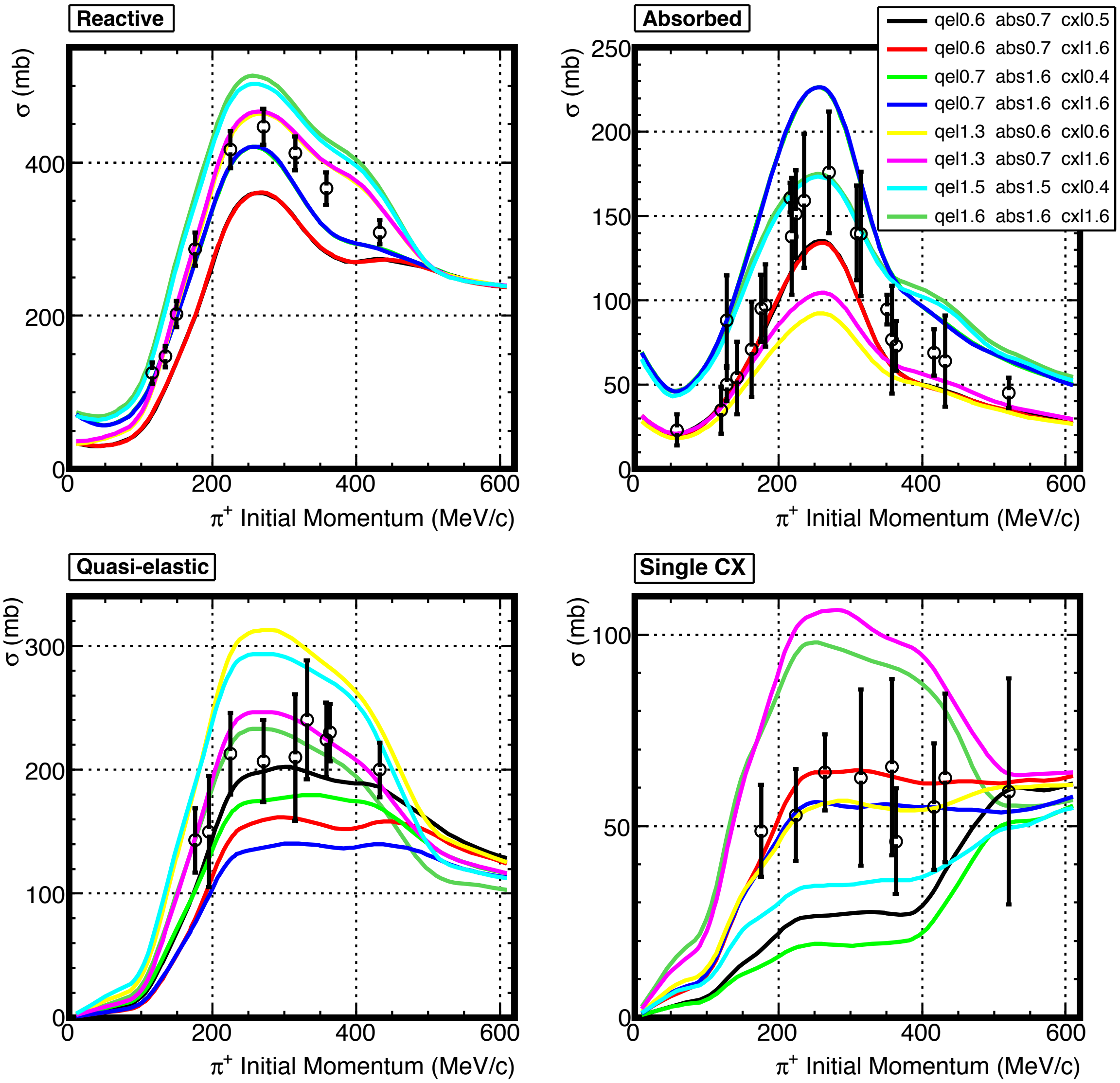

Figure 6.11: The eight low momentum parameter variation 1σ curves from the fit to pion scattering data. The legend corresponds to Tables 6.1 and 6.2 as follows: “qel”: f_{QEL}, “abs”: f_{ABS}, and “cxl”: f_{CXL}. The high momentum parameters are set to the tuned values in Table 6.2.

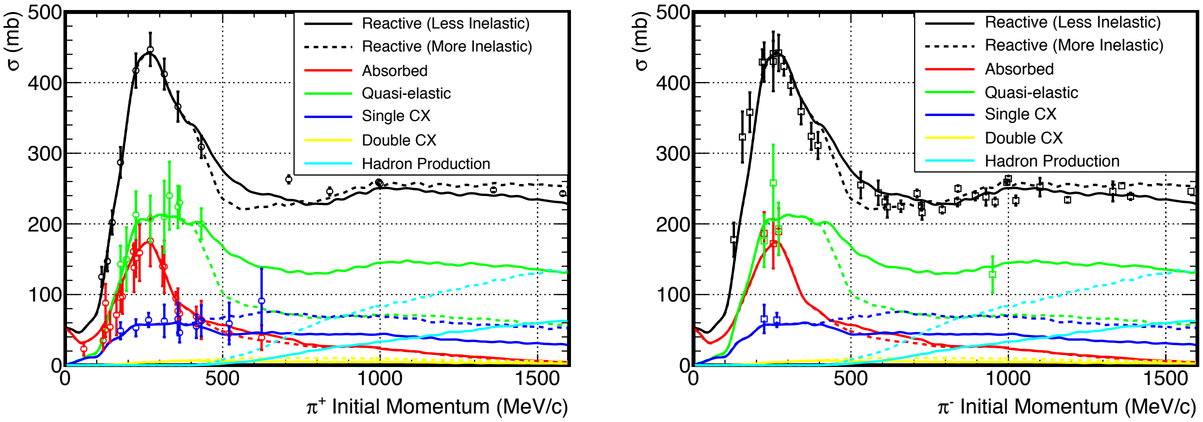

Figure 6.12: π^+ (left) and π^- (right) ^{12}C data with NEUT predictions after variation of the high momentum FSI parameters. The legend corresponds to "Less Inelastic": ($f_{ELH} = 2.3$, $f_{HAD} = 0.5$, $f_{CXH} = 1.3$) and "More Inelastic": ($f_{ELH} = 1.1$, $f_{HAD} = 1.5$, $f_{CXH} = 2.3$). The low momentum parameters are set to the tuned values in Table 6.2.

Parameter Set	f_{QEL}	f_{ABS}	f_{CXL}	f_{ELH}	f_{HAD}	f_{CXH}
Tuned	1.0	1.1	1.0	1.8	1	1.8
1	0.6	0.7	0.5	1.1	1.5	2.3
2	0.6	0.7	1.6	1.1	1.5	2.3
3	0.7	1.6	0.4	1.1	1.5	2.3
4	0.7	1.6	1.6	1.1	1.5	2.3
5	1.4	0.6	0.6	1.1	1.5	2.3
6	1.3	0.7	1.6	1.1	1.5	2.3
7	1.5	1.5	0.4	1.1	1.5	2.3
8	1.6	1.6	1.6	1.1	1.5	2.3
9	0.6	0.7	0.5	2.3	0.5	1.3
10	0.6	0.7	1.6	2.3	0.5	1.3
11	0.7	1.6	0.4	2.3	0.5	1.3
12	0.7	1.6	1.6	2.3	0.5	1.3
13	1.4	0.6	0.6	2.3	0.5	1.3
14	1.3	0.7	1.6	2.3	0.5	1.3
15	1.5	1.5	0.4	2.3	0.5	1.3
16	1.6	1.6	1.6	2.3	0.5	1.3

Table 6.2: NEUT FSI 1-sigma parameter sets from the comparisons to pion scattering data. Two high momentum variations are combined with eight low momentum variations as described in the text.

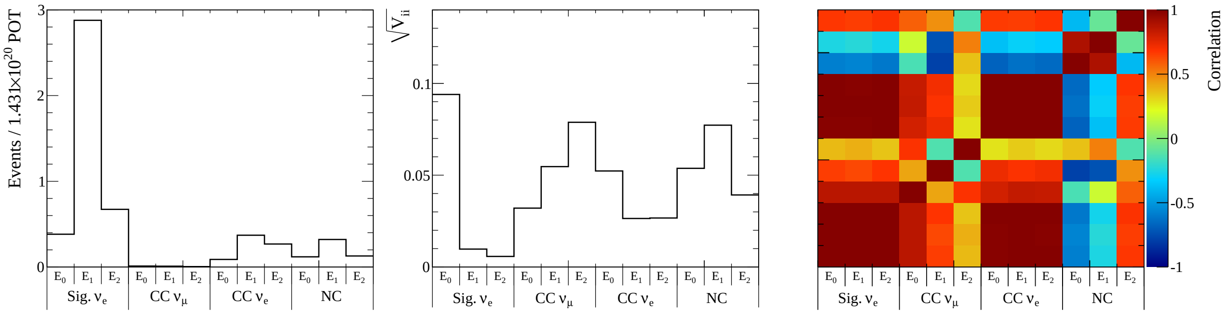

Figure 6.13: The number of events (left), diagonals of the covariance matrix (middle) and correlation matrix (right) calculated by Equation 6.6 for the SK ν_e candidate event sample as a function of reconstructed neutrino energy bins, ($0 < \mathrm{E}_0 < 350$), ($350 < \mathrm{E}_1 < 800$) and ($800 < \mathrm{E}_2 < 1250$) MeV. The sample is divided into four components: signal ν_e (from $\nu_\mu \rightarrow \nu_e$ oscillation) CC interactions, ν_μ CC interactions (negligible), intrinsic beam ν_e CC interactions and NC interactions, assuming the oscillation parameters in Table 9.2.

6.3.1 Example Application to SK ν_e Sample

An example covariance matrix (or equivalently the diagonals and correlation matrix) for the SK ν_e candidate (single ring) selection, described in Chapter 8, is shown in Figure 6.13. The sample is divided into four components: signal ν_e (from $\nu_\mu \rightarrow \nu_e$ oscillation) CC interactions, ν_μ CC interactions (negligible), intrinsic beam ν_e CC interactions and NC interactions. The systematic error across all components and energy bins due to FSI is of the order of 5%. Pion absorption is the dominant effect giving rise to two immediately apparent features:

- There is a large increase in the error towards low reconstructed neutrino energy due to a higher population of misreconstructed events with pion absorption.

- There is a strong anti-correlation between the signal ν_e and NC components since absorption increases the background contribution to the former and decreases the amount of π^0 in the final state in the latter.

Similar matrices are constructed for the SK ν_μ sample and ND280 samples used in the oscillation analysis.

6.4 SKDETSIM Pion Secondary Interactions

In neutrino interaction events, *secondary interactions* (SI) of pions occur after they have escaped the target nucleus. This can affect the observable topology of an event as in the following examples:

- A $\pi^\pm$ may CX into a π^0, resulting in a higher likelihood that the event is misidentified as e-like.
- A π^+ may be absorbed, resulting in the loss of the decay electron. The visible energy of the event decreases, since the π^+ stops emitting Čerenkov radiation.
- $\pi^\pm$ elastic (coherent) and quasi-elastic scattering can alter the ring reconstruction by blurring from small angle scatters or creating a second ring from a large angle scatter. The visible energy is also affected.

Thus, accurate modelling and understanding of the systematic errors of these processes is necessary for the oscillation analysis.

The default SKDETSIM model (Section 5.4) uses GCALOR [138] above 500 MeV/c pion momentum and a custom model below. Previous analyses (e.g. [41, 196]) typically used "black box" models such as GCALOR, GHEISHA [197] and GFLUKA [198], which are non-conducive to parameter tuning and systematic variation, then took the difference between models as a systematic error. For T2K, the SKDETSIM model below 500 MeV/c is replaced by the NEUT pion FSI cascade model. Thus, the simulation and systematic errors of pion interactions within (FSI) and outside (SI) the target nucleus are unified for the first time.

Section 6.4.1 summarizes the main changes from the previous SKDETSIM model to the NEUT model. Section 6.4.2 describes the systematic error evaluation for propagation to the oscillation analysis.

6.4.1 Implementation of the NEUT FSI Model

The details of the implementation and validation of the NEUT pion FSI model in SKDETSIM (GEANT3) are given in Appendix A.4. This appendix is included for posterity since the documentation of the previous model is in Japanese [199]. Various modifications to the previous model are summarized in this section.

In GEANT3, the total hadronic interaction cross section, $\sigma_{\mathrm{T}} = \sigma_{\mathrm{O}} + 2\sigma_{\mathrm{H}}$ (for water), must be provided. The total cross section on oxygen, σ_{O}, is determined from an updated fit to pion scattering data [200–202]. The total cross section on free hydrogen, σ_{H}, is updated to use the SAID fit [188–190] shown in Figure 6.4.

If an interaction occurs, then the interaction channel and final state must be determined based on the branching fractions (e.g. $\sigma_i/\sigma_{\mathrm{T}}$) and a kinematic model. A few issues were discovered in the previous simulation:

- The absorption cross section was tuned to ^{27}Al data [199], which slightly overestimates the cross section in oxygen since it is a larger nucleus.
- The interaction cross sections for oxygen were applied to water. For example, absorption was allowed on free hydrogen, which is physically forbidden.
- The kinematic model for elastic and QE (including SCX) scattering was too forward-going compared to pion scattering data.

In the new model, first the interaction is determined to be on free hydrogen or the oxygen nucleus based on the ratio $\sigma_{\mathrm{O}}/\sigma_{\mathrm{T}}$. If the interaction occurs on hydrogen, the cross sections in Figure 6.4 are used to determine the interaction channel. If the interaction occurs on the oxygen nucleus, it is determined to be reactive or elastic based on the ratio $\sigma_{\mathrm{R}}/\sigma_{\mathrm{O}}$, where σ_{R} is the reactive cross section calculated by NEUT and shown in Figure 6.7. If a reactive type interaction occurs, the actual interaction channel and final state kinematics are determined by the NEUT cascade, which resolves the first two issues and the QE scattering kinematics. For free hydrogen elastic scattering (and π^-p SCX), the SAID differential cross section calculation [189, 190] is adopted in the new model.

The main difference arising from the new model in the full neutrino and detector simulation with event reconstruction is a slight increase in the rate of multi-ring and multi-decay-e events, corresponding to a decrease in the number of single-ring events by $\sim$1%.

6.4.2 Systematic Error

Systematic errors arise from uncertainties in the various pion-nucleus interaction cross sections. The purpose of the cascade model is to reproduce fundamental processes which should be common to interactions of pions produced within or outside the target nucleus. Thus, the implementation of the NEUT cascade model into SKDETSIM for SI, allows for the unified treatment of the correlated uncertainties present in each case.

The constraint on the microscopic parameters is described in Section 6.3. This translates into a constraint on the macroscopic cross sections as shown in Figure 6.11 (except on oxygen). These variations in cross sections are propagated through the MC simulation via reweighting based on an analysis of the SI occurring in each event, described further in Appendix A.3.2. The total cross section is kept constant, assuming that the $\sim$ 5% uncertainty in total cross section measurements [200–202] is negligible compared to the uncertainty in each interaction channel.

The propagation of the systematic error to the oscillation analysis is the same as prescribed by Equation 6.6. The error due to SI-only variations in the ν_e candidate sample is shown in Figure 6.14. The effect is small, on the order of 1%, but is expected to be more significant in future analyses that include pion production channels. The uncertainty peaks toward low energy, similarly to the FSI-only case, due to absorption. In the background component, this peak is more apparent for SI, which is mostly $\pi^{\pm}$ absorption and a small amount of CX, compared to FSI which also affects π^0 from high energy interactions. Previous analyses typically added errors in quadrature, or the sum of the covariances matrices produced from variations of SI and FSI separately (uncorrelated). When correlations are taken into account, by creating a single covariance matrix with the simultaneous variation of SI and FSI, the resulting errors are larger (corresponding to approximately adding the individual errors linearly). This FSI+SI correlated matrix, similar to the one shown in Figure 6.13, is propagated to the oscillation analysis.

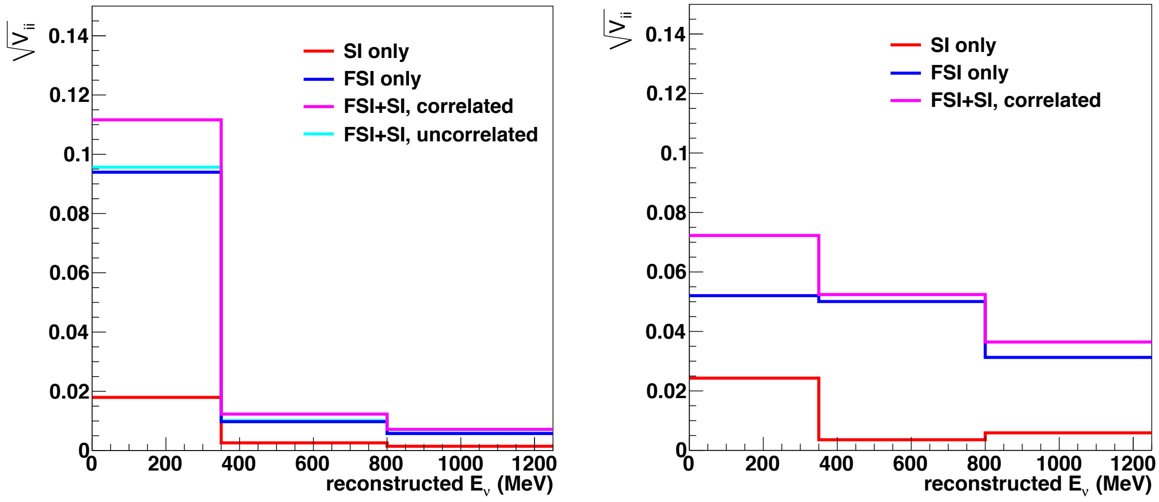

Figure 6.14: Diagonals of the covariance matrix calculated by Equation 6.6 for the SK ν_e candidate event sample as a function of reconstructed neutrino energy. The sample is divided into two components: signal ν_e (from $\nu_\mu \rightarrow \nu_e$ oscillation) CC interactions (left) and background (right), assuming the oscillation parameters in Table 9.2. Various configurations of the model variations are shown as described in the text.

Chapter 7

Statistical Framework for Analysis

This chapter describes a common framework used to solve two separate problems:

1. Estimating oscillation parameters based on the T2K data, described in Chapter 9.
2. Estimating the SK detector systematic errors, described in Chapter 8.

The oscillation analysis determines oscillation parameters using a fit to T2K neutrino beam data at ND280 and SK (*T2K-SK*). As described in Chapter 5, the event rates are affected by the presence of flux, cross section and detector systematic uncertainties. These variations are constrained by other data sets, referred to as *prior constraints*. Section 7.1 outlines the statistical framework, a likelihood function including the prior constraints, used in fitting the ND280 and T2K-SK data. Section 7.2 describes the Markov Chain Monte Carlo (MCMC) method used to calculate the likelihood function and determine the most probable values (best-fits) and allowed regions for the parameters of interest.

An extension of the likelihood function to include the SK atmospheric neutrino data [45] (Atm-ν or *Atm-SK*) is described in Section 7.1.1. However, due to the current level of T2K statistics and understanding of the SK detector systematics, a joint fit of the T2K-SK and Atm-ν data is beyond the scope of this thesis. Instead, the Atm-ν data is used as a prior constraint on the SK detector systematic errors. In anticipation of a future joint fit, the estimation of the SK detector errors uses the same statistical and MCMC framework described here with some approximations.

7.1 Likelihood Function

The likelihood function [203] $\mathcal{L}$ for the T2K oscillation analysis is given by [204]

$$\begin{aligned} \mathcal{L}(\mathbf{o}, \mathbf{b}, \mathbf{x}, \mathbf{d_{ND}}, \mathbf{d_{SK}} | \mathbf{M}_{ND280}, \mathbf{M}_{T2K-SK}) = \\ P(\mathbf{M}_{ND280} | \mathbf{b}, \mathbf{x}, \mathbf{d_{ND}}) \times P(\mathbf{M}_{T2K-SK} | \mathbf{o}, \mathbf{b}, \mathbf{x}, \mathbf{d_{SK}}) \\ \times \pi(\mathbf{o}) \times \pi(\mathbf{b}) \times \pi(\mathbf{x}) \times \pi(\mathbf{d_{ND}}) \times \pi(\mathbf{d_{SK}}), \end{aligned} \tag{7.1}$$

where P is the conditional probability of the data $\mathbf{M}_{ND280}$ and $\mathbf{M}_{T2K-SK}$, given the parameters[1]. The parameters are as defined for Equation 5.1 (summarized in Table 9.3) with the detector parameters $\mathbf{d}$ separated into $\mathbf{d_{ND}}$ and $\mathbf{d_{SK}}$ for ND280 and SK, respectively. The prior probabilities, π, come from the various data constraints described in this thesis. The likelihood function can be maximized, or sampled in the case of a MCMC, under variations of all parameters to determine the set of parameters that is preferred by the data.

The conditional probability $P(\mathbf{M}|\mathbf{f})$, for some data set $\mathbf{M}$ and subset $\mathbf{f}$ of the parameters above, is derived from the product of a Poisson and multinomial probability mass function such that [205]

$$-\ln\left[P\left(\mathbf{M}|\mathbf{f}\right)\right] = \sum_i \left[\left(\hat{N}_i(\mathbf{f}) - N_i\right) + N_i \ln\left(\frac{N_i}{\hat{N}_i(\mathbf{f})}\right)\right], \tag{7.2}$$

where $\hat{N}_i$ and N are the predicted and measured number of events in a given observable bin i. The variable i is, in general, multi-dimensional across sub-samples of the given data set and kinematic bins. It is defined specifically for each analysis described in Chapters 8 and 9.

---

[1] A normalization term is neglected since it is irrelevant when the likelihood function is maximized or sampled.

The prior probabilities $\pi(\mathbf{f})$ are typically assumed to be multivariate Gaussian distributions, if a constraint exists, such that

$$\pi(\mathbf{f}) = (2\pi)^{-k/2}|V_f|^{-1/2}e^{-\frac{1}{2}\mathbf{\Delta f}(V_f^{-1})\mathbf{\Delta f}^T}, \tag{7.3}$$

where $\mathbf{\Delta f} = \mathbf{f}' - \mathbf{f_{nom}}$, $\mathbf{f}'$ is some variation of the parameters, $\mathbf{f_{nom}}$ is the nominal value after any tuning, V_f is the covariance that describes the uncertainties and correlations in $\mathbf{f}$, and k is the dimension of $\mathbf{f}$. References for each $\mathbf{f_{nom}}$ and V_f are summarized in Table 9.3. Some parameters assume a flat (uniform) prior such as the neutrino interaction spectral function parameter (Table 5.2) and the oscillation parameters of interest (θ_{13}, θ_{23}, Δm^2_{32}, δ_{CP}).

7.1.1 Use of Atmospheric Neutrino Data

For a future joint T2K and Atm-SK oscillation fit, a term for the Atm-ν data $\mathbf{M}_{Atm-SK}$ and flux $\mathbf{a}$ can be added such that Equation 7.1 becomes

$$\begin{gathered}\mathcal{L}(\mathbf{o},\mathbf{b},\mathbf{a},\mathbf{x},\mathbf{d_{ND}},\mathbf{d_{SK}}|\mathbf{M}_{ND280},\mathbf{M}_{T2K-SK},\mathbf{M}_{Atm-SK}) = \\ P(\mathbf{M}_{ND280}|\mathbf{b},\mathbf{x},\mathbf{d_{ND}}) \times P(\mathbf{M}_{T2K-SK}|\mathbf{o},\mathbf{b},\mathbf{x},\mathbf{d_{SK}}) \times P(\mathbf{M}_{Atm-SK}|\mathbf{o},\mathbf{a},\mathbf{x},\mathbf{d_{SK}}) \\ \times\pi(\mathbf{o}) \times \pi(\mathbf{b}) \times \pi(\mathbf{a}) \times \pi(\mathbf{x}) \times \pi(\mathbf{d_{ND}}) \times \pi(\mathbf{d_{SK}}),\end{gathered} \tag{7.4}$$

which can then be maximized or sampled across all three data sets simultaneously. This is difficult due to limitations in the current understanding of the systematics, for example:

- Correlations of uncertainties due to hadron production in the T2K target and the atmosphere (in other words, $\pi(\mathbf{b},\mathbf{a})$ cannot actually be factorized as in Equation 7.4).
- The interactions parameterization $\mathbf{x}$ must be extended to describe higher energy and anti-neutrino interactions.
- A more fundamental (microscopic) description of the SK detector systematics $\mathbf{d_{SK}}$ is required.

Thus, in the present analysis, the Atm-ν data, with much higher statistics than T2K, is used to constrain an effective (macroscopic) parameterization β of the SK detector systematics. A similar form of the likelihood is assumed for the Atm-ν data only:

$$\mathcal{L}(\mathbf{d_{SK}^{Atm}}; \mathbf{a}, \mathbf{x_{atm}}, \beta | \mathbf{M}_{Atm-SK}) = P(\mathbf{M}_{Atm-SK} | \mathbf{a}, \mathbf{x_{atm}}, \beta) \times \pi(\mathbf{a}) \times \pi(\mathbf{x_{atm}}) \times \pi(\beta), \quad (7.5)$$

where the oscillation parameters have been fixed and $\mathbf{x_{atm}}$ is an independent set of cross section parameters. Correlations with the T2K parameters in Equation 7.1 are assumed to be negligible when evaluating a constraint on detector parameters. Then, Equation 7.5 can be marginalized (Section 7.1.2) over the parameters to determine the constraint $\pi(\mathbf{d_{SK}^{Atm}})$ in Equation 7.1.

7.1.2 Marginalization

Equations 7.1 and 7.5 are multi-dimensional *posterior probability distributions* that describe the probability of some set of parameters given the measured data. There are typically only a few parameters of interest, θ, while the rest are considered *nuisance parameters*, ϕ. A *marginal likelihood* $\mathcal{L}_M$ is constructed by integrating the posterior likelihood:

$$\mathcal{L}_M(\theta | \mathbf{M}) = \int P(\mathbf{M} | \theta, \phi) \times \pi(\phi) d\phi, \quad (7.6)$$

where the specific data and parameter sets have been suppressed for generality. The marginal likelihood, or *posterior* for brevity, describes the probability of θ given the data and includes the uncertainties due to the nuisance parameters. This posterior is the main result of a Bayesian inference analysis, but can be further analyzed and represented in more concise forms, such as the most probable set or some allowed region of θ. The specific forms of representation are described in Sections 8.4.5 and 9.3.

7.2 Markov Chain Monte Carlo

A simultaneous fit of ND280 and T2K-SK (Equation 7.1) necessitates a large number of parameters. Also, the Atm-ν fit (Equation 7.5) is parameterized in a way that allows event migrations across multiple sub-samples in $\mathbf{M}_{Atm-SK}$. Traditional minimizers such as MINUIT [206] are more likely to fail to converge with these non-linear, discrete and large-dimensional problems. Thus, a Metropolis-Hastings algorithm MCMC [72, 207] is used to sample the likelihoods in Equations 7.1 and 7.5. Furthermore, the MCMC method facilitates the evaluation of the multi-dimensional integral in Equation 7.6, which is in general non-trivial.

The MCMC randomly *steps* around the parameter space, tending to accept the steps that have a larger contribution to the integral, or equivalently a larger likelihood, than the previous step. This process is described more formally as follows. Let $P(\mathbf{f})$ represent either Equation 7.1 or Equation 7.5. To generate steps that follow the shape of $P(\mathbf{f})$, a proposal function $Q(\mathbf{f};\mathbf{f_0})$ is used to draw random values of $\mathbf{f}$ depending on some other set of parameters $\mathbf{f_0}$. For the analyses in Sections 8.4 and 9.3, $Q(\mathbf{f};\mathbf{f_0})$ are independent Gaussians centered about $\mathbf{f_0}$ with widths tuned based on the priors (or the posterior if there is no prior constraint). The starting point $\mathbf{f_0}$ for each chain is chosen to be a random fluctuation of all the parameters $\mathbf{f}$ according to the prior uncertainties about the nominal values. Then, the Metropolis-Hastings algorithm is the following iteration:

1. Randomly select a proposed parameter set $\mathbf{f}$ from the distribution $Q(\mathbf{f};\mathbf{f_0})$.
2. Calculate the acceptance ratio $\mathit{\Omega} = \min\left(1, \frac{P(\mathbf{f})}{P(\mathbf{f_0})}\right)$.
3. Generate a uniformly distributed random number $u \in [0,1]$.
4. If $u \leqslant \mathit{\Omega}$, then accept this step in the chain and let $\mathbf{f_0} = \mathbf{f}$ in the next proposal, otherwise reject the current proposal $\mathbf{f}$ and keep the current $\mathbf{f_0}$.
5. Return to Step 1 until a sufficient number of steps have been accepted.

The result of the MCMC is a set of points or *chain* distributed according to the posterior probability. This chain can then be used to infer representative quantities, such as the marginal likelihood in Equation 7.6 by projecting onto the θ parameter axes over all steps of the chain.

Chapter 8

Super-Kamiokande Analysis

The SK analysis consists of detector calibration, event reduction, event reconstruction and sample selection. The calibration consists of various light sources, radioactive sources, an electron LINAC, Atm-ν π^0, cosmic ray muons and their associated decay electrons, described elsewhere [174, 208–210]. The event reduction consists of *good spill* selection, including the GPS timing synchronization with the beamline [95, 211, 212]. The event reconstruction [210] consists of vertex fitting, ring counting (RC), PID based on showering or non-showering topologies (Section 3.3.1), momentum determination, decay-e tagging and π^0 fitting. The sample selection, which was designed to identify ν_e and ν_μ CCQE candidate events from single-ring (1-ring) topologies, is summarized in Section 9.1.2.

Section 8.1 introduces a new event reconstruction algorithm, named *fiTQun* . In principle, it can replace the previous algorithm referred to above. However, due to time constraints it is currently only applied at the π^0 fitting stage, where it provides superior background rejection in the ν_e analysis, leading to a high significance for the ν_e appearance observation [56]. The algorithm is validated against cosmic ray muon, decay-e and Atm-ν data samples in Sections 8.2 and 8.3. The existing systematic error estimates derived from the cosmic ray muon data, provided to the oscillation analysis, are reproduced using the new reconstruction. The systematic errors for the ν_e and ν_μ selection derived from the Atm-ν data are described in Section 8.4. A summary of the systematic error sources is given in Section 8.5.

8.1 Likelihood-Based Event Reconstruction

FiTQun is a new water Čerenkov event reconstruction algorithm based on [213]. It is used in SK to characterize an event based on the measured charges and times recorded for every PMT hit. An event is divided into time clusters of hits, called *sub-events*, corresponding to a primary interaction and later decays. A likelihood function that depends on a set of parameters describing the particle(s) in a sub-event is defined (Section 8.1.1). Various likelihoods can be constructed based on different hypothesized event topologies, such as the number of particle tracks (or rings) and the PID for each track. These likelihoods are then maximized with respect to the measured charges and times for all PMTs in a sub-event to obtain the best-fit parameters for each hypothesis. Finally, the most likely hypothesis is determined by comparing the best-fit likelihoods.

This section summarizes the quantities that are used in the validation studies. A more detailed description of these quantities and the full algorithm is given in [214].

8.1.1 The Likelihood Function

The kinematics of a single particle in an event in SK are characterized by the following 7 parameters:

- the event 4-vertex (t, x, y, z),
- the zenith and azimuth angle of the direction (θ, ϕ) and
- the magnitude of the momentum p.

Let $\mathbf{x} = (t, x, y, z, \theta, \phi, p)$, then the goal of the reconstruction algorithm is to determine the most likely value for $\mathbf{x}$ given the observed measurements of the PMTs.

For a given sub-event, a likelihood function is constructed based on the measured charge q_i and time t_i from each ID PMT i as follows:

$$\mathcal{L}(\mathbf{x}) = \prod_j^{\text{unhit}} P_j(\text{unhit}|\mathbf{x}) \prod_i^{\text{hit}} \left[1 - P_i(\text{unhit}|\mathbf{x})\right] P_q(q_i|\mathbf{x}) P_t(t_i|\mathbf{x}). \tag{8.1}$$

The index j is over all PMTs that did not register a hit and i is over the PMTs that did register a hit. $P_j(\text{unhit}|\mathbf{x})$ is the conditional probability density function (PDF) of the j-th tube not registering a hit given the track parameters $\mathbf{x}$. The charge likelihood $P_q(q_i|\mathbf{x})$ and time likelihood $P_t(t_i|\mathbf{x})$ are PDFs for observing q_i and t_i, respectively, given the track parameters $\mathbf{x}$.

The likelihood function can be more simply understood when written as follows:

$$\mathcal{L}(\hat{q}_i) = \prod_j^{\text{unhit}} P_j(\text{unhit}|\hat{q}_i) \prod_i^{\text{hit}} \left[1 - P_i(\text{unhit}|\hat{q}_i)\right] P_q(q_i|\hat{q}_i) P_t(t_i|\hat{t}_i), \tag{8.2}$$

where the quantities $\hat{q}_i$ and $\hat{t}_i$ are the predicted charge and time for the ith PMT, which implicitly depend on $\mathbf{x}$. The factors P contain all the prior physics knowledge encoded in the MC simulation and other relevant models, including Čerenkov light generation and propagation, and PMT charge and time response models. The calculation of each factor is described in [214]. The likelihood is then maximized by varying $\mathbf{x}$ using MINUIT [206] to obtain a best-fit or most likely set of parameters for a given track hypothesis. For the single-track case, each hypothesis corresponds to a different particle type, such as electron or muon, which results in different predicted quantities. The maximum likelihoods for the electron and muon hypotheses, denoted $\mathcal{L}_e$ and $\mathcal{L}_\mu$, can then be compared to determine if a sub-event is more e-like or μ-like.

8.1.2 Extending to Multiple Track Final States

The single-track formalism above can be extended to multi-track hypotheses by adding parameters to $\mathbf{x}$ that correspond to the additional particles. For example, the predicted charge $\hat{q}_i$ becomes the sum of the predicted charges of all the individual tracks. Physical constraints are imposed depending on the hypothesis. For the π^0 hypothesis, two electron-hypothesis tracks are assumed for the decay photons, characterized by the following 12 parameters:

- the π^0 4-vertex (t, x, y, z), common to both tracks,
- the directions of each track (θ_1, ϕ_1), (θ_2, ϕ_2),
- the magnitude of the momentum of each track p_1, p_2 and
- a conversion distance for each track, d_1^{conv}, d_2^{conv}, allowing the electron tracks to start some distance downstream of the π^0 vertex.

The maximum likelihood for this hypothesis is denoted $\mathcal{L}_{\pi^0}$ and can be compared to $\mathcal{L}_e$ to determine if a sub-event is more π^0-like or e-like. The π^0 mass can be calculated directly from the photon momenta.

8.2 Cosmic Ray Muon Reconstruction Validation

A stopping cosmic ray muon and its decay-e (Michel) typically produce two separate sub-events that are reconstructed by fiTQun. A sample of events is selected using reconstructed quantities to validate the fiTQun algorithm by comparing data to MC. The quantities are checked at each selection stage and the final sample is used to construct a decay-e momentum spectrum and muon momentum/range distributions. These distributions can be used to check the accuracy of the simulated energy scale since the underlying models are well-understood for the Michel spectrum [215] and energy loss.

A diagram illustrating the event selection is shown in Figure 8.1 and is defined as follows:

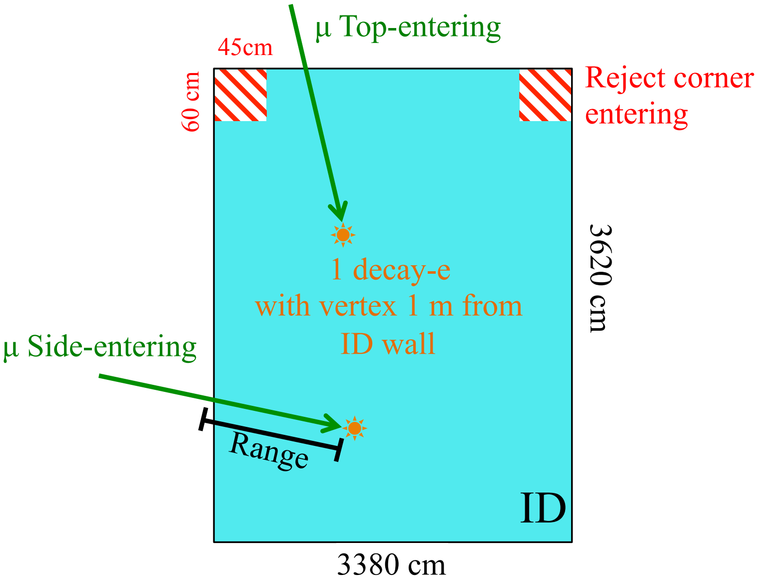

Figure 8.1: Diagram of selection for cosmic muon analysis described in the text. (Not to scale.)

1. A maximum charge threshold corresponding to about a 5 GeV/c momentum muon is applied to the first sub-event. The resulting reconstructed muon momentum distribution is shown in Figure 8.2.

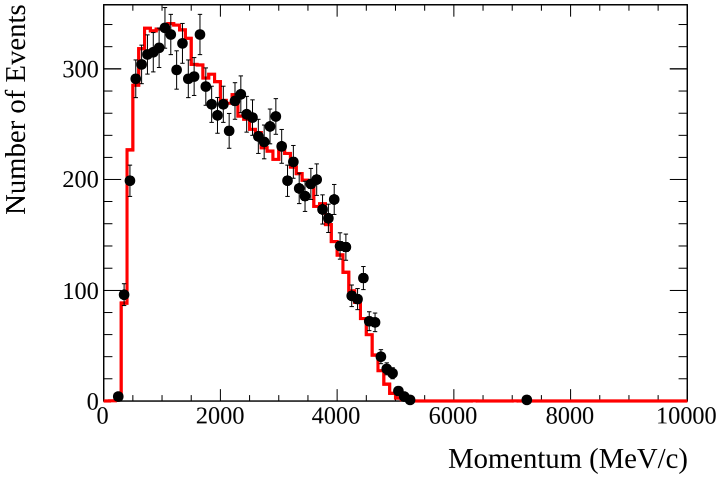

Figure 8.2: Reconstructed muon momentum after cut on total charge.

2. Exactly 1 decay-e with decay time $1.2 < \Delta t < 10$ μs and 1 m away from the wall. The decay time distribution is shown in Figure 8.3 (left) A decay-e tagging efficiency can be calculated and the data/MC difference of $\sim$1% is assigned as a

systematic error. The distance from the nearest wall of the reconstructed vertex is shown in Figure 8.3 (right).

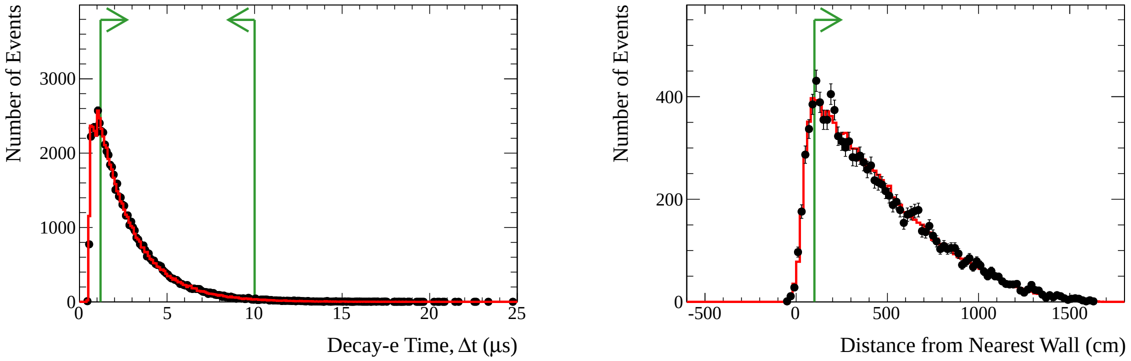

Figure 8.3: Left: The decay-e timing distribution, corresponding to the difference between 1st and 2nd fiTQun reconstructed sub-event times. The fitted lifetime assuming a single exponential is 2.027 μs for data and 2.044 μs for MC. Right: The reconstructed decay-e vertex distance from the nearest wall (with the next selection criteria, cut 3, applied).

3. The muon must be top-entering ($17.5 < z < 18.5$ m and $R < 16$ m) or side-entering ($16 < R < 17.5$ m and $z < 17.5$ m) as shown diagrammatically in Figure 8.1. The reconstructed vertex positions are shown in Figure 8.4. The difference in the means of the z and R distributions is < 5 cm, which is assigned as a systematic error.

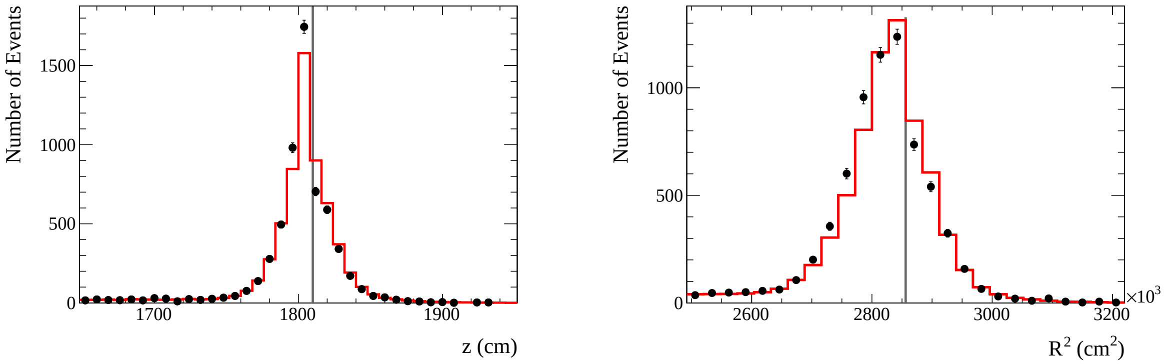

Figure 8.4: Reconstructed muon entering vertex in z (left) and R^2 (right). The vertical grey lines show the expected top-cap wall position ($z = 1810$ cm) and barrel wall position ($R = 1690$ cm).

Following this selection, the decay-e momentum distribution and the muon momentum/range distributions, for ranges between 5 and 10 m are shown in Figure 8.5. The data-MC discrepancies in the means of the distributions are summarized in Figure 8.6 and are within the previously estimated SK energy scale error (2.4%) [212] used in the oscillation analysis. These quantities were found to be stable throughout the entire T2K time period [216].

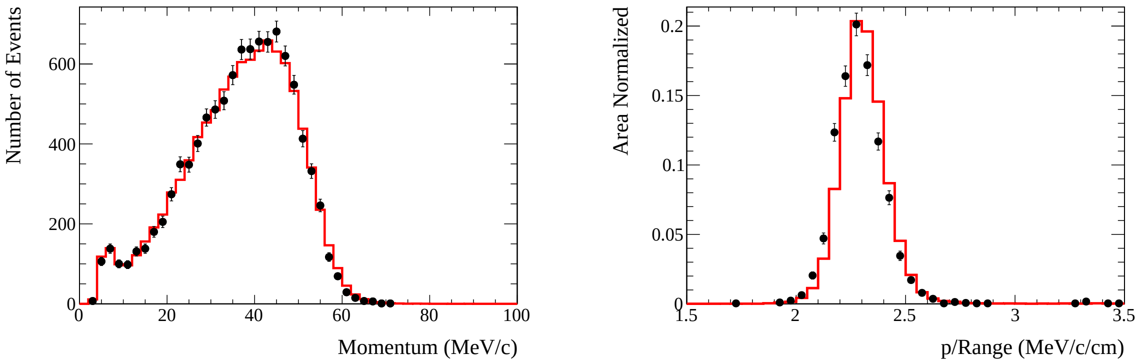

Figure 8.5: Left: Reconstructed decay-e momentum. Right: Muon momentum divided by range for ranges between 5 and 10 m.

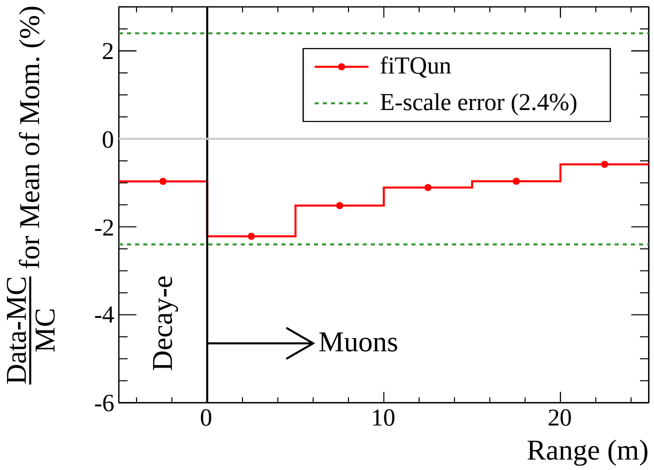

Figure 8.6: Fractional deviation of the data from the MC for the means of the decay-e spectrum in the left panel of Figure 8.5 and the muon momentum/range distributions in, e.g., the right panel of Figure 8.5. The previously estimated SK energy scale error of 2.4% [212] is shown by the dashed lines.

8.3 Atmospheric Neutrino Reconstruction Validation

The Atm-ν sample, with a relatively high number of events, is used to validate fiTQun performance with more complicated event topologies. The Atm-ν flux simulation and event reduction are described elsewhere [210, 217]. The same neutrino interaction simulation (NEUT), detector simulation (SKDETSIM) and event reconstruction are used. A 2-flavour oscillation model is assumed with $\Delta m^2 = 2.5 \times 10^{-3}$ eV^2 and $\sin^2(2\theta) = 1$.

A PID and ring-counting selection using the fiTQun likelihood variables is defined and validated with cosmic muon and Atm-ν data in Appendix B. These variables are then used to define a NC enhanced π^0 sample, described in Appendix B.4. The resulting π^0 mass and momentum is shown in Figure 8.7. The data-MC agreement demonstrates that the fiTQun π^0 fitter is performing well.

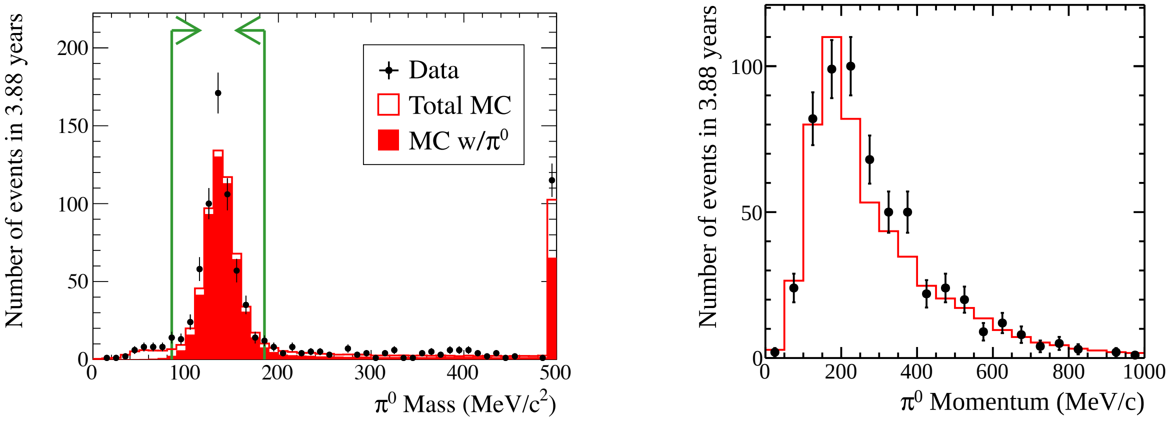

Figure 8.7: Reconstructed π^0 mass (left) and momentum (right) for the fiTQun NC enhanced π^0 selection. The shaded histogram (left) includes events that have at least 1 π^0 after FSI and SI. A π^0 mass cut between 85 and 185 MeV/c^2 (left) is applied for the momentum spectrum distribution (right).

For the ν_e appearance analysis (Section 9.1.2), the selection is based on the previous reconstruction except for the π^0 rejection stage. The T2K fiTQun π^0 rejection cut is defined by a line in $\ln(\mathcal{L}_{\pi^0}/\mathcal{L}_e)$ versus π^0 mass space given by [214][1]

$$\ln(\mathcal{L}_{\pi^0}/\mathcal{L}_e) = -0.875 \times (M_{\pi^0} - 120) + 70. \tag{8.3}$$

This is shown in Figure 8.8 for Atm-ν MC with $p_e < 1.25$ GeV/c, where events below the line are identified as ν_e candidates.

The 2D distribution can be collapsed into 1D as a function of the distance to the cut line as shown in Figure 8.9. A negative (positive) value corresponds to e-like (π^0-like). This cut reduces the NC (π^0) background by $\sim$ 60% compared to the previous reconstruction. The remaining NC component contributes $\sim$20% of the total background with the rest coming from the intrinsic (irreducible) beam ν_e. There is some data-MC disagreement in the efficiency of the cut, which is taken into account in systematic error analysis described in Section 8.4.

8.4 Systematic Errors in Topological Selection

The Atm-ν data provide useful control samples for T2K events since it covers the T2K neutrino energy range as shown in Figure 5.4 and the same detector response is expected. Control samples are defined to match the *signal* channels in T2K, namely where there is a charged lepton and no other particles in the final state (FS). Systematic errors in the efficiency of the T2K topological selection (Section 9.1.2), including RC, PID and π^0 rejection, are estimated based on the Atm-ν data-MC discrepancies extracted from a MCMC analysis. The same Atm-ν sample as in Section 8.3 is used, except updated to 4.47 years of data.

---

[1] The cut line was tuned to achieve the same signal efficiency as the previous reconstruction.

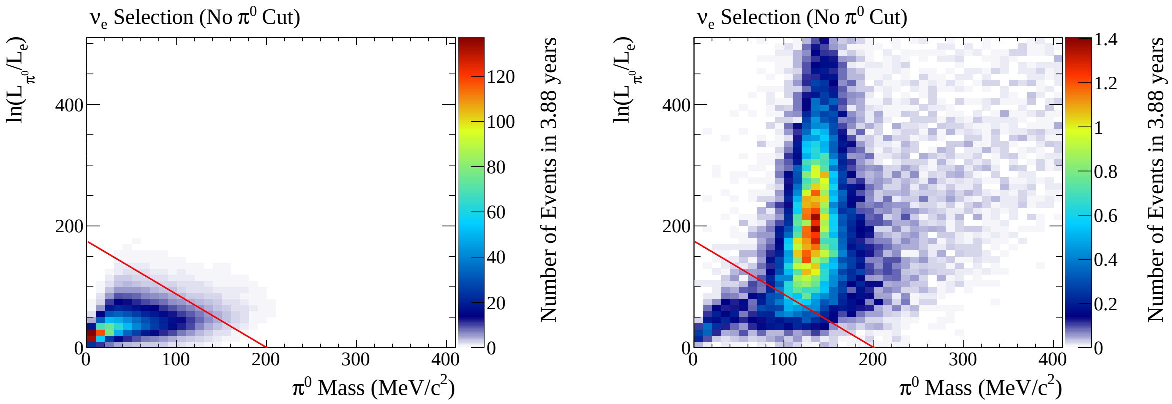

Figure 8.8: For the Atm-ν MC sample with $p_e < 1.25$ GeV/c, $\ln(\mathcal{L}_{\pi^0}/\mathcal{L}_e)$ versus π^0 mass for the ν_e candidate selection prior to the π^0 rejection cut. The left panel are events with no true π^0 after FSI and SI, while the events in the right panel have at least 1 π^0. The T2K fiTQun π^0 rejection cut line (Equation 8.3) is shown.

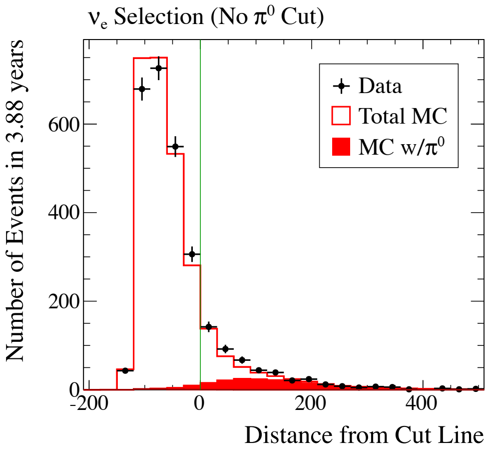

Figure 8.9: Distance from the fiTQun π^0 rejection cut line for the Atm-ν MC sample with $p_e < 1.25$ GeV/c and the ν_e candidate selection prior to the π^0 cut. The shaded histogram includes events that have at least 1 π^0 after FSI and SI.

8.4.1 Control Sample Definition

The MC is separated into final state (FS) topologies based on the lepton flavour and final observable particles of the event after FSI and SI. The topologies are defined in Table 8.1.

l	MC Topology	Selection Criteria
0	ν_e CC1e	ν_e CC and $N_{\pi^0} = 0$ and $N_{\pi^\pm} = 0$ and $N_P = 0$
1	ν_e CC-Other	ν_e CC and not ν_e CC1e
2	ν_μ CC1μ	ν_μ CC and $N_{\pi^0} = 0$ and $N_{\pi^\pm} = 0$ and $N_P = 0$
3	ν_μ CC-Other	ν_μ CC and not ν_μ CC1μ
4	NCπ^0	NC and $N_{\pi^0} \geqslant 1$ and not NCγ
5	NC-Other	NC and not NCπ^0

Table 8.1: MC topologies or event types shown in the figures of this section, where N_X refers to the true number of X particles above Cherenkov threshold that exit the target nucleus after FSI and SI. The topologies are index by l.

Each control sample is designed to achieve a relatively high purity for a given MC topology, referred to as an *enriched* sample. A careful distinction must be made between, for example, a *CCQE-enriched* sample, which contains events from many neutrino interaction processes, and the *true CCQE* process. The selection criteria are shown in Table 8.3, including a topological selection based on the *cut parameters* L_m summarized in Table 8.2 (described in Appendix C.1). The RC and PID parameters are based on the previous reconstruction, *APfit*, while the π^0 parameter is based on fiTQun (Equation 8.3). The cut parameter distributions are shown for various sub-samples in Figures 8.10 and 8.11.

The ν_e (i) and ν_μ (iii) CCQE-enriched samples (Table 8.3) are used to determine the error in the efficiency for selecting the CC (signal-like) topologies in the T2K sample.

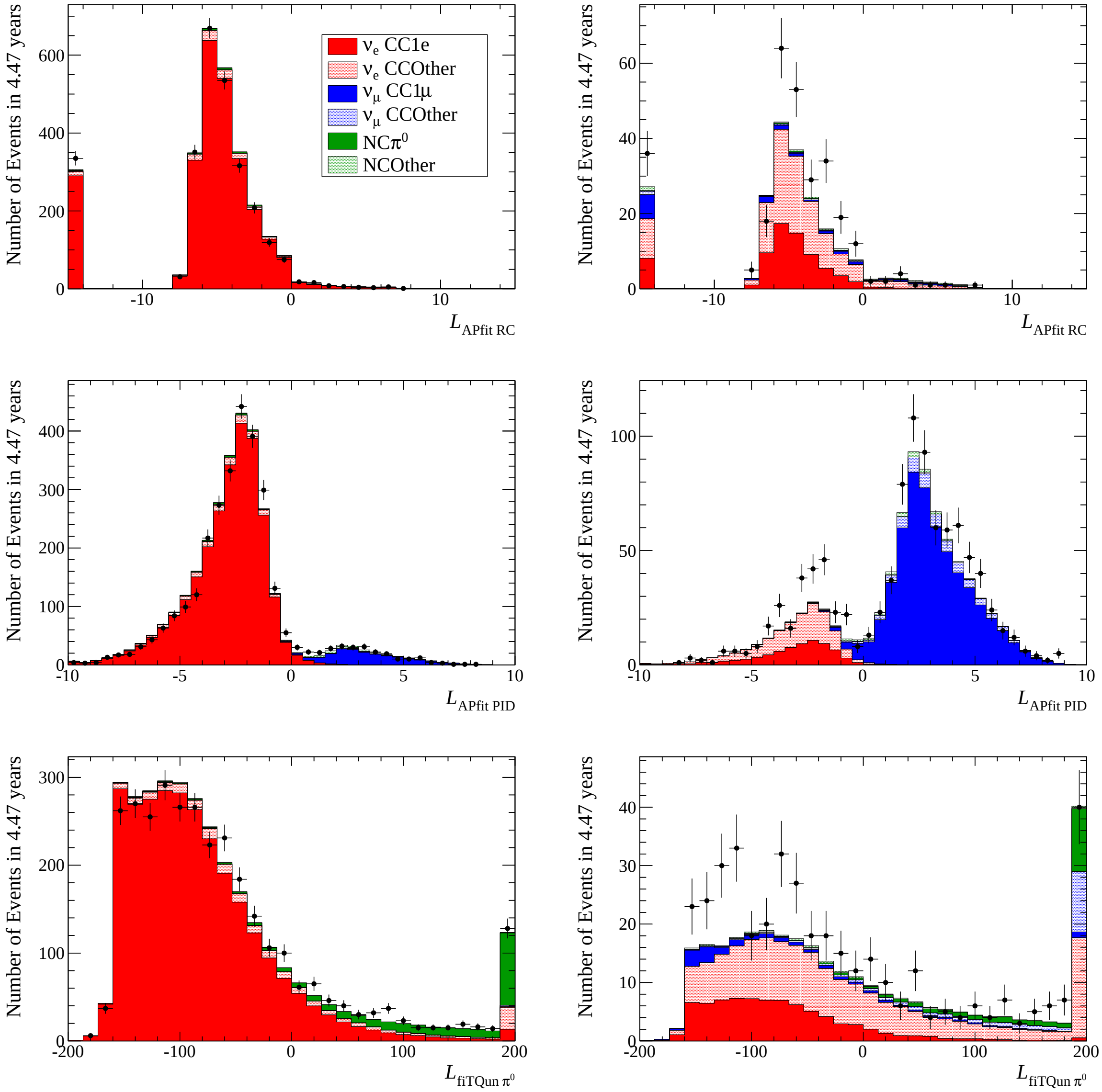

Figure 8.10: Cut parameter distributions for the ν_e CCQE (left) and CCnQE (right), $100 < E_{vis} < 1250$ MeV, samples. All cuts are applied except that which corresponds to the parameter that is drawn. The cut line is at 0, with the classifications defined in Table 8.2.

m	Topological Cut	Cut Parameter	< 0	$\geqslant 0$
0	Ring-counting (RC)	$L_{\text{APfit RC}}$	1-ring (1R)	multi-ring (mR)
1	Particle identification (PID)	$L_{\text{APfit PID}}$	e-like	μ-like
2	π^0 rejection	$L_{\text{fiTQun } \pi^0}$	e-like	π^0-like

Table 8.2: Topological cuts used to evaluate systematic errors from the Atm-ν data. The cut parameters are defined in Appendix C.1; which are then used to define the control samples in Table 8.3. The event classification is shown for values of the parameter above and below 0. The parameters are index by m.

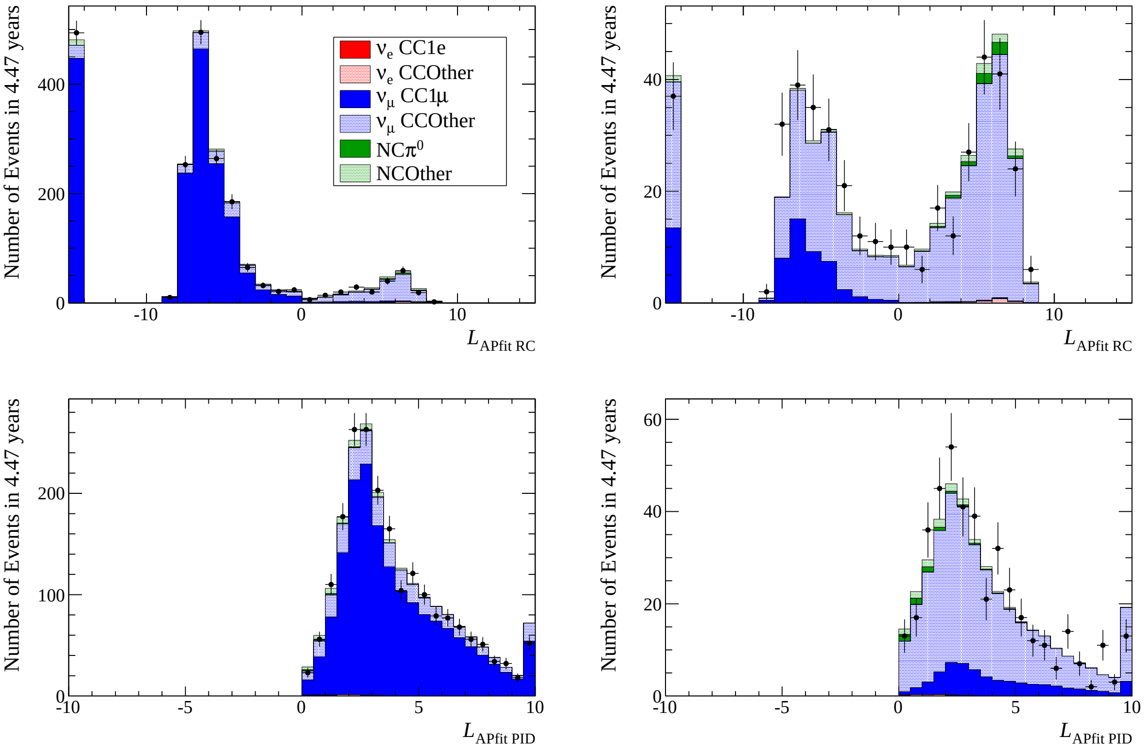

Figure 8.11: Cut parameter distributions for the ν_μ CCQE-enriched (left) and CCnQE-enriched (right), $E_{vis} < 5$ GeV, samples. All cuts are applied except that which corresponds to the parameter that is drawn. The cut line is at 0, with the classifications defined in Table 8.2.

Table 8.3: Control sample definitions for the Atm-ν fit. The parent sample is defined to be fully contained and in the fiducial volume (FCFV): distance from the ID wall $D_{wall} > 200$ cm, visible energy $E_{vis} > 30$ MeV and number of hits in an OD cluster $N_{HitAC} < 16$. The topological selection is based on the parameters summarized in Table 8.2. The distance from the expected muon stopping point to the nearest decay-e, D_{dcy-e}, is used to select high purity ν_μ CCQE-enriched and CCnQE-enriched samples. The control samples are indexed by j.

Type of control sample in FCFV		Branch of control sample			
		j-th sample (0 - 12)	Topological Selection		
			RC cut	PID cut	π^0 cut / Dcy-e Dist. cut
(i) ν_e CCQE-enriched	$N_{dcy-e} = 0$ & $E_{vis} > 100$	0: Core	1R	& e-like	& $L_{\text{fiTQun}\ \pi^0} < 0$
		1: RC tail	**mR**	& e-like	& $L_{\text{fiTQun}\ \pi^0} < 0$
		2: PID tail	1R	& **μ-like**	& $L_{\text{fiTQun}\ \pi^0} < 0$
		3: π^0 tail	1R	& e-like	& $L_{\text{fiTQun}\ \pi^0} \geqslant 0$
(ii) ν_e CCnQE-enriched	$N_{dcy-e} \geqslant 1$ & $E_{vis} > 100$	4: Core	1R	& e-like	& $L_{\text{fiTQun}\ \pi^0} < 0$
		5: RC tail	**mR**	& e-like	& $L_{\text{fiTQun}\ \pi^0} < 0$
		6: PID tail	1R	& **μ-like**	& $L_{\text{fiTQun}\ \pi^0} < 0$
		7: π^0 tail	1R	& e-like	& $L_{\text{fiTQun}\ \pi^0} \geqslant 0$
(iii) ν_μ CCQE-enriched	$N_{dcy-e} = 1$	8: Core	1R	& μ-like	& $D_{dcy-e} < 80$ cm
		9: RC tail	**mR**	& μ-like	& $D_{dcy-e} < 80$ cm
(iv) ν_μ CCnQE-enriched	$N_{dcy-e} \geqslant 2$	10: Core	1R	& μ-like	& $D_{dcy-e} < 160$ cm
		11: RC tail	**mR**	& e-like	& $D_{dcy-e} < 160$ cm
(v) BG-enriched	$N_{dcy-e} = 0$	12: NC π^0	mR	& e-like	& $L_{\text{fiTQun}\ \pi^0} \geqslant 0$ & $m_{\text{POLfit}\ \pi^0} < 170$ MeV/c^2

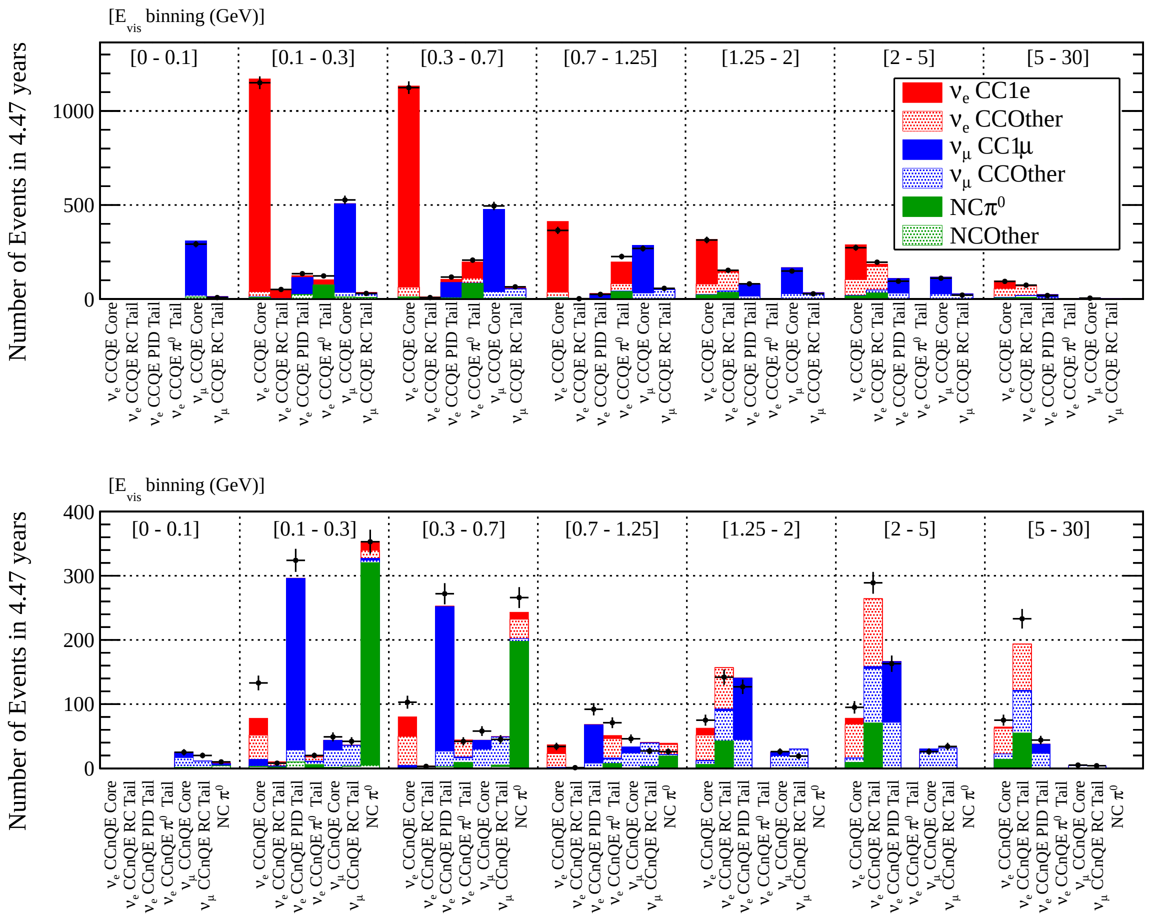

Figure 8.12: Number of events in each control sample defined in Table 8.3 for default MC. The top panel displays CCQE-enriched samples while the bottom panel displays CCnQE-enriched and BG-enriched samples. Note, the actual binning used in the likelihood definition (Equation 7.2) is given in Table 8.4.

The ν_e (ii) and ν_μ (iv) CCnQE-enriched sample are defined to constrain the error on the ν_e and ν_μ CC-Other topologies, respectively. The BG-enriched sample (v) is NC π^0 enhanced to constrain the NC component. Each CC sample consists of a *core* sample that passes all the selection cuts and *tail* samples that fail a given topological cut, which then constrain the efficiency for each cut.

The samples are binned in E_{vis} according to Table 8.4 for the likelihood definition (Equation 7.5). The event rates for each control sample are shown in Figure 8.12 (with a finer binning in some cases).

Table 8.4: Kinematic binning for each control sample defined in Table 8.3. The kinematic bins are indexed by i. The β parameters introduced in Section 8.4.2 are binned similarly, where instead "CCQE-enriched" ("CCnQE-enriched") corresponds to the MC topology "CC1-lepton" ("CC-Other"), and the tail samples correspond to each cut parameter.

Type of control sample	j-th sample (0 - 12)	Index i	E_{vis} Bins [GeV]
(i) ν_e CCQE-enriched	0: Core	0 - 5	[0.1, 0.3, 0.7, 1.25, 2, 5, 30]
	1: RC tail	0 - 5	[0.1, 0.3, 0.7, 1.25, 2, 5, 30]
	2: PID tail	0 - 5	[0.1, 0.3, 0.7, 1.25, 2, 5, 30]
	3: π^0 tail	0 - 2	[0.1, 0.3, 0.7, 1.25]
(ii) ν_e CCnQE-enriched	4: Core	0 - 2	[0.1, 1.25, 5, 30]
	5: RC tail	0 - 2	[0.1, 1.25, 5, 30]
	6: PID tail	0 - 5	[0.1, 0.3, 0.7, 1.25, 2, 5, 30]
	7: π^0 tail	0	[0.1, 1.25]
(iii) ν_μ CCQE-enriched	8: Core	0 - 6	[0, 0.1, 0.3, 0.7, 1.25, 2, 5, 30]
	9: RC tail	0 - 6	[0, 0.1, 0.3, 0.7, 1.25, 2, 5, 30]
(iv) ν_μ CCnQE-enriched	10: Core	0 - 2	[0, 1.25, 5, 30]
	11: RC tail	0 - 2	[0, 1.25, 5, 30]
(v) BG-enriched	12: NC π^0	0	[0, 1.25]

8.4.2 Detector Error Parameterization

Systematic errors in the topological selection arising from fundamental (microscopic) sources are effectively parameterized as variations β for each cut parameter m:

$$L'_m = L_m + \beta_{i,l,m}. \tag{8.4}$$

The applicable kinematic bin i is given in Table 8.4 for CC MC topology l. Each β is physically bounded, given by the prior

$$\pi(\beta_{i,l,m}) = \begin{cases} 1 & [0 \leqslant \epsilon(\beta_{i,l,m}) \leqslant 1] \\ 0 & [\text{otherwise}] \end{cases}, \tag{8.5}$$

where ϵ is the selection efficiency as a function of β. This prior is used in Equation 7.5.

8.4.3 Atm-ν Flux and Cross Section Parameterization

The uncertainties in the Atm-ν flux $\mathbf{a}$ and cross sections $\mathbf{x_{atm}}$ are parameterized as in Table 8.5 and Figure 8.13, where $\alpha = (\mathbf{a}, \mathbf{x_{atm}})$. The prior uncertainties correspond to the width of each Gaussian in Equation 7.3 for the parameters in Equation 7.5.

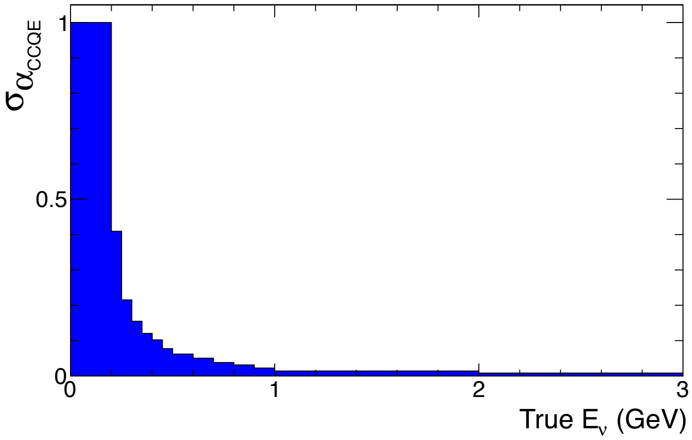

Figure 8.13: Energy dependence of the CCQE cross section error (α_{CCQE} in Table 8.5) as a function of true E_ν.

k	Event Class	Nuisance parameter (α_k)	Error type	Prior Uncertainty (σ_{α_k})
0	$E_{\nu,true} < 1$ GeV	α_{NormLowE}	Flux	0.25
1	$E_{\nu,true} \geqslant 1$ GeV	$\alpha_{\text{NormHighE}}$	Flux	0.15
2	True CCQE	α_{CCQE}	Cross section	Figure 8.13
3	True CCnQE	α_{CCnQE}	Cross section	0.20
4	True CC ν_μ	α_{ν_μ/ν_e}	$\sigma_{\nu_\mu}/\sigma_{\nu_e}$ ratio	0.05
5	True NC	α_{NC}	Cross section	0.20

Table 8.5: Atm-ν flux and cross section normalization parameters. The prior uncertainty assumes a Gaussian of width σ_{α_k}, except for the CCQE parameter $\sigma_{\alpha_{CCQE}}$, which varies as a function of energy as shown in Figure 8.13.

8.4.4 Event Rate Prediction

The remaining factor to define in Equation 7.5 is the conditional probability P, which takes the form of Equation 7.2. Table 8.6 summarizes the indices introduced in this section.

Index	Description	Reference
i	Kinematic Bin	Table 8.4
j	Control Sample	Table 8.3
k	MC Event Class for α Parameters	Table 8.5
l	MC FS Topology	Table 8.1
m	Topological Cut	Table 8.2 and Section 8.4.2

Table 8.6: Description of the indices used in this section.

The total predicted event rate is

$$\hat{N}_{i,j} = \sum_{l=0}^{5} \hat{N}_{i,j}^{l}, \tag{8.6}$$

where

$$\hat{N}_{i,j}^{l} = \sum_{h=0}^{\text{all events}} \left[D_h(i,j,l) \prod_{k=0}^{5} [1 + \alpha_k \delta_h(k)] \right]. \tag{8.7}$$

$D_h(i,j,l)$ is non-zero if event h is of MC topology l, passes the selection for control sample j with modified cut parameters $L'_m(\beta_{i,l,m})$ and is in kinematic bin i. Otherwise, $D_h(i,j,l)$ is 0. Similarly, $\delta_h(k) = 1$ if event h is of event class k, otherwise $\delta_h(k) = 0$.

8.4.5 Results

A MCMC (Section 7.2) sample is generated according to the likelihood in Equation 7.5, which at this point is fully defined. Inferences about various parameters can be made from this chain. For example, a *best-fit* $\bar{N}_{i,j}^{l}$ for the observable number of events can be inferred by replacing θ in the marginal likelihood (Equation 7.6) with $\hat{N}_{i,j}^{l}$, then evaluating the mean such that

$$\bar{N}_{i,j}^{l} = \langle \mathcal{L}_M(\hat{N}_{i,j}^{l} | \mathbf{M}_{Atm-SK}) \rangle, \tag{8.8}$$

marginalizing over all α and β. The result is shown in Figure 8.14.

The systematic error propagated to T2K is parameterized as the difference between the total efficiency before and after the fit. The total efficiency ε for selecting ν_e CC1e and ν_e CC-Other (ν_μ CC1μ and ν_μ CC-Other) events in the ν_e (ν_μ) CCQE-enriched core sample is defined as:

$$\varepsilon_{i,j}^{l} = \frac{\hat{N}_{i,j=\{0,8\}}^{l}}{\sum_{j=\{0,8\}}^{\{3,9\}} \hat{N}_{i,j}^{l}}, \tag{8.9}$$

where the numerator is the core sample and the denominator is the total number of events prior to the topological cuts. Then, similar to Equation 8.8, the mode (most probable value) is defined as

$$\bar{\varepsilon}_{i,j}^{l} = Mo\left(\mathcal{L}_M(\varepsilon_{i,j}^{l} | \mathbf{M}_{Atm-SK}) \right). \tag{8.10}$$

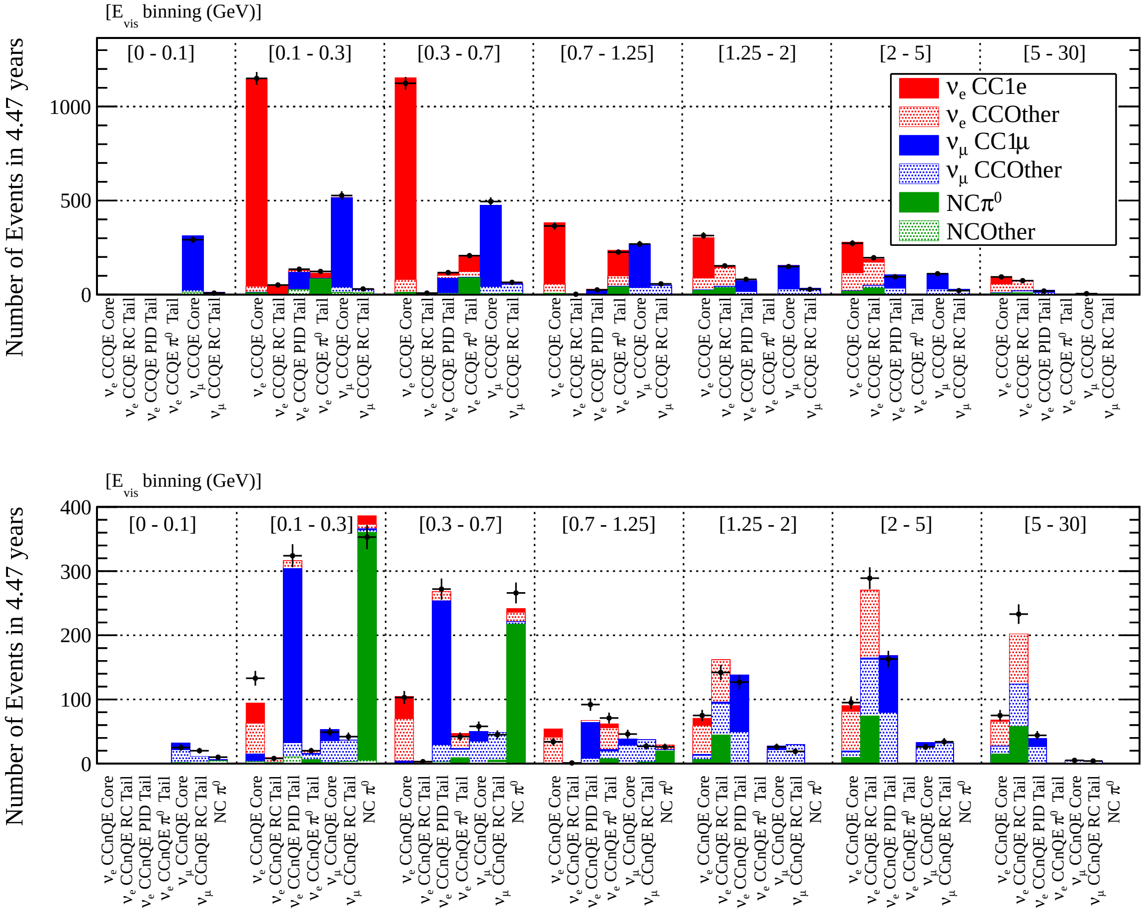

Figure 8.14: Posterior means of the predicted number of events, as defined in Equation 8.8. The top panel displays CCQE-enriched samples while the bottom panel displays CCnQE-enriched and BG-enriched samples.

The fractional differences from the default MC efficiency,

$$\Delta\bar{\varepsilon}^{l}_{i,j}/\varepsilon = \frac{\bar{\varepsilon}^{l}_{i,j} - \varepsilon_{\text{def}}}{\varepsilon_{\text{def}}}, \tag{8.11}$$

referred to as the *shift error*, are shown as the points in Figure 8.15. The RMS of the marginal likelihoods, referred to as the *fit errors*, are shown as the error bars. The data-MC discrepancy discovered in ssec:atmnu is reflected in the ν_e CC1e 0.7–1.25 GeV bin.

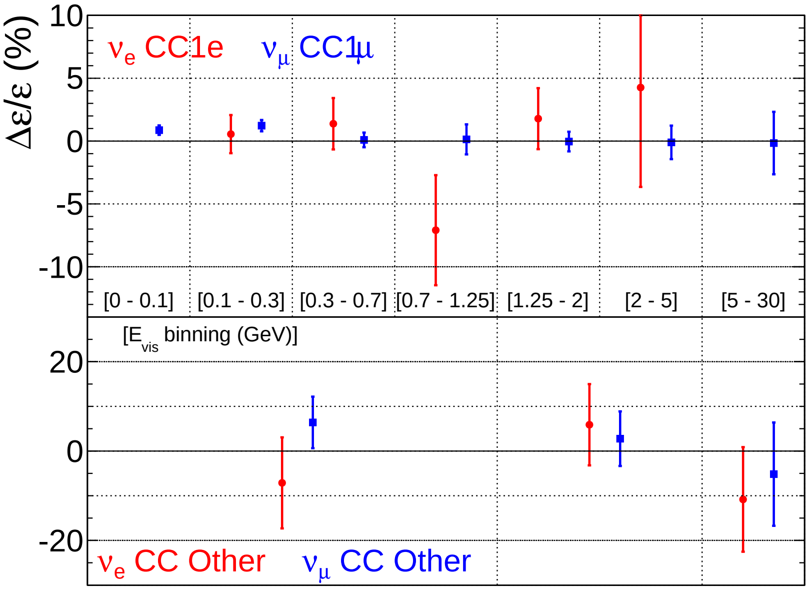

Figure 8.15: The inferred data-MC discrepancy (points) as defined in Equation 8.11 and RMS of the marginal likelihood for each $\Delta\varepsilon/\varepsilon$ (error bars).

The shift errors are assumed to be fully correlated when propagating to the T2K oscillation analysis. The fit errors are correlated according to the covariance of the 2D marginal likelihood distributions (Equation 7.6) for each pair of parameters, as shown in Figure 8.16 (described in Appendix Section C.1.2).

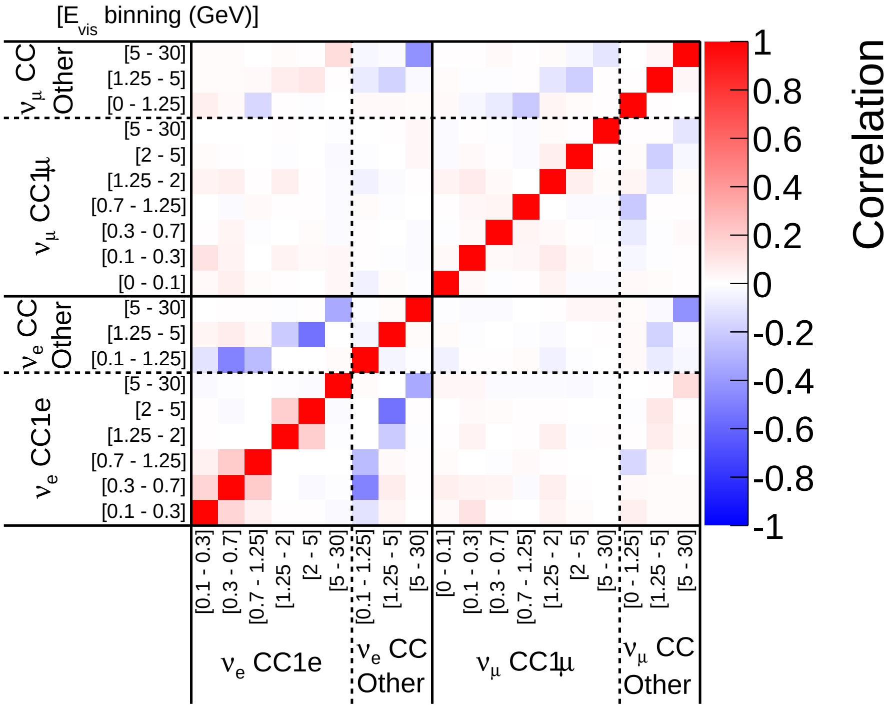

Figure 8.16: Fit error correlations as estimated from the covariance of the 2D marginal likelihood distributions.

8.5 Summary of Systematic Errors

Sections 8.2 and 8.3 discuss some of the systematic errors derived from the cosmic ray muon and Atm-ν samples. Additional constraints on the background topologies of the T2K ν_e and ν_μ samples come from specialized Atm-ν NC $\pi^{\pm}$ [218] and *hybrid*-π^0 [219][2] samples. The systematic error sources are summarized in Tables 8.7–8.9.

Error source	Systematic Uncertainty	Reference
Reduction, OD cut	1.0%	Internal Note [220]
Vertex	1.0%	Section 8.2
Decay electron cut	~1.0%	Section 8.2

Table 8.7: Systematic uncertainties on the T2K ν_e and ν_μ event rate from fully correlated sources.

Event Topology	Systematic Error Constraint	Reference
ν_e CC1e	atm-ν fit	Section 8.4
ν_e CC-Other	atm-ν fit	Section 8.4
ν_μ CC	126%	Internal note [221]
ν_μ CCπ^0-Other	hybrid-π^0	Internal note [219]
NC1π^0	hybrid-π^0	Internal note [219]
NCπ^0-Other	hybrid-π^0	Internal note [219]
NCγ	ν_e CC1e + 1%	Internal note [221]
NC1$\pi^{\pm}$	173%	Internal note [221]
NC-Other	173%	Internal note [221]

Table 8.8: Prior constraints assigned to each MC topology for the systematic error due to the topological (RC, PID, π^0) cuts in the ν_e selection.

---

[2] A hybrid-π^0 is constructed from a real data ring combined with a MC ring according to the π^0 decay kinematics.

	Systematic Error Constraint	
Event type	Ring-counting	Particle ID
ν_μ CC1μ	atm-ν fit (Section 8.4)	0.3% (Appendix B.1)
ν_μ CC other	atm-ν fit (Section 8.4)	0.3% (Appendix B.1)
ν_e CC	100% (Internal note [218])	
NC	21.8%	55% (Internal note [218])

Table 8.9: Prior constraints assigned to each MC topology for the systematic error due to topological cuts in the ν_μ selection. The references are given in () brackets.

Figure 8.17 shows the reconstructed neutrino energy spectrum and the 1σ systematic error envelopes for both the ν_e appearance and ν_μ disappearance event samples. Figure 8.18 shows the corresponding correlation matrix and the square root of the diagonal elements of the covariance matrix separated by the true MC interaction and kinematic binning defined in the oscillation analysis. This defines the matrix V in Equation 7.3 for $\pi(\mathbf{d_{SK}})$ in Equation 7.1.

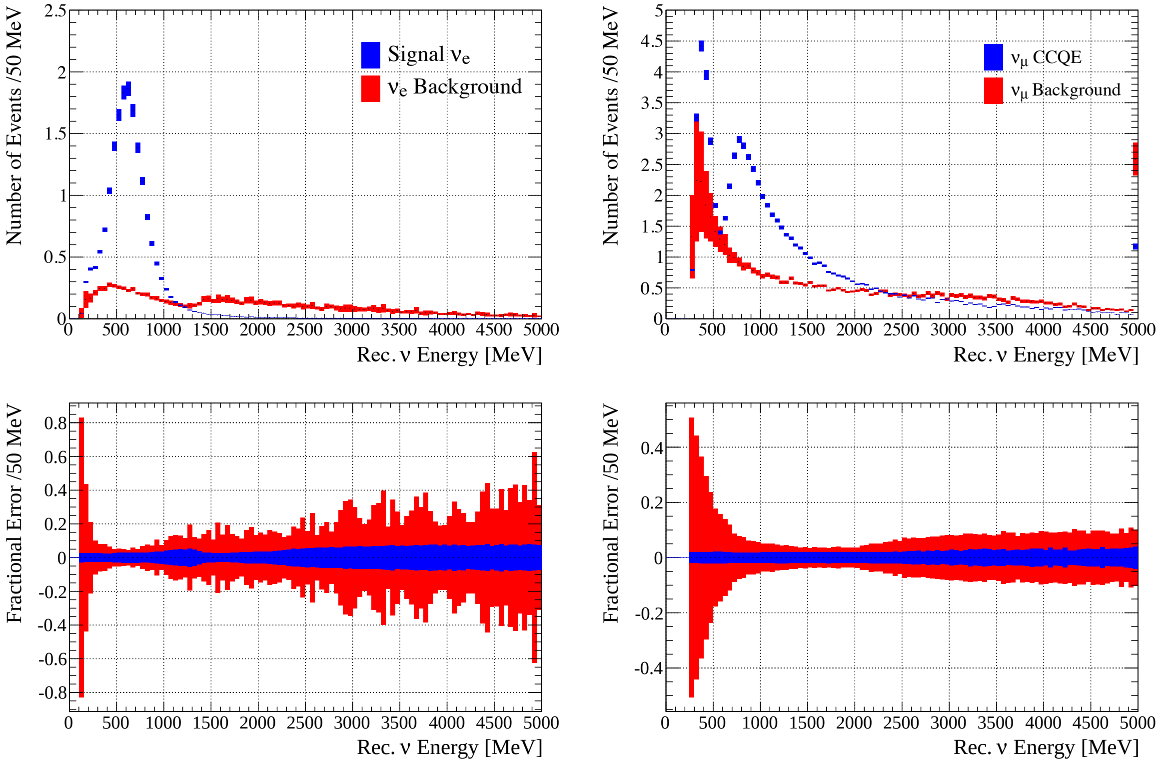

Figure 8.17: Reconstructed energy spectra (top) and 1σ systematic uncertainty envelope (bottom) for the T2K ν_e (left) and ν_μ (right) sample event rate predictions.

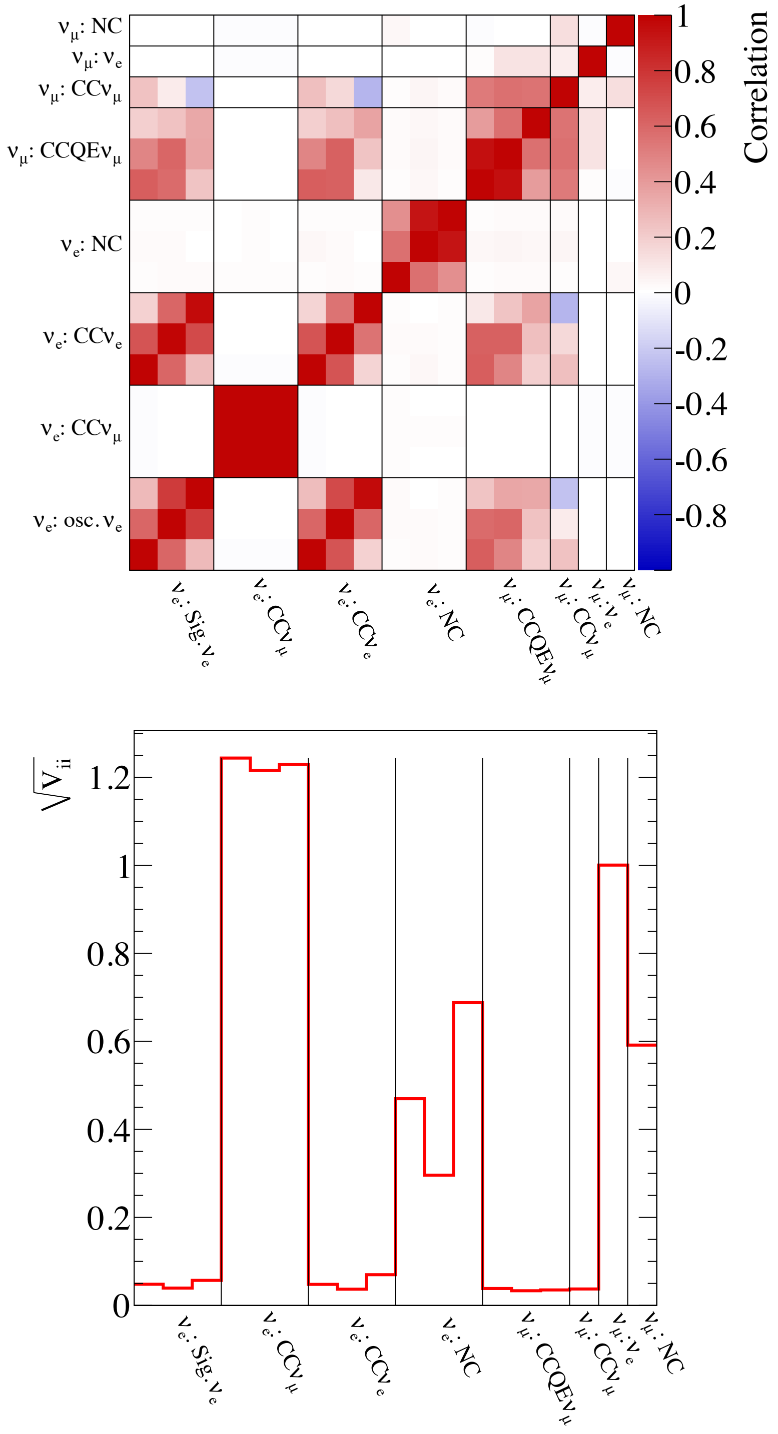

Figure 8.18: Correlation matrix (left) and the square root of the diagonal elements of the covariance matrix (right). The binning in E_{rec} for each component of the ν_e sample is 0-350-800-1250 MeV (3 bins) and for the CCQE ν_μ component in the ν_μ sample is 0-400-1100-30000 MeV (3 bins).

Chapter 9

Joint Analysis of ν_μ Disappearance and ν_e Appearance

Independent fits of the T2K ν_μ disappearance sample and ν_e appearance sample [56] have yielded world-leading results with a precision measurement of θ_{23} [96] and the discovery of ν_e appearance from a ν_μ beam [56]. With the precise determination of θ_{13} (Section 2.2.3), the next step is a joint, 3-flavour oscillation fit of ν_μ disappearance and ν_e appearance in order to precisely account for the correlations in the parameters shown in Equation 2.42. This chapter summarizes the results of a new joint fit based on a previous MCMC analysis [222, 223], described in more detail in [224].

ND280 and SK are considered simultaneously in this analysis. The selection criteria for each detector are summarized in Section 9.1. The systematic errors, mostly the same as in the independent fits, are summarized in Section 9.2. The joint estimation of the SK detector errors, described in Section 8.4, is one of the necessary changes for the joint fit. The best-fit, credible regions and model comparisons of the oscillation parameters, based on a MCMC analysis, are reported in Section 9.3.

9.1 Sample Definitions

The ND280 and SK samples, M in Equation 7.1, are defined in this section. The SK criteria, described in Section 9.1.2, are designed to select one lepton and no other particles in the final state in order to reconstruct the neutrino energy based on a CCQE interaction assumption. Correspondingly, the ND280 samples, described in Section 9.1.1, are designed to constrain the relevant cross section parameters for predicting the SK signal and backgrounds. This analysis uses the T2K Run1-4 data set corresponding to 5.9×10^{20} and 6.57×10^{20} POT for ND280 and SK, respectively.

The MC predictions are shown with the flux, cross section and FSI tuning with external data as described in Sections 5.1 and 5.2 and Chapter 6, referred to as the *prefit MC*.

9.1.1 ND280 Tracker ν_μ Samples

A ν_μ CC inclusive sample is defined as follows [173]:

1. Good data quality: The full spill global ND280 data quality flag must be good to ensure detector stability.
2. Bunching: Tracks must be in the same beam bunch of a spill, with each bunch considered a separate event.
3. Fiducial volume (FV): There must be at least one negative track beginning in the FV of FGD1 and entering a TPC.
4. TPC track quality: The track must have more than 18 vertical clusters in the TPC.
5. Backward-going tracks and TPC1 veto: The event is rejected based on TPC1 activity.
6. No broken tracks in FGD1: If a track exists in the FGD only and starts outside the FV, the event is rejected if the highest momentum negative track (HMNT) starts

more than 425 mm away from the FGD1 upstream edge.

7. Muon PID: The HMNT must be μ-like according to the TPC PID.

The CC inclusive sample is further divided into three sub-samples as follows:

- CC0π sample: No events with a $\pi^\pm$ or $e^\pm$ reconstructed in the TPC, nor any decay-e or $\pi^\pm$ reconstructed in the FGDs.
- CC1π sample: One π^+ or one decay-e reconstructed in the TPCs and FGDs, with no π^- nor $e^\pm$ in the TPCs.
- CC Other sample: The rest of the CC inclusive events that are not in the CC0π or CC1π samples.

Each sub-sample is binned in (p_μ, $\cos\theta$), where θ is relative to the neutrino beam direction, as shown in Figure 9.1 for the data. Figures 9.2 and 9.3 show the projections onto p_μ and $\cos\theta$, respectively, for data and prefit MC. Table 9.1 shows the integrated number of events in the 0–30 GeV/c momentum region for each sample.

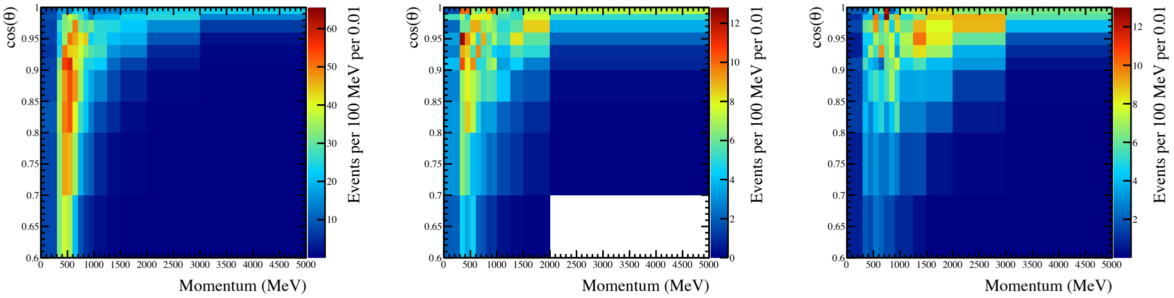

Figure 9.1: The ND280 CC0π (left), CC1π (middle) and CC Other (right) event rates for data.

An independent measurement of the intrinsic ν_e component of the beam is also performed by ND280, which validates the corresponding flux prediction and systematic error [225].

9.1.2 SK ν_e and ν_μ Candidate Samples

A fully contained fiducial volume (FCFV) 1-ring sample is defined as follows [212]:

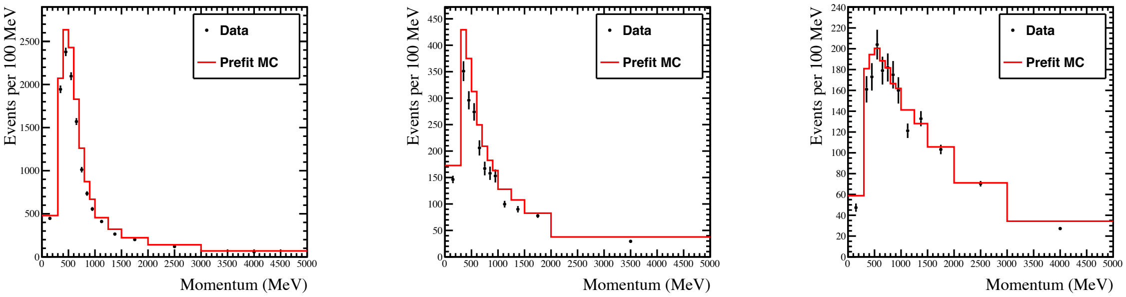

Figure 9.2: The ND280 CC0π (left), CC1π (middle) and CC Other (right) event rates projected onto p_μ for data and prefit MC.

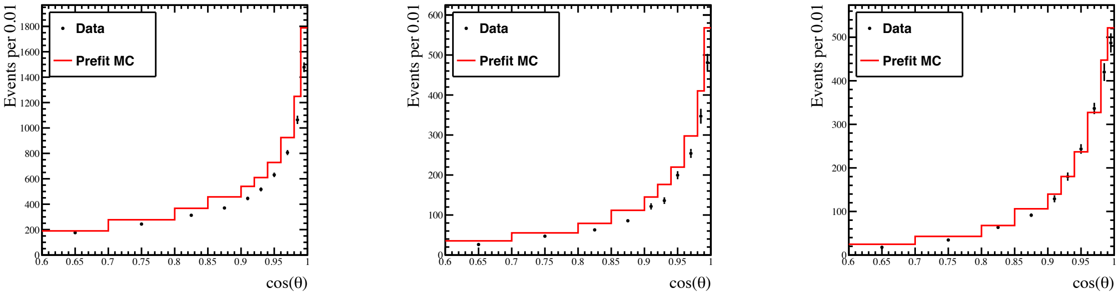

Figure 9.3: The ND280 CC0π (left), CC1π (middle) and CC Other (right) event rates projected onto $\cos\theta$ for data and prefit MC.

	CC0π	CC1π	CC Other	CC Inclusive
Data	17369	4047	4173	25589
MC	19980	5037.2	4729.1	29746.3

Table 9.1: The integrated number of events in the ND280 CC inclusive and three sub-samples for data and prefit MC.

1. Good data quality: The SK and beam quality flag must be good, including a check of the GPS timing for spill synchronization.
2. Fully-contained (FC): The visible energy $E_{vis} > 30$ MeV and less than 16 hits in any OD cluster.
3. Fiducial volume: The distance between the reconstructed vertex and the ID wall must be greater than 2 m, corresponding to 22.5 kton of fiducial mass.
4. 1-ring: Only one reconstructed ring.

The FCFV 1-ring sample is further divided into two sub-samples as follows:

- ν_e candidates
    1. e-like: The ring is reconstructed as electron-like.
    2. Minimum visible energy: $E_{vis} > 100$ MeV.
    3. decay-e cut: There must no decay-e.
    4. Reconstructed neutrino energy: $E_{rec} < 1.25$ GeV.
    5. fiTQun π^0 rejection: The event must not be π^0-like as defined by Equation 8.3.
- ν_μ candidates
    1. μ-like: The ring is reconstructed as muon-like.
    2. Minimum momentum: $p_\mu > 200$ MeV/c.
    3. decay-e cut: There must be 0 or 1 decay-e.

Each sub-sample is binned in E_{rec} as shown in Figure 9.4 for data and prefit MC without oscillation and with oscillation assuming the parameters given in Table 9.2.

9.2 Systematic Errors

Most of the systematic errors have been described earlier. They are represented by $\pi(\mathbf{f})$ in Equation 7.1 and summarized in Table 9.3, including references to the relevant sections.

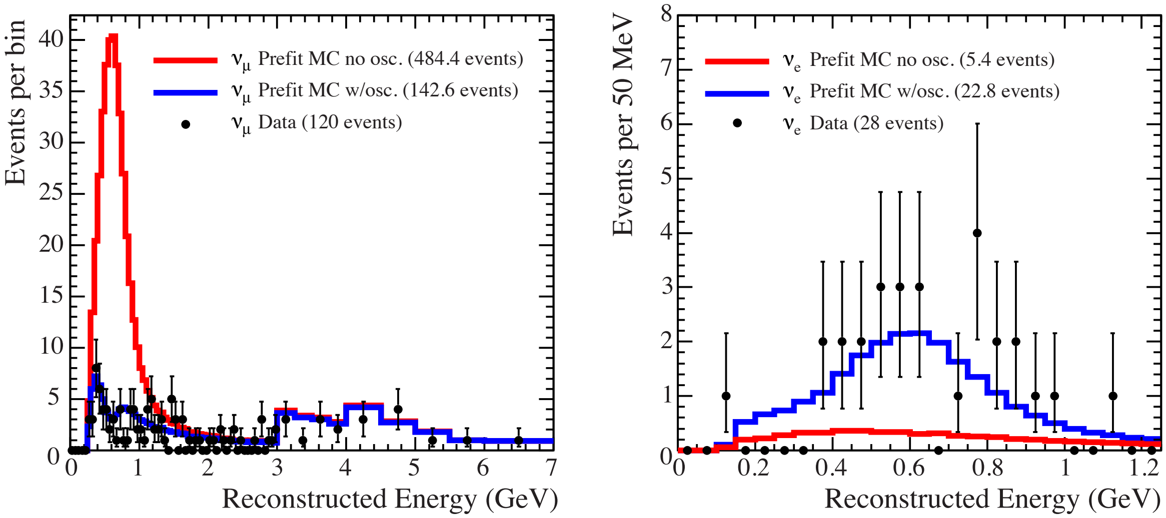

Figure 9.4: The SK ν_μ (left) and ν_e (right) candidate samples for data and prefit MC. The MC is shown without oscillation (red) and with oscillation (blue) assuming the MCMC input parameters in Table 9.2. The total integrated numbers of events are shown in () brackets.

Parameter	Default Value	MCMC Input
Δm^2_{21} $[10^{-5}\ \mathrm{eV}^2]$	7.6	7.5 ± 0.2
Δm^2_{32} $[10^{-3}\ \mathrm{eV}^2]$	2.4	
$\sin^2\theta_{12}$	0.306	0.311 ± 0.017
$\sin^2\theta_{23}$	0.5	
$\sin^2 2\theta_{13}$	0.1	0.095 ± 0.01
δ_{CP}	0	
Mass hierarchy	Normal	
Baseline length	295 km	
Earth matter density	2.6 g/cm^3 [226]	

Table 9.2: Neutrino oscillation parameters used in default MC expectation calculations. The MCMC input values and constraints (Gaussian prior) are from [227]. The PDG (average reactor) constraint on θ_{13} is applied to the *reactor constrained analysis* only. A flat prior or no constraint is used for θ_{13} (T2K-only analysis), θ_{23}, Δm^2_{32} and δ_{CP}. The mass hierarchy parameter assumes a discrete prior with a probability of 0.5 for NH or IH (in practice in the MCMC, this is encoded in the sign of Δm^2_{32}).

Parameter Set	Description	Reference
$\mathbf{o}$	Oscillation	Section 2.2.5, Table 9.2
$\mathbf{b}$	Beam flux	Section 5.1
$\mathbf{x}$	Interactions	Sections 5.2.5 and 6.3
$\mathbf{d_{ND}}$	ND280 detector	Internal note [173]
$\mathbf{d_{SK}}$	SK detector	Section 8.5

Table 9.3: Description of the parameters in Equation 7.1 with references to the details about each prior constraint.

The ND280 detector systematic errors are delivered in the form of a covariance matrix relating all three sub-samples [173], which defines $\mathbf{d_{ND}}$.

A summary of the effect of the systematic errors on the SK sub-samples is shown in Table 9.4 for the integrated event rate and Figure 9.5 as a function of reconstructed neutrino energy. An independent fit of the ND280 samples [228] was performed and the resulting constraint was used to evaluate the *ND280 constrained* values. In the MCMC analysis a similar constraint is incorporated implicitly in the likelihood function.

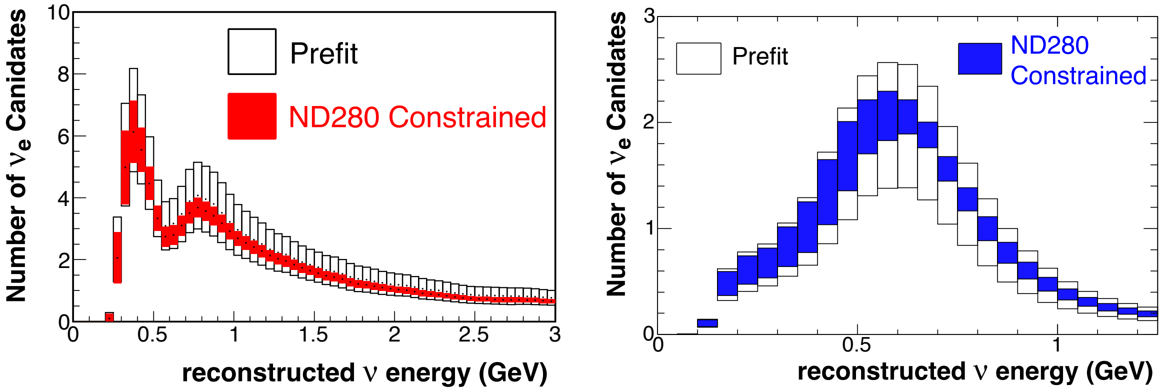

Figure 9.5: Total systematic error effect on the number of SK ν_μ (left) and ν_e (right) candidates, assuming the default oscillation parameters in Table 9.2. The ND280 constrained errors are from an independent ND280 fit [228].

The oscillation parameters are tuned and constrained based on the PDG combination

Systematic Error Source	Relative Uncertainty (%)	
	ν_μ Candidates	ν_e Candidates
Flux & Xsec. ND280 Constrained (Prior)	2.7 (21.7)	3.1 (26.0)
Xsec. ND280 Independent	5.0	4.7
Pion Hadronic Interactions	3.5	2.3
SK Detector	3.6	2.9
Total ND280 Constrained (Prior)	7.6 (23.4)	6.8 (26.8)

Table 9.4: Summary of the effect of the systematic errors on the SK ν_e and ν_μ total event rates, assuming the default oscillation parameters in Table 9.2. The ND280 constrained errors are from an independent ND280 fit [228].

of world data [227] as shown in Figure 9.2. The MCMC analysis is performed in two configurations:

- T2K-only analysis: $\sin^2\theta_{13}$ is unconstrained (flat prior).
- Reactor-constrained analysis: $\sin^2 2\theta_{13}$ is constrained assuming a Gaussian prior with width 0.01, calculated from the average of reactor neutrino data [227].

9.3 Results

Two MCMC (Section 7.2) samples (T2K-only and reactor-constrained) are generated according to the likelihood in Equation 7.1, which at this point is fully defined. The validation and full description of this analysis is given in [224].

A *best-fit* for the event rates can be inferred (similarly to Equation 8.8 in the Atm-ν analysis) by marginalizing over all the parameters in each bin. This is shown in Figures 9.6 and 9.7 for the ND280 samples and in Figure 9.8 for the SK samples in the T2K-only analysis.

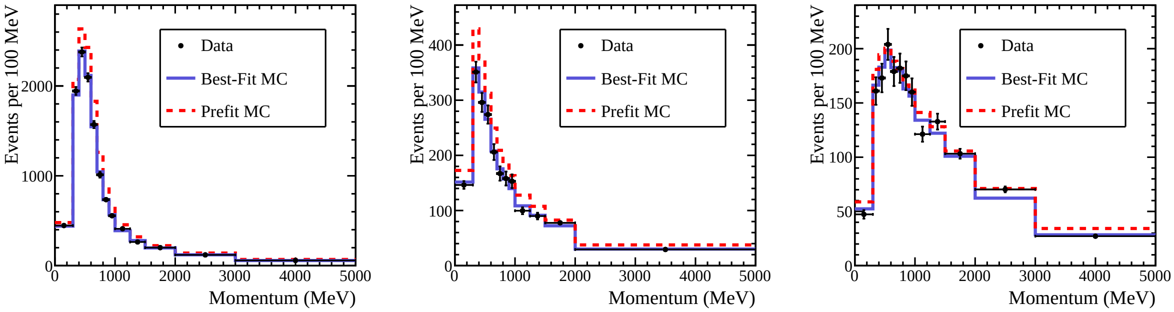

Figure 9.6: The ND280 CC0π (left), CC1π (middle) and CC Other (right) event rates projected onto p_μ for data, prefit MC and best-fits.

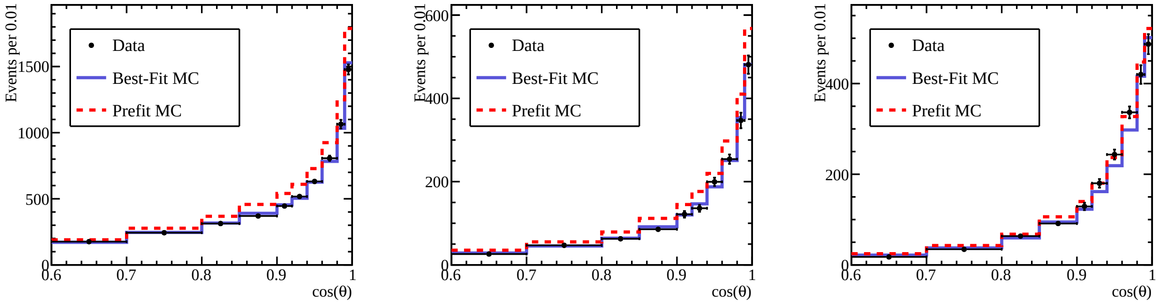

Figure 9.7: The ND280 CC0π (left), CC1π (middle) and CC Other (right) event rates projected onto $\cos\theta$ for data, prefit MC and best-fits.

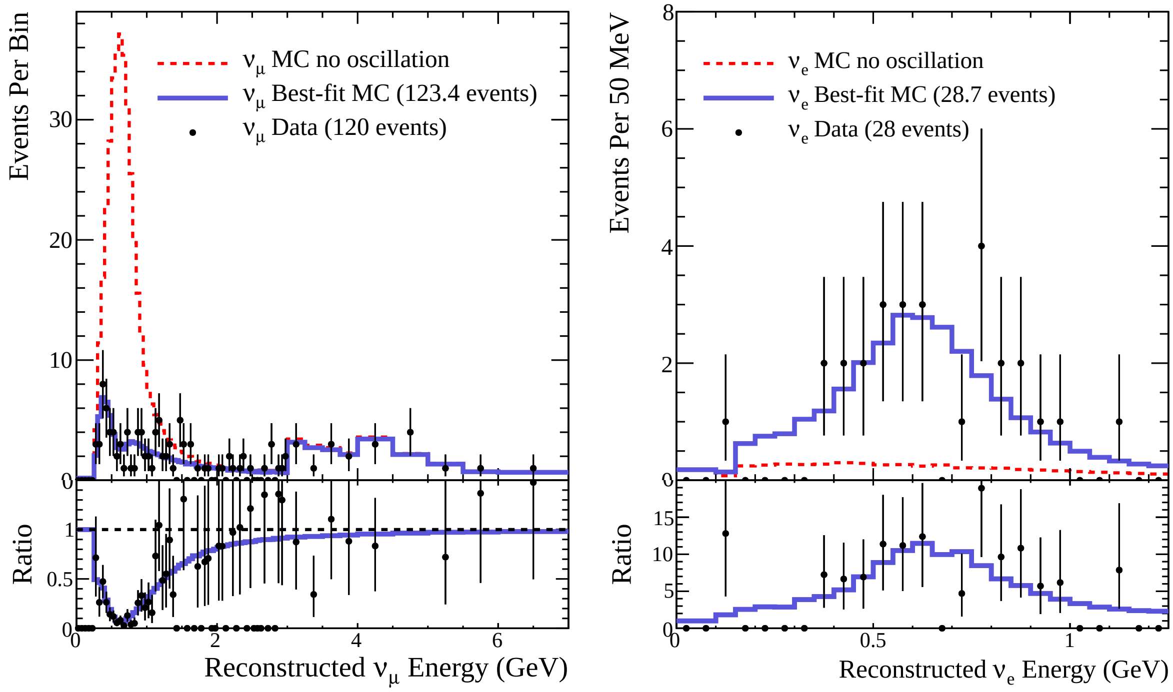

Figure 9.8: The SK ν_μ (left) and ν_e (right) candidate samples for data, prefit MC and best-fits. The total integrated numbers of events are shown in () brackets. The "no oscillation case" is marginalized over the posterior assuming $\theta_{12} = \theta_{13} = \theta_{23} = 0$. The ratio is the best-fit over the no oscillation spectrum. The bottom left panel can be compared to Figure 2.4.

A best-fit in the 4D oscillation parameter space ($\sin^2\theta_{13}$, $\sin^2\theta_{23}$, Δm^2_{32}, δ_{CP}) is determined by slicing the posterior in δ_{CP}, smoothing each resulting 3D posterior [229], then finding the mode (most probable value) using MINUIT [206]. A credible region (CR) of, say, $X\%$ in some 2D parameter space, marginalized over all the other parameters, is defined as the region that contains $X\%$ of the probability (number of MCMC steps) relative to the maximum[1]. The best-fit and the 68% and 90% CRs are shown for various parameter spaces in Figure 9.9 comparing the T2K-only analysis and the reactor constrained analysis.

A *goodness-of-fit* is difficult to define in a Bayesian framework, which typically compares different models given the data. However, the probability to obtain the observed data given the posterior (*p-value*) can be evaluated as in [230]. The p-values when considering each data sample alone and jointly are shown in Table 9.5.

	ND280 only	SK ν_e only	SK ν_μ only	All Samples
T2K-only	0.044	0.32	0.35	0.036
with reactor	0.042	0.44	0.34	0.040

Table 9.5: The goodness-of-fit (p-values) as reported in [224] for each sample independently and jointly, with and without the reactor constraint.

A comparison of the T2K credible region contours with the SK [231] atmospheric and MINOS [66] confidence level contours in the Δm^2_{32}-$\sin^2\theta_{23}$ space is shown in Figure 9.10. T2K measures $\sin^2\theta_{23}$ with world-leading precision and is competitive in Δm^2_{32}.

A credible interval (CI) for one parameter is defined similarly to a CR except integrating in 1D. This is shown for δ_{CP} with the reactor constraint in Figure 9.11. The

---

[1] More formally, the $X\%$ CR is the domain D of 2 parameters (x, y) such that

$$X = \iint_D \mathcal{L}_M(x, y|\mathbf{M})\mathrm{d}x\mathrm{d}y, \tag{9.1}$$

where $\mathcal{L}_M$ is defined in Equation 7.6 and is normalized to unity. In practice, D is determined by integrating bins of decreasing magnitude from the maximum bin until $X\%$ of the distribution is obtained.

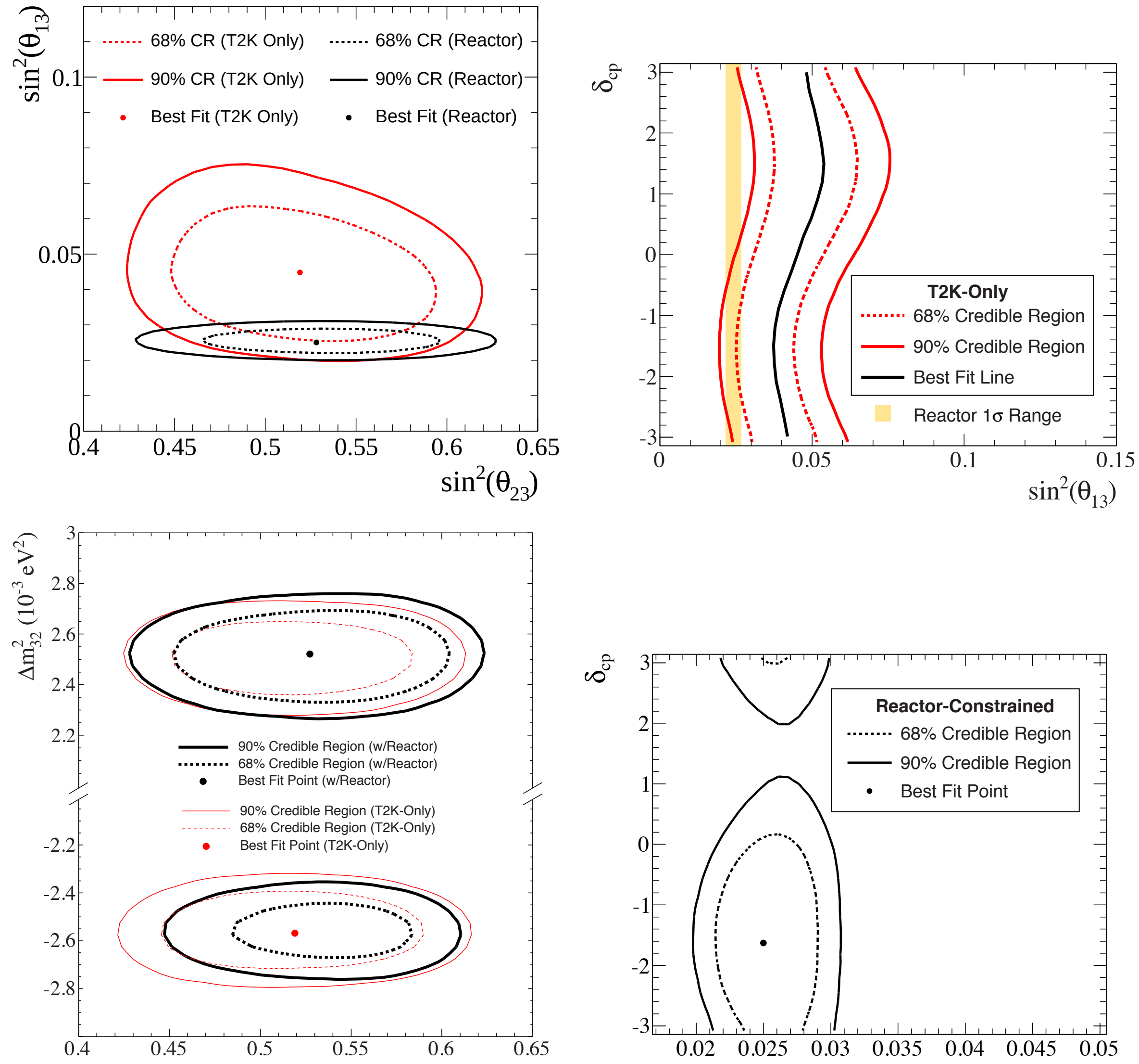

Figure 9.9: The 68% and 90% credible regions in the $\sin^2\theta_{13}$-$\sin^2\theta_{23}$ (top left), Δm^2_{32}-$\sin^2\theta_{23}$ (bottom left), T2K-only δ_{CP}-$\sin^2\theta_{13}$ (top right) and reactor-constrained δ_{CP}-$\sin^2\theta_{13}$ (bottom right) spaces. The best-fit in the T2K-only $\sin^2\theta_{13}$-$\sin^2\theta_{23}$ and Δm^2_{32}-$\sin^2\theta_{23}$ spaces assumes $\delta_{CP} = 0$.

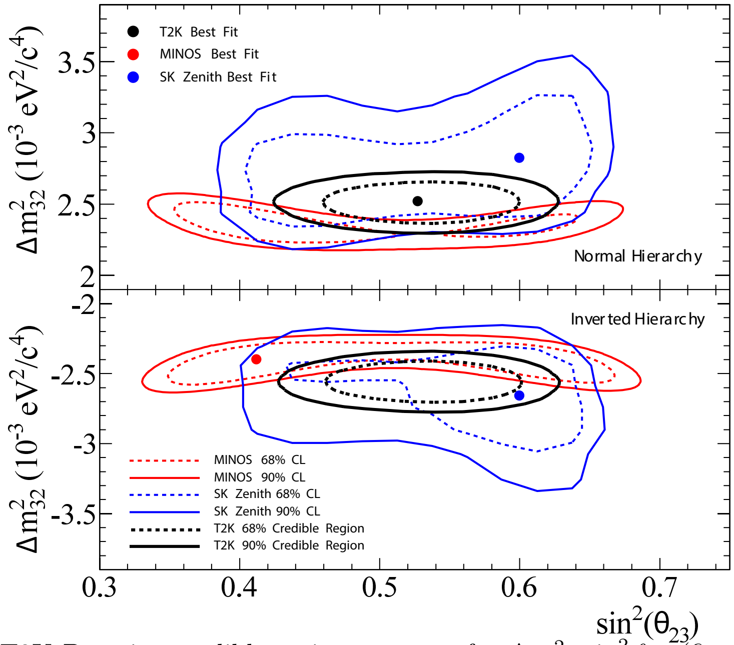

Figure 9.10: The T2K Bayesian credible region contours for Δm^2_{32}-$\sin^2\theta_{23}$ (fitted θ_{13} [227]) assuming normal hierarchy $P(\text{NH}) = 1$ (top) and inverted hierarchy $P(\text{IH}) = 1$ (bottom), compared to the frequentist confidence level contours from the SK atmospheric [231] (fixed θ_{13} [72]) and MINOS [66] (fitted θ_{13} [227]) analyses.

combination of T2K and reactor data suggests $\delta_{CP} \approx -\pi/2$ with CIs given by the shaded regions. The 90% CI for δ_{CP} is $[-1.13, 0.43]\pi$. Similarly, the 68% CIs, except expressed as a 1σ Gaussian error, for the other oscillation parameters are given in Table 9.6.

	Pref. MH	$\lvert\Delta m^2_{32}\rvert$ [$\times 10^{-3}$ eV^2]	$\sin^2\theta_{23}$	$\sin^2\theta_{13}$	δ_{CP}
T2K-only	IH	2.57 ± 0.11	$0.520^{+0.045}_{-0.050}$	$0.0454^{+0.011}_{-0.014}$	0 (fixed)
with reactor	NH	2.51 ± 0.11	$0.528^{+0.055}_{-0.038}$	0.0250 ± 0.0026	-1.601

Table 9.6: Best-fit and 68% credible intervals for the oscillation parameters extracted from the 1D marginal posteriors. The probabilities of the preferred MH are shown in Table 9.7.

To extract information about the MH and the θ_{23} octant, Figure 9.12 shows the posteriors as a function of δ_{CP} without marginalizing over these discrete parameters. Correspondingly, marginalizing over δ_{CP} yields the probability for each MH and octant configuration shown in Table 9.7. The comparison of Figure 9.12 for T2K and Figure 2.3

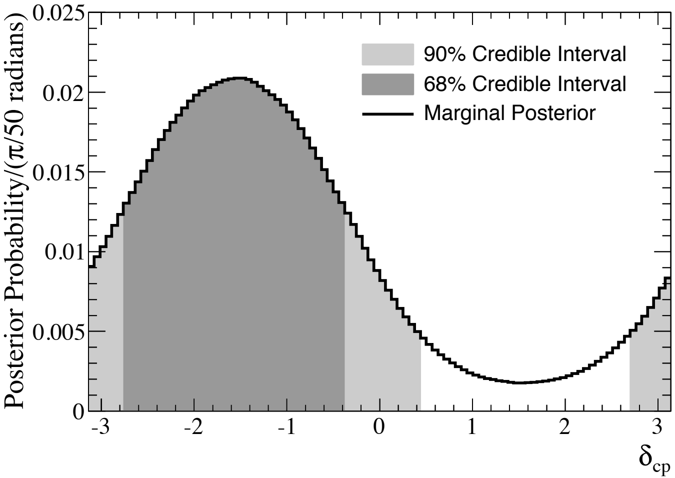

Figure 9.11: The δ_{cp} posterior and the 68% and 90% credible intervals, marginalized over all the other parameters with the reactor constraint. The 90% CI is $[-1.11, 0.38]\pi$.

for MINOS [66] shows some tension in the ordering of the preferred MHs and octants. Though the results are not sufficiently significant to make a strong claim, this analysis demonstrates how T2K, with increasing statistics, and combined with other ongoing experiments such as NOνA [63], can lift the degeneracies in the oscillation parameter space.

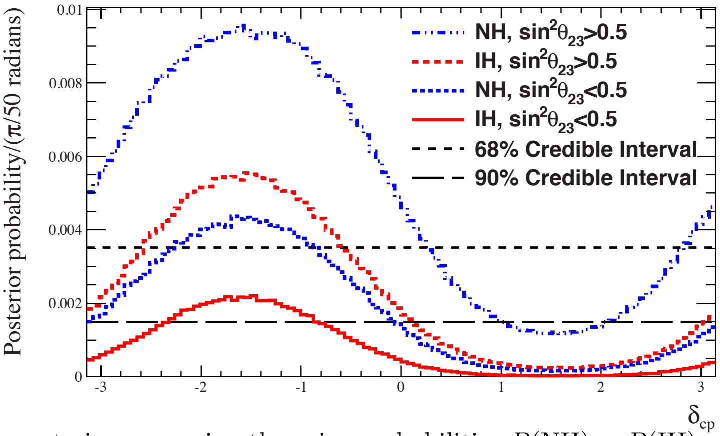

Figure 9.12: The δ_{cp} posteriors assuming the prior probabilities $P(\text{NH}) = P(\text{IH}) = 0.5$ and $P(\sin^2\theta_{23} < 0.5) = P(\sin^2\theta_{23} > 0.5) = 0.5$, without marginalization over the MH nor the θ_{23} octant. All other parameters are marginalized with the reactor constraint. The 68% and 90% allowed regions correspond to the portions of the posteriors above the horizontal lines. See for comparison the MINOS results in Figure 2.3.

T2K-Only

	NH	IH	Sum
$\sin^2\theta_{23} \leqslant 0.5$	0.165	0.200	0.365
$\sin^2\theta_{23} > 0.5$	0.288	0.347	0.635
Sum	0.453	0.547	

Reactor-Constrained

	NH	IH	Sum
$\sin^2\theta_{23} \leqslant 0.5$	0.179	0.078	0.257
$\sin^2\theta_{23} > 0.5$	0.505	0.238	0.743
Sum	0.684	0.316	

Table 9.7: The posterior probability for each MH and θ_{23} octant combination, assuming prior probabilities $P(\text{NH}) = P(\text{IH}) = 0.5$ and $P(\sin^2\theta_{23} < 0.5) = P(\sin^2\theta_{23} > 0.5) = 0.5$. All other parameters are marginalized without (left) and with (right) the reactor constraint.

Chapter 10

Conclusions and Outlook

The T2K experiment has produced world-leading results with the discovery of ν_e appearance from a ν_μ beam and the precision measurement of the θ_{23} neutrino mixing angle with ν_μ disappearance. A new joint analysis combining the ND280 and SK ν_e and ν_μ samples using a Markov Chain Monte Carlo was presented. This properly takes into account correlations between the oscillation parameters allowing for the elucidation of the full 3-flavour oscillation framework. The results are shown in Table 10.1 for the T2K data alone and with the reactor data constraint on θ_{13}. Sensitivity to the mass hierarchy, θ_{23} and δ_{CP} is currently limited by statistical uncertainty, with about 8% of the expected total POT.

	Pref. MH	$\lvert\Delta m^2_{32}\rvert$ [$\times 10^{-3}$ eV^2]	$\sin^2\theta_{23}$	$\sin^2\theta_{13}$	δ_{CP}
T2K-only	IH	2.57 ± 0.11	$0.520^{+0.045}_{-0.050}$	$0.0454^{+0.011}_{-0.014}$	0 (fixed)
with reactor	NH	2.51 ± 0.11	$0.528^{+0.055}_{-0.038}$	0.0250 ± 0.0026	-1.601

Table 10.1: Best fit and 68% credible intervals for the oscillation parameters assuming uniform priors. The results are from a joint MCMC analysis of the T2K Run1-4 ν_e and ν_μ samples. The reactor constrained result assumes a Gaussian prior on θ_{13} given by the reactor data [227]. The 90% CI for δ_{CP} is $[-1.13, 0.43]\pi$ with the reactor constraint.

As the data collected by T2K increases, the understanding and constraint of systematic errors will become increasingly important. Figures 10.1 to 10.3 show the future sensitivities for the various oscillation parameters with the total expected POT of 7.8×10^{21} (3.6×10^{21}) for T2K (NOνA [63]), 1:1 $\nu : \bar{\nu}$ running, assuming true parameters $\Delta m^2_{32} = 2.4 \times 10^{-3}$ eV^2, $\sin^2 2\theta_{13} = 0.1 \pm 0.005$ [65] and NH. T2K alone has sensitivity to the θ_{23} octant and to $\sin \delta_{CP} \neq 0$. Sensitivity to the MH and $\sin \delta_{CP} \neq 0$ improves with the combination of NOνA.

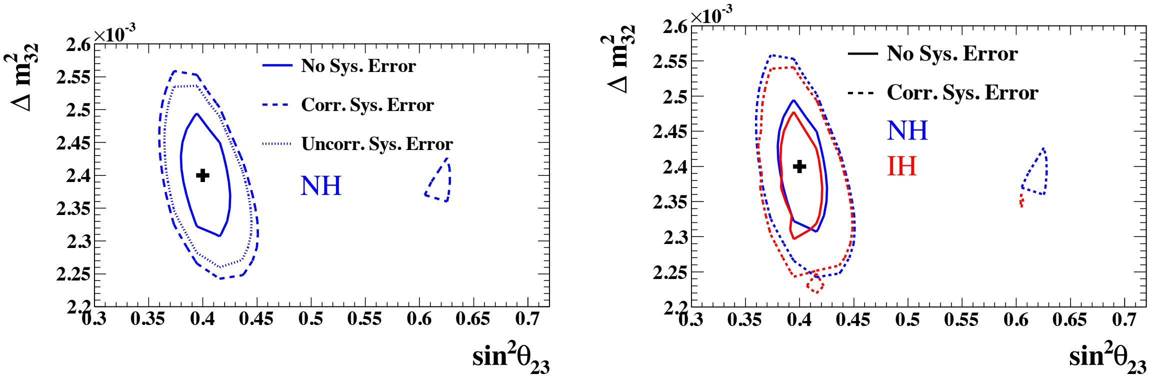

Figure 10.1: The 90% C.L. allowed regions in Δm^2_{32}-$\sin^2 \theta_{23}$ space for the full T2K data set, assuming the true parameters defined in the text and $\sin^2 \theta_{23} = 0.4$, $\delta_{CP} = 0$. The colour of the contours indicates the assumption of the labelled MH in the test fit. A comparison of fully correlated and uncorrelated realistic systematic errors between ν and $\bar{\nu}$ (left) and of incorrect MH assumption (right) is shown [232].

This thesis discussed several developments for the reductions of background and systematic errors in the T2K analyses:

- A novel optical transition radiation proton beam monitor was designed and commissioned in a high radiation environment near the T2K target. It has successfully monitored the beam stability and determined the beam position and direction (combined with upstream monitor results) with the required precision.

- Neutrino interaction modelling is a significant source of systematic error. A software framework was developed to propagate systematics in the neutrino interaction model to the ND280 and SK analyses. This framework was used in a program of fits to external neutrino interaction measurements to provide a prior constraint on

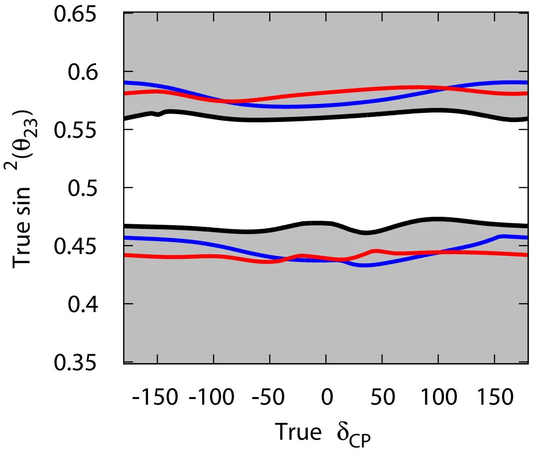

Figure 10.2: The 90% C.L. θ_{23} octant resolution sensitivity regions in $\sin^2\theta_{23}$-δ_{CP} space for the full T2K and NOνA data set. The true parameters are defined in the text. The test MH and δ_{CP} are unconstrained while the test θ_{23} is constrained to the opposite octant. A simple 5% (10%) normalization systematic is assumed for signal (background). Points inside the grey region can be determined to 90% C.L. [233].

the relevant SK signal and background interaction processes. The framework can be easily extended to include new interaction models and parameters, as the ND280 and SK analyses become more sophisticated.

- Pion production contributes to a significant portion of the backgrounds in CCQE-like samples at ND280 and SK, where the pion may be mis-reconstructed as a lepton in a NC process or lost to absorption in a CC process. Furthermore, the kinematics of an event are modified by the scattering of pions, which will become more important as the ND280 and SK analyses mature and incorporate pion kinematics. The NEUT simulation pion interaction model was improved and tuned. A novel algorithm for constraining the model parameters and propagating the systematics was developed. The model was implemented in a detector simulation (SK) for the first time allowing a unified treatment of pion interactions within the neutrino target nucleus and interactions after the pion has escaped.

- A new water Čerenkov detector reconstruction algorithm was developed. Superior performance relative to the previous SK algorithm has been demonstrated in

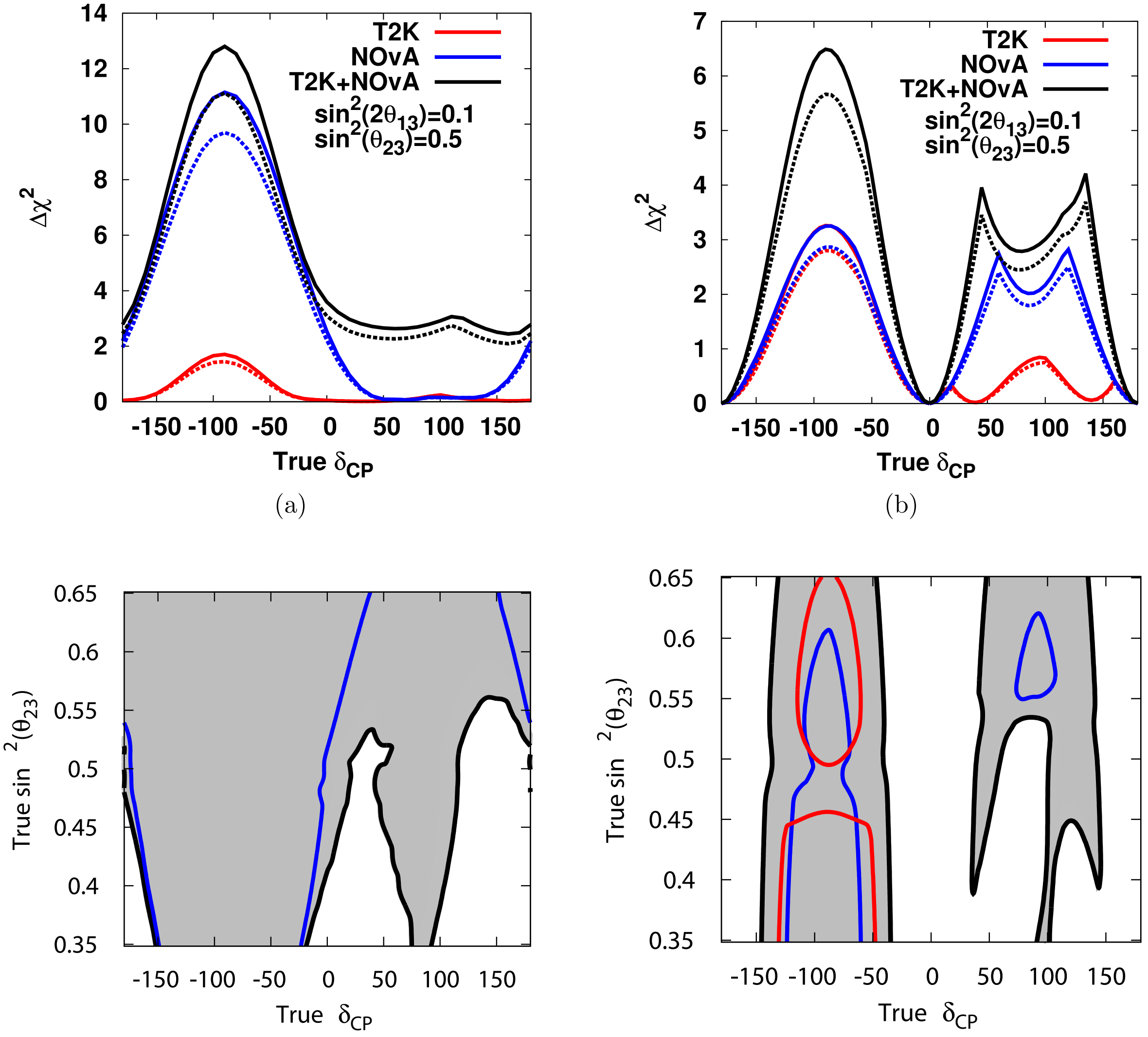

(a) (b)

(c) (d)

Figure 10.3: $\Delta\chi^2$ vs δ_{CP} (top) and 90% C.L. sensitivity regions (bottom) for mass hierarchy (left) and $\sin\delta_{CP} \neq 0$ (right) for the full T2K and NOνA data set. The true parameters are defined in the text. The test parameters for each case are as follows: (a) The test MH is constrained to the opposite MH, while δ_{CP}, Δm^2_{32} and $\sin^2\theta_{23}$ are unconstrained. (b) The test MH, Δm^2_{32} and $\sin^2\theta_{23}$ are unconstrained. The $\Delta\chi^2$ is minimized with respect to test values of $\delta_{CP} = [0, \pi]$. (c) The test MH, θ_{23} octant and δ_{CP} are unconstrained. (d) The test MH and θ_{23} are unconstrained. Points within the grey regions are where the MH (left) and $\sin\delta_{CP} \neq 0$ (right) can be determined to 90% CL. In all cases, a simple 5% (10%) normalization systematic is assumed for signal (background) [233].

many aspects. In particular, it has been implemented in the T2K ν_e analysis for π^0 rejection, where it decreases the reducible background by $\sim 60\%$. Future applications include charged pion reconstruction, searches for proton decay and the next generation experiment, Hyper-Kamiokande [234].

- The new reconstruction has been applied to SK control samples, revealing some detector model deficiencies, which will lead to the overall improvement of the understanding of the detector. The detector systematic errors have been evaluated based on the control samples. In particular, an analysis of the atmospheric neutrino data was developed to determine the systematic error in both the T2K ν_e and ν_μ samples simultaneously, necessary for the joint oscillation analysis. In anticipation of a future analysis combining atmospheric neutrino and T2K data, this analysis used the same MCMC framework as was used for the T2K oscillation results here.

All of these systematic error frameworks were developed with the goal of properly accounting for correlations across detectors and sub-samples. This serves as the foundation for including additional samples from the T2K beam in ND280 and SK, and from atmospheric neutrinos in SK, in a joint oscillation analysis. The MCMC framework facilitates increasing numbers of samples and model parameters as well as the combination with external experiments. With these analysis upgrades and future data collection, T2K will make a strong contribution to the measurement of δ_{CP}, and with the combination of atmospheric neutrino data and other long-baseline experiments, precisely determine the 3-flavour neutrino oscillation parameters.

Appendices

Appendix A

The NEUT Pion Interaction Model

A.1 Pion Scattering Data

Data from publications of pion-nuclei scattering data were used for comparison to the NEUT pion FSI model described in Section 6.2.1. Table A.1 summarizes the data used from various experiments including different targets, beam polarities and measured interaction channels. The data are shown in Figures 6.6 to 6.9 and Figures A.1 to A.5.

An important correction was made to the Ashery absorption and charge exchange data [235] that was not included in similar studies for past neutrino experiments. Ashery *et al* re-measured the charge exchange cross section [236] and obtained a larger value than the previous measurement. For this analysis, the original data is corrected by scaling up the charge exchange data and scaling down the absorption data accordingly (since the absorption measurements come from $\sigma_{abs} = \sigma_{abs+scx} - \sigma_{scx}$).

A.1.1 Double Charge Exchange

Double charge exchange, $\pi^{\pm} \rightarrow \pi^{\mp}$, is an interesting check of the cascade model since it arises from multiple microscopic SCX interactions, for example $\pi^{+}n \rightarrow \pi^{0}p$, then $\pi^{0}n \rightarrow \pi^{-}p$ (reversing the arrow for incoming π^{-}). Thus, observed cross section is sensitive

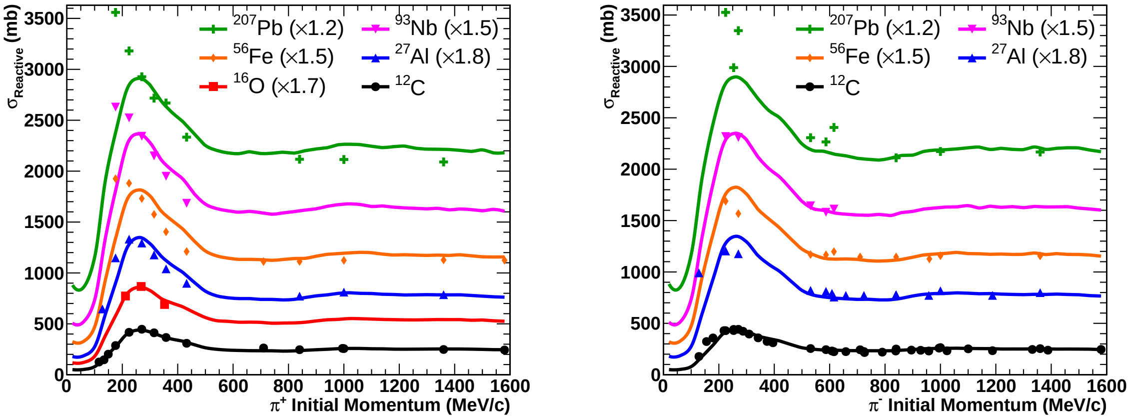

Figure A.1: The tuned model compared to π^+ (right) and π^- (right) reactive data with various nuclei on one interaction channel plot. Note some curves have been scaled to facilitate viewing.

to the p/n ratio of the nucleus. The NEUT cascade model qualitatively reproduces the data [237, 238] as shown in Figure A.5, especially the decreased cross section for π^- DCX in lead due to the excess of neutrons. The discrepancy is likely related to the discrepancy in the absorption channel.

A.1.2 Differential Cross Section

The differential cross section for a single pion in the FS is calculated as

$$\frac{d\sigma_k}{d\Omega} = \pi R_N^2 \frac{n_k}{N_T} \frac{1}{2\pi sin\theta\Delta\theta} \tag{A.1}$$

where n_k is the number of events falling in angular bin k, and $\Delta\theta$ is the bin width.

The scattering kinematics predicted by the FSI model is checked by comparing to measured pion QE scattering differential cross sections in Figure A.6. No significant change in the shape is expected from the model tuning since only the interaction probabilities were modified at low momentum. Agreement is satisfactory for the purposes of the T2K neutrino simulation.

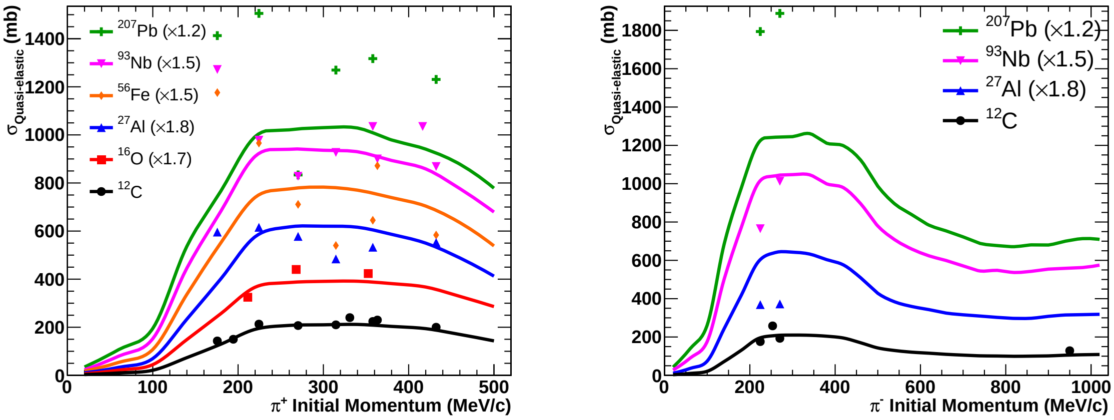

Figure A.2: The tuned model compared to π^+ (right) and π^- (right) QE scattering data with various nuclei on one interaction channel plot. Note some curves have been scaled to facilitate viewing.

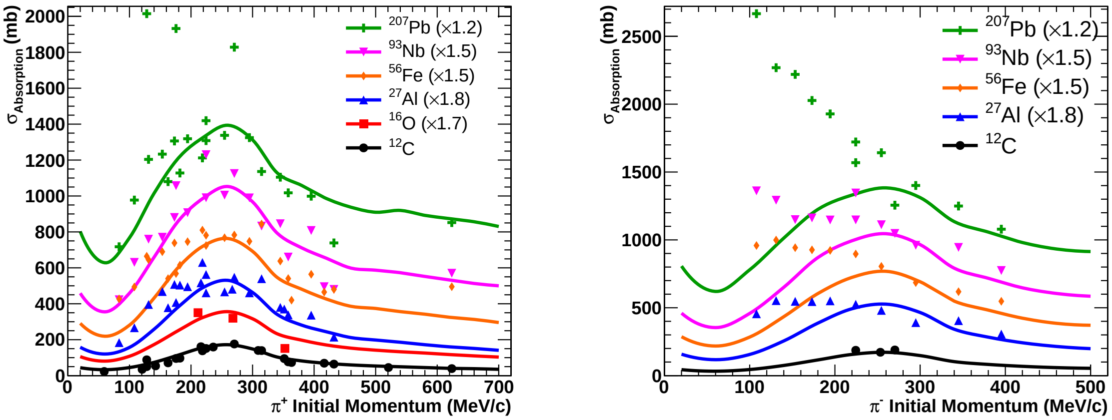

Figure A.3: The tuned model compared to π^+ (right) and π^- (right) absorption data with various nuclei on one interaction channel plot. Note some curves have been scaled to facilitate viewing.

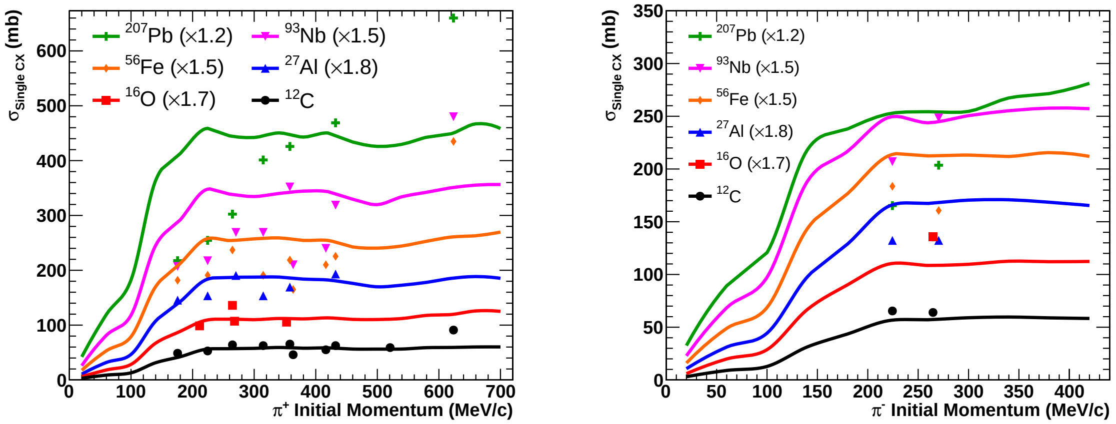

Figure A.4: The tuned model compared to π^+ (right) and π^- (right) SCX data with various nuclei on one interaction channel plot. Note some curves have been scaled to facilitate viewing.

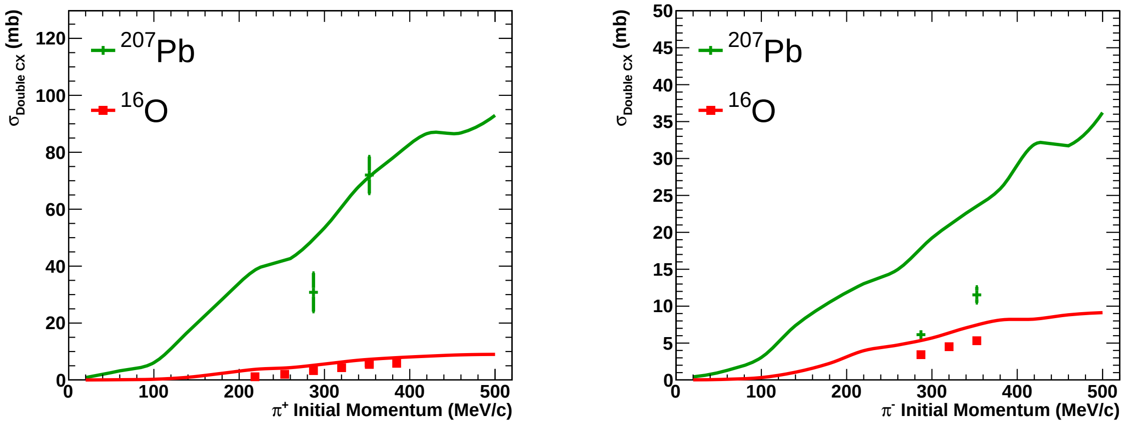

Figure A.5: The tuned model compared to π^+ (right) and π^- (right) DCX data.

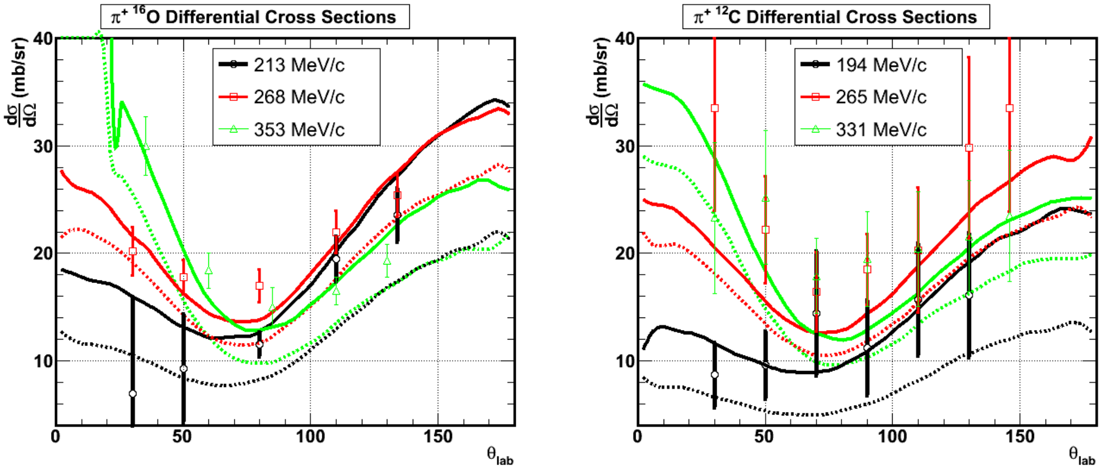

Figure A.6: Differential cross section data for oxygen [237] (left) and carbon [239] (right) at various incident beam momenta, compared to NEUT predictions (inelastic channel). Solid lines: tuned, dotted lines: default.

Reference	Beam	Targets	p_{lab} [MeV/c]	Tot	Reac	Elas	QE	Abs	SCX	DCX	HP
R. A. Giannelli [240]	π^+	C, Al, Ni, Pb	59-236					✓			
K. Nakai [241]	$\pi^\pm$	Al, Ti, Cu, Sn, Au	83-395					✓			
A. Saunders [202]	$\pi^\pm$	H, Li, C, Al, Si, S, Ca	116-149	✓	✓	✓					
I. Navon [242]	$\pi^\pm$	Li, C, Fe, Nb, Bi	128					✓	✓		
T. J. Bowles [243]	$\pi^\pm$	Be, C, O, Ni, Pb	128-194						✓		
A. S. Carroll [200]	π^+	Li, C, Al, Fe, Sn, Pb	149-437	✓							
F. Binon [244]	π^-	C	155-395	✓	✓	✓					
D. Ashery [235], [236]	$\pi^\pm$	Li, C, O, Al, Fe, Nb, Bi	175-432	✓	✓	✓	✓	✓	✓		
A. S. Clough [201]	$\pi^\pm$	Li, Be, C	179-983	✓							
S. M. Levenson [239]	π^+	He, C, Ni, Pb	194-416				✓				
C. H. Q. Ingram [237]	π^+	O	211-353	✓	✓	✓	✓	✓	✓	✓	
D. Rowntree [185]	π^+	N, Ar	216-352					✓			
S. A. Wood [238]	$\pi^\pm$	O, Ca, Rh, Pb	219-385							✓	
R. H. Miller [245]	π^-	C, Pb	253		✓						
M. K. Jones [246]	π^+	C, Ni, Zr, Sn, Pb	363-624				✓	✓	✓		
C. J. Gelderloos [247]	π^-	Li, C, Al, S, Ca, Cu, Zr, Sn, Pb	531-615	✓	✓						
M. Crozon [248]	π^-	Be, C, Al, Cu	608-1388	✓	✓	✓					
T. Takahashi [249]	π^-	C	610-895	✓	✓	✓					
B. W. Allardyce [250]	$\pi^\pm$	C, Al, Ca, Ni, Sn, Ho, Pb	710-2000		✓						
J. W. Cronin [251]	π^-	C, Al, Ca, Cu, Sn, Pb	726-1332		✓						
Y. Fujii [252]	π^-	H, Li, C, Ca, Zr, Pb	950				✓				
K. Aoki [253]	$\pi^\pm$	C	995	✓	✓	✓					
N. Grion [254]	π^+	O	395								✓
A. Rahav [255]	π^-	C	408								✓

Table A.1: Summary of pion-nuclei scattering data, including beam polarity, nuclear target types, momentum range and interaction types measured.

A.2 Pion Photoproduction

A simple pion photoproduction simulation was developed as follows. For a given incoming photon energy, a random position is selected in the nucleus based on the density distribution as in Figure 6.2. Fermi motion and binding energy (27 MeV) of the target nucleon is considered when calculating the effective photon energy. The outgoing pion charge and direction is randomly selected based on differential cross sections calculated from the SAID fit of free nucleon photoproduction data [256], as shown in Figure A.7. The pion energy and outgoing nucleon momentum, p_N, are then determined by 2-body kinematics. Pauli blocking is applied by requiring that $p_N \geqslant 225$ MeV/c. The pion is then propagated through the FSI cascade. Finally, for absolute normalization, the event is weighted by the total cross section of the four channels considered in Figure A.8.

A.2.1 Cross Section Measurements

The simulation is compared to the total cross section [194, 257] and double differential cross section [194] measurements of π^+ production in Figures A.9 to A.11. The discrepancies may be due to additional physics with the photon interaction or threshold effects that are not being considered in the simulation, which becomes apparent toward lower E_γ in Figure A.10. The general (order of magnitude) agreement is taken as sufficient to validate the model for use in the neutrino interaction simulation at the current level of T2K statistics. As FSI systematics become more dominant and ND280/SK analyses mature with more pion samples, this should be reconsidered. The model tuning does not significantly affect the total cross section at low energy (<400 MeV).

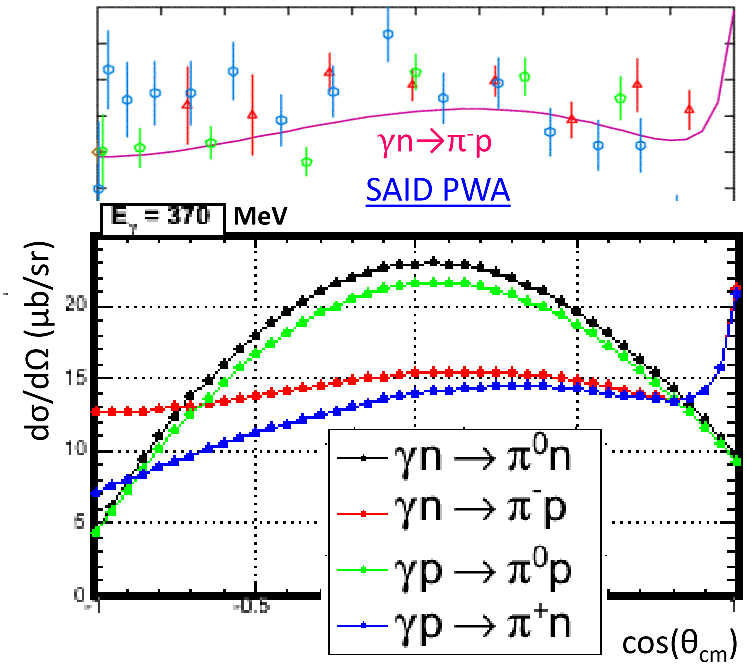

Figure A.7: Differential cross sections for π photoproduction at $E_\gamma = 370$ MeV. The top panel shows world data and the SAID fit taken from [190]. The bottom panel shows the comparison of the SAID fits of each channel.

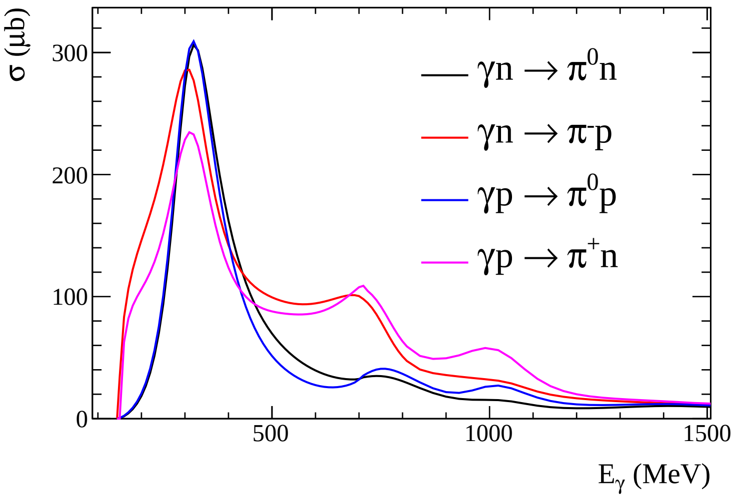

Figure A.8: Total cross sections for the four free nucleon π photoproduction channels considered in the photoproduction simulation, calculated from the SAID fits [190].

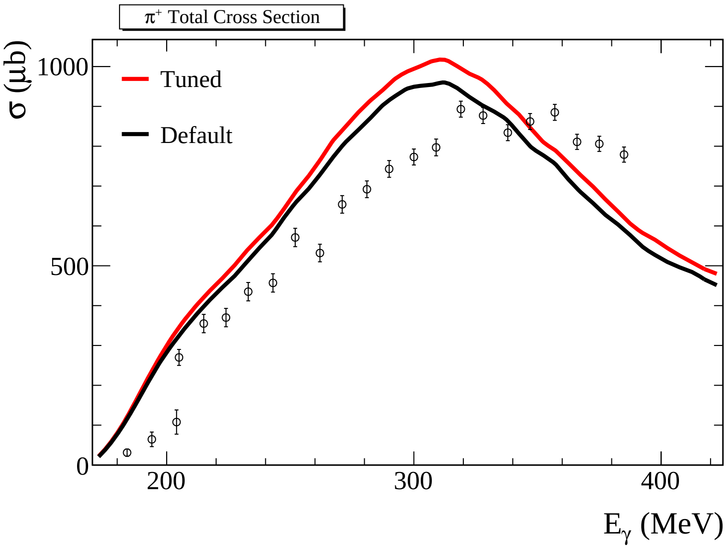

Figure A.9: Default (black) and tuned (red) NEUT predictions for the total cross section of π^+ photoproduction from carbon, as a function of incoming photon energy. Data points are from [257] and [194].

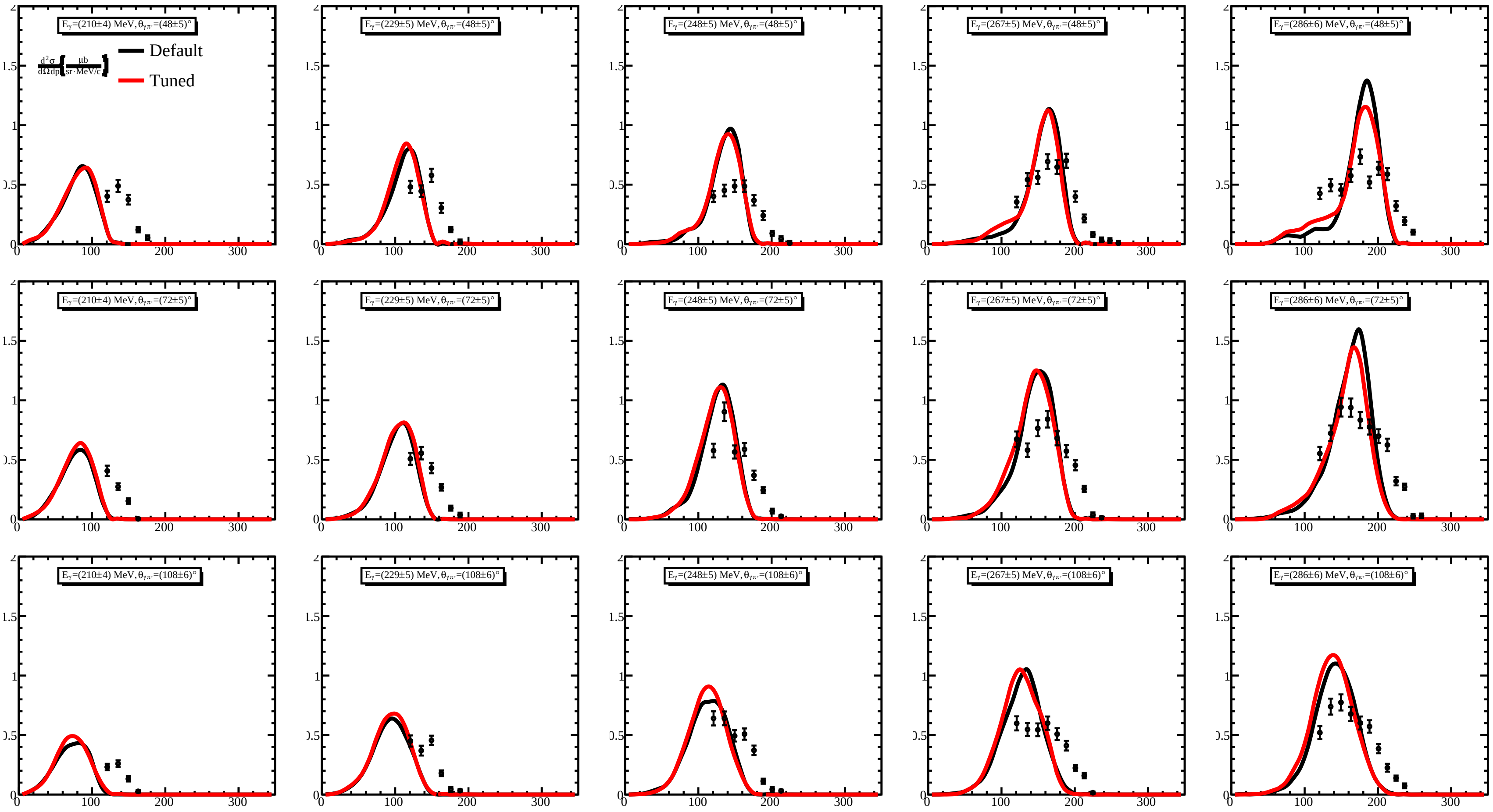

Figure A.10: Default (black) and tuned (red) NEUT predictions for π^+ photoproduction from carbon; $\frac{d^2\sigma}{d\Omega dp}$ in units of $\frac{\mu b}{sr\cdot\text{MeV}/c}$ (vertical axis) as a function of pion momentum in units of MeV/c (horizontal axis). Columns from left to right are in increasing $E_\gamma = \{210, 229, 248, 267, 286\}$ MeV, and rows from top to bottom are in increasing $\theta_{\gamma\pi^+} = \{48, 72, 108\}^\circ$. Data points are from [194].

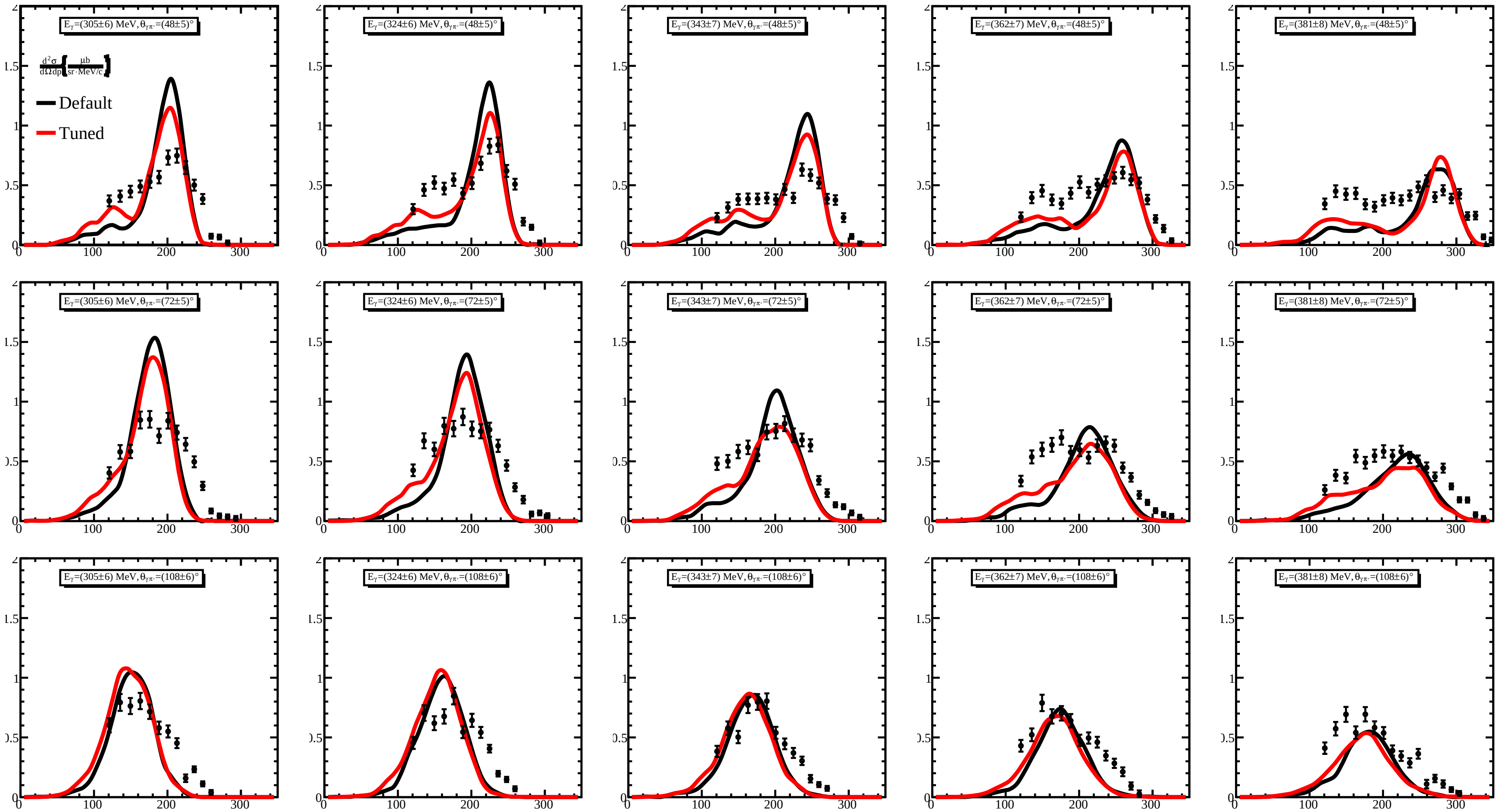

Figure A.11: Default (black) and tuned (red) NEUT predictions for π^+ photoproduction from carbon; $\frac{d^2\sigma}{d\Omega dp}$ in units of $\frac{\mu b}{sr\cdot \mathrm{MeV}/c}$ (vertical axis) as a function of pion momentum in units of MeV/c (horizontal axis). Columns from left to right are in increasing $E_\gamma = \{305, 324, 343, 362, 381\}$ MeV, and rows from top to bottom are in increasing $\theta_{\gamma\pi^+} = \{48, 72, 108\}^\circ$. Data points are from [194].

A.3 Reweighting

The generation of detector MC and event reconstruction is a compute-intensive task, so reweighting schemes were developed to propagate variations in pion interaction model parameters. The algorithm for the microscopic cascade reweighting is described in Section A.3.1 and for macroscopic cross section reweighting in Section A.3.2. Both schemes are validated by comparing reweighted samples and regenerated MC with multiple sets of parameter variations.

A.3.1 Microscopic Cascade

For events where the pion is produced within the nucleus, for example in neutrino nucleus scattering, the interaction probabilities must be varied at the microscopic level. Recall that the FSI probabilities, P, are position (density) and energy dependent, as described in Sections 6.1.1 and 6.1.2, and shown in Figure 6.3[1]. Hence, in the NEUT MC the following information is stored:

- Pion starting position and exit position (if not absorbed).
- Position of each FSI vertex.
- Interaction mechanism at each vertex.
- Pion type and direction between each vertex.
- Pion absolute momentum in the lab and target nucleon rest frame.
- Nucleus type.

With this information, the same cascade can be rerun using the exact trajectory but with modified interaction probabilities to obtain a weight for the event. An example trajectory

---

[1] At high energies, the interaction probabilities also depend on the target nucleon type. However, storing this information at every step of the cascade is not practical. Hence, the weighted (by p/n ratio) average probability for each step is used.

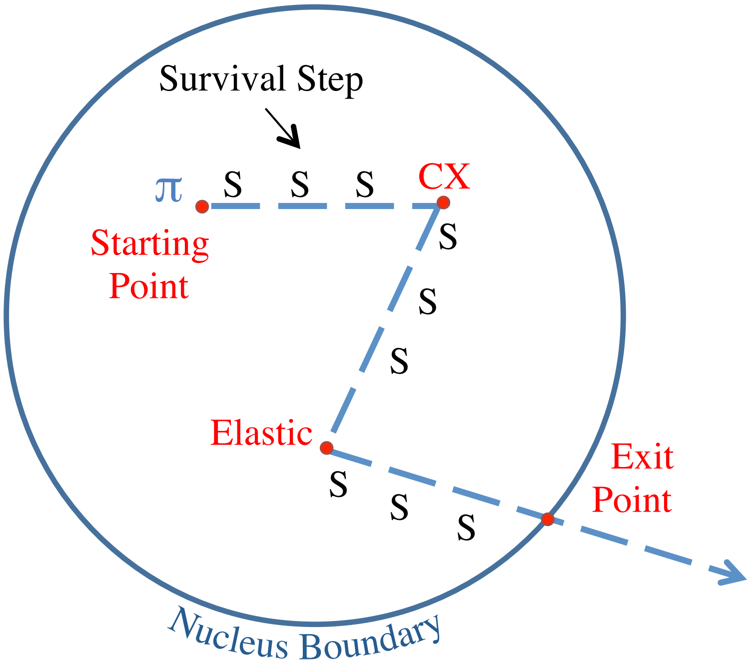

Figure A.12: Example trajectory of a pion in the cascade model showing the starting and exit points, FSI vertices and survival steps (not to scale).

is shown in Figure A.12. The survival probability in a given step of the cascade is

$$P_{surv}(\mathbf{r}, h, p) = 1 - \sum_i P_i(\mathbf{r}, h, p), \tag{A.2}$$

where $\mathbf{r}$ is the current position within the nucleus, h is the hadron (pion) type, p is the momentum and i denotes the various interaction mechanisms (absorption, QE scattering, SCX, hadron production). Then the probability for this event (or this given trajectory) is

$$P_{evt} = \prod_{all\ \ steps} P_{step}, \tag{A.3}$$

where $P_{step} = P_{surv}$ or P_i depending on what occurred in the given step. Note the functional dependence of P is suppressed for clarity.

We then define a set of energy and position (density) independent scaling parameters, f_i, which scales the probability of each interaction, P_i.[2] Then the modified probability of interaction for a given step is $P_i' = f_i P_i$ and Equations A.2 and A.3 are recalculated using P_i'. The weight for the event given a set of modified scaling parameters is then

$$w_{evt}(\mathbf{f}) = \frac{P'_{evt}(\mathbf{f})}{P_{evt}}. \tag{A.4}$$

A.3.2 Macroscopic Cross Section

Reweighting at the macroscopic level, for example in pion scattering in SKDETSIM, is simple if the variations in the interaction cross sections σ_i are known. The reweighting scheme assigns a weight, w_k, to each event, given by

$$w_k = \prod_i \frac{\sigma_{i,k}(p)}{\sigma_{i,default}(p)}, \tag{A.5}$$

where σ_i is the cross section for a given interaction vertex i, p is the incident pion momentum at the interaction vertex, and k enumerates the parameter sets in Table 6.2. The $\sigma_{i,k}$ are calculated from the NEUT pion scattering simulation and microscopic reweighting scheme resulting in cross sections as shown in Figure 6.11. The elastic (coherent) scattering cross section is the difference between the total cross section (fixed) and the reactive cross section (variable). Note that an event may have multiple interaction vertices from one or more pions, and the total weight is the product over all vertices.

A.4 SKDETSIM Pion Interaction Models

In principle, the physics describing interactions of pions with the nucleus, regardless whether the pion was produced within the nuclear medium as in a neutrino interaction,

---

[2] The low energy QE scattering mechanism includes SCX. Thus, f_{QE} also scales the SCX probability. To independently tweak the SCX mechanism, f_{SCX} scales the amplitude for SCX which in turn modifies the probability for SCX given a QE scattering (this results in a change in the opposite direction for the probability of same charge scattering).

or outside the target nucleus as in pion-nuclei scattering, should be the same. This was the primary motivation for using the NEUT FSI model in SKDETSIM. Upon study of the original custom SKDETSIM pion interaction model, discrepancies were found when comparing to external pion scattering data, which further motivated the change to the heavily-validated NEUT model Section 6.2.1. This section describes the original SKDETSIM pion interaction model, implementation of the NEUT pion cascade model, and comparisons to external pion scattering data.

In GEANT3, the simulation of hadronic interactions happens in a well-defined, step-wise manner. First, the total hadronic interaction cross section, σ_{T}, must be provided, which is then used to calculate the mean free path and interaction probability for a given step of a particle in the simulation. If a hadronic interaction occurs, then a model must determine the resulting final state particles and kinematics. In SKDETSIM, due to a significant production of pions in the $< 500\,\mathrm{MeV}/c$ range from atmospheric and T2K neutrino interactions, a custom model was implemented for pions only in this momentum region, while GCALOR [138] is used for everything else. The original ∼20 year old model, hereafter referred to as SGPI, for pion hadronic interactions is documented (in Japanese) in the appendix of [199]. Some comparisons were made with the K2K 1 kT detector. However, it is unclear how complete the validation was. We attempt to translate the relevant parts here and perform comparisons with other external data. The new model, hereafter referred to as SGNUCEFF, is a combination of the NEUT cascade and features inherited from SGPI. The SK 10a MC for the 2010a T2K oscillation analyses used SGPI, while the SK 11c MC for the 2012a analyses use SGNUCEFF.

The current implementation suffers from the fact that both models are only valid for water, but are currently applied to other materials in the OD simulation. Thus, we expect the rate of secondary interactions in heavier materials, such as rock and steel, to be underestimated. The effect of this should be checked in the future and proper modelling revisited. The NEUT pion scattering simulation has been validated against heavier nuclei data, so it should be straightforward to extend SGNUCEFF.

Total Hadronic Interaction Cross Section

We calculate the total cross section on water as $\sigma_{\mathrm{T}} = \sigma_{\mathrm{O}} + 2\sigma_{\mathrm{H}}$, where $\sigma_{\mathrm{O}}^{\mathrm{SGPI}}$ is given by a parameterization defined in [200] fitted to π-O total cross section data contained therein. For $\sigma_{\mathrm{O}}^{\mathrm{SGNUCEFF}}$, the fit is re-done with additional data from [201] and [202] (carbon data scaled to oxygen using the A-scaling measured in [235]). The results of the fits are shown in Figure A.13. It is unclear why the original fit implemented with SGPI does not match the data. The parametrization is asymptotic towards zero momentum, which can be seen in the SGPI result. In the current simulation, π^+ below 10 MeV kinetic energy ($\sim$53.7 MeV/c momentum) are forced to decay[3], so the effect of this large increase is not significant. For $\sigma_{\mathrm{O}}^{\mathrm{SGNUCEFF}}$, the fit is performed down to 100 MeV/c and then extrapolated to zero momentum based on a sum of the NEUT interaction channels described in the next subsection.

The total cross section on free hydrogen, $\sigma_{\mathrm{H}}^{\mathrm{SGPI}}$, was obtained from a rough interpolation of data compiled by the PDG [72]. To improve accuracy, $\sigma_{\mathrm{H}}^{\mathrm{SGNUCEFF}}$ was obtained from SAID [188, 189]. A comparison of $\sigma_{\mathrm{H}}^{\mathrm{SGPI}}$ and $\sigma_{\mathrm{H}}^{\mathrm{SGNUCEFF}}$ is shown in Figure A.14 and a comparison of the SAID fit ($\sigma_{\mathrm{H}}^{\mathrm{SGNUCEFF}}$) to the PDG data is shown in Figure 6.4.

Determination of Secondary Interaction Channel

If an interaction occurs, then the final state must be determined. SGPI uses a table of branching fractions as a function of momentum for elastic scattering, absorption, quasi-elastic (QE) scattering and single charge exchange (SCX). For the purpose of illustration, these branching fractions (BFs) are multiplied by $\sigma_{\mathrm{O}}^{\mathrm{SGPI}}$ to obtain the interaction cross sections in Figure A.13. It is unclear how exactly these branching fractions were determined. However, they result in fairly good agreement with π^+-^{16}O data [236, 237]. It

---

[3] The value of this threshold should be revisited and potentially removed.

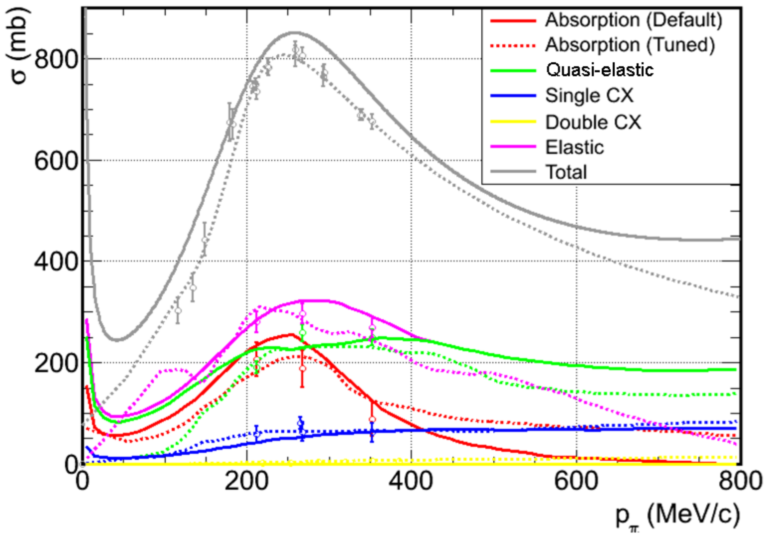

Figure A.13: Total cross sections for σ_{O} in grey, and for the other interaction channels in various colours. Solid lines are for the old SGPI model, while dotted lines are for the new SGNUCEFF model. As explained in the text, the three low momentum points are from carbon data scaled up to oxygen, to provide additional constraint in the fit.

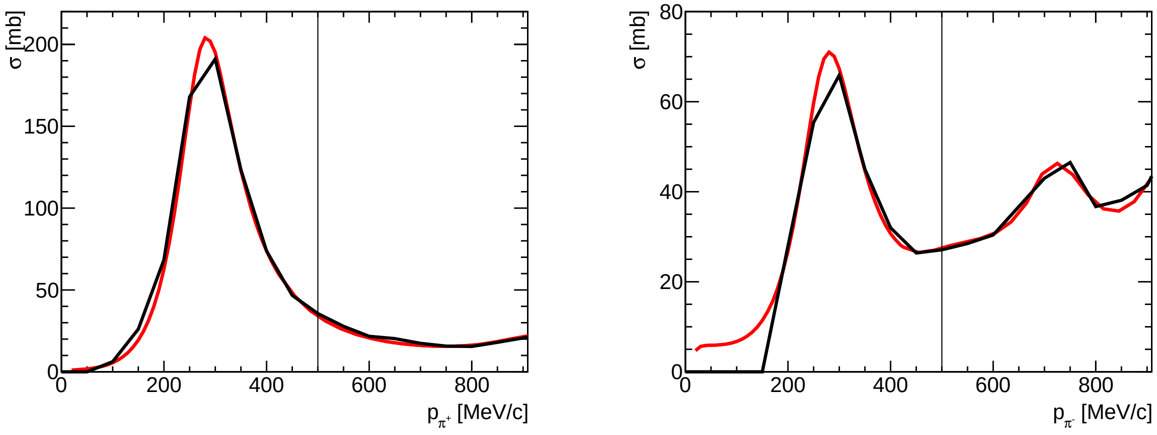

Figure A.14: Total cross section on free hydrogen, σ_{H}, for π^+ (left) and π^- (right), SGPI (black) and SGNUCEFF (red).

was mentioned in [199] that the absorption BF was tuned to ^{27}Al data which can explain the slight overestimation of the cross section relative to the data, since a pion spends more time in a larger nucleus leading to a higher rate of absorption. In the actual simulation, these BFs for interactions on oxygen are assumed for all pion interactions on water (multiplied by $\sigma_{\mathrm{T}}^{\mathrm{SGPI}}$), including free hydrogen. This is not exactly correct since it allows, for example, absorption on free hydrogen which is physically forbidden. Note this is not apparent in Figure A.13 since the BFs are multiplying $\sigma_{\mathrm{O}}^{\mathrm{SGPI}}$, but the effect will be shown in the next subsection.

In SGNUCEFF, we first determine if the interaction occurs on free hydrogen or the oxygen nucleus using $\sigma_{\mathrm{H}}^{\mathrm{SGNUCEFF}}$ and $\sigma_{\mathrm{O}}^{\mathrm{SGNUCEFF}}$. If the interaction occurs on hydrogen, we use the cross sections in Figure 6.4 to determine the interaction channel. There is currently no custom model for inelastic scattering (particle production) from free hydrogen, thus for π^+ we ignore the small inelastic cross section below 500 MeV/c and assume the total cross section is QE: $\sigma_{\mathrm{H}}^{\mathrm{SGNUCEFF}} = \sigma_{\mathrm{H,QE}}^{\mathrm{SGNUCEFF}}$. For π^-, the inelastic channel is simulated as SCX, so the effective SCX cross section is $\sigma_{\mathrm{H,SCX}}^{\mathrm{SGNUCEFF}} + \sigma_{\mathrm{H,Inel}}^{\mathrm{SGNUCEFF}}$. SCX is assumed instead of QE as a conservative approximation for SK analyses, since it maximizes the rate of particle changing interactions.

If the interaction occurs on the oxygen nucleus, an elastic or reactive interaction is determined using the elastic cross section, σ_{Elas}, and the reactive cross section, σ_{R}, which is the sum of the non-elastic interaction cross sections in Figure A.13: $\sigma_{\mathrm{R}} = \sum_i \sigma_i$, where i is absorption, QE scattering, SCX or double CX (DCX). Note we have omitted the superscript SGNUCEFF and the subscript O for brevity. The interaction cross sections, σ_i, are calculated from the NEUT pion-nucleus scattering simulation and analysis described in detail in Section 6.2.1. Above 100 MeV/c, $\sigma_{\mathrm{Elas}} = \sigma_{\mathrm{O}} - \sigma_{\mathrm{R}}$. Below 100 MeV/$c$, σ_{Elas} is linearly extrapolated to 0, and the total cross section is $\sigma_{\mathrm{O}} = \sigma_{\mathrm{Elas}} + \sigma_{\mathrm{R}}$. The dip in σ_{Elas} around 150 MeV/c in Figure A.13 is due to the smooth shape of σ_{O} and the subtraction of σ_{R}, which includes an arbitrary extrapolation of the QE (including

SCX) and absorption microscopic interaction probabilities Section 6.1.1. This should not have a large effect on SK observables, since elastic scattering is typically forward-going. If a reactive type interaction occurs, to determine the final state (the actual interaction channel), the NEUT cascade (NUCEFF) is called starting with the pion at a random incident position on the surface of the nucleus, similar to the pion-nucleus scattering simulation[4].

For external validation of the interaction cross sections (and BFs), the SGPI and SGNUCEFF models were implemented into a GEANT3 thin-target simulation as used in [258]. The simulation uses a thin (line) π^+ beam incident on a cylindrical volume of water small enough to neglect multiple interactions. Interactions on hydrogen are subtracted using the MC truth information. The final state is categorized similarly as above and in Section 6.2.1. The interaction cross section at a given momentum is then given by

$$\sigma_i = \frac{N_i}{N_{trig}\rho l} \tag{A.6}$$

where N_i is the number of interactions observed in the ith interaction channel, l is the length of the cylinder and ρ is the number density of water (except normalized to atomic number of 16).

The results are shown in Figure A.15 and compared to data. The effect of the issue in SGPI mentioned at the beginning of this section, about using oxygen BFs for all interactions on water, appears in the absorption channel where a large excess is observed. The excess follows the shape of σ_{H}, around the Delta resonance peak, as expected. Note also that there is no DCX channel in SGPI, but it is reasonably modelled by SGNUCEFF.

---

[4] If the cascade fails to produce an interaction (transmitted pion), then it is re-run until an interaction occurs.

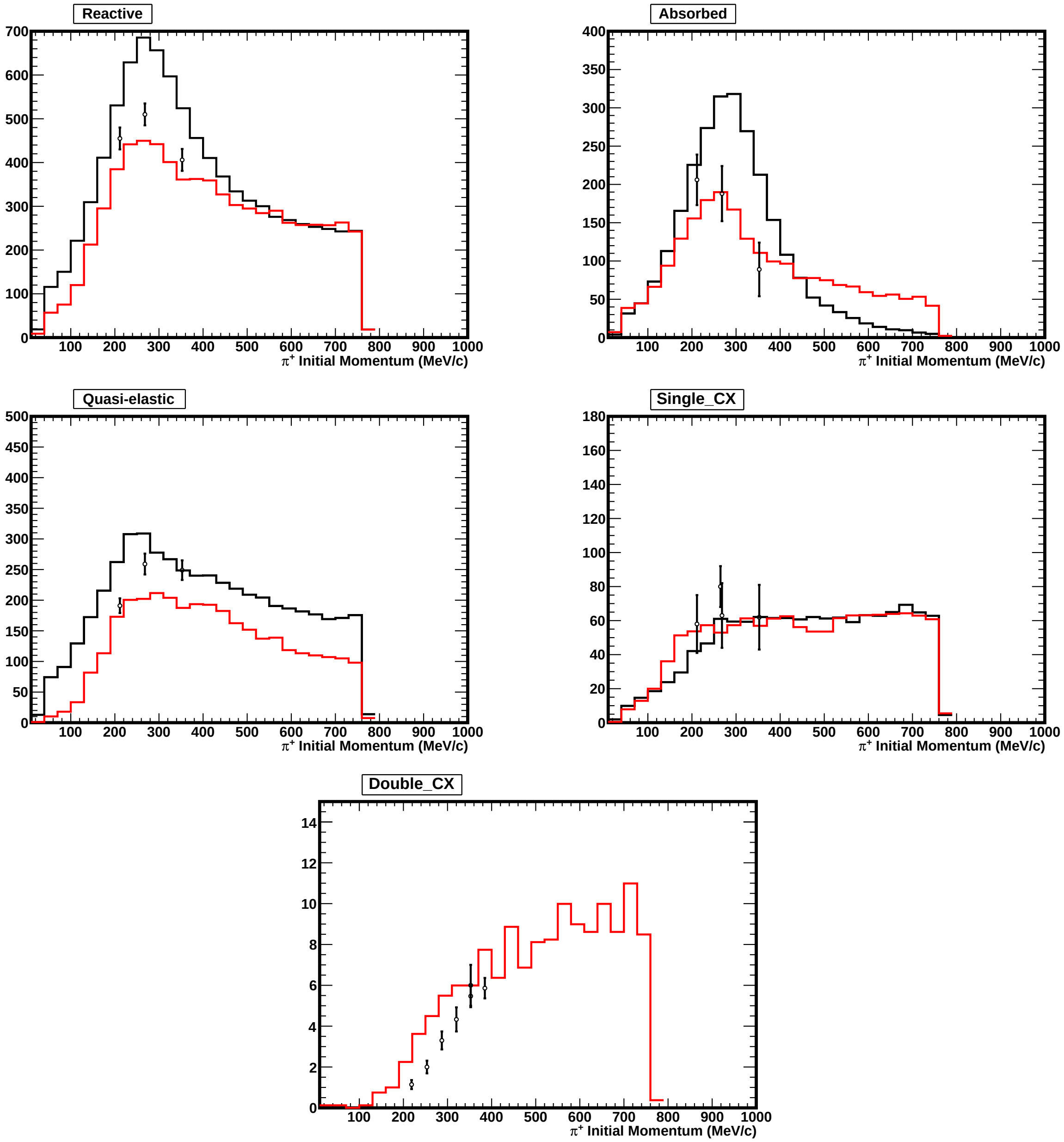

Figure A.15: Interaction cross section, σ_i, results of the thin-target pion scattering simulation for SGPI (black) and SGNUCEFF (red) compared to data [236–238]. The model is applied in the simulation below 500 MeV/c.

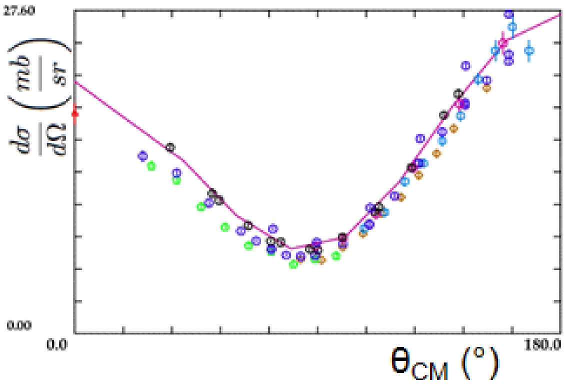

Figure A.16: Differential cross section for 250 MeV/c π^+-p calculated by SAID PWA, compared to their compilation of data.

Determination of Final State Particles and Kinematics

Once the interaction channel has been selected in SGPI, the kinematics of the final state must be determined. For elastic scattering, the angle is selected based on the differential cross section:

$$\frac{d\sigma}{d\Omega}\propto e^{105.4t}, \tag{A.7}$$

where t is the momentum transfer squared in GeV^2/c^4, and the factor comes from a fit to π^--C scattering data between 120-280 MeV [199]. After the scattering angle is determined, the outgoing momentum is kinematically fixed, but smeared by a Gaussian of width 10 MeV/c to approximate Fermi motion in the nucleus. In principle, the smearing should not be applicable to scattering from free hydrogen, and it is unclear if it is correct for elastic (coherent) type scattering off a nucleus. In SGNUCEFF, for simplicity we inherit the SGPI formulation of elastic scattering off the oxygen nucleus, since pion-nuclei scattering data suggest elastic scattering is mostly forward-going. For free hydrogen elastic scattering (and $\pi^- - \text{p}$ SCX), we use the SAID PWA [189] (phase shift) implementation in NEUT [259] to determine the scattering angle and outgoing momentum. An example differential cross section calculated from this model is shown in Figure A.16.

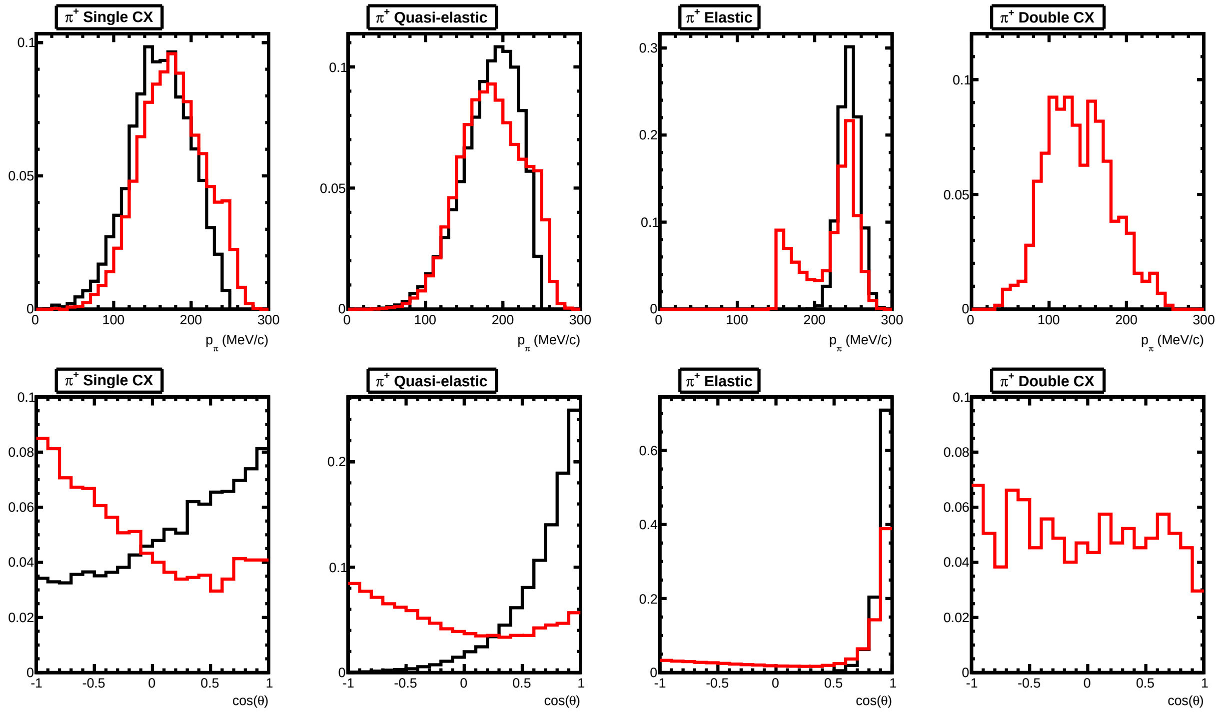

Figure A.17: Outgoing lab momentum and angle distributions for 250 MeV/c π^+ in water using SKDETSIM particle gun simulation, for SGPI (black) and SGNUCEFF (red).

The resulting outgoing scattering angle and momentum distributions for SGPI and SGNUCEFF are shown in Figure A.17, where SKDETSIM was run in *particle gun* mode with π^+s of momentum 250 MeV/c. For elastic scattering, a new low momentum peak appears corresponding to the increase in backward going pions from scattering on free hydrogen.

For QE scattering in SGPI, the angular distribution is given by a Gaussian with a forward peak:

$$\frac{d\sigma}{d\Omega} \propto e^{\frac{1}{2}\cdot\frac{\theta^2_{CM}}{S^2}}, \quad \begin{array}{ll} S = 50^\circ & \text{if } p \leqslant 250\,\text{MeV}/c \\ S = 25^\circ & \text{if } p > 250\,\text{MeV}/c, \end{array} \tag{A.8}$$

where p is the incoming pion momentum in the center of mass frame. This was motivated by $\pi^- - \mathrm{C}$ data [199]. However, it is suspected that this data was incomplete. To account for Fermi motion, the outgoing momentum is smeared by a Gaussian of width 50 MeV/c.

In SGNUCEFF, QE scattering events arise from NEUT cascades in which the pion

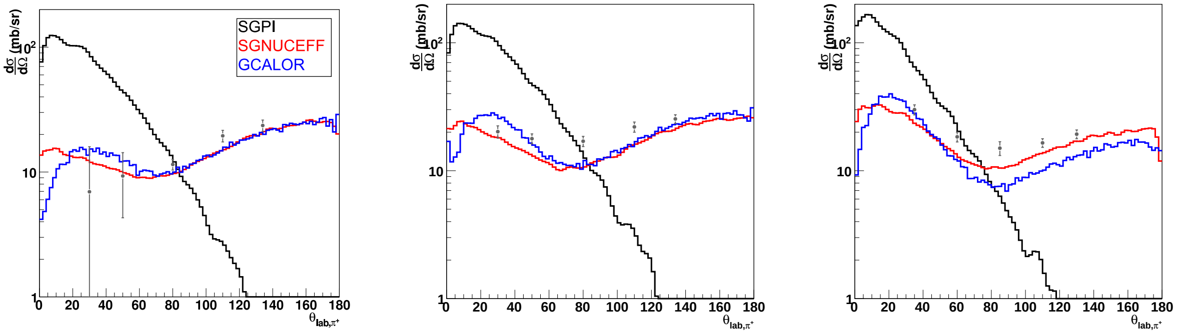

Figure A.18: QE differential cross section, $\frac{d\sigma_{QE}}{d\Omega}$, results of the thin-target π^+ scattering simulation with incoming momenta of 213 (left), 268 (middle) and 353 (right) MeV/c, for SGPI (black) and SGNUCEFF (red) compared to data [237]. The results using GCALOR (blue) are included for reference but is not actually used in any current SK MC.

escapes the nucleus after some number of microscopic scatters. Thus, the resulting scattering angle is the combination of all scatters within the nucleus, each of which are determined from a phase shift analysis of $\pi - \mathrm{N}$ data (similar to the SAID analysis) with in-medium corrections. Fermi motion is also taken into account at each microscopic scattering vertex with NEUT's S/P-wave formulation, up to 225 MeV/c. The backwards-going scattering is enhanced and the outgoing momentum distribution is wider compared to SGPI, as seen in Figure A.17.

The models can be tested against external pion QE scattering differential cross section data by using the thin-target simulation described above. Here the differential cross section is given by

$$\frac{d\sigma_{QE}}{d\Omega} = \frac{N_{QE}}{N_{trig}\rho l(2\pi \sin\theta d\theta)} \tag{A.9}$$

and the results are shown in Figure A.18 for three different incoming pion momenta. Compared to the data [237], SGPI is too forward peaked, while SGNUCEFF (NEUT) models the outgoing scattering angle well.

For SCX in SGPI, the outgoing angle of the π^0 is isotropic for $p < 300\,\mathrm{MeV}/c$, where

p is the incoming pion momentum in the CM frame, and otherwise determined by

$$\frac{d\sigma}{d\Omega} \propto \{ \begin{array}{ll} cos\theta_{CM} & 0 < \theta_{CM} \leqslant \frac{\pi}{2} \\ 0 & \frac{\pi}{2} < \theta_{CM} \leqslant \pi \end{array} \tag{A.10}$$

Similar to the QE case, the outgoing momentum is smeared by a Gaussian of width 50 MeV/c. In SGNUCEFF, the outgoing π^0 kinematics comes from the NEUT cascade as in QE scattering.

The NEUT cascade allows for DCX, not present in the old SGPI model. This arises from multiple microscopic SCX interactions and thus results in a lower average energy and more isotropic distribution compared to SCX as seen in Figure A.17. Since SK cannot distinguish between oppositely charged pions, the effect of this on observables is similar to QE scattering.

In principle, absorption events should result in nucleons emitted in the final state. There are no such particles modelled in SGPI. A model for this was developed for the FSI simulation and is described in detail in [259], but due to technical difficulties it was not implemented in SGNUCEFF. For the T2K oscillation analyses, this is not an issue since most of the emitted protons are below Cherenkov threshold. However, it may be significant for analyses that use neutron tagging, such as in the SK low energy analyses or anti-neutrino analyses, and should be revisited. There are efforts to implement the model into GEANT4 similarly for the ND280 simulation.

Appendix B

SK Reconstruction Validation

The cosmic ray muon and decay-e samples in this appendix are selected according to Section 8.2 and [216]. The Atm-ν sample, introduced in Section 8.3, have a fully-contained fiducial volume (FCFV) requirement (Section 9.1.2) and a maximum visible energy threshold of 1.33 GeV (*sub-GeV* region), while higher energy comparisons are shown elsewhere [216].

B.1 Particle Identification

The fiTQun likelihood ratios are checked using the selected muons and decay-e. A proposed cut for separating electrons from muons in a 1-ring sample is a line in $\ln(\mathcal{L}_e/\mathcal{L}_\mu)$ vs p_e space given by [214]

$$\ln(\mathcal{L}_e/\mathcal{L}_\mu) = 0.2 \times p_e[\mathrm{MeV}/c], \tag{B.1}$$

and shown in Figure B.1.

The 2D distribution can be collapsed into 1D by calculating the distance to this cut line, for example in Figure B.2. A negative (positive) value for the decay-e (muon) corresponds to a mis-PID. The mis-PID rate is $< 1\%$ with a data-MC discrepancy of 0.3% which is assigned as a systematic error.

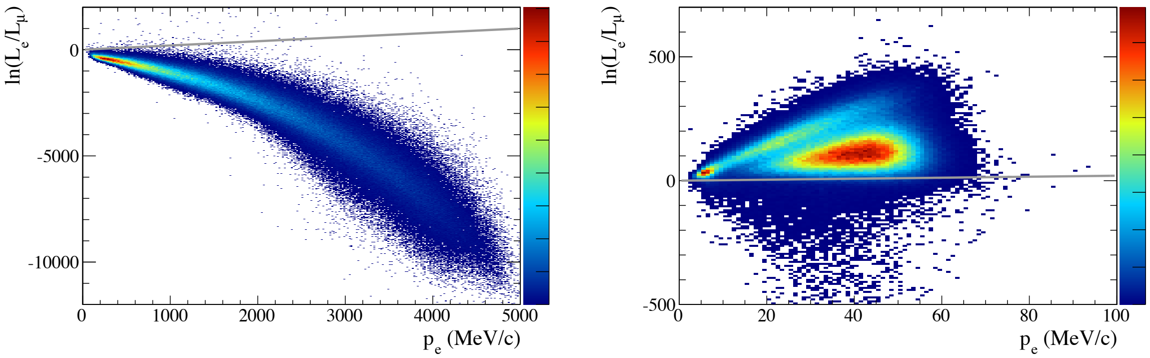

Figure B.1: $\ln(\mathcal{L}_e/\mathcal{L}_\mu)$ vs p_e (momentum assuming electron hypothesis) for muon (left) and decay-e (right) data events. The cut line for 1R e/μ separation is shown (Equation B.1).

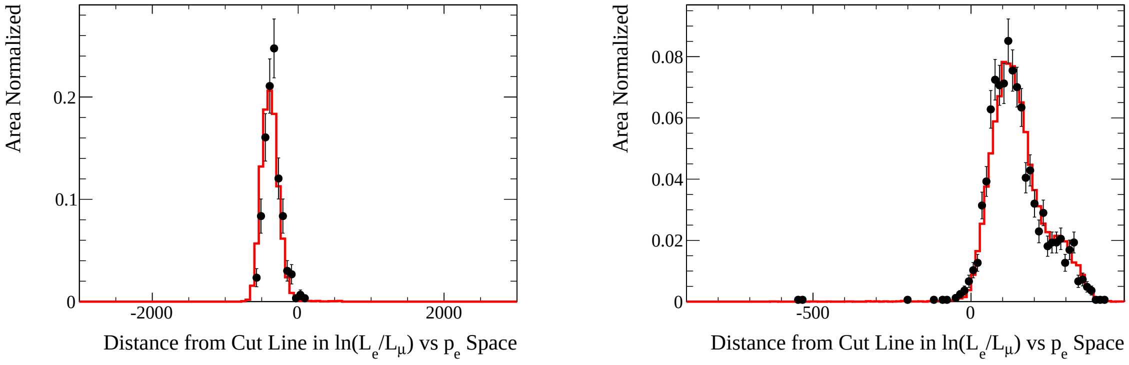

Figure B.2: Distance from cut line in $\ln(\mathcal{L}_e/\mathcal{L}_\mu)$ versus p_e space of cosmic muons with momentum from 0–500 MeV/c (left) and decay-e with momentum from 40–45 MeV/c (right).

The cut line defined in Equation B.1 is used to define an e-like and μ-like sample in the Atm-ν data. The distance to the cut line is shown in Figure B.3, after selecting a 1-ring-like sample as prescribed in Section B.2. Good data-MC agreement as well as the separation of true electron and muon events can be seen.

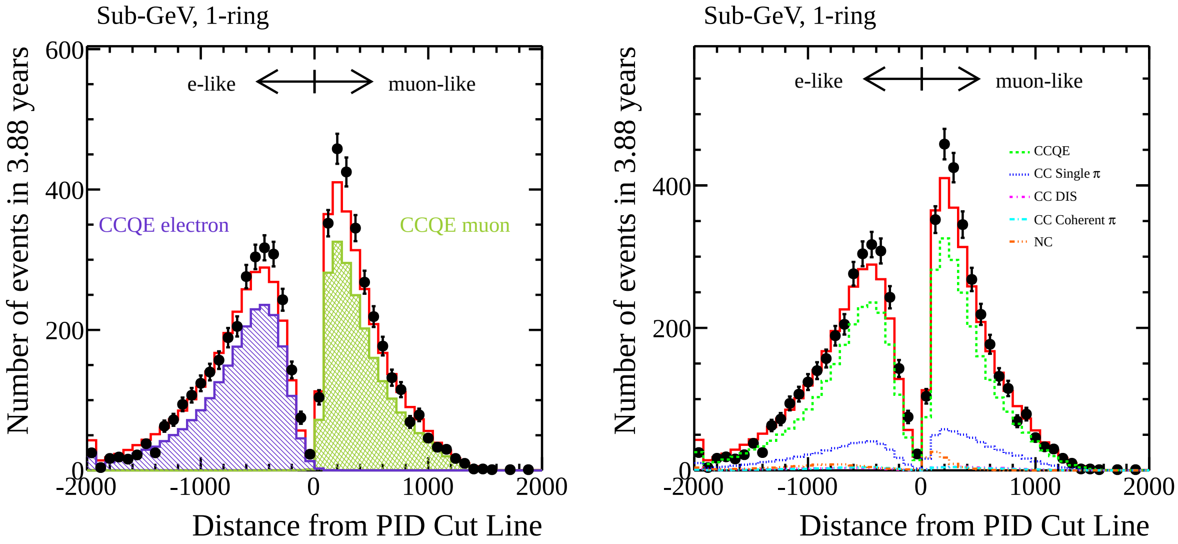

Figure B.3: Distance from the PID cut line (Equation B.1) for FCFV 1-ring sub-GeV events. Negative values are selected as e-like while positive values are selected as μ-like. A minimum threshold on the momentum of e-like events ($p_e > 100$ MeV/c) is applied. The integrated number of events shown corresponds to the FCFV sample.

B.2 Multi-Track Fitter

The idea of a multi-track fitter is introduced in Section 8.1.2, but only discussed for the π^0 fitter. A more generic multi-track fitter considers all combinations of particle hypotheses across each track, for example (e, e), (e, π^+), (π^+, e), (π^+, π^+) for a 2-track fit. The π^+ hypothesis includes an additional parameter E_{loss} describing the energy loss prior to the end-point of the track to account for hadronic interactions[1]. For the cosmic ray muon and Atm-ν analyses in Sections 8.2 and 8.3, the n-ring likelihood $\mathcal{L}_n$ is defined to be the

---

[1] Since the π^+ hypothesis approximately approaches the muon hypothesis as E_{loss} approaches its maximum, it can be used instead to reduce the computational time.

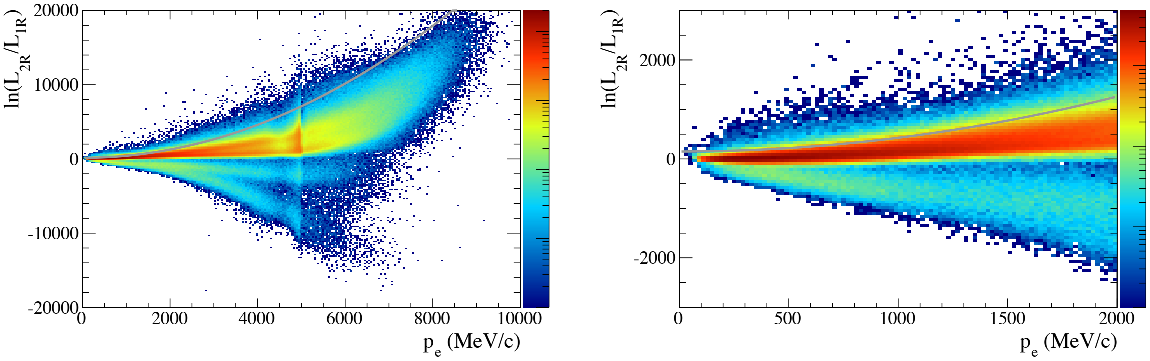

Figure B.4: $\ln(\mathcal{L}_{2R}/\mathcal{L}_{1R})$ vs p_e (momentum assuming electron hypothesis) for data events in the entire momentum region (left) and zoomed (right). The z scale is logarithmic. The grey cut line for selecting single-ring μ-like events in Section 8.3 is: $\ln(\mathcal{L}_{2R}/\mathcal{L}_{1R}) = \frac{1}{60}(p_e[\mathrm{MeV/c}])^2 + 150$.

largest (best) likelihood of all the combinations.

A stopping cosmic muon should produce a single ring most of the time. Hence, the ring counting likelihood can also be checked with the sample defined in Section 8.2. Figure B.4 shows $\ln(\mathcal{L}_{2R}/\mathcal{L}_{1R})$ versus p_e (momentum assuming electron hypothesis), where $\mathcal{L}_{2R}$ is the best 2-ring likelihood between the four (e, π^+) hypothesis combinations, and $\mathcal{L}_{1R}$ is the best likelihood chosen by the e/μ separation cut line. The features in this figure are described elsewhere [216]. For the Atm-ν analysis Section 8.3, it is sufficient to define the following PID-dependent, ring-counting cut selecting 1-ring-like events:

$$\begin{array}{ll} \ln(\mathcal{L}_{2R}/\mathcal{L}_{1R}) < 150 + \frac{1}{60}(p_e[\mathrm{MeV/c}])^2 & , \text{ for } \ln(\mathcal{L}_e/\mathcal{L}_\mu) < 0.2 \times p_e[\mathrm{MeV/c}] \ (\mu\text{-like}) \\ \ln(\mathcal{L}_{2R}/\mathcal{L}_{1R}) < 150 & , \text{ for } \ln(\mathcal{L}_e/\mathcal{L}_\mu) > 0.2 \times p_e[\mathrm{MeV/c}] \ (e\text{-like}). \end{array} \tag{B.2}$$

The cut line defined in Equation B.2 is used to define a 1-ring-like and multi-ring-like sample in the Atm-ν data. The distance to the cut line is shown in Figure B.5, after the PID selection as prescribed in Section B.1. Good data-MC agreement as well as the separation of true single-ring and multi-ring events can be seen.

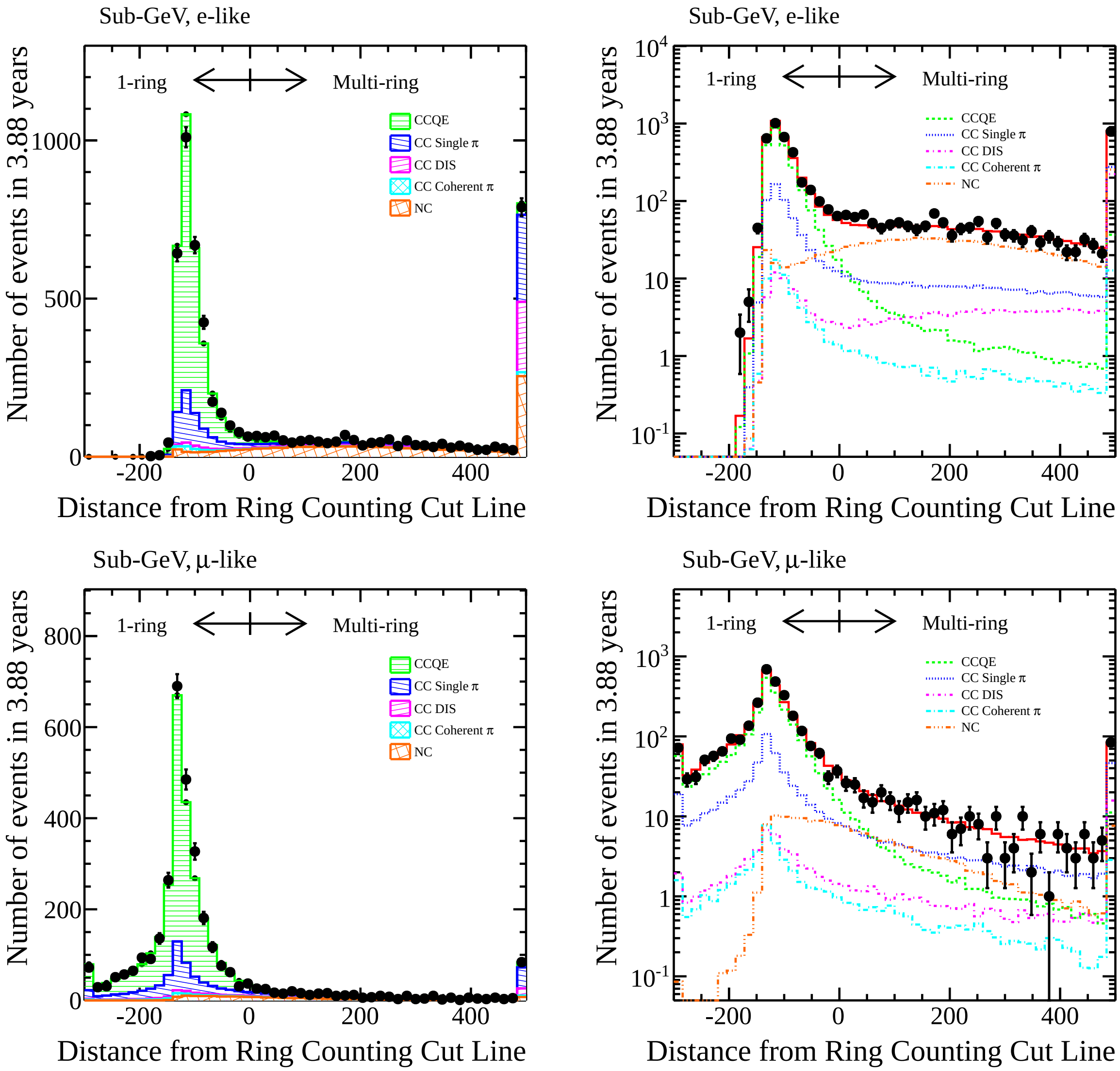

Figure B.5: Ring counting cut parameter (distance from the cut lines defined in Equation B.2) for e-like (top) and μ-like (bottom) sub-GeV FCFV events. Negative values are selected as single-ring. True neutrino interaction modes are stacked on the left (linear vertical scale) and unstacked on the right (logarithmic vertical scale).

B.3 Atm-ν Vertex Distributions

The reconstructed vertex positions separated into 1-ring, e-like and μ-like sub-GeV samples are shown in Figure B.6. Good data-MC agreement can be seen.

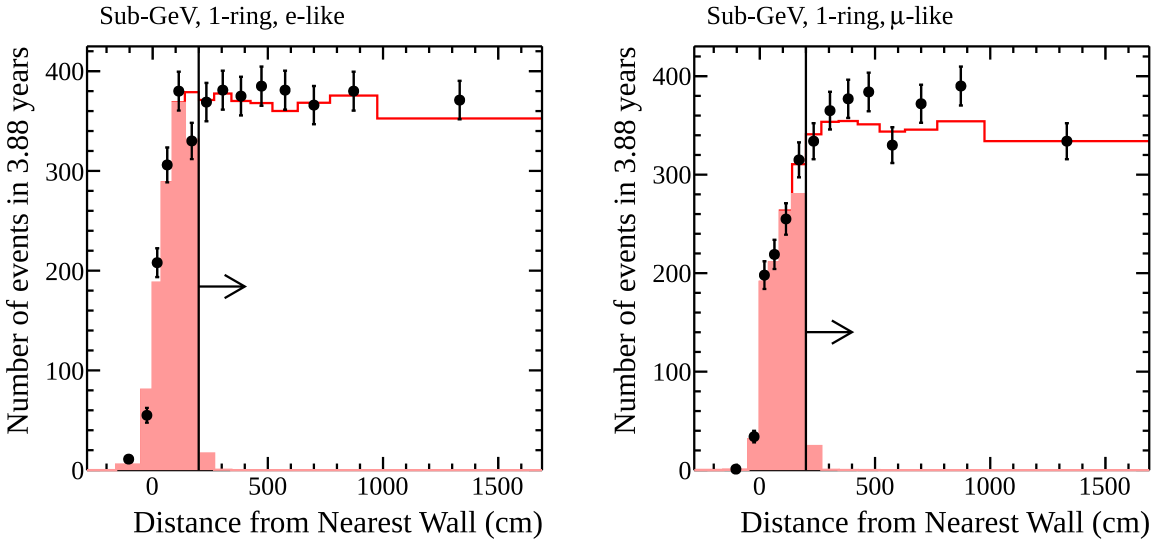

Figure B.6: Vertex distance (D_{wall}) from ID wall for 1R sub-GeV e-like (left) and μ-like (right) events. A minimum threshold on the momentum of e-like events ($p_e > 100$ MeV/c) is applied. Negative values correspond to vertices reconstructed outside the tank. The filled histogram is MC true out of fiducial volume events ($D_{wall,true} < 200$ cm).

B.4 NC π^0 Selection

This section describes a preliminary NC π^0 selection using fiTQun and provides additional validation of basic variables and reconstruction of the π^0 invariant mass peak. The top panel of the figures in this section show the cut variable, the bottom panel shows the 2-ring invariant mass ("π^0 mass" from the fiTQun π^0 fit) distribution following the given and all previous cuts including vertical lines marking the 85-185 MeV/c^2 range, and the left and right panels show linear and logarithmic vertical scales. The filled histogram (defined as signal) is true MC events with at least one π^0 produced in the neutrino interaction or through reinteractions in the water, and no other particles 10 MeV/c above Cerenkov threshold. The selection is as follows:

1. FC events (number of OD hits $nhitac < 16$ and $E_{vis} > 30$ MeV)

2. Reconstructed vertex is in the FV ($\text{wall}_{\pi^0} > 200$ cm), as shown in Figure B.7.

    - Since this series of selections is designed to eventually select a sample of π^0, the π^0 hypothesis is assumed for the most accurate vertex reconstruction. Of course this may not be accurate for other (e.g. 1-ring) events, but later cuts should remove such events.

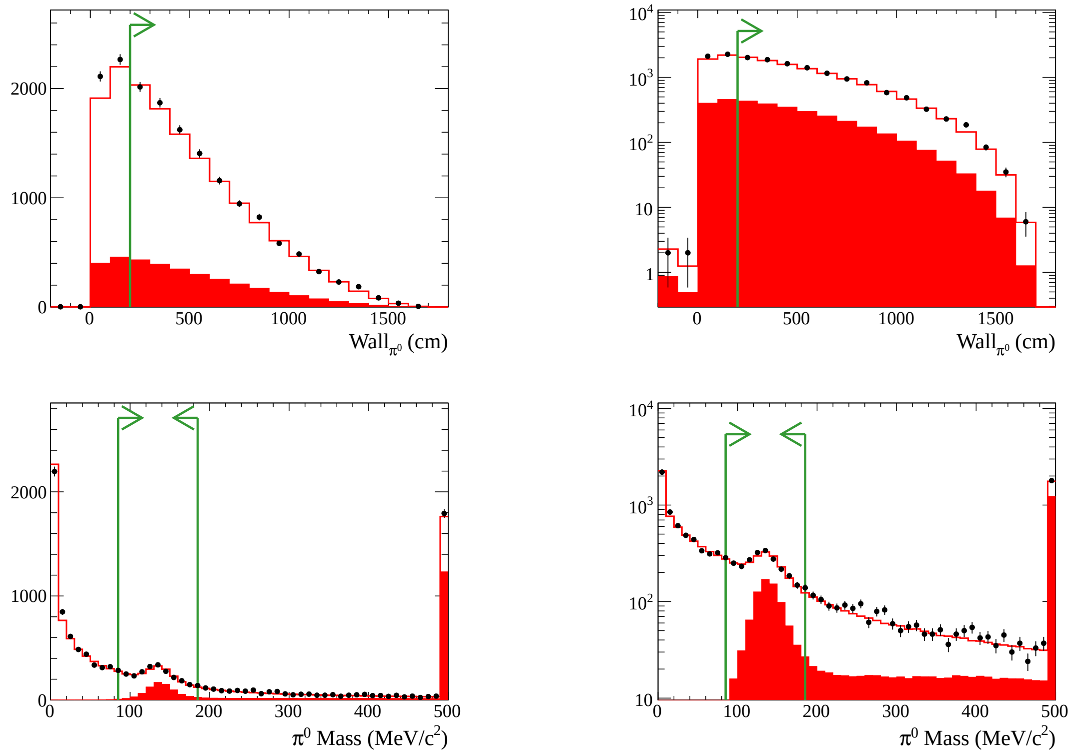

Figure B.7: Top: Vertex distance from ID wall, assuming the π^0 hypothesis after previous cuts. No minimum threshold on the momentum of e-like events is applied, resulting in the data excess near the wall (but outside the FV) from accidental cosmic muon decay-e. Bottom: cut 2 ($\text{wall}_{\pi^0} > 200$ cm) and previous cuts are applied to produce the invariant mass distribution.

3. No decay-e, as shown in Figure B.8.

    - Events with no decay-e are selected to increase the purity of NC interactions by rejecting events with particles below Čerenkov threshold (muons, pions) and low energy particles that may bias the reconstruction of the π^0.

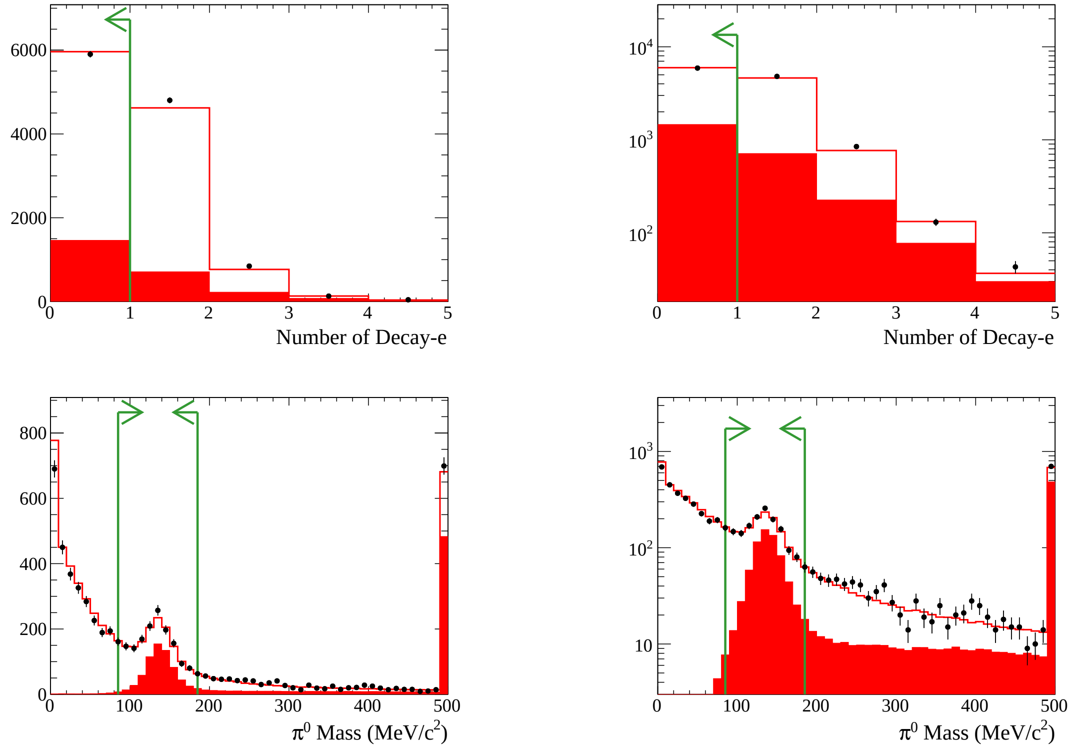

Figure B.8: Top: Number of decay-e (fiTQun sub-events - 1) as detected by fiTQun after previous cuts. Bottom: cut 3 (no decay-e) and previous cuts are applied to produce the invariant mass distribution.

4. Multiring-like ($\ln(\mathcal{L}_{2R}/\mathcal{L}_{1R}) > 80$), as shown in Figure B.9.

    - This cut removes most of the 1 ring-like events that appear at low invariant mass. It was roughly designed using MC by plotting $\ln(\mathcal{L}_{2R}/\mathcal{L}_{1R})$ versus the 1-ring momentum (note here $\mathcal{L}_{1R}$ is the maximum likelihood of the electron and π^+ hypotheses, different from the previous section), separated into two samples: 1 true particle and > 1 true particles. It was observed that this cut ($\ln(\mathcal{L}_{2R}/\mathcal{L}_{1R}) > 80$), independent of momentum, effectively separates the two samples. This cut design was an attempt at a more generic ring-counting cut, but again, depending on the analysis it can be optimized further.

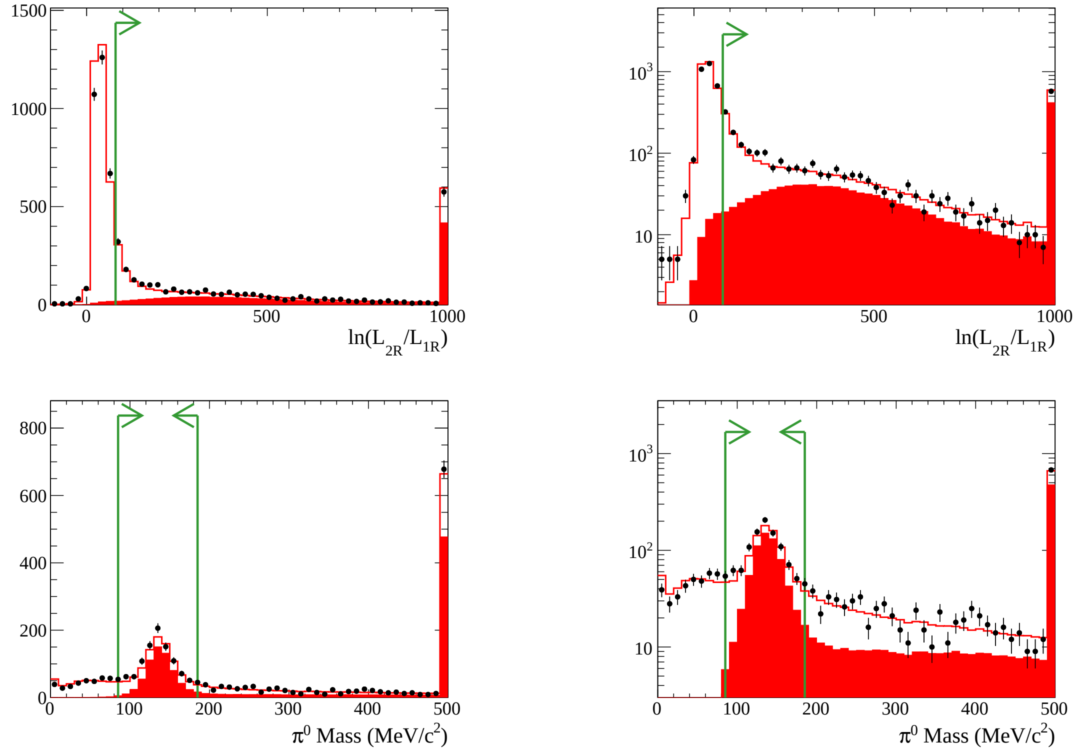

Figure B.9: Top: $\ln(\mathcal{L}_{2R}/\mathcal{L}_{1R})$ distribution after previous cuts. Bottom: cut 4 ($\ln(\mathcal{L}_{2R}/\mathcal{L}_{1R}) > 80$) and previous cuts are applied to produce the invariant mass distribution.

5. Less than 3 ring-like, as shown in Figure B.10. ($\ln(\mathcal{L}_{3R}/\mathcal{L}_{2R}) < 70$)

    - This cut was roughly designed similarly to Cut 4, except by separating the MC into $\leqslant 2$ true particles and > 2 true particles. It removes most of the high invariant mass events.

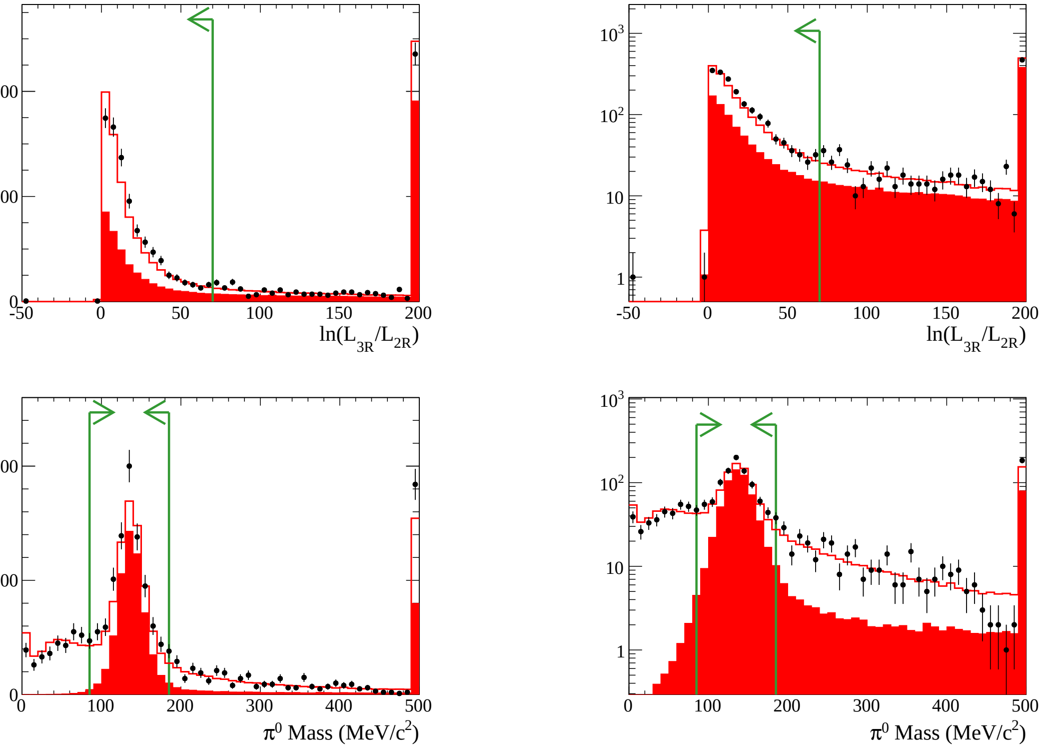

Figure B.10: Top: After previous cuts, the $\ln(\mathcal{L}_{3R}/\mathcal{L}_{2R})$ distribution, where $\mathcal{L}_{3R}$ is the maximum (best) 3-ring likelihood between the six (e, π^+) combinations. Bottom: cut 5 ($\ln(\mathcal{L}_{3R}/\mathcal{L}_{2R}) < 70$) and previous cuts are applied to produce the invariant mass distribution.

6. Both rings are *e*-like, as shown in Figure B.11.

- The PID of the two rings in the 2-ring hypothesis with the best likelihood ($\mathcal{L}_{2R}$) must both be *e*-like. This reduces the backgrounds across all invariant mass, especially again in the low invariant mass region.

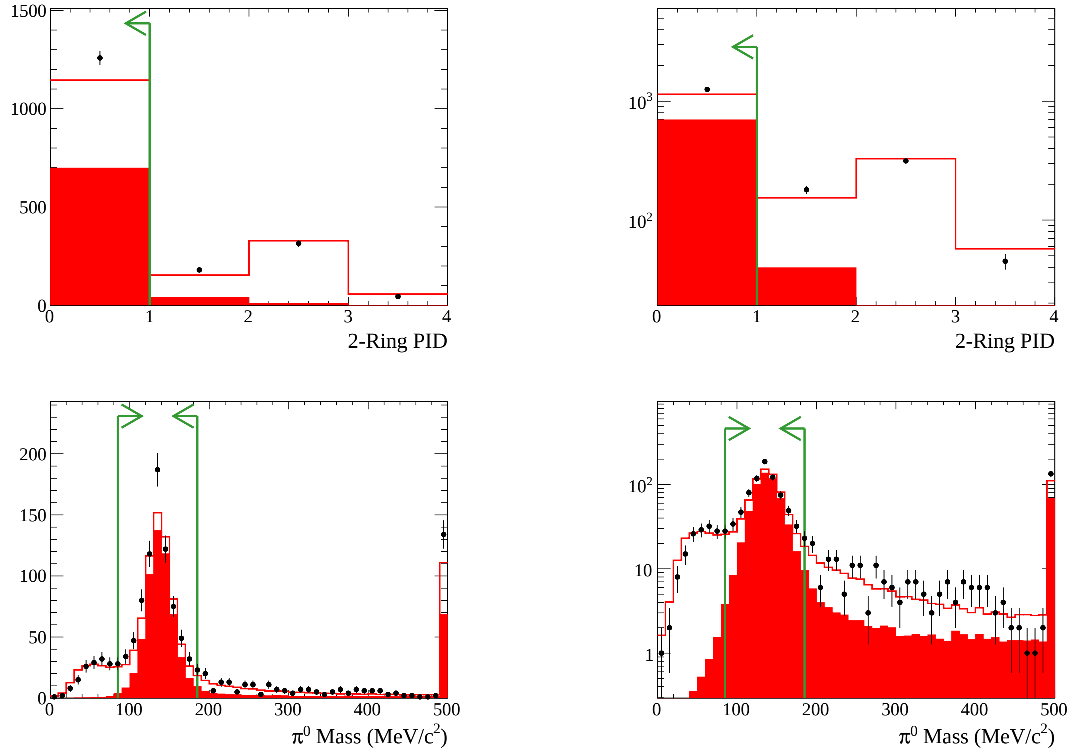

Figure B.11: Top: PID combination of the 2-ring hypothesis (0: Both *e*-like, 1: first ring is *e*-like, 2nd ring is π^+-like, 2: first ring is π^+-like, 2nd ring is *e*-like, 3: both π^+-like). Cut 6: Both rings are *e*-like and previous cuts are applied to produce the invariant mass distribution (bottom).

7. More π^0-like than e-like ($\ln(\mathcal{L}_{\pi^0}/\mathcal{L}_e) > 160$), as shown in Figure B.10.

    - The likelihood from the π^0 hypothesis is compared to that from the e-like hypothesis to further reduce backgrounds, especially in the low invariant mass region.

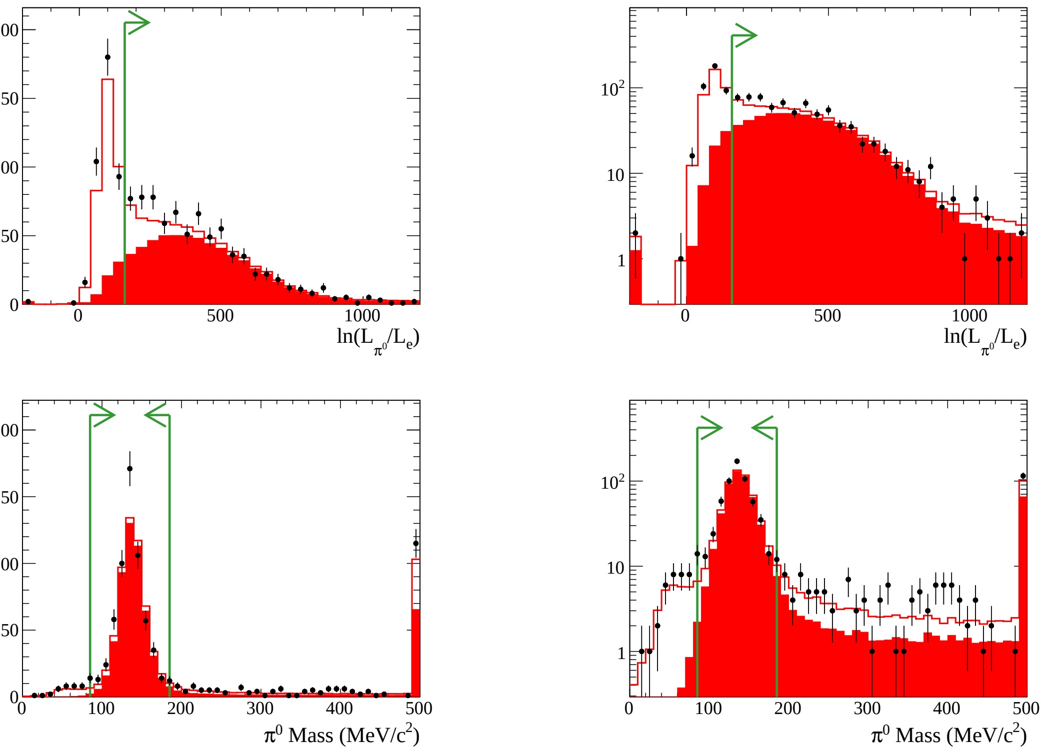

Figure B.12: Top: $\ln(\mathcal{L}_{\pi^0}/\mathcal{L}_e)$ distribution. Bottom: cut 7 ($\ln(\mathcal{L}_{\pi^0}/\mathcal{L}_e) > 160$) and previous cuts are applied to produce the invariant mass distribution, which is then used for cut 8 ($85 < M_{\pi^0} < 185$ MeV/c^2).

8. Invariant mass near expected π^0 mass ($85 < M_{\pi^0} < 185$ MeV/c^2)

After all cuts, the number of events are counted and the mass peak is fitted with results shown in Table B.1. The reconstructed momentum and direction distributions are shown in Figure B.13. Overall data/MC agreement is good, except for a slight data excess in the number of events and slightly harder momentum spectrum in data, though these are not necessarily reconstruction issues.

	Data	MC	(Data-MC)/MC
Number of Events	589 ± 25	551.3 ± 2.2	$6.84 \pm 4.43\%$
Fitted Mean	135.70 ± 0.76 MeV/c^2	137.83 ± 0.07 MeV/c^2	$-1.54 \pm 0.55\%$
Fitted Width	17.44 ± 0.74 MeV/c^2	17.48 ± 0.07 MeV/c^2	$-0.22 \pm 4.23\%$

Table B.1: Integrated number of events and Gaussian fitted mean and width after all π^0 selection cuts.

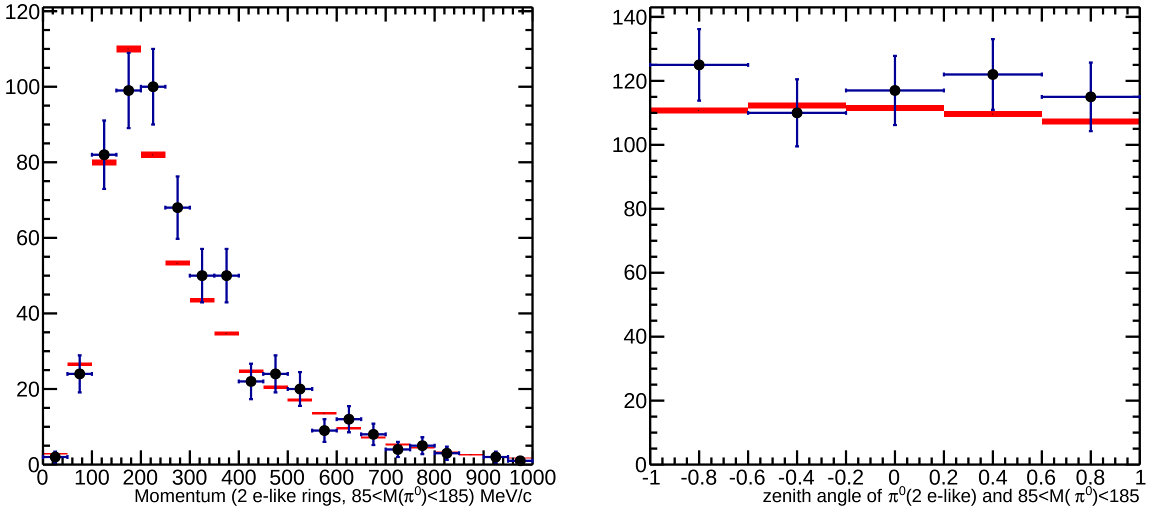

Figure B.13: Reconstructed π^0 momentum (left) and direction (right) after all π^0 selection cuts.

Appendix C

SK Systematic Error from Atm-ν

C.1 Topological Cut Parameters

Each topological cut in Table 8.2 is based on a corresponding cut parameter, L_m, defined in this section. The RC and PID parameters are based on the previous reconstruction, *APfit*, while the π^0 parameter is based on fiTQun.

Single-ring (1R) and multi-ring (mR) events are distinguished using the RC likelihood as reported by APfit in the variable $Dlfct$. However, this variable only contains information from an earlier stage of reconstruction, prior to some corrections that determine the final number of rings, N_{ring}. Therefore, we define the following RC cut parameter to be used in this analysis:

$$L_{\text{APfit RC}} = \begin{cases} 99 & Dlfct < 0 \;\&\; N_{ring} > 1 \\ -99 & Dlfct \geqslant 0 \;\&\; N_{ring} = 1 \\ Dlfct & \text{Otherwise,} \end{cases} \tag{C.1}$$

where $L_{\text{APfit RC}} < 0$ corresponds to 1R and $L_{\text{APfit RC}} \geqslant 0$ corresponds to mR. This parameter is varied for both ν_e and ν_μ channels.

For PID of the event, we use the *brightest ring* which is defined to be the ring with the largest reconstructed momentum assuming it is an electron. The PID cut parameter to separate e-like and μ-like for the brightest ring is defined as follows:

$$L_{\text{APfit PID}} = \sqrt{-\log P_e} - \sqrt{-\log P_\mu}, \tag{C.2}$$

where P is the probability for the given particle type reported by APfit. An event is identified as e-like when $L_{\text{APfit PID}} < 0$ and μ-like when $L_{\text{APfit PID}} \geqslant 0$ for the brightest ring. This parameter is only varied for ν_e MC channels in the Atm-ν fit since the uncertainty in muon PID is constrained by cosmic ray data (only RC error is considered).

The π^0 cut is defined using the fiTQun reconstruction algorithm as described in Sections 8.1.2 and 8.3. The cut parameter is defined, similarly to Equation 8.3, as follows:

$$L_{\text{fiTQun }\pi^0} = \ln(\mathcal{L}_{\text{fiTQun }\pi^0}/\mathcal{L}_{\text{fiTQun 1R}e\text{−like}}) - 70 - \frac{(140-70)}{(40-120)} \times (m_{\text{fiTQun }\pi^0}[MeV/c^2] - 120) \tag{C.3}$$

where $L_{\text{fiTQun }\pi^0} < 0$ corresponds to 1R e-like and $L_{\text{fiTQun }\pi^0} \geqslant 0$ corresponds to π^0-like. This cut is only applied to the ν_e sample.

These three topological cut parameters, $L_m = \{L_{\text{APfit RC}},\ L_{\text{APfit PID}},\ L_{\text{fiTQun }\pi^0}\}$, are used to define the control samples in Table 8.3, among the other fixed parameters. The distributions for L_m are shown in Figures 8.10 and 8.11.

C.1.1 Results

The detector parameters β (Section 8.4.2), are effective parameters which are marginalized over to obtain the final results, namely the error estimate $\Delta\varepsilon$ (Section 8.4.4) and α (Section 8.4.2) parameters. The marginal likelihoods for α are shown in Figure C.1. The posterior distributions are centered close to nominal within the the prior uncertainty of each parameter. The posteriors are also well-approximated by a Gaussian.

To extract the systematic error on ε, the marginal likelihoods for $\Delta\varepsilon/\varepsilon$ are shown in Figures C.2 and C.3. The mode, estimated from the mean of a Gaussian fitted around the peak, and RMS are used to define the shift errors and fit errors in Section 8.4.5,

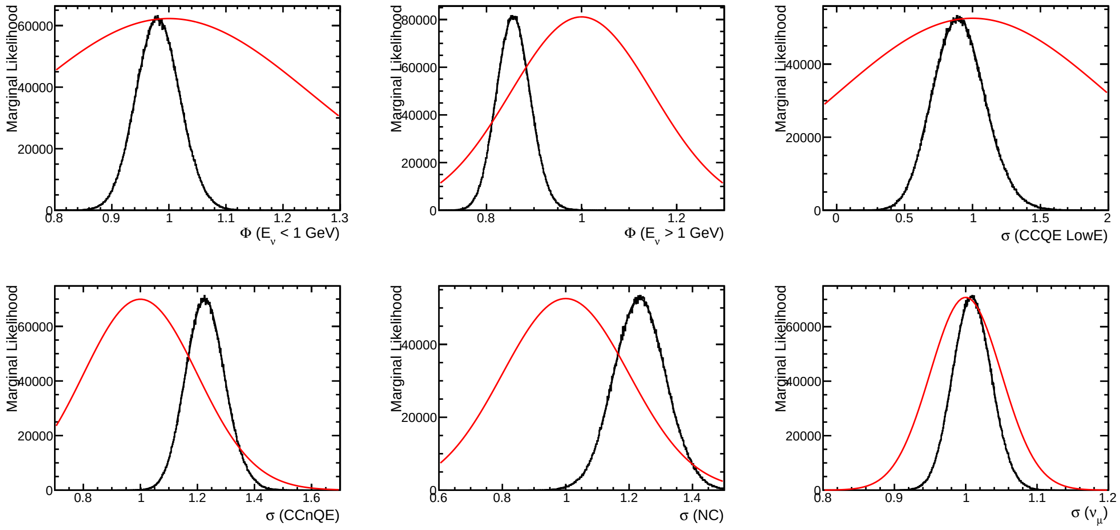

Figure C.1: The marginal likelihoods for $1+\alpha_k$. The red curves are Gaussians centered at 1 with width σ_{α_k} and the black curves are Gaussians fitted around the peak of the distributions (almost indistinguishable).

which are depicted as a Gaussian (red) curve in Figures C.2 and C.3 and summarized in Figure 8.15. This approximation is made for propagating to the toy MC and most of the T2K oscillation analyses which currently only accept Gaussian errors in the form of a covariance matrix. In most bins, the posterior falls off by 1-2 orders of magnitude before the Gaussian approximation underestimates the tail. For ν_e, this occurs in the high energy bins that are currently not considered in T2K. This approximation has a negligible effect on the final error [260].

The error matrix, calculated from the covariance of the 2D marginal likelihood distributions (Equation 7.6), is shown in Figure C.4.

C.1.2 Fit Error Correlations

The final deliverable correlation matrix in Figure 8.16 shows the correlations between dependent variables (ε). To gain insight on these correlations, the correlations with the independent variables α and β must be investigated as in Figures C.5 and C.6 respectively.

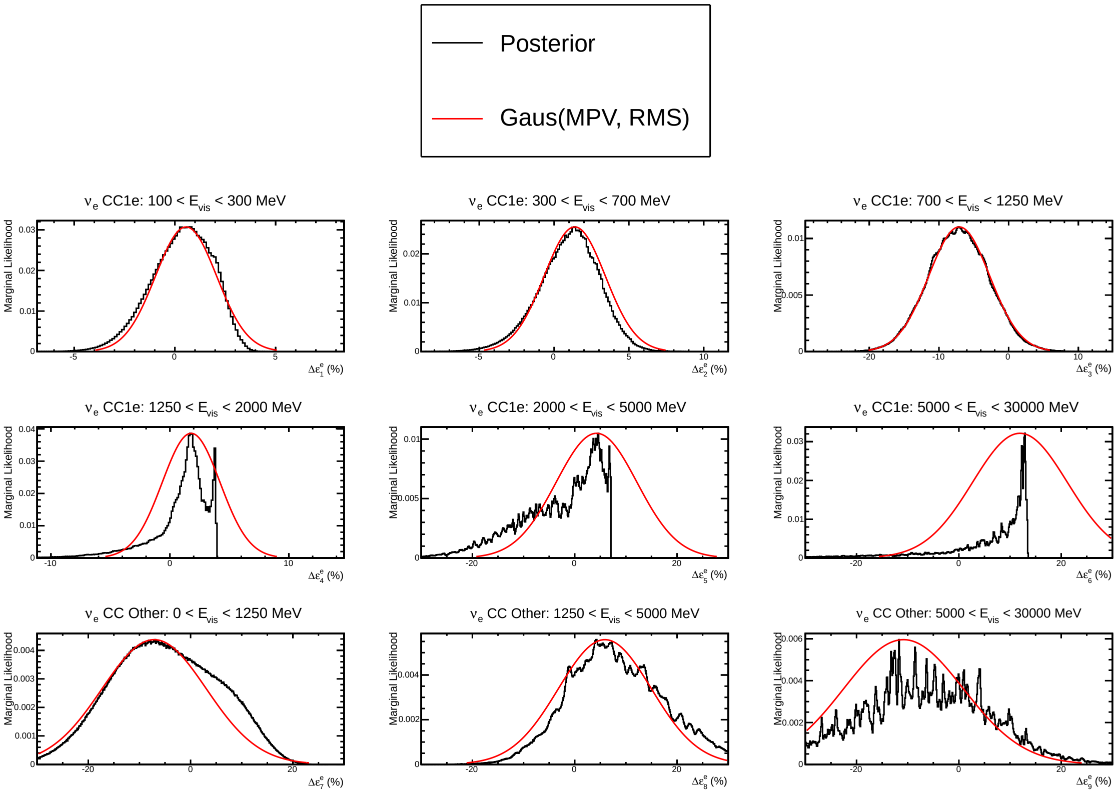

Figure C.2: The marginal likelihood posterior distributions for $\Delta\varepsilon/\varepsilon$ in %. The red curves are Gaussians center at the MPV (determined by the mean of a Gaussian fitted around the peak) with σ equal to the RMS of the distribution. The vertical axis is area normalized.

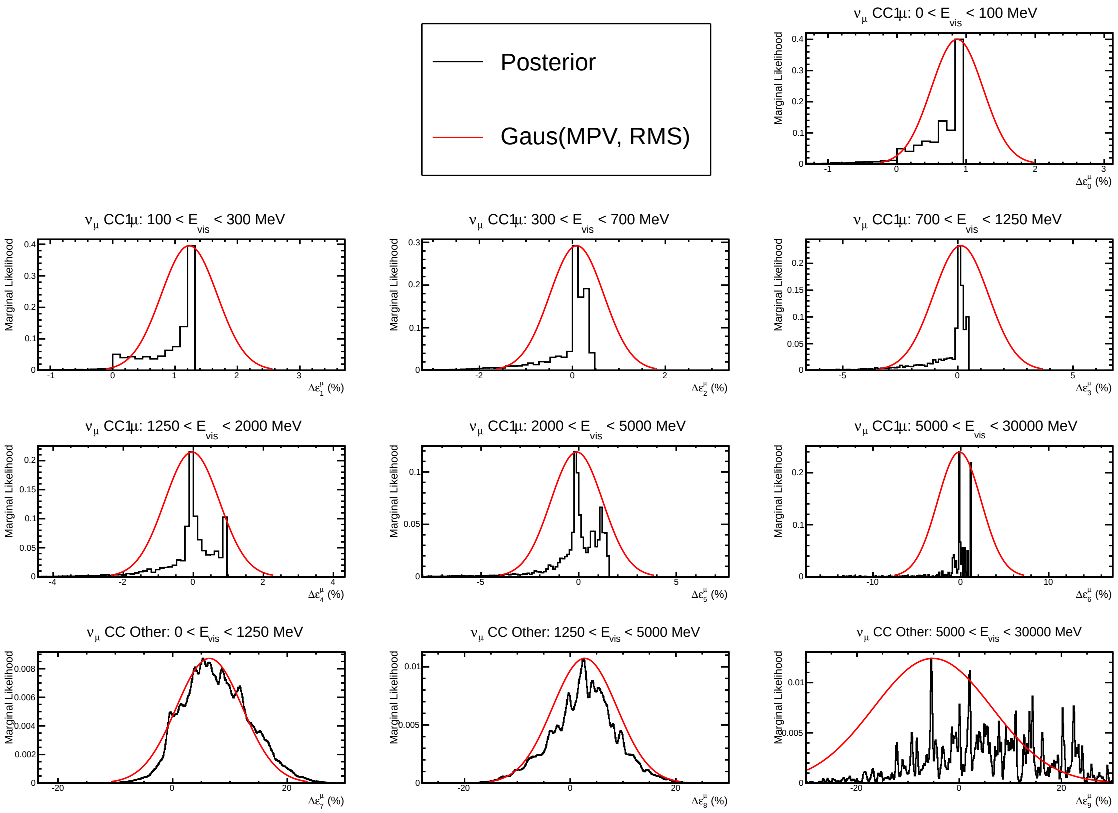

Figure C.3: The marginal likelihood posterior distributions for $\Delta\varepsilon/\varepsilon$ in %. The red curves are Gaussians center at the MPV (determined by the mean of a Gaussian fitted around the peak) with σ equal to the RMS of the distribution. The vertical axis is area normalized.

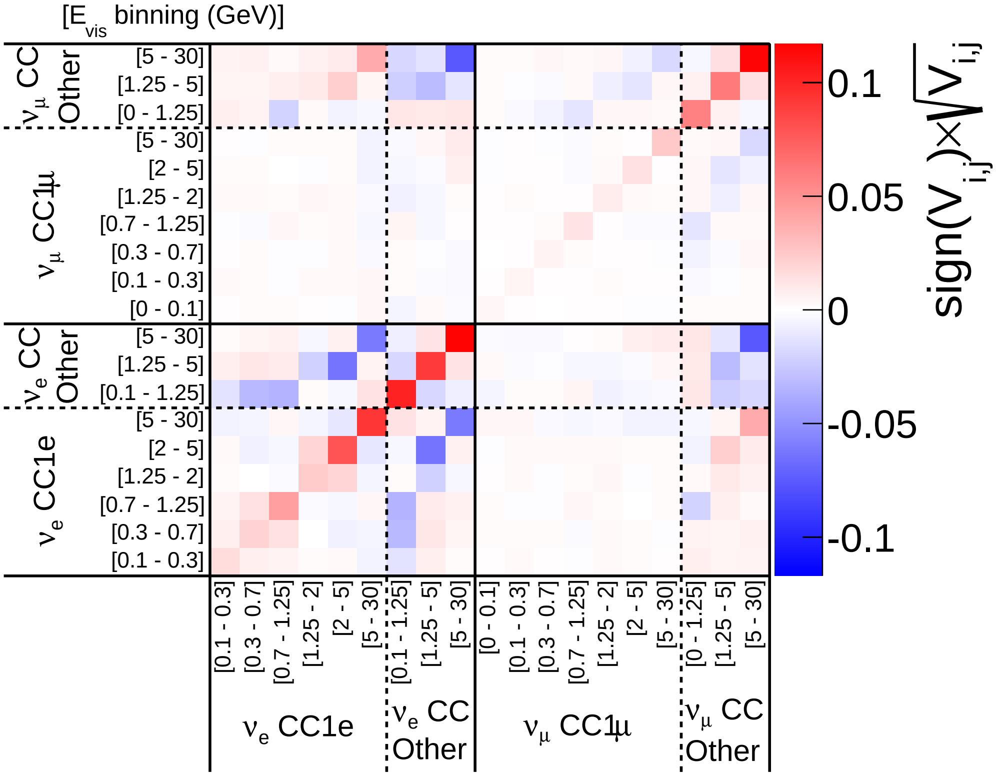

Figure C.4: The error matrix corresponding to Figure 8.16 and 8.15 showing the relative significance of the errors and their correlations.

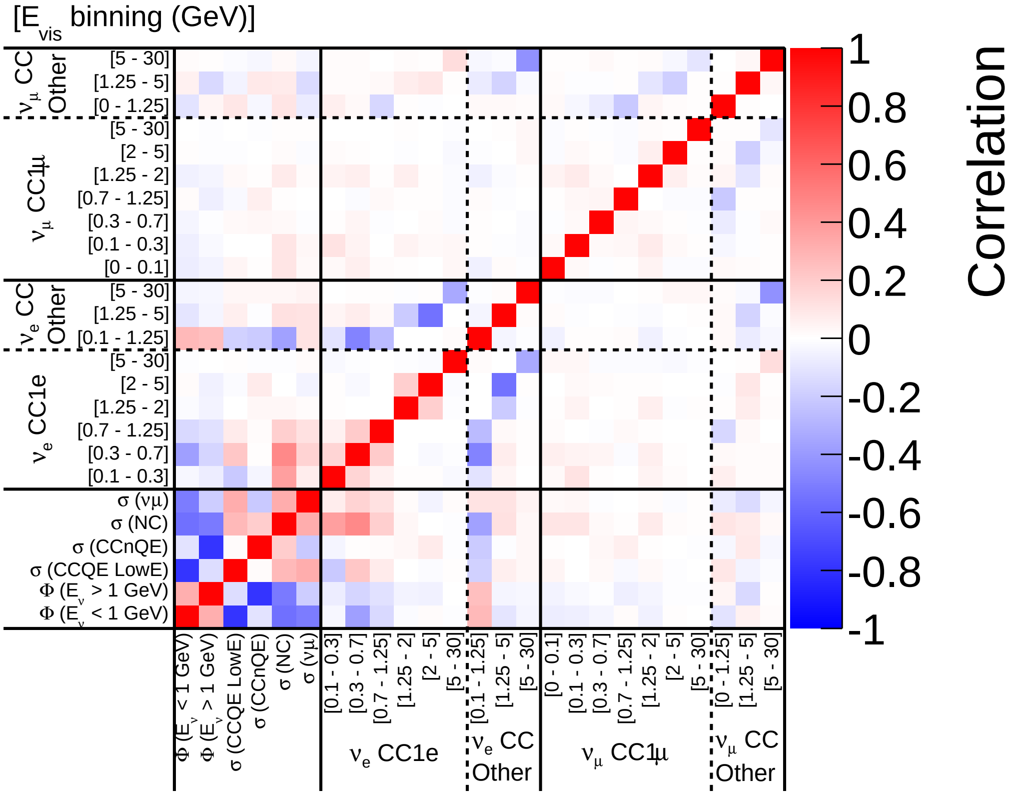

Figure C.5: Correlation matrix from Figure 8.16 including the α parameters.

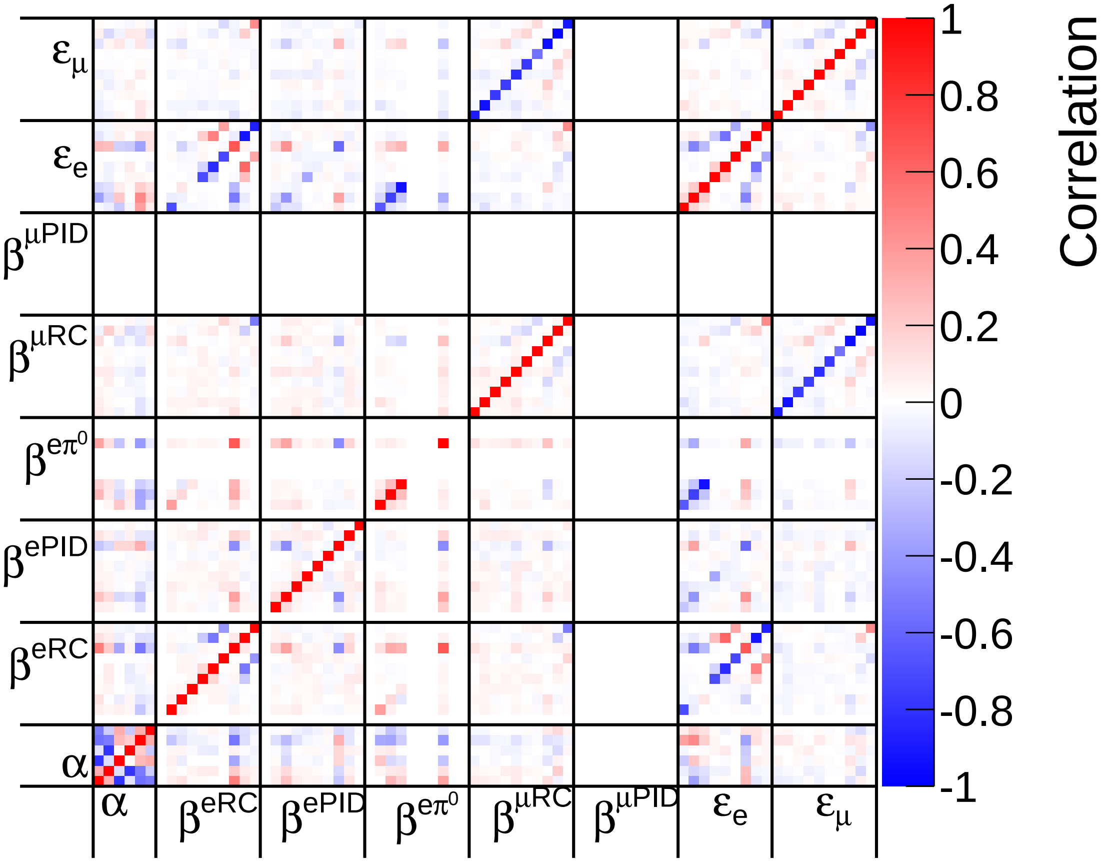

Figure C.6: Correlation matrix from Figure 8.16 including the α and β parameters. The α parameters, as well as the kinematic binning of β and ε, are the same as in Figure C.5. $\beta^{\mu PID}$ is included for completeness but is fixed to nominal in the MCMC.

For example, it can be deduced that the anti-correlations between ε are due to anti-correlations between the CC1e/μ and CC Other β parameters since they affect separate components in a single bin and the normalization in that bin must be conserved.

Some positive correlation is apparent between CC1e ε bins with $E_{vis} < 1.25$ GeV due to the NC cross section normalization parameter since there is a large population of NC events in the π^0 tail sample compared to the core sample, as shown in Figure 8.12. In this case, in order to maintain normalization when the NC cross section is increased, the β parameters must be decreased to migrate events from the tail samples to the core sample thus increasing ε (recalling the definition of β in Equation 8.4). A similar argument can be made for the positive correlation between the 1.25-5 GeV bins, except considering CCnQE and RC tail instead of NC and π^0 tail.

Bibliography

[1] W. Pauli, "Letter to the Physical Society of Tubingen." Reprint Translation into English Physics Today vol. 31, 1978. Cited on page 3.

[2] J. Chadwick, "Intensity Distribution in Magnetic Spectrum of β-Rays of Radium B + C," *Verhandl. Dtsch. phys. Ges.* **16** (1914) 383. Cited on page 3.

[3] H. Bethe and R. Peierls, "The Neutrino," *Nature* **133** (Apr., 1934) 532. Cited on page 3.

[4] F. Reines and C. L. Cowan, "The neutrino," *Nature* **178** no. 4531, (09, 1956) 446–449. `http://dx.doi.org/10.1038/178446a0`. Cited on page 3.

[5] G. Danby, J.-M. Gaillard, K. Goulianos, *et al.*, "Observation of high-energy neutrino reactions and the existence of two kinds of neutrinos," *Phys. Rev. Lett.* **9** (Jul, 1962) 36–44. `http://link.aps.org/doi/10.1103/PhysRevLett.9.36`. Cited on page 4.

[6] K. Kodama, N. Ushida, C. Andreopoulos, *et al.*, "Observation of tau neutrino interactions," *Physics Letters B* **504** no. 3, (2001) 218 – 224. `http://www.sciencedirect.com/science/article/pii/S0370269301003070`. Cited on page 4.

[7] **The ALEPH Collaboration The DELPHI Collaboration The L3 Collaboration The OPAL Collaboration The SLD Collaboration The**

LEP Electroweak Working Group The SLD Electroweak and Heavy Flavour Groups , "Precision electroweak measurements on the z resonance," *Physics Reports* **427** no. 5–6, (2006) 257 – 454. `http://www.sciencedirect.com/science/article/pii/S0370157305005119`. Cited on page 4.

[8] M. Goldhaber, L. Grodzins, and A. W. Sunyar, "Helicity of neutrinos," *Phys. Rev.* **109** (Feb, 1958) 1015–1017. `http://link.aps.org/doi/10.1103/PhysRev.109.1015`. Cited on page 4.

[9] **(Super-Kamiokande Collaboration)** , Y. Fukuda, T. Hayakawa, E. Ichihara, *et al.*, "Evidence for oscillation of atmospheric neutrinos," *Phys. Rev. Lett.* **81** (Aug, 1998) 1562–1567. `http://link.aps.org/doi/10.1103/PhysRevLett.81.1562`. Cited on pages 4 and 18.

[10] J. H. Christenson, J. W. Cronin, V. L. Fitch, and R. Turlay, "Evidence for the 2π Decay of the K_2^0 Meson," *Phys. Rev. Lett.* **13** (Jul, 1964) 138–140. `http://link.aps.org/doi/10.1103/PhysRevLett.13.138`. Cited on page 4.

[11] **(BABAR Collaboration)** , B. Aubert, D. Boutigny, J.-M. Gaillard, *et al.*, "Observation of CP Violation in the B^0 Meson System," *Phys. Rev. Lett.* **87** (Aug, 2001) 091801. `http://link.aps.org/doi/10.1103/PhysRevLett.87.091801`. Cited on page 4.

[12] C. Giunti and C. W. Kim, *Fundamentals of Neutrino Physics and Astrophysics*. Oxford University Press, Oxford, UK, 2007. ISBN 978-0-19-850871-7. Cited on pages 7, 12, and 28.

[13] L. Wolfenstein, "Neutrino oscillations in matter," *Phys. Rev. D* **17** (May, 1978)

2369–2374. `http://link.aps.org/doi/10.1103/PhysRevD.17.2369`. Cited on page 14.

[14] S. Mikheev and A. Y. Smirnov, "Resonance Amplification of Oscillations in Matter and Spectroscopy of Solar Neutrinos," *Sov.J.Nucl.Phys.* **42** (1985) 913–917. Cited on page 14.

[15] M. Freund, "Analytic approximations for three neutrino oscillation parameters and probabilities in matter," *Phys. Rev. D* **64** (Jul, 2001) 053003. `http://link.aps.org/doi/10.1103/PhysRevD.64.053003`. Cited on pages 14 and 21.

[16] J. N. Bahcall and M. H. Pinsonneault, "Standard solar models, with and without helium diffusion, and the solar neutrino problem," *Rev. Mod. Phys.* **64** (Oct, 1992) 885–926. `http://link.aps.org/doi/10.1103/RevModPhys.64.885`. Cited on page 15.

[17] R. Davis, D. S. Harmer, and K. C. Hoffman, "Search for neutrinos from the sun," *Phys. Rev. Lett.* **20** (May, 1968) 1205–1209. `http://link.aps.org/doi/10.1103/PhysRevLett.20.1205`. Cited on page 15.

[18] B. T. Cleveland, T. Daily, J. Raymond Davis, *et al.*, "Measurement of the solar electron neutrino flux with the homestake chlorine detector," *The Astrophysical Journal* **496** no. 1, (1998) 505. `http://stacks.iop.org/0004-637X/496/i=1/a=505`. Cited on page 15.

[19] P. Anselmann, W. Hampel, G. Heusser, *et al.*, "Solar neutrinos observed by {GALLEX} at gran sasso," *Physics Letters B* **285** no. 4, (1992) 376 – 389. `http://www.sciencedirect.com/science/article/pii/037026939291521A`. Cited on page 15.

[20] W. Hampel, J. Handt, G. Heusser, *et al.*, "{GALLEX} solar neutrino observations: results for {GALLEX} {IV}," *Physics Letters B* **447** no. 1–2, (1999) 127 – 133. `http://www.sciencedirect.com/science/article/pii/S0370269398015792`. Cited on page 15.

[21] A. I. Abazov, O. L. Anosov, E. L. Faizov, *et al.*, "Search for neutrinos from the sun using the reaction 71ga(nue, e-)71ge," *Phys. Rev. Lett.* **67** (Dec, 1991) 3332–3335. `http://link.aps.org/doi/10.1103/PhysRevLett.67.3332`. Cited on page 15.

[22] J. Abdurashitov, E. Veretenkin, V. Vermul, *et al.*, "Solar neutrino flux measurements by the soviet-american gallium experiment (sage) for half the 22-year solar cycle," *Journal of Experimental and Theoretical Physics* **95** no. 2, (2002) 181–193. `http://dx.doi.org/10.1134/1.1506424`. Cited on page 15.

[23] K. S. Hirata, T. Kajita, T. Kifune, *et al.*, "Observation of b8 solar neutrinos in the kamiokande-ii detector," *Phys. Rev. Lett.* **63** (Jul, 1989) 16–19. `http://link.aps.org/doi/10.1103/PhysRevLett.63.16`. Cited on page 15.

[24] K. S. Hirata, K. Inoue, T. Ishida, *et al.*, "Real-time, directional measurement of b8 solar neutrinos in the kamiokande ii detector," *Phys. Rev. D* **44** (Oct, 1991) 2241–2260. `http://link.aps.org/doi/10.1103/PhysRevD.44.2241`. No cited.

[25] K. S. Hirata, K. Inoue, T. Ishida, *et al.*, "Erratum: Real-time, directional measurement of b8 solar neutrinos in the kamiokande ii detector," *Phys. Rev. D* **45** (Mar, 1992) 2170–2170. `http://link.aps.org/doi/10.1103/PhysRevD.45.2170`. Cited on page 15.

[26] **(SNO Collaboration)** , Q. R. Ahmad, R. C. Allen, T. C. Andersen, *et al.*, "Measurement of the rate of nue+d to p+p+e- intractions produced by 8b solar

neutrinos at the sudbury neutrino observatory," *Phys. Rev. Lett.* **87** (Jul, 2001) 071301. `http://link.aps.org/doi/10.1103/PhysRevLett.87.071301`. Cited on page 15.

[27] S. Fukuda, Y. Fukuda, M. Ishitsuka, *et al.*, "Determination of solar neutrino oscillation parameters using 1496 days of super-kamiokande-i data," *Physics Letters B* **539** no. 3–4, (2002) 179 – 187. `http://www.sciencedirect.com/science/article/pii/S0370269302020907`. Cited on page 15.

[28] Q. R. Ahmad, R. C. Allen, T. C. Andersen, *et al.*, "Direct evidence for neutrino flavor transformation from neutral-current interactions in the sudbury neutrino observatory," *Phys. Rev. Lett.* **89** (Jun, 2002) 011301. `http://link.aps.org/doi/10.1103/PhysRevLett.89.011301`. Cited on page 16.

[29] **SNO Collaboration** , S. N. Ahmed, A. E. Anthony, E. W. Beier, *et al.*, "Measurement of the total active b8 solar neutrino flux at the sudbury neutrino observatory with enhanced neutral current sensitivity," *Phys. Rev. Lett.* **92** (May, 2004) 181301. `http://link.aps.org/doi/10.1103/PhysRevLett.92.181301`. Cited on page 16.

[30] **(Super-Kamiokande Collaboration)** , M. B. Smy, Y. Ashie, S. Fukuda, *et al.*, "Precise measurement of the solar neutrino day-night and seasonal variation in super-kamiokande-i," *Phys. Rev. D* **69** (Jan, 2004) 011104. `http://link.aps.org/doi/10.1103/PhysRevD.69.011104`. Cited on page 16.

[31] S. Bilenky and B. Pontecorvo, "Lepton mixing and neutrino oscillations," *Physics Reports* **41** no. 4, (1978) 225 – 261.

`http://www.sciencedirect.com/science/article/pii/0370157378900959`. Cited on page 16.

[32] P. de Holanda, W. Liao, and A. Smirnov, "Toward precision measurements in solar neutrinos," *Nuclear Physics B* **702** no. 1–2, (2004) 307 – 332. `http://www.sciencedirect.com/science/article/pii/S0550321304007333`. Cited on page 16.

[33] A. Y. Smirnov, "The msw effect and matter effects in neutrino oscillations," *Physica Scripta* **2005** no. T121, (2005) 57. `http://stacks.iop.org/1402-4896/2005/i=T121/a=008`. Cited on page 16.

[34] **SNO Collaboration** , B. Aharmim, S. N. Ahmed, A. E. Anthony, *et al.*, "Electron energy spectra, fluxes, and day-night asymmetries of 8b solar neutrinos from measurements with nacl dissolved in the heavy-water detector at the sudbury neutrino observatory," *Phys. Rev. C* **72** (Nov, 2005) 055502. `http://link.aps.org/doi/10.1103/PhysRevC.72.055502`. Cited on page 16.

[35] **KamLAND Collaboration** , S. Abe, T. Ebihara, S. Enomoto, *et al.*, "Precision measurement of neutrino oscillation parameters with kamland," *Phys. Rev. Lett.* **100** (Jun, 2008) 221803. `http://link.aps.org/doi/10.1103/PhysRevLett.100.221803`. Cited on pages 16 and 24.

[36] **SNO Collaboration** , B. Aharmim, S. N. Ahmed, A. E. Anthony, *et al.*, "Combined analysis of all three phases of solar neutrino data from the sudbury neutrino observatory," *Phys. Rev. C* **88** (Aug, 2013) 025501. `http://link.aps.org/doi/10.1103/PhysRevC.88.025501`. Cited on page 17.

[37] **KamLAND Collaboration** , A. Gando *et al.*, "Reactor On-Off Antineutrino Measurement with KamLAND," `arXiv:1303.4667 [hep-ex]`. Cited on page 17.

[38] **(Super-Kamiokande Collaboration)** , Y. Fukuda, T. Hayakawa, E. Ichihara, *et al.*, “Measurement of the flux and zenith-angle distribution of upward throughgoing muons by super-kamiokande,” *Phys. Rev. Lett.* **82** (Mar, 1999) 2644–2648. `http://link.aps.org/doi/10.1103/PhysRevLett.82.2644`. Cited on page 18.

[39] **The Super-Kamiokande Collaboration** , Y. Ashie, J. Hosaka, K. Ishihara, *et al.*, “Evidence for an oscillatory signature in atmospheric neutrino oscillations,” *Phys. Rev. Lett.* **93** (Sep, 2004) 101801. `http://link.aps.org/doi/10.1103/PhysRevLett.93.101801`. Cited on pages 18, 24, and 44.

[40] **Super-Kamiokande Collaboration** , K. Abe, Y. Hayato, T. Iida, *et al.*, “Search for differences in oscillation parameters for atmospheric neutrinos and antineutrinos at super-kamiokande,” *Phys. Rev. Lett.* **107** (Dec, 2011) 241801. `http://link.aps.org/doi/10.1103/PhysRevLett.107.241801`. Cited on page 18.

[41] **K2K Collaboration** , M. H. Ahn, E. Aliu, S. Andringa, *et al.*, “Measurement of neutrino oscillation by the k2k experiment,” *Phys. Rev. D* **74** (Oct, 2006) 072003. `http://link.aps.org/doi/10.1103/PhysRevD.74.072003`. Cited on pages 18, 44, and 111.

[42] **MINOS Collaboration** , D. G. Michael, P. Adamson, T. Alexopoulos, *et al.*, “Observation of muon neutrino disappearance with the minos detectors in the numi neutrino beam,” *Phys. Rev. Lett.* **97** (Nov, 2006) 191801. `http://link.aps.org/doi/10.1103/PhysRevLett.97.191801`. Cited on page 18.

[43] **MINOS Collaboration** , P. Adamson, I. Anghel, C. Backhouse, *et al.*,

"Measurement of neutrino and antineutrino oscillations using beam and atmospheric data in minos," *Phys. Rev. Lett.* **110** (Jun, 2013) 251801. `http://link.aps.org/doi/10.1103/PhysRevLett.110.251801`. Cited on pages 19 and 24.

[44] **Super-Kamiokande Collaboration** , K. Abe, Y. Hayato, T. Iida, *et al.*, "Solar neutrino results in super-kamiokande-iii," *Phys. Rev. D* **83** (Mar, 2011) 052010. `http://link.aps.org/doi/10.1103/PhysRevD.83.052010`. Cited on page 19.

[45] **The Super-Kamiokande Collaboration** , R. Wendell, C. Ishihara, K. Abe, *et al.*, "Atmospheric neutrino oscillation analysis with subleading effects in super-kamiokande i, ii, and iii," *Phys. Rev. D* **81** (May, 2010) 092004. `http://link.aps.org/doi/10.1103/PhysRevD.81.092004`. Cited on pages 19, 21, and 115.

[46] **CHOOZ Collaboration** , M. Apollonio *et al.*, "Search for neutrino oscillations on a long baseline at the CHOOZ nuclear power station," *Eur.Phys.J.* **C27** (2003) 331–374, `arXiv:hep-ex/0301017 [hep-ex]`. Cited on page 19.

[47] F. Boehm, J. Busenitz, B. Cook, *et al.*, "Final results from the palo verde neutrino oscillation experiment," *Phys. Rev. D* **64** (Nov, 2001) 112001. `http://link.aps.org/doi/10.1103/PhysRevD.64.112001`. Cited on page 19.

[48] **T2K Collaboration** , K. Abe, N. Abgrall, Y. Ajima, *et al.*, "Indication of electron neutrino appearance from an accelerator-produced off-axis muon neutrino beam," *Phys. Rev. Lett.* **107** (Jul, 2011) 041801. `http://link.aps.org/doi/10.1103/PhysRevLett.107.041801`. Cited on page 20.

[49] **MINOS Collaboration** , P. Adamson, D. J. Auty, D. S. Ayres, *et al.*, "Improved search for muon-neutrino to electron-neutrino oscillations in minos,"

Phys. Rev. Lett. **107** (Oct, 2011) 181802.
`http://link.aps.org/doi/10.1103/PhysRevLett.107.181802`. Cited on page 20.

[50] **Double Chooz Collaboration** , Y. Abe, C. Aberle, T. Akiri, *et al.*, "Indication of reactor anti-nue disappearance in the double chooz experiment," *Phys. Rev. Lett.* **108** (Mar, 2012) 131801.
`http://link.aps.org/doi/10.1103/PhysRevLett.108.131801`. Cited on page 20.

[51] F. P. An, J. Z. Bai, A. B. Balantekin, *et al.*, "Observation of electron-antineutrino disappearance at daya bay," *Phys. Rev. Lett.* **108** (Apr, 2012) 171803.
`http://link.aps.org/doi/10.1103/PhysRevLett.108.171803`. Cited on page 20.

[52] **RENO Collaboration** , J. K. Ahn, S. Chebotaryov, J. H. Choi, *et al.*, "Observation of reactor electron antineutrinos disappearance in the RENO experiment," *Phys. Rev. Lett.* **108** (May, 2012) 191802.
`http://link.aps.org/doi/10.1103/PhysRevLett.108.191802`. Cited on pages 20 and 23.

[53] **Double Chooz Collaboration** , Y. Abe *et al.*, "Background-independent measurement of θ_{13} in Double Chooz," `arXiv:1401.5981 [hep-ex]`. Cited on page 20.

[54] **RENO** , S.-H. Seo, "New results from RENO," `arXiv:1312.4111 [physics]`. XVth International Workshop on Neutrino Telescopes (March 2013 at Venice, Italy). Cited on page 20.

[55] **Daya Bay Collaboration** , F. An *et al.*, "Spectral measurement of electron

antineutrino oscillation amplitude and frequency at Daya Bay," `arXiv:1310.6732 [hep-ex]`. Cited on pages 20 and 24.

[56] **T2K Collaboration** , K. Abe, J. Adam, H. Aihara, *et al.*, "Observation of electron neutrino appearance in a muon neutrino beam," *Phys. Rev. Lett.* **112** (Feb, 2014) 061802. `http://link.aps.org/doi/10.1103/PhysRevLett.112.061802`. Cited on pages 20, 35, 121, and 147.

[57] Y. Itow, "Recent results in atmospheric neutrino oscillations in the light of large θ_{13}," *Nuclear Physics B - Proceedings Supplements* **235–236** no. 0, (2013) 79 – 86. `http://www.sciencedirect.com/science/article/pii/S0920563213001175`. The {XXV} International Conference on Neutrino Physics and Astrophysics. Cited on page 21.

[58] **IceCube-PINGU Collaboration** , "Letter of intent: The precision icecube next generation upgrade (pingu)," `arXiv:physics.ins-det/1401.2046 [physics.ins-det]`. Cited on page 21.

[59] H. Nunokawa, S. Parke, and R. Z. Funchal, "Another possible way to determine the neutrino mass hierarchy," *Phys. Rev. D* **72** (Jul, 2005) 013009. `http://link.aps.org/doi/10.1103/PhysRevD.72.013009`. Cited on page 21.

[60] L. Zhan, Y. Wang, J. Cao, and L. Wen, "Experimental requirements to determine the neutrino mass hierarchy using reactor neutrinos," *Phys. Rev. D* **79** (Apr, 2009) 073007. `http://link.aps.org/doi/10.1103/PhysRevD.79.073007`. No cited.

[61] X. Li, "Daya bay ii: Jiangmen underground neutrino observatory (JUNO),". `http:`

`//vietnam.in2p3.fr/2013/Inauguration/transparencies/XiaoNanLi.pdf`. Windows on the Universe (Vietnam). Cited on page 21.

[62] **MINOS Collaboration** , P. Adamson, I. Anghel, C. Backhouse, *et al.*, "Electron neutrino and antineutrino appearance in the full minos data sample," *Phys. Rev. Lett.* **110** (Apr, 2013) 171801. `http://link.aps.org/doi/10.1103/PhysRevLett.110.171801`. Cited on page 23.

[63] **NOvA Collaboration** , D. Ayres *et al.*, "NOvA: Proposal to build a 30 kiloton off-axis detector to study numu to nue oscillations in the NuMI beamline," `arXiv:hep-ex/0503053 [hep-ex]`. Cited on pages 23, 160, and 163.

[64] **Double Chooz Collaboration** , Y. Abe, C. Aberle, J. C. dos Anjos, *et al.*, "Reactor $\bar{\nu}_e$ disappearance in the Double Chooz experiment," *Phys. Rev. D* **86** (Sep, 2012) 052008. `http://link.aps.org/doi/10.1103/PhysRevD.86.052008`. Cited on page 23.

[65] F. P. An, Q. An, J. Z. Bai, *et al.*, "Improved measurement of electron antineutrino disappearance at daya bay," *Chinese Physics C* **37** no. 1, (2013) 011001. `http://stacks.iop.org/1674-1137/37/i=1/a=011001`. Cited on pages 23 and 163.

[66] **MINOS Collaboration** , P. Adamson *et al.*, "Combined analysis of ν_μ disappearance and $\nu_\mu \rightarrow \nu_e$ appearance in MINOS using accelerator and atmospheric neutrinos," `arXiv:1403.0867 [hep-ex]`. Cited on pages 23, 157, 159, and 160.

[67] **MINOS Collaboration** , P. Adamson, I. Anghel, C. Backhouse, *et al.*, "Measurement of neutrino and antineutrino oscillations using beam and atmospheric data in minos,".

`http://www-numi.fnal.gov/pr_plots/MINOS_Disappearance_June2013.pdf`. Cited on page 24.

[68] G. Fogli, E. Lisi, A. Marrone, and A. Palazzo, "Global analysis of three-flavor neutrino masses and mixings," *Progress in Particle and Nuclear Physics* **57** no. 2, (2006) 742 – 795. `http://www.sciencedirect.com/science/article/pii/S0146641005000980`. Cited on page 25.

[69] M. Gonzalez-Garcia and M. Maltoni, "Phenomenology with massive neutrinos," *Physics Reports* **460** no. 1–3, (2008) 1 – 129. `http://www.sciencedirect.com/science/article/pii/S0370157308000148`. Cited on page 25.

[70] G. L. Fogli, E. Lisi, A. Marrone, *et al.*, "Global analysis of neutrino masses, mixings, and phases: Entering the era of leptonic cp violation searches," *Phys. Rev. D* **86** (Jul, 2012) 013012. `http://link.aps.org/doi/10.1103/PhysRevD.86.013012`. Cited on pages 25 and 26.

[71] M. Gonzalez-Garcia, M. Maltoni, J. Salvado, and T. Schwetz, "Global fit to three neutrino mixing: critical look at present precision," *Journal of High Energy Physics* **2012** no. 12, (2012) 1–24. `http://dx.doi.org/10.1007/JHEP12%282012%29123`. Cited on page 25.

[72] **Particle Data Group** , J. Beringer, J. F. Arguin, R. M. Barnett, *et al.*, "Review of particle physics," *Phys. Rev. D* **86** (Jul, 2012) 010001. `http://link.aps.org/doi/10.1103/PhysRevD.86.010001`. Cited on pages 26, 81, 97, 98, 119, 159, and 183.

[73] S. King, "Importance of neutrino oscillation parameter measurements,"

Beta-beam task group (2005) .
`http://beta-beam.web.cern.ch/beta-beam/Meetings/RAL05/RAL_king.pdf`.
Cited on page 26.

[74] S. M. Bilenky and S. T. Petcov, "Massive neutrinos and neutrino oscillations," *Rev. Mod. Phys.* **59** (Jul, 1987) 671–754.
`http://link.aps.org/doi/10.1103/RevModPhys.59.671`. Cited on page 27.

[75] C. Kraus, B. Bornschein, L. Bornschein, *et al.*, "Final results from phase ii of the mainz neutrino mass searchin tritium β decay," *The European Physical Journal C - Particles and Fields* **40** no. 4, (2005) 447–468.
`http://dx.doi.org/10.1140/epjc/s2005-02139-7`. Cited on page 29.

[76] V. N. Aseev, A. I. Belesev, A. I. Berlev, *et al.*, "Upper limit on the electron antineutrino mass from the troitsk experiment," *Phys. Rev. D* **84** (Dec, 2011) 112003. `http://link.aps.org/doi/10.1103/PhysRevD.84.112003`. Cited on page 29.

[77] K. Eitel, "Direct neutrino mass experiments," *Nuclear Physics B - Proceedings Supplements* **143** no. 0, (2005) 197 – 204.
`http://www.sciencedirect.com/science/article/pii/S0920563205001076`.
{NEUTRINO} 2004 Proceedings of the {XXIst} International Conference on Neutrino Physics and Astrophysics. Cited on page 29.

[78] G. Drexlin, V. Hannen, S. Mertens, and C. Weinheimer, "Current direct neutrino mass experiments," *Advances in High Energy Physics* **2013** (2013) 39.
`http://dx.doi.org/10.1155/2013/293986`. Cited on page 29.

[79] **Planck Collaboration** , P. Ade *et al.*, "Planck 2013 results. XVI. Cosmological parameters," `arXiv:1303.5076 [astro-ph.CO]`. Cited on page 29.

[80] W. H. Furry, "On transition probabilities in double beta-disintegration," *Phys. Rev.* **56** (Dec, 1939) 1184–1193. `http://link.aps.org/doi/10.1103/PhysRev.56.1184`. Cited on page 30.

[81] M. Goeppert-Mayer, "Double beta-disintegration," *Phys. Rev.* **48** (Sep, 1935) 512–516. `http://link.aps.org/doi/10.1103/PhysRev.48.512`. Cited on page 30.

[82] J. Suhonen and O. Civitarese, "Weak-interaction and nuclear-structure aspects of nuclear double beta decay," *Physics Reports* **300** no. 3–4, (1998) 123 – 214. `http://www.sciencedirect.com/science/article/pii/S0370157397000872`. Cited on page 30.

[83] S. M. BILENKY and C. GIUNTI, "Neutrinoless double-beta decay: A brief review," *Modern Physics Letters A* **27** no. 13, (2012) 1230015, `http://www.worldscientific.com/doi/pdf/10.1142/S0217732312300157`. `http://www.worldscientific.com/doi/abs/10.1142/S0217732312300157`. Cited on page 30.

[84] **EXO Collaboration** , M. Auger, D. J. Auty, P. S. Barbeau, *et al.*, "Search for neutrinoless double-beta decay in xe-136 with exo-200," *Phys. Rev. Lett.* **109** (Jul, 2012) 032505. `http://link.aps.org/doi/10.1103/PhysRevLett.109.032505`. Cited on page 31.

[85] M. Chen, "The sno liquid scintillator project," *Nuclear Physics B - Proceedings Supplements* **145** no. 1-3 SPEC. ISS., (2005) 65–68. `http://www.scopus.com/inward/record.url?eid=2-s2.0-18144389408&partnerID=40&md5=cba9d5e5dfa1e392a3c6014939b4900e`. cited By (since 1996)39. Cited on page 31.

[86] **KamLAND-Zen Collaboration** , A. Gando, "First result from

KamLAND-Zen : Double beta decay with ^{136}Xe," `arXiv:1205.6130 [hep-ex]`. Cited on page 31.

[87] C. Aalseth, D. Anderson, R. Arthur, *et al.*, "The MAJORANA neutrinoless double-beta decay experiment," *Physics of Atomic Nuclei* **67** no. 11, (2004) 2002–2010. `http://dx.doi.org/10.1134/1.1825519`. Cited on page 31.

[88] D. G. Phillips, E. Aguayo, F. T. Avignone, *et al.*, "The MAJORANA experiment: an ultra-low background search for neutrinoless double-beta decay," *Journal of Physics: Conference Series* **381** no. 1, (2012) 012044. `http://stacks.iop.org/1742-6596/381/i=1/a=012044`. Cited on page 31.

[89] C. L. Bennett, D. Larson, J. L. Weiland, *et al.*, "Nine-year wilkinson microwave anisotropy probe (wmap) observations: Final maps and results," *The Astrophysical Journal Supplement Series* **208** no. 2, (2013) 20. `http://stacks.iop.org/0067-0049/208/i=2/a=20`. Cited on page 31.

[90] A. D. Sakharov, "Violation of cp in variance, c asymmetry, and baryon asymmetry of the universe," *Soviet Physics Uspekhi* **34** no. 5, (1991) 392. `http://stacks.iop.org/0038-5670/34/i=5/a=A08`. Cited on page 32.

[91] M. Fukugita and T. Yanagida, "Barygenesis without grand unification," *Physics Letters B* **174** no. 1, (1986) 45 – 47. `http://www.sciencedirect.com/science/article/pii/0370269386911263`. Cited on page 32.

[92] P. Arnold and L. McLerran, "Sphalerons, small fluctuations, and baryon-number violation in electroweak theory," *Phys. Rev. D* **36** (Jul, 1987) 581–595. `http://link.aps.org/doi/10.1103/PhysRevD.36.581`. Cited on page 32.

[93] S. Davidson, E. Nardi, and Y. Nir, "Leptogenesis," *Physics Reports* **466** no. 4–5, (2008) 105 – 177.

`http://www.sciencedirect.com/science/article/pii/S0370157308001889`. Cited on page 32.

[94] R. N. Mohapatra, S. Antusch, K. S. Babu, *et al.*, "Theory of neutrinos: a white paper," *Reports on Progress in Physics* **70** no. 11, (2007) 1757. `http://stacks.iop.org/0034-4885/70/i=11/a=R02`. Cited on page 32.

[95] **T2K Collaboration** , K. Abe, N. Abgrall, H. Aihara, *et al.*, "The T2K experiment," *Nuclear Instruments and Methods in Physics Research Section A: Accelerators, Spectrometers, Detectors and Associated Equipment* **659** no. 1, (2011) 106 – 135. `http://www.sciencedirect.com/science/article/pii/S0168900211011910`. Cited on pages 33, 37, 91, and 121.

[96] **(T2K Collaboration)** , K. Abe, J. Adam, H. Aihara, *et al.*, "Precise Measurement of the Neutrino Mixing Parameter θ_{23} from Muon Neutrino Disappearance in an Off-Axis Beam," *Phys. Rev. Lett.* **112** (May, 2014) 181801. `http://link.aps.org/doi/10.1103/PhysRevLett.112.181801`. Cited on pages 35 and 147.

[97] N. A. *et al.*, "Flux Prediction and Uncertainties for the 2012a Oscillation Analysis," *T2K-TN-099 (Internal)* (2012) . Cited on page 38.

[98] A. Ichikawa, "Design concept of the magnetic horn system for the T2K neutrino beam," *Nuclear Instruments and Methods in Physics Research Section A: Accelerators, Spectrometers, Detectors and Associated Equipment* **690** no. 0, (2012) 27 – 33. `http://www.sciencedirect.com/science/article/pii/S0168900212007115`. Cited on page 39.

[99] D. Beavis, A. Carroll, and I. Chiang, "Long baseline neutrino oscillation experiment at the AGS," Tech. Rep. 52878, Apr., 1995. Cited on page 42.

[100] **T2K Collaboration** , K. Abe, N. Abgrall, H. Aihara, *et al.*, "T2K neutrino flux prediction," *Phys. Rev. D* **87** (Jan, 2013) 012001. `http://link.aps.org/doi/10.1103/PhysRevD.87.012001`. Cited on pages 43, 80, and 81.

[101] K. Abe, N. Abgrall, Y. Ajima, *et al.*, "Measurements of the T2K neutrino beam properties using the INGRID on-axis near detector," *Nuclear Instruments and Methods in Physics Research Section A: Accelerators, Spectrometers, Detectors and Associated Equipment* **694** no. 0, (2012) 211 – 223. `http://www.sciencedirect.com/science/article/pii/S0168900212002987`. Cited on page 44.

[102] D. B. CLINE, "Some recent results from the UA1 experiment at CERN," *Annals of the New York Academy of Sciences* **490** no. 1, (1987) 120–144. `http://dx.doi.org/10.1111/j.1749-6632.1987.tb40369.x`. Cited on page 46.

[103] S. Assylbekov, G. Barr, B. Berger, *et al.*, "The T2K ND280 off-axis pi–zero detector," *Nuclear Instruments and Methods in Physics Research Section A: Accelerators, Spectrometers, Detectors and Associated Equipment* **686** no. 0, (2012) 48 – 63. `http://www.sciencedirect.com/science/article/pii/S0168900212005153`. Cited on page 47.

[104] N. Abgrall, B. Andrieu, P. Baron, *et al.*, "Time projection chambers for the T2K near detectors," *Nuclear Instruments and Methods in Physics Research Section A: Accelerators, Spectrometers, Detectors and Associated Equipment* **637** no. 1,

(2011) 25 – 46.
`http://www.sciencedirect.com/science/article/pii/S0168900211003421`.
Cited on page 47.

[105] P.-A. Amaudruz, M. Barbi, D. Bishop, *et al.*, "The T2K fine-grained detectors," *Nuclear Instruments and Methods in Physics Research Section A: Accelerators, Spectrometers, Detectors and Associated Equipment* **696** no. 0, (2012) 1 – 31.
`http://www.sciencedirect.com/science/article/pii/S0168900212008789`.
Cited on page 48.

[106] D. Allan, C. Andreopoulos, C. Angelsen, *et al.*, "The electromagnetic calorimeter for the T2K near detector ND280," *Journal of Instrumentation* **8** no. 10, (2013) P10019. `http://stacks.iop.org/1748-0221/8/i=10/a=P10019`. Cited on page 48.

[107] S. Aoki, G. Barr, M. Batkiewicz, *et al.*, "The T2K Side Muon Range Detector (SMRD)," *Nuclear Instruments and Methods in Physics Research Section A: Accelerators, Spectrometers, Detectors and Associated Equipment* **698** no. 0, (2013) 135 – 146.
`http://www.sciencedirect.com/science/article/pii/S0168900212011242`.
Cited on page 49.

[108] S. Fukuda, Y. Fukuda, T. Hayakawa, *et al.*, "The Super-Kamiokande detector," *Nuclear Instruments and Methods in Physics Research Section A: Accelerators, Spectrometers, Detectors and Associated Equipment* **501** no. 2–3, (2003) 418 – 462.
`http://www.sciencedirect.com/science/article/pii/S016890020300425X`.
Cited on page 49.

[109] **(The Super-Kamiokande Collaboration)** , Y. Hayato, M. Earl, Y. Fukuda,

et al., “Search for proton decay through $p \to \bar{\nu} + K^+$ in a large water cherenkov detector,” *Phys. Rev. Lett.* **83** (Aug, 1999) 1529–1533. `http://link.aps.org/doi/10.1103/PhysRevLett.83.1529`. Cited on page 49.

[110] **The Super-Kamiokande Collaboration** , C. Regis, K. Abe, Y. Hayato, *et al.*, “Search for proton decay via $p \to \mu^+ + K^0$ in super-kamiokande i, ii, and iii,” *Phys. Rev. D* **86** (Jul, 2012) 012006. `http://link.aps.org/doi/10.1103/PhysRevD.86.012006`. No cited.

[111] **Super-Kamiokande Collaboration** , H. Nishino, S. Clark, K. Abe, *et al.*, “Search for proton decay via $p \to e^+(\mu^+) + \pi^0$ in a large water cherenkov detector,” *Phys. Rev. Lett.* **102** (Apr, 2009) 141801. `http://link.aps.org/doi/10.1103/PhysRevLett.102.141801`. No cited.

[112] **The Super-Kamiokande Collaboration** , H. Nishino, K. Abe, Y. Hayato, *et al.*, “Search for nucleon decay into charged antilepton plus meson in super-kamiokande i and ii,” *Phys. Rev. D* **85** (Jun, 2012) 112001. `http://link.aps.org/doi/10.1103/PhysRevD.85.112001`. Cited on page 49.

[113] T. Tanaka, K. Abe, Y. Hayato, *et al.*, “An indirect search for weakly interacting massive particles in the sun using 3109.6 days of upward-going muons in super-kamiokande,” *The Astrophysical Journal* **742** no. 2, (2011) 78. `http://stacks.iop.org/0004-637X/742/i=2/a=78`. Cited on page 49.

[114] **Super-Kamiokande Collaboration** , K. Bays, T. Iida, K. Abe, *et al.*, “Supernova relic neutrino search at super-kamiokande,” *Phys. Rev. D* **85** (Mar, 2012) 052007. `http://link.aps.org/doi/10.1103/PhysRevD.85.052007`. Cited on page 49.

[115] K. Ueno, K. Abe, Y. Hayato, *et al.*, “Search for GUT monopoles at super–kamiokande,” *Astroparticle Physics* **36** no. 1, (2012) 131 – 136.

`http://www.sciencedirect.com/science/article/pii/S0927650512001120`. Cited on page 49.

[116] B. M. Bolotovskii, "Vavilov – cherenkov radiation: its discovery and application," *Physics-Uspekhi* **52** no. 11, (2009) 1099. `http://stacks.iop.org/1063-7869/52/i=11/a=R03`. Cited on page 51.

[117] J. D. Jackson, *Classical Electrodynamics*. John Wiley and Sons, third ed., 1998. Cited on pages 52 and 54.

[118] V. Ginsburg and I. Frank, "Radiation of a uniformly moving electron due to its transition from one medium to another," *JETP* **16** (1946) . Cited on page 54.

[119] P. Goldsmith and J. V. Jelley, "Optical transition radiation from protons entering metal surfaces," *Philosophical Magazine* **4** no. 43, (1959) 836–844. `http://www.tandfonline.com/doi/abs/10.1080/14786435908238241`. Cited on page 54.

[120] V. Scarpine, A. Lumpkin, W. Schappert, and G. Tassotto, "Optical transition radiation imaging of intense proton beams at fnal," *Nuclear Science, IEEE Transactions on* **51** no. 4, (Aug, 2004) 1529–1532. Cited on pages 54, 55, and 56.

[121] J. Bosser, J. Mann, G. Ferioli, and L. Warts, "Optical transition radiation proton beam profile monitor," *Nuclear Instruments and Methods in Physics Research Section A: Accelerators, Spectrometers, Detectors and Associated Equipment* **238** no. 1, (1985) 45 – 52. `http://www.sciencedirect.com/science/article/pii/0168900285910253`. No cited.

[122] A. Toyoda, "First Light for Optical Transition Radiation Monitor at J-PARC," in *Proceedings of DIPAC09*. 2009.

`http://dipac09.web.psi.ch/Proceedings/papers/tupd33.pdf`. Cited on pages 54, 55, and 56.

[123] M. L. Ter-Mikaelian, *High-energy Electromagnetic Processes in Condensed Media*. John Wiley and Sons, english language ed., 1972. Cited on page 55.

[124] L. Wartski, S. Roland, J. Lasalle, M. Bolore, and G. Filippi, "Interference phenomenon in optical transition radiation and its application to particle beam diagnostics and multiplescattering measurements," *Journal of Applied Physics* **46** no. 8, (1975) 3644–3653. `http://scitation.aip.org/content/aip/journal/jap/46/8/10.1063/1.322092`. Cited on page 55.

[125] "B-Con Engineering Inc.." `http://www.bconeng.com`. Cited on page 58.

[126] S. Bhadra, M. Cadabeschi, P. de Perio, *et al.*, "Optical transition radiation monitor for the T2K experiment," *Nuclear Instruments and Methods in Physics Research Section A: Accelerators, Spectrometers, Detectors and Associated Equipment* **703** no. 0, (2013) 45 – 58. `http://www.sciencedirect.com/science/article/pii/S0168900212013812`. Cited on pages 58, 59, 71, 74, 75, and 76.

[127] "Thermo Scientific CID8710D1M." `http://www.thermo.com.cn/Resources/200802/productPDF_26885.pdf`. Cited on page 58.

[128] P. de Perio, "Prototyping and Simulation of the T2K OTR Monitor," *Work Report* (2007) . `http://www.physics.utoronto.ca/~pdeperio/pub/otr/dePerio-ReportS07.pdf`. Cited on pages 60, 67, and 69.

[129] "Niki glass co., ltd, demarquest af995r." `http://www.nikiglass.co.jp/supplier/radiation/demar/demar.html`. Cited on page 61.

[130] SHOTT, "Radiation resistant optical glasses." `http://www.couriertronics.com/docs/notes/General_Machine_Vision_Appnotes/TIE-42_Radiation_resistant_glasses_(1).pdf`. Cited on page 67.

[131] "ThorLabs DL3147-060." `http://www.thorlabs.com/thorproduct.cfm?partnumber=DL3147-060`. Cited on page 67.

[132] V. Galymov, *Neutrino flux predictions for the T2K long baseline neutrino oscillation experiment*. PhD thesis, York University, 2012. `http://inspirehep.net/record/1218070`. Cited on pages 71, 73, 78, 80, and 81.

[133] labsphere, "A guide to integrating sphere radiometry and photometry." `http://www.labsphere.com/uploads/technical-guides/a-guide-to-integrating-sphere-theory-and-applications.pdf`. Cited on page 72.

[134] R. A. Wendell, "Prob3++ neutrino oscillation probability calculator." `http://www.phy.duke.edu/~raw22/public/Prob3++`. Cited on page 80.

[135] V. Barger, K. Whisnant, S. Pakvasa, and R. J. N. Phillips, "Matter effects on three-neutrino oscillations," *Phys. Rev. D* **22** (Dec, 1980) 2718–2726. `http://link.aps.org/doi/10.1103/PhysRevD.22.2718`. Cited on page 80.

[136] G. Battistoni, F. Cerutti, A. Fassò, *et al.*, "The fluka code: description and benchmarking," *AIP Conference Proceedings* **896** no. 1, (2007) 31–49. `http:`

`//scitation.aip.org/content/aip/proceeding/aipcp/10.1063/1.2720455`. Cited on page 80.

[137] R. Brun, F. Bruyant, M. Maire, A. McPherson, and P. Zanarini, "GEANT3,". Revised version. Cited on pages 80 and 92.

[138] C. Zeitnitz and T. Gabriel, "The GEANT-CALOR interface and benchmark calculations of ZEUS test calorimeters," *Nuclear Instruments and Methods in Physics Research Section A: Accelerators, Spectrometers, Detectors and Associated Equipment* **349** no. 1, (1994) 106 – 111. `http://www.sciencedirect.com/science/article/pii/0168900294906130`. Cited on pages 80, 92, 111, and 182.

[139] Y. Hayato, "A neutrino interaction simulation program library neut," *Acta Physica Polonica B* **40** no. 9, (Sep, 2009) 2477. `http://th-www.if.uj.edu.pl/acta/vol40/abs/v40p2477.htm`. Cited on pages 84 and 87.

[140] G. Mitsuka, "Neut," *AIP Conference Proceedings* **981** no. 1, (2008) 262–264. `http://scitation.aip.org/content/aip/proceeding/aipcp/10.1063/1.2898954`. Cited on page 84.

[141] D. Casper, "The NUANCE neutrino physics simulation, and the future," *Nuclear Physics B - Proceedings Supplements* **112** no. 1–3, (2002) 161 – 170. `http://www.sciencedirect.com/science/article/pii/S0920563202017565`. Cited on pages 84 and 85.

[142] J. A. Formaggio and G. P. Zeller, "From eV to EeV: Neutrino cross sections across energy scales," *Rev. Mod. Phys.* **84** (Sep, 2012) 1307–1341.

`http://link.aps.org/doi/10.1103/RevModPhys.84.1307`. Cited on pages 84 and 85.

[143] **MiniBooNE Collaboration** , A. A. Aguilar-Arevalo, C. E. Anderson, A. O. Bazarko, *et al.*, "Neutrino flux prediction at miniboone," *Phys. Rev. D* **79** (Apr, 2009) 072002. `http://link.aps.org/doi/10.1103/PhysRevD.79.072002`. Cited on pages 84 and 85.

[144] M. Honda, T. Kajita, K. Kasahara, and S. Midorikawa, "Improvement of low energy atmospheric neutrino flux calculation using the jam nuclear interaction model," *Phys. Rev. D* **83** (Jun, 2011) 123001. `http://link.aps.org/doi/10.1103/PhysRevD.83.123001`. Cited on page 85.

[145] **SciBooNE Collaboration** , Y. N. *et al.*, "Measurement of inclusive charged current interactions on carbon in a few-gev neutrino beam," *Phys. Rev. D* **83** (Jan, 2011) 012005. `http://link.aps.org/doi/10.1103/PhysRevD.83.012005`. Cited on page 85.

[146] **MINOS Collaboration** , P. Adamson, C. Andreopoulos, K. E. Arms, *et al.*, "Neutrino and antineutrino inclusive charged-current cross section measurements with the minos near detector," *Phys. Rev. D* **81** (Apr, 2010) 072002. `http://link.aps.org/doi/10.1103/PhysRevD.81.072002`. Cited on pages 85, 87, and 89.

[147] Q. Wu, S. Mishra, A. Godley, *et al.*, "A precise measurement of the muon neutrino–nucleon inclusive charged current cross section off an isoscalar target in the energy range by {NOMAD}," *Physics Letters B* **660** no. 1–2, (2008) 19 – 25. `http://www.sciencedirect.com/science/article/pii/S0370269307015390`. Cited on page 85.

[148] C. L. Smith, "Neutrino reactions at accelerator energies," *Physics Reports* **3**

no. 5, (1972) 261 – 379.
`http://www.sciencedirect.com/science/article/pii/0370157372900105`.
Cited on page 86.

[149] R. Smith and E. Moniz, "Neutrino reactions on nuclear targets," *Nuclear Physics B* **43** no. 0, (1972) 605 – 622.
`http://www.sciencedirect.com/science/article/pii/0550321372900405`.
Cited on page 86.

[150] "Neutrino reactions on nuclear targets: Errata on R.A. Smith and E.J. Moniz, Nucl. Phys. B43 (1972) 605.," *Nuclear Physics B* **101** no. 2, (1975) 547 –.
`http://www.sciencedirect.com/science/article/pii/0550321375906124`.
Cited on page 86.

[151] **K2K Collaboration** , R. Gran, E. J. Jeon, E. Aliu, *et al.*, "Measurement of the quasielastic axial vector mass in neutrino interactions on oxygen," *Phys. Rev. D* **74** (Sep, 2006) 052002.
`http://link.aps.org/doi/10.1103/PhysRevD.74.052002`. Cited on page 86.

[152] **MiniBooNE Collaboration** , A. A. Aguilar-Arevalo, C. E. Anderson, A. O. Bazarko, *et al.*, "First measurement of the muon neutrino charged current quasielastic double differential cross section," *Phys. Rev. D* **81** (May, 2010) 092005. `http://link.aps.org/doi/10.1103/PhysRevD.81.092005`. Cited on page 86.

[153] P. de Perio, M. Hartz, Y. Hayato, *et al.*, "Cross section parameters for the 2012a oscillation analysis," *T2K-TN-108 (Internal)* (2012) . Cited on pages 86 and 89.

[154] D. Rein and L. M. Sehgal, "Neutrino-excitation of baryon resonances and single pion production," *Annals of Physics* **133** no. 1, (1981) 79 – 153.

`http://www.sciencedirect.com/science/article/pii/0003491681902426`. Cited on page 86.

[155] D. Rein, “Angular distribution in neutrino-induced single pion production processes,” *Zeitschrift für Physik C Particles and Fields* **35** no. 1, (1987) 43–64. `http://dx.doi.org/10.1007/BF01561054`. Cited on page 86.

[156] S. Singh, M. Vicente-Vacas, and E. Oset, “Nuclear effects in neutrino production of δ at intermediate energies,” *Physics Letters B* **416** no. 1–2, (1998) 23 – 28. `http://www.sciencedirect.com/science/article/pii/S0370269397013257`. Cited on page 86.

[157] **MiniBooNE Collaboration** , A. A. Aguilar-Arevalo, C. E. Anderson, A. O. Bazarko, *et al.*, “Measurement of ν_μ-induced charged-current neutral pion production cross sections on mineral oil at $E_\nu \in 0.5$˘2.0GeV,” *Phys. Rev. D* **83** (Mar, 2011) 052009. `http://link.aps.org/doi/10.1103/PhysRevD.83.052009`. Cited on pages 87 and 100.

[158] **MiniBooNE Collaboration** , A. A. Aguilar-Arevalo, C. E. Anderson, A. O. Bazarko, *et al.*, “Measurement of neutrino-induced charged-current charged pion production cross sections on mineral oil at $E_\nu \sim 1$GeV,” *Phys. Rev. D* **83** (Mar, 2011) 052007. `http://link.aps.org/doi/10.1103/PhysRevD.83.052007`. Cited on page 88.

[159] **The MiniBooNE Collaboration** , A. A. Aguilar-Arevalo, C. E. Anderson, A. O. Bazarko, *et al.*, “Measurement of ν_μ and $\bar{\nu}_\mu$ induced neutral current single π^0 production cross sections on mineral oil at $E_\nu \sim \mathcal{O}(1 \text{ GeV})$,” *Phys. Rev. D* **81** (Jan, 2010) 013005. `http://link.aps.org/doi/10.1103/PhysRevD.81.013005`. Cited on pages 87, 88, and 100.

[160] M. Glück, E. Reya, and A. Vogt, “Dynamical parton distributions revisited,” *The*

European Physical Journal C - Particles and Fields **5** (1998) 461–470. `http://dx.doi.org/10.1007/s100529800978`. 10.1007/s100529800978. Cited on page 87.

[161] A. Bodek and U. Yang, "Modeling neutrino and electron scattering inelastic cross-sections in the few GeV region with effective LO PDFs TV Leading Order," *Nucl.Phys.Proc.Suppl.* (2003) , `arXiv:hep-ex/0308007 [hep-ex]`. Cited on page 87.

[162] M. Derrick, P. Gregory, L. G. Hyman, *et al.*, "Properties of the hadronic system resulting from $\bar{\nu}_\mu p$ interactions," *Phys. Rev. D* **17** (Jan, 1978) 1–15. `http://link.aps.org/doi/10.1103/PhysRevD.17.1`. Cited on page 87.

[163] S. Barlag, P. Dam, E. Wolf, *et al.*, "Charged hadron multiplicities in high energy $\bar{\nu}_\mu n$ and $\bar{\nu}_\mu p$ interactions," *Zeitschrift für Physik C Particles and Fields* **11** no. 4, (1982) 283–292. `http://dx.doi.org/10.1007/BF01578279`. Cited on page 87.

[164] T. Sjostrand, "PYTHIA 5.7 and JETSET 7.4: Physics and manual," `arXiv:hep-ph/9508391 [hep-ph]`. Cited on page 87.

[165] D. Rein and L. M. Sehgal, "Coherent π^0 production in neutrino reactions," *Nuclear Physics B* **223** no. 1, (1983) 29 – 44. `http://www.sciencedirect.com/science/article/pii/0550321383900901`. Cited on page 89.

[166] D. Rein and L. Sehgal, "PCAC and the deficit of forward muons in production by neutrinos," *Physics Letters B* **657** no. 4–5, (2007) 207 – 209. `http://www.sciencedirect.com/science/article/pii/S0370269307012580`. Cited on page 89.

[167] **K2K Collaboration** , M. Hasegawa, E. Aliu, S. Andringa, *et al.*, "Search for coherent charged pion production in neutrino-carbon interactions," *Phys. Rev.*

Lett. **95** (Dec, 2005) 252301.
`http://link.aps.org/doi/10.1103/PhysRevLett.95.252301`. Cited on page 89.

[168] **The SciBooNE Collaboration** , K. Hiraide, J. L. Alcaraz-Aunion, S. J. Brice, *et al.*, "Search for charged current coherent pion production on carbon in a few-gev neutrino beam," *Phys. Rev. D* **78** (Dec, 2008) 112004. `http://link.aps.org/doi/10.1103/PhysRevD.78.112004`. Cited on pages 89 and 91.

[169] **The SciBooNE Collaboration** , Y. Kurimoto, J. L. Alcaraz-Aunion, S. J. Brice, *et al.*, "Improved measurement of neutral current coherent π^0 production on carbon in a few-gev neutrino beam," *Phys. Rev. D* **81** (Jun, 2010) 111102. `http://link.aps.org/doi/10.1103/PhysRevD.81.111102`. Cited on pages 89 and 91.

[170] M. Day and K. S. McFarland, "Differences in quasielastic cross sections of muon and electron neutrinos," *Phys. Rev. D* **86** (Sep, 2012) 053003. `http://link.aps.org/doi/10.1103/PhysRevD.86.053003`. Cited on page 90.

[171] S. Agostinelli, J. Allison, K. Amako, *et al.*, "Geant4—a simulation toolkit," *Nuclear Instruments and Methods in Physics Research Section A: Accelerators, Spectrometers, Detectors and Associated Equipment* **506** no. 3, (2003) 250 – 303. `http://www.sciencedirect.com/science/article/pii/S0168900203013688`. Cited on page 91.

[172] A. Cervera-Villanueva, J. Gómez-Cadenas, and J. Hernando, ""recpack" a reconstruction toolkit," *Nuclear Instruments and Methods in Physics Research Section A: Accelerators, Spectrometers, Detectors and Associated Equipment* **534** no. 1–2, (2004) 180 – 183.

`http://www.sciencedirect.com/science/article/pii/S0168900204015220`. Proceedings of the {IXth} International Workshop on Advanced Computing and Analysis Techniques in Physics Research. Cited on page 91.

[173] C. Bojechko, J. Caravaca, R. Castillo, *et al.*, "CC-multiple-pion event selections in the ND280 tracker using Run 1-4 data," *T2K-TN-152 (Internal)* (2013) . Cited on pages 92, 148, and 153.

[174] K. Abe, Y. Hayato, T. Iida, *et al.*, "Calibration of the super-kamiokande detector," *Nuclear Instruments and Methods in Physics Research Section A: Accelerators, Spectrometers, Detectors and Associated Equipment* **737** no. 0, (2014) 253 – 272. `http://www.sciencedirect.com/science/article/pii/S016890021301646X`. Cited on pages 92 and 121.

[175] H. W. Bertini, "Nonelastic interactions of nucleons and π mesons with complex nuclei at energies below 3 gev," *Phys. Rev. C* **6** (Aug, 1972) 631–659. `http://link.aps.org/doi/10.1103/PhysRevC.6.631`. Cited on page 93.

[176] B. Martin and M. Pidcock, "KN interactions in the resonance region: (i). analysis of data," *Nuclear Physics B* **126** no. 2, (1977) 266 – 284. `http://www.sciencedirect.com/science/article/pii/0550321377903820`. No cited.

[177] B. Martin and M. Pidcock, "{KN} interactions in the resonance region: (ii). amplitudes," *Nuclear Physics B* **126** no. 2, (1977) 285 – 297. `http://www.sciencedirect.com/science/article/pii/0550321377903832`. No cited.

[178] J. S. Hyslop, R. A. Arndt, L. D. Roper, and R. L. Workman, "Partial-wave

analysis of k^+-nucleon scattering," *Phys. Rev. D* **46** (Aug, 1992) 961–969. `http://link.aps.org/doi/10.1103/PhysRevD.46.961`. No cited.

[179] D. A. Sparrow, "Effects of the nuclear medium on the observation of baryon number violation," *AIP Conference Proceedings* **123** no. 1, (1984) 1019–1025. `http://scitation.aip.org/content/aip/proceeding/aipcp/10.1063/1.34840`. Cited on page 93.

[180] P. de Perio, "Neut pion fsi," *AIP Conference Proceedings* **1405** no. 1, (2011) 223–228. `http://scitation.aip.org/content/aip/proceeding/aipcp/10.1063/1.3661590`. Cited on page 93.

[181] R. D. Woods and D. S. Saxon, "Diffuse surface optical model for nucleon-nuclei scattering," *Phys. Rev.* **95** (Jul, 1954) 577–578. `http://link.aps.org/doi/10.1103/PhysRev.95.577`. Cited on page 95.

[182] C. W. De Jager *et al.*, "Nuclear charge- and magnetization-density-distribution parameters from elastic electron scattering," *Atomic Data and Nuclear Data Tables* **14** (1974) 479. Cited on page 95.

[183] L. Salcedo *et al.*, "Computer simulation of inclusive pion nuclear reactions," *Nucl. Phys. A* **484** (1988) 557. Cited on pages 95, 97, and 100.

[184] G. Rowe *et al.*, "Energy-dependent phase shift analysis of pion-nucleon scattering below 400 MeV," *Phys. Rev. C* **18** no. 1, (1978) 584. Cited on page 97.

[185] D. Rowntree *et al.*, "π^+ absorption on N and Ar," *Phys. Rev. C* **60** (1999) 054610. Cited on pages 97 and 173.

[186] B. G. Ritchie, “Parametrization of total and differential cross sections for $\pi d \to pp$ below 1 GeV,” *Phys. Rev. C* **44** (1991) 533. Cited on page 97.

[187] K. Ueno, *Study of neutral-current de-excitation gamma-rays with the T2K neutrino beam.* PhD thesis, University of Tokyo, 2012. Cited on page 97.

[188] C. Oh *et al.*, “Combined analysis of the reactions $pp \to pp$, $\pi d \to \pi d$ and $\pi d \to pp$,” *Phys. Rev. C* **56** no. 2, (1997) 635. Cited on pages 97, 98, 112, and 183.

[189] R. Arndt *et al.*, “Dispersion relation constrained partial wave analysis of πN elastic and $\pi N \to \eta N$ scattering data: The baryon spectrum,” *Phys. Rev. C* **69** (2004) 035213. Cited on pages 99, 113, 183, and 188.

[190] R. Workman *et al.*, “SAID Partial Wave Analysis Program,” *Center for Nuclear Studies, George Washington University* (Accessed 2009) . `http://gwdac.phys.gwu.edu`. Cited on pages 97, 98, 112, 113, and 175.

[191] J. Whitmore, “Multiparticle production in the Fermilab bubble chambers,” *Physics Reports (Section C of Physics Letters)* **27** no. 5, (1976) 187. Cited on page 99.

[192] P. Rodrigues, “Comparing pion production models to MiniBooNE data,” `arXiv:1402.4709 [hep-ex]`. Cited on page 100.

[193] G. Bellettini *et al.*, “Proton-nuclei cross sections at 20 GeV,” *Nucl. Phys.* **79** (1966) 609. Cited on page 101.

[194] J. Arends *et al.*, “Inclusive charged pion photoproduction on ^{12}C using tagged photons in the energy range (200-390) MeV,” *Z. Phys. A* **305** (1982) 205. Cited on pages 104, 174, 176, 177, and 178.

[195] K. Baba *et al.*, “Quasi-free pion photoproduction from carbon above 300 MeV,” *Nucl. Phys. A* **306** (1978) 292. Cited on pages 104 and 105.

[196] **The MiniBooNE Collaboration** , A. Aguilar-Arevalo *et al.*, “A Search for electron neutrino appearance at the $\Delta m^2 \sim 1\text{eV}^2$ scale,” *Phys.Rev.Lett.* **98** (2007) 231801, `arXiv:0704.1500 [hep-ex]`. Cited on page 111.

[197] H. Fesefeldt, “THE SIMULATION OF HADRONIC SHOWERS: PHYSICS AND APPLICATIONS,”. See also the BOOKS subfile under the following call number: QA76:E81:LONG. Cited on page 111.

[198] A. Fasso, A. Ferrari, J. Ranft, and P. Sala, “FLUKA: Present status and future developments,” *Conf.Proc.* **C9309194** (1993) 493–502. Cited on page 111.

[199] K. Fujita, “1000 (Measurement of the Response of a 1000t Water Cherenkov Detector to Charged Particles),” Master’s thesis, 1994. Cited on pages 112, 182, 185, 188, and 189.

[200] A. S. Carroll *et al.*, “Pion-nucleus total cross sections in the (3, 3) resonance region,” *Phys. Rev. C* **14** no. 2, (1976) 635. Cited on pages 112, 113, 173, and 183.

[201] A. S. Clough *et al.*, “Pion-nucleus total cross sections from 88 to 860 MeV,” *Nucl. Phys. B* **76** (1974) 15. Cited on pages 173 and 183.

[202] A. Saunders *et al.*, “Reaction and total cross sections for low energy π^+ and π^- on isospin zero nuclei,” *Phys. Rev. C* **53** no. 4, (1996) 1745. Cited on pages 112, 113, 173, and 183.

[203] L. Lyons, *Statistical for Nuclear and Particle Physicists.* Cambridge University Press, 1992. Cited on page 116.

[204] P. de Perio, M. Hartz, K. Mahn, , and S. Oser, “Constraining the Flux and Cross Section Models with Data from the ND280 Detector for the 2012a Oscillation Analysis,” *T2K-TN-106* (2012) . `http://www.t2k.org/docs/technotes/106`. Cited on page 116.

[205] C. Andreopoulos *et al.*, “T2K 3.23×10^{19}-POT Muon-Neutrino Disappearance Analysis,” *T2K-TN-036 (Internal)* (2010) . Cited on page 116.

[206] F. James and M. Winkler, “MINUIT User’s Guide,”. Cited on pages 119, 123, and 157.

[207] S. Brooks, A. Gelman, G. L. Jones, and X.-L. Meng, *Handbook of Markov Chain Monte Carlo: Methods and Applications*. Chapman and Hall/CRC, 2014/03/07, 2011. `http://dx.doi.org/10.1201/b10905-1`. Cited on page 119.

[208] E. Blaufuss, G. Guillian, Y. Fukuda, *et al.*, “16N as a calibration source for Super-Kamiokande,” *Nuclear Instruments and Methods in Physics Research Section A: Accelerators, Spectrometers, Detectors and Associated Equipment* **458** no. 3, (2001) 638 – 649. `http://www.sciencedirect.com/science/article/pii/S0168900200009001`. Cited on page 121.

[209] M. Nakahata, Y. Fukuda, T. Hayakawa, *et al.*, “Calibration of super-kamiokande using an electron linac: The super-kamiokande collaboration,” *Nuclear Instruments and Methods in Physics Research Section A: Accelerators, Spectrometers, Detectors and Associated Equipment* **421** no. 1–2, (1999) 113 – 129. `http://www.sciencedirect.com/science/article/pii/S0168900298012005`. No cited.

[210] **Super-Kamiokande Collaboration** , Y. Ashie, J. Hosaka, K. Ishihara, *et al.*,

"Measurement of atmospheric neutrino oscillation parameters by super-kamiokande i," *Phys. Rev. D* **71** (Jun, 2005) 112005. `http://link.aps.org/doi/10.1103/PhysRevD.71.112005`. Cited on pages 121 and 128.

[211] K. Iyogi, S. Nakayama, and Y. Obayashi, "T2K data acquisition and FC event selection at Super-Kamiokande," *T2K-TN-027* (2011) . `http://www.t2k.org/docs/technotes/027`. Cited on page 121.

[212] J. Hignight, A. Himmel, J. Imber, *et al.*, "Super-Kamiokande events and data quality studies for T2K Run4," *T2K-TN-148* (2013) . `http://www.t2k.org/docs/technotes/148`. Cited on pages 121, 127, and 149.

[213] R. Patterson, E. Laird, Y. Liu, *et al.*, "The extended-track event reconstruction for miniboone," *Nuclear Instruments and Methods in Physics Research Section A: Accelerators, Spectrometers, Detectors and Associated Equipment* **608** no. 1, (2009) 206 – 224. `http://www.sciencedirect.com/science/article/pii/S0168900209012480`. Cited on page 122.

[214] S. Berkman, P. de Perio, A. Konaka, *et al.*, "fiTQun: A New Reconstruction Algorithm for Super-K," *T2K-TN-146* (2013) . `http://www.t2k.org/docs/technotes/146`. Cited on pages 122, 123, 129, and 192.

[215] L. Michel, "Interaction between four half-spin particles and the decay of the -meson," *Proceedings of the Physical Society. Section A* **63** no. 5, (1950) 514. `http://stacks.iop.org/0370-1298/63/i=5/a=311`. Cited on page 124.

[216] S. Berkman, P. de Perio, A. Konaka, *et al.*, "Data/Monte Carlo Simulation

Comparisons with fiTQun v3r1," *T2K-TN-153* (2013) . `http://www.t2k.org/docs/technotes/153`. Cited on pages 127, 192, and 195.

[217] L. K. Pik, *Study of the neutrino mass hierarchy with the atmospheric neutrino data observed in Super-Kamiokande*. PhD thesis, University of Tokyo, 2012. Cited on page 128.

[218] J. Kameda, "Updated study of the systematic error in ν_μ disappearance analysis from Super-Kamiokande," *T2K-TN-159-v2* (2013) . `http://www.t2k.org/docs/technotes/159/2nddraft/view`. Cited on pages 143 and 144.

[219] T. Mueller and S. Mine, "SK π^0 systematic errors for ν_e analysis with T2K 6.4×10^{20} POT (RUN1-4) data," *T2K-TN-156* (2013) . `http://www.t2k.org/docs/technotes/156`. Cited on page 143.

[220] J. Kameda and R. Wendell, "Study on Super-K events and systematic errors relevant for the ν_μ disappearance analysis with T2K 3.23×10^{19} POT data," *T2K-TN-034* (2010) . `http://www.t2k.org/docs/technotes/034`. Cited on page 143.

[221] Y. Nishimura and H.-K. Tanaka, "Super-K systematic uncertainties for the νe analysis with T2K 6.393×10^{20} POT (RUN1-4) data," *T2K-TN-157* (2013) . `http://www.t2k.org/docs/technotes/157`. Cited on page 143.

[222] **T2K Collaboration** , K. Abe, J. Adam, H. Aihara, *et al.*, "Measurement of neutrino oscillation parameters from muon neutrino disappearance with an off-axis beam," *Phys. Rev. Lett.* **111** (Nov, 2013) 211803. `http://link.aps.org/doi/10.1103/PhysRevLett.111.211803`. Cited on page 147.

[223] C. Bojechko, *Simultaneous Analysis of Near and Far Detector Samples of the T2K Experiment to Measure Muon Neutrino Disappearance*. PhD thesis, University of Victoria, 2013. Cited on page 147.

[224] A. Kaboth, R. Calland, and D. Payne, "Joint ND280 and SK 3-flavor oscillation fit using Markov Chain Monte Carlo (MaCh3)," *T2K-TN-171* (2014) . `http://www.t2k.org/docs/technotes/171`. Cited on pages 147, 154, and 157.

[225] **(T2K Collaboration)** , K. Abe, J. Adam, H. Aihara, *et al.*, "Measurement of the intrinsic electron neutrino component in the T2K neutrino beam with the ND280 detector," *Phys. Rev. D* **89** (May, 2014) 092003. `http://link.aps.org/doi/10.1103/PhysRevD.89.092003`. Cited on page 149.

[226] K. Hagiwara, N. Okamura, and K.-i. Senda, "The earth matter effects in neutrino oscillation experiments from Tokai to Kamioka and Korea," *JHEP* **1109** (2011) 082, `arXiv:1107.5857 [hep-ph]`. Cited on page 152.

[227] **Particle Data Group** , J. Beringer, J. F. Arguin, R. M. Barnett, *et al.*, "Review of particle physics (2013 partial update for the 2014 edition),". `http://pdg.lbl.gov/2013/tables/rpp2013-sum-leptons.pdf`. Cited on pages 152, 154, 159, and 162.

[228] M. Hartz, A. Kaboth, and K. Mahn, "Constraining the Flux and Cross Section Models with Data from the ND280 Detector for the 2013 Oscillation Analysis," *T2K-TN-166* (2013) . `http://www.t2k.org/docs/technotes/166`. Cited on pages 153 and 154.

[229] P. Mills, "Efficient statistical classification of satellite measurements," *International Journal of Remote Sensing* **32** no. 21, (2014/03/07, 2011) 6109–6132. `http://dx.doi.org/10.1080/01431161.2010.507795`. Cited on page 157.

[230] A. Gelman, X.-L. Meng, and H. Stern, “Posterior predictive assessment of model fitness via realized discrepancies,” *Statistica Sinica* **6** (1996) 733–759. Cited on page 157.

[231] **Super-Kamiokande** , A. Himmel, “Recent Atmospheric Neutrino Results from Super-Kamiokande,” `arXiv:1310.6677 [hep-ex]`. Cited on pages 157 and 159.

[232] M. Friend and M. Ikeda, “Future Sensitivity Task Force – Three Flavor Log Likelihood Fitter using a Realistic Systematic Error Covariance Matrix,” *T2K-TN-151* (2013) . `http://www.t2k.org/docs/technotes/151`. Cited on page 163.

[233] M. Bass, D. Cherdack, and R. Wilson, “Future Sensitivity to the Neutrino Oscillation Parameters for T2K and NOνA,” *T2K-TN-167* (2013) . `http://www.t2k.org/docs/technotes/167`. Cited on pages 164 and 165.

[234] K. Abe, T. Abe, H. Aihara, *et al.*, “Letter of Intent: The Hyper-Kamiokande Experiment — Detector Design and Physics Potential —,” `arXiv:1109.3262 [hep-ex]`. Cited on page 166.

[235] D. Ashery *et al.*, “True absorption and scattering of pions on nuclei,” *Phys. Rev. C* **23** no. 5, (1981) 2173. Cited on pages 168, 173, and 183.

[236] D. Ashery *et al.*, “Inclusive pion single-charge-exchange reactions,” *Phys. Rev. C* **30** no. 3, (1984) 946. Cited on pages 168, 173, 183, and 187.

[237] C. H. Q. Ingram *et al.*, “Quasielastic scattering of pions from ^{16}O at energies around the $\Delta(1232)$ resonance,” *Phys. Rev. C* **27** no. 4, (1983) 1578. Cited on pages 169, 172, 173, 183, and 190.

[238] S. A. Wood *et al.*, “Systematics of inclusive pion double charge exchange in the

delta resonance region," *Phys. Rev. C* **46** no. 5, (1992) 1903. Cited on pages 169, 173, and 187.

[239] S. M. Levenson *et al.*, "Inclusive pion scattering in the Δ(1232) region," *Phys. Rev. C* **28** no. 1, (1983) 326. Cited on pages 172 and 173.

[240] R. Giannelli *et al.*, "Multiproton final states in positive pion absorption below the Δ(1232) resonance," *Phys. Rev. C* **61** (2000) 054615. Cited on page 173.

[241] K. Nakai *et al.*, "Measurements of Cross Sections for Pion Absorption by Nuclei," *Phys. Rev. Lett.* **44** no. 22, (1979) 1446. Cited on page 173.

[242] I. Navon *et al.*, "True absorption and scattering of 50 MeV pions," *Phys. Rev. C* **28** no. 6, (1983) 2548. Cited on page 173.

[243] T. J. Bowles *et al.*, "Inclusive ($\pi^{\pm}$, π^{0}) reactions in nuclei," *Phys. Rev. C* **23** no. 1, (1981) 439. Cited on page 173.

[244] F. Binon *et al.*, "Scattering of negative pions on carbon," *Nucl. Phys. B* **17** (1969) 168. Cited on page 173.

[245] R. Miller, "Inelastic Scattering of 150 MeV Negative Pions by Carbon and Lead," *Il Nuovo Cimento* **6** no. 4, (1957) 882. Cited on page 173.

[246] M. K. Jones *et al.*, "Pion absorption above the Δ(1232) resonance," *Phys. Rev. C* **48** no. 6, (1993) 2800. Cited on page 173.

[247] C. J. Gelderloos *et al.*, "Reaction and total cross sections for 400 to 500 MeV π^{-} on nuclei," *Phys. Rev. C* **62** (2000) 024612. Cited on page 173.

[248] M. Crozon *et al.*, "Etude de la diffusion π-noyau entre 500 et 1300 MeV," *Nucl. Phys.* **64** (1964) 567. Cited on page 173.

[249] T. Takahashi *et al.*, "$\pi^- -^{12} c$ elastic scattering above the δ resonance," *Phys. Rev. C* **51** no. 5, (1995) 2542. Cited on page 173.

[250] B. W. Allardyce *et al.*, "Pion reaction cross sections and nuclear sizes," *Nucl. Phys. A* **209** (1973) 1. Cited on page 173.

[251] J. W. Cronin *et al.*, "Cross Sections of Nuclei for High-Energy Pions," *Phys. Rev.* **107** no. 4, (1957) 1121. Cited on page 173.

[252] Y. Fujii *et al.*, "Quasielastic π^--nucleus scattering at 950 MeV/c," *Phys. Rev. C* **64** (2001) 034608. Cited on page 173.

[253] K. Aoki *et al.*, "Elastic and inelastic scattering of π^+ and π^- on ^{12}c at 995 MeV/c," *Phys. Rev. C* **76** (2007) 024610. Cited on page 173.

[254] N. Grion *et al.*, "Pion production by pions in the $^{16}\mathrm{O}(\pi^+, \pi^+\pi^-)$ reaction at $T_{\pi^+} = 280$ MeV," *Nucl. Phys. A* **492** (1989) 509. Cited on page 173.

[255] A. Rahav *et al.*, "Measurement of the $^{12}\mathrm{c}(\pi, 2\pi)$ Reactions and Possible Evidence of a Double-Δ Excitation," *Phys. Rev. Lett.* **66** no. 10, (1991) 1279. Cited on page 173.

[256] R. Arndt *et al.*, "Analysis of pion photoproduction data," *Phys. Rev. C* **66** (2002) 055213. Cited on page 174.

[257] K. G. Fissum *et al.*, "Inclusive positive pion photoproduction," *Phys. Rev. C* **53** no. 3, (1996) 1278. Cited on pages 174 and 176.

[258] N. Abgrall *et al.*, "Neutrino Flux Prediction for the 2010a Analysis ," *T2K-TN-038 (Internal)* (2010) . Cited on page 186.

[259] P. de Perio *et al.*, "NEUT Nuclear Effects (FSI)," *T2K-TN-033 (Internal)* (2010) . `http://www.t2k.org/docs/technotes/033`. Cited on pages 188 and 191.

[260] P. de Perio and J. Imber, “Super-K Systematic Uncertainties for RUN1-4 Joint ν_e + ν_μ Analyses,” *T2K-TN-186* (2014) .

`http://www.t2k.org/docs/technotes/186`. Cited on page 207.